Gold mineralization in the Um El Tuyor area, South Eastern Desert, Egypt: geologic context, characteristics and genesis

Inaugural-Dissertation
zur Erlangung der Doktorwürde
an der Fakulät für Geowissenschaften
der Ludwig-Maximilians-Universität München

vorgelegt von

Basem Ahmed Zoheir

München, 05 Mai 2004

Gold mineralization in the Um El Tuyor area, South Eastern Desert, Egypt: geologic context, characteristics and genesis

by

Basem Ahmed Zoheir

A thesis submitted in partial fulfillment
of the requirements for the award of the degree of
DOCTOR in GEOLOGY

Faculty of Earth Sciences,
University of Munich
May 2004

CONTENTS

LIST OF FIGURES

LIST OF TABLES

ACKNOWLEDGEMENTS

ABSTRACT

This thesis reports petrographic, mineralogical and geochemical data that constrain the hydrothermal alteration and gold mineralization in the Um El Tuyor area, SE Egypt. In order to distinguish the characteristics and envisage the genesis of gold mineralization in the study area, insights into the geologic context, structural evolution and geochemistry of the country rocks are provided. The geochemical investigations have been integrated with field and petrographic relationships, along with Landsat (TM) imagery interpretations to better constraints on the tectonic setting of the basement complex in the study area.

The particular geographic location near the intersection of two major high strain zones, namely the Allaqi-Heiani suture and Hamisana Shear Zone, played a crucial role in the deformation history of the Um Tuyor area. The basement complex cropping out in the Um El Tuyor area is part of the Neoproterozoic Allaqi-Heiani ophiolitic belt, comprising allochtonous ophiolitic thrust slices and detached sheets, island arc volcano-sedimentary-plutonic assemblages, and syn-orogenic and post-orogenic intrusions. The ophiolitic rocks exhibit field and geochemical characteristics that make them akin to the supra-subduction zone ophiolites, formed most likely in a back-arc basin. The island arc assemblage comprises mainly calc-alkaline metavolcanic-plutonic rocks and back-arc pelitic metasediments. Early calc-alkaline granite intrusions tapered along the foliation and thrust planes during the orogenic episodes, whereas less fractionated tholeiitic olivine gabbro and peraluminous monzogranite encompass a course of post-orogenic plutonism evolved in a within plate setting.

An early period of crustal shortening (Dm) involved transportation and overriding of huge ophiolitic sheets from the north to south is manifested by major thrust faults and imbricate ophiolitic thrust slices. Regional folds and pervasive foliation cleavage signify a NE-SW compressional regime (D2) superimposed on the thrust fabrics. A third deformation increment is indicated by the presence of abundant NNW-trending major folds and left-lateral faults superimposed on the older structural fabrics (D3). D4 records an episode of transcurrent deformation yielded slip reactivation of the pre-existing NW-trending faults and formation of discrete shear zones, one of which accommodates gold mineralization in the study area. Finally, a weak shear strain (D5) is indicated by the intersecting fault and joint trends traversing the post-orogenic rocks. Regional metamorphism was coeval with deformation, and peaked under conditions of amphibolite facies during D2. Geothermobarometry calculations point to temperatures of 534-561°C and pressure of 5.26-6.20 kbar for the peak of the metamorphic path of Um El Tuyor basement.

Gold is mainly confined to the quartz veins and less commonly to narrow domains of the next quartz-sericite alteration zones. Field, microscopic and microprobe observations suggest that hydrothermal alteration in the Um El Tuyor mine area was post-peak metamorphism, and syn-kinematic with local shearing. The main auriferous veins in the Um El Tuyor mine area consist of massive, partially recrystallized, or laminated quartz ±carbonate. The quartz-carbonate veins are essentially fault-fill bodies, which have been fractured and re-filled with milky to grey laminated quartz in later stages of the geothermal system. The laminated quartz veins contain narrow elongate slivers of the host pelitic rocks (composed essentially of chrorite-sericite-sulphides±graphite), assumed to have been peeled off and incorporated during incremental (crack-seal) vein growth.

Gold occurs as inclusions or within the lattice in arsenopyrite and arsenian pyrite, commonly in association with subordinate sphalerite, chalcopyrite, and pyrrhotite in the auriferous quartz veins. Another, high fineness type of gold fills microfractures in sulphides and quartz, and/or occurs as dispersed blebs and globules in domains of pervasive alteration, particularly where sericite and carbonate are intergrown. In the mine area, a metal zonation extends from an inner Fe-As-Zn-Au ±Pb±Ag±Te bearing veins through an intermediate Fe-As-Cu rich wallrocks to a distal halo enriched in Fe-Cu-Co, and Ni.

A three stage hydrothermal alteration model (initial, transitional and advanced) is proposed for the Um El Tuyor ore-forming hydrothermal system, on basis of the field and microscopic observations and the electron microprobe data. The initial stage involved hydrolysis of the wallrocks in presence of a near acid fluid, whose pH was buffered by the wallrock mineralogy. The transitional stage involved also hydrolysis reactions, but was dominated by carbonatization, sulphidation and redox reactions. The latter reduced the interacting fluids, particularly where the fluid : rock ratio was low and provided favourable conditions for gold deposition. It is interpreted that sulphidation has affected the gold solubility via changes in oxygen fugacity through redox reactions. The advanced stage was most likely a phase of intense sericitization (after chlorite), which consumed K^+, liberated H^+, and buffered the solution pH. Cation-exchange reactions were limited to the time when favoured Na^+ activity and temperature conditions promoted deposition of albite. Sulphidation remained operating through this stage, and the un-buffered conditions were locally attained under high fluid/rock ratios.

Compositional zoning of the auriferous pyrite and arsenopyrite crystals, along with the presence of patchy pyrrhotite and sphalerite inclusions in these crystals, and the absence of these features in pyrite and arsenopyrite of the late sulphide assemblage may imply incipient low oxygen fugacity conditions during gold deposition. Further, compositional zoning of the large arsenian pyrite crystals, from barren cores to auriferous margins, is considered as a function of redox reactions involving oxidation of Au and reduction of As.

Fluid inclusion studies revealed heterogeneous entrapping of immiscible aqueous and carbonic fluids in the Um El Tuyor auriferous quartz veins. Criteria including the primary and secondary modes of occurrence of the carbonic inclusions, coexistence of inclusions with carbonic and aqueous fluids of variable relative proportions, densities, filling degrees, partial homogenization temperatures, and bulk compositions are considered evocative for phase separation as gold deposition mechanism in the Um El Tuyor auriferous quartz veins. The initially homogenous ore fluid was likely a low salinity aqueous-carbonic solution (±1-2 mol% CH_4 or N_2), which started to separate into two phases and precipitate gold when conditions attained ~340°C at ~1.5 kbar (at depth of ~6 km under lithostatic condition). Destabilization of gold-sulphur complexes through interplay of cooling, redox state variation, pH changes, and decrease in sulphur fugacity should have contributed in gold deposition in the auriferous veins. The entire gold-base metal mineralization and quartz veining event extended over conditions of 170-429°C at 0.9-2.1 kbar respectively, equivalent to depths of 3-8 km and compatible with crustal conditions of greenschist metamorphism and brittle–ductile transition. This wide range of pressure probably represents the total fluid pressure regime within the shear zone from the formation of the auriferous quartz veins to periods of continuous pressure decrease during uplift, including a sudden pressure decrease occurred as a consequence of incremental opening of the fissure, followed by filling by newly deposited quartz.

Kurzfassung

Diese Dissertation beschreibt die petrographischen, mineralogischen und geochemischen Hintergründe, die zur Goldmineralisation und zur hydrothermalen Nebengesteinsalteration im Gebiet von Um El Tuyor, Südost Ägypten beigetragen haben. Um jedoch die genetischen Hintergründe und Charakteristika der Goldmineralisation im Untersuchungsgebiet näher zu verstehen, bedarf es zunächst einer eingehenden Analyse der geologischen Zusammenhänge, der strukturgeologischen Entwicklungsgeschichte und Geochemie der gesamten Nebengesteinsabfolgen. Die geochemischen Auswertungen wurden in die Feldarbeiten und die petrographischen Untersuchungen eingebunden, ebenso die Satellitenbildinterpretationen (TM-Szenen) zum besseren Verständnis der Tektonik des Grundgebirges im Untersuchungsgebiet.

Die spezielle geographische Position des Um El Tuyor Gebietes im Umfeld der Überschneidung von zwei „high strain" Suturzonen, nämlich des Allaqi-Heiani Gürtels und der von Süden kommenden Hamisana Zone trug wesentlich sowohl zu deren komplexen Deformationsgeschichte als auch Lagerstättengenese bei. Der anstehende Grundgebirgskomplex des Um El Tuyor Gebietes stellte sich als ein Teil des Neoproterozoischen Allaqi-Heiani Ophiolit Gürtels heraus, der aus allochtonen ophiolitischen Überschiebungspartien und abgesonderten Schuppen vulkano-sedimentärer und plutonischer Abfolgen vom Inselbogentyp sowie syn-und post-orogener Intrusionen besteht. Die ophiolitischen Gesteine lassen sich sowohl nach den Geländedaten als auch geochemisch als Supra-Subduktionszonen-Ophiolite eines Back-Arc Beckens deuten. Während des Pan-African (Spätes Proterozoikum) wurden diese Ophiolite transportiert, durch mittlere bis steile Verfaltung verkürzt und verschuppt wobei sie immature Inselbogenabfolgen mit zwischengeschalteten Back-Arc Metasedimenten überlagerten. Die Inselbogenabfolge besteht hauptsächlich aus kalk-alkalinen metavulkanisch-plutonischen Gesteinen und pelitischen Back-Arc Metasedimenten. Frühe kalk-alkaline Granitintrusionen drangen entlang der Faltungs- und Überschiebungflächen während der orogenen Episoden ein, wohingegen tektonisch weniger beanspruchte Olivin-Gabbros und Peraluminium-Mozogranite sich als postorogene Plutonite mit einer „Within plate" Affinität darstellen.

Eine frühe Krustenverkürzungsperiode (Dm) verursachte den Transport und die Überschiebung mächtiger ophiolitischer Decken von Nord nach Süd. Die Deformation ist Hauptüberschiebungsbahnen und durch verschuppte ohiolitische Splitter belegt. Regionale Störungen und Foliationsflächen, den Deckenbau überlagern deuten auf ein NE-SW verlaufendes Kompressionsregime (D2) hin.. Eine dritte Deformatiosphase (D3) wird durch zahlreiche NNW verlaufende größere Störungen und linkslaterale Verfaltungen repräsentiert, die älteren Strukturelemente überprägt. weist auf Eine Episode querverlaufender Deformation (D4), die zur Reaktivierung präexistenter NW-gerichtete Störungen und der Bildung diskreter Scherzonen führte, beherbergt einen Teil der Goldführung im Untersuchungsgebiet. Schließlich verursachte eine schwache Scherrichtung (D5) die Störungs- und Kluftrichtungen der post-orogenen Plutonite. Die Regionalmetamorphose fand gleichzeitig mit der Deformation statt und hatte während der D2-Phase unter amphibolitfaziellen Bedingungen ihren Höhepunkt. Geothermobarometrischen Berechnungen deuten auf Temperaturen von 534-561°C und Drücken von 5.26-6.20 kbar während dieses Metamorphose Maximums .

Die Goldmineralisation ist im Wesentlichen auf Quarzgänge und gelegentlich auf schmale Bereiche der gangnahen Quarz-Serizit Alterationszonen beschränkt. Feldbeobachtungen, mikroskopische und Mikrosonden-Analysen ergaben, dass die hydrothermale Alteration im Gebiet der Um El Tuyor Mine nach dem Höhepunkt der Metamorphose und syn-kinematisch mit lokalen Zerscherungen stattfand. Die wichtigsten goldhaltigen Quarzgänge im Minengebiet von Um El Tuyor sind massiv, teilweise rekristallisiert oder lamelliert. Sie bestehen hauptsächlich aus Quarz-Karbonat-Gängen, die zerbrochen und mit milchigem bis grau lamellierten Quarz späterer Phasen des geothermalen Systems aufgefüllt sind. Die lamellierten Quarzgänge enthalten schmale, ausgelängte Einschlüsse des pelitischen Nebengesteins (bestehend vorwiegend aus Chlorit-Serizit-Sulfiden$\pm$Graphit), die vermutlich während des Aufspaltens der Gänge abgerissen und eingeschlossen wurden (Crack-seal Vorgang).

Gold tritt in den goldführenden Gängen als Einschlüsse oder im Kristallgefüge in Arsenkies und arsenhaltigem Pyrit auf, gewöhnlich in Verbindung mit untergeordnet Zinkblende, Kupferkies und Magnetkies. Ein weiterer hochreiner Goldtyp füllt Mikrorisse in Sulfiden und Quarz und/oder tritt als disperse Bläschen und Kügelchen in Bereichen mehrfacher Alteration besonders bei Verwachsungen mit Serizit und Karbonat auf. Im Minengebiet lässt sich eine Zonierung vom Fe-As-Zn-Au$\pm$Pb$\pm$Ag$\pm$Te-haltigen Inneren der Gänge über ein Fe-As-Cu-haltiges Zwischenbereich und in einen distalen Rand mit Fe-Cu-Co und Ni beobachten.

Ein dreistufiges Alterationsmodell (frühes, Übergang- und fortgeschrittenes Stadium) wird für das erzbringende Hydrothermalsystem von Um El Tuyor vorgeschlagen. Das frühe Stadium bewirkt eine Nebengesteinshydrolyse in Gegenwart eines schwach sauren Fluids, dessen pH durch die Nebengesteinsmineralogie gepuffert wird. Während des Übergangsstadiums kommt es zu ebenfalls Hydrolysereaktionen, es dominieren jedoch Karbonatisierung und Sulfidisierung neben Redoxreaktionen. Letztere reduzierten die Fluide vor allem dort, wo das Fluid/Gesteins Verhältnis niedrig war und stellten damit günstige Bedingungen zur Goldfällung dar. Es lässt sich folgern, dass die Sulfidisierung die Goldlöslichkeit über die Änderung der Sauerstofffugazität als Folge der Redoxreaktionen beeinflusst hat. Das fortgeschrittene Stadium stellte höchstwahrscheinlich eine Phase intensiver Serizitisierung nach Chlorit dar, die K+ verbrauchte, H$^+$ erzeugte und den pH-Wert der Lösung erniedrigte. Kationenaustauschreaktionen waren auf die Zeiten günstiger a_{Na}^+/a_K^+ und Temperaturbedingungen beschränkt, die Albitbildung ermöglichten. Sulfidisierung fand weiterhin während dieses Stadiums statt und ungepufferte Bedingungen waren lokal bei hohen Fluid/Gesteins Verhältnissen wirksam.

Chemische Zonierung der goldhaltigen Pyrit- und Arsenkieskristalle in Gegenwart kleiner Einschlüsse von Magnetkies und Zinkblende in diesen Kristallen und das Fehlen derartiger Verwachsungen im Pyrit und Arsenkies der späten Sulfidabfolge dürfte mit einer beginnenden niedrigeren Sauerstofffugazität während der Goldablagerung zu erklären sein. Weiterhin wird der chemische Übergang großer arsenführender Pyritkristalle von den tauben inneren Gangkernen zu den goldführenden Randbereichen als eine Funktion der Redoxreaktionen angesehen, die eine Oxidation der Goldkomplexe und Arsenreduktion bewirken.

Untersuchungen der Flüssigkeitseinschlüsse ergaben heterogene Einschlüsse nicht mischbarer, wässriger und kabonischer (CO_2-dominierter) Fluide in den goldführenden Quarzgängen von Um El Tuyor. Kriterien wie primäre und sekundäre Formen der karbonischen Einschlüsse, die Koexistenz von Einschlüssen mit karbonischen und wässrigen Fluiden in unterschiedlichen Verhältnissen, Dichten, Füllungsgrad, partialen Homogenisationstemperaturen und Zusammensetzungen weisen auf eine Phasentrennung als Mechanismus der Goldfällung in den goldführenden Quarzgängen von Um El Tuyor hin. Das ursprünglich homogene, erzbringende Fluid war eine gering salinare wässrig-karbonische Lösung ($\pm$1-2 mol% CH_4 oder N_2) das sich in zwei Phasen zu separieren und Gold auszuscheiden begann als die Druck-Temperaturbedingungen von ~340°C bei ~ 1.5 kbar erreicht wurden (bei Tiefen von ~6 km unter lithostatischen Gegebenheiten). Der Zerfall der Gold-Schwefel Komplexe durch das Wechselspiel von Abkühlung, Änderung des Redoxpotentials und pH-Wertes und Abnahme der Schwefelfugazität haben mit großer Wahrscheinlichkeit zur Goldmineralisation der Gänge geführt. Die gesamte Gold-Buntmetallmineralisation und die Bildung des Quarzgangsystems entstand bei Bedingungen von 170-429°C und 0.9-2.1 kbar, d.h. wahrscheinlich in einer Tiefe von 3-8 km und unter Bedingungen der Grünschiefermetamorphose im Übergang von duktiler zu spröder Deformation. Der weite Druckbereich steht vermutlich für das gesamte Fluiddruckregime innerhalb der Scherzone. Er beinhaltet die Bildung der goldhaltigen Quarzgänge während Perioden kontinuierlicher Druckabnahme als Folge des Aufstieges und ebenso plötzlichen Druckabfalls als Folge zunehmender Rissöffnungen, gefolgt von Verfüllungen neuerlich gebildeten Quarzes.

CHAPTER 1

INTRODUCTION & GEOLOGY

1 INTRODUCTION & GEOLOGY

1.1 Introduction

The present study addresses the characteristics and genesis of gold mineralization in the Um El Tuyor area, South Eastern Desert of Egypt. Manifestations of the ore-forming hydrothermal system, distribution and geometry of the auriferous quartz veins, and structural context of the mineralization have been investigated. The study is aimed at determining the relationships among alteration, veining and mineralization, with respect to the local and regional geologic and structural contexts.

As a prerequisite to start this study, a detailed geological map was prepared, based on field observations, aerial photographs and Landsat (TM) images of appropriate scales. Petrography, geochemistry, deformation and metamorphism of the country rocks have been studied. Although these topics were subjects of numerous studies at regional scales in the west of the Um El Tuyor area (e.g. Kröner et al., 1987; Sadek, 1994; Stern, 1994; Abdelsalam and Stern, 1996, El Shimi, 1996, etc.), detailed geological information, critical to tie gold mineralization with the geologic evolution of the area, did not previously exist.

Investigations including mineralogy, geochemistry and microthermometry of the auriferous quartz veins are carried out in order to elucidate the genesis and evolution of the hydrothermal fluid and the probable source of the ore fluid in the Um El Tuyor mine area.

1.2 Methodology

In order to achieve the envisaged goals, the following was carried out:

- Field work was accomplished during a number of field campaigns, and the geological map (1:100,000) was compiled from field data, aerial photographs at a scale of 1:40,000, topographic sheets at a scale of 1:50,000, and Landsat (TM) images.
- The mine maps have been prepared by compiling field data and aerial photographs at a scale of 1:20,000. Locations of samples were determined using the GPS readings.
- More than 175 rock samples representing the various rock units were collected outside the mine area for petrographic and petrochemical studies.
- About 300 samples from the mine area have been collected according to a grid crossing the vein system, normal to the main foliation direction in Um El Tuyor mine area. The sample set includes mineralized quartz veins and different alteration types.
- The structural data, including orientation of faults, fold axes, boudinage structures, foliation, cleavage, lineation, slickensides, and grooves have been documented.
- In order to elucidate the paragenetic relationships among the different deformation, metamorphic and hydrothermal events, more than 200 thin sections representing the different rock units were microscopically examined.
- Sixty nine samples from outside the mine area were analyzed for their major, trace and rare earth elements to investigate the geochemical characteristics of the different rocks units.
- Major, trace and rare earth elements composition of 14 samples, collected from the different alteration types within the Um El Tuyor mine have been determined. Chemical comparison between the altered and least-altered host rocks, along with the mass balance calculations on the basis of whole-rock geochemistry, is

done. Based on the petrographic and geochemical findings, the likely mechanism caused alteration of these rocks during the ore-forming hydrothermal events is speculated (and/or modelled).

- Ore microscopy studies of the mineralized quartz veins and the altered wallrocks were performed to elucidate the paragenetic relationships among ore and gangue minerals.

- Electron microprobe technique was employed to determine mineral chemistry of the metamorphic and hydrothermal mineral phases. Based on the obtained data, geothermobarometry of metamorphism, and nature of the hydrothermal solution were determined. Back-scattered imaging was applied to visualize sub-microscopic textures and further investigate paragenetic relationships between ore and gangue minerals.

- Fluid inclusion studies were carried out on the auriferous vein quartz in an attempt to elucidate the characteristics and evolution of the mineralizing fluid, to assess possible mechanisms that were responsible for gold deposition and to drive the pressure-temperature conditions of mineralization.

1.3 The study area

The Um El Tuyor area is situated in the extreme south of the Eastern Desert of Egypt, between latitudes 22º 05` N and 22º 25`N and longitudes 34º 27`E and 34º 50`E, near the border with Sudan (Figs. 1.1, 1.2). The area extends over approximately 1000 km^2, in the eastern part of the Wadi Allaqi region. It is covered by two topographic sheets namely; Gebel Um El Tuyor El Foqani and Gebel Jugub*. The area is characterized by a moderate to high mountainous topography in the central part, where elevation of the hills and mountainous peaks reach up to 975 m.a.s.l. In contrast, extensive areas underlain by eroded and intensively weathered granitoids form low lands in the northern part of the study area. The Um El Tuyor area is traversed by the E-W striking Wadi Defeit, which drains into the west in the main Wadi Allaqi. Gravel and boulders mixed with aeolian sands constitute the stream sediments and cover the gentle slopes of the hills.

1.4 Regional geologic context

The basement rocks of the NE Africa and Arabia are a continuation of those seen further south, forming the Mozambique belt (Holmes, 1951). These rocks are recognized to be strongly affected by the 'Pan-African thermo-tectonic episode' defined by Kennedy (1964), which was later proposed to encompass the time span between 900 and 450 Ma (Kröner, 1984). The Pan-African orogenic cycle has been documented as a period of major crustal accretion, where continental, island-arc, and oceanic terranes were brought together to form the crystalline basement of the African continent as part of a late Neoproterozoic supercontinent (Unrug, 1997). Although some parts of the Pan-African orogen are characterized by continental collision tectonics (Burke and Sengör, 1986; Stern, 1994), others are typical for accretionary orogens (see Windley, 1992, for definition). The Arabian–Nubian Shield (Al Shanti, 1979), the northeastern part of Africa–Arabia, is a typical example of accretionary orogens, with lateral accretion and suturing (Gass, 1981; Kröner, 1985; Kröner et al., 1987; Stern, 1994).

The basement complex of the Egyptian Eastern Desert, a part of the Arabian-Nubian Shield, forms a belt of rugged mountains widens southward into the Red Sea Hills (Stern, 1994). This basement complex is composed of a heterogeneous assemblage of metamorphosed (volcani)clastic successions and ophiolitic rocks intruded by voluminous granitic plutons (Bakor et al., 1976; Vail, 1983; Shackleton, 1988).

---

* drawn by the Egyptian Surveying Authority using aerial photographs taken in 1988 and revised according to the field observations till 1993

The Wadi Allaqi region, SE Egypt, was and still is subject of numerous regional scale investigations since it is considered as a key area for understanding the evolution of the Arabian-Nubian Shield (e.g. Kröner et al., 1987; Stern et al. 1989; Sultan et al., 1993; Taylor et al., 1993; Greiling et al., 1994; Sadek, 1994; Stern, 1994; Abdelsalam and Stern, 1996 and Kusky and Ramadan, 2002). These authors have referred the putative tectonic setting of the Wadi Allaqi region as a major shear or suture zone (i.e. Allaqi-Heiani suture). The latter marks a curvilinear ophiolitic belt, which can be followed for more than 200 km in the southern Eastern Desert of Egypt (Kröner et al., 1987). It extends from Gebel Heiani in the east, along Wadi Allaqi to the Lake of Nasser in the west. The WNW-trending Allaqi-Heiani suture separates the Gabgaba-Gebeit arc terranes in the south from the Gerf terrane in the north (Fig. 1.1). This structure is associated with the large Allaqi-Heiani-Gerf and Onib-Sol Hamed ophiolites in SE Egypt and NE Sudan (Kröner et al., 1987; Stern et al., 1989; Abdelsalam and Stern, 1996). Based on integrated field, Landsat TM and SIR-C/X SAR observations, Kusky and Ramadan (2002) suggested that the circa 750-720 Ma Allaqi-Heiani suture is an arc/arc collision zone, formed when the Gerf terrane overrode the Gabgaba terrane prior to closure of the Mozambique Ocean.
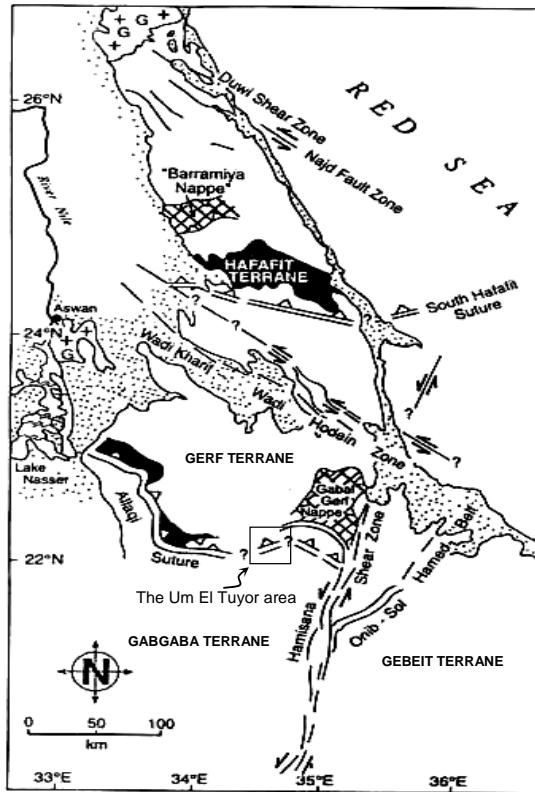
Fig. (1.1): Tectonic sketch map of the Arabian-Nubian Shield in eastern Egypt and northern Sudan (modified after Dixon et al., 1987, Kröner et al., 1987 and Greiling et al, 1994). The location of Um El Tuyor area through the Allaqi-Heiani suture is indicated.

In the Wadi Allaqi region, the basement complex is grouped into three tectono-stratigraphic units, namely; the ophiolitic association, island arc volcanic/volcano-sedimentary/plutonic assemblages, and late- to post-orogenic granitic intrusions (e.g. Kröner et al., 1987; Greiling et al., 1988; Taylor et al., 1993; Kusky and Ramadan, 2002, Abdelsalam et al., 2003, etc.).

LEGEND

- ⊗ Gold mine
- Shear zone
- Joint trend
- F₃ fold
- Strike slip fault
- F₂ fold
- Thrust fault
- Fₘ fold

- Alluvial deposit (Wadi filling)
- Muscovite-biotite granite } **Post orogenic intrusions**
- Olivine gabbro
- Syn-orogenic granitoid
- Island arc metagabbro
- Metavolcanoclastic rock
- Metavolcanic rock
- Metasedimentary rock

Island arc assemblage

- Talc carbonate, talc schist
- Metabasalt
- Amphibolite
- Tectonized serpentinite
- Massive serpentinite

Ophiolites and derivatives

Fig. (1.2): Geological map of the Um El Tuyor area, SE Egypt

Labels on map: A, A', B, B', G. Um El Tuyor El Tahtani, Wadi Maladuib, Wadi Um Teneqib, G. Al Adrag, G.Jugub, Bir Jugub, Wadi Defiet, G. Um El Tuyor El Foqani, Wadi Sohani, G. Sohani, 34° 45', 22° 20', 22° 10'

Scale: 0 — 2.5 — 5 km

Inset: RED SEA, EASTERN DESERT, RIVER NILE, Um El Tuyor area, SUDAN, 28°, 26°, 24°, 22°

Fig. (1.3): Geological cross-sections along A – A′ and B – B′ directions in Figure 1.2 (not to scale). Also given are the lower-hemisphere stereographic projections referring to the prominent foliations in the island arc domains.

1.5 Geology of the Um El Tuyor area

The basement complex cropping out in the Um El Tuyor area comprises mafic–ultramafic ophiolitic rocks, island arc-related metasedimentary-metavolcanic-plutonic assemblages, and syn- and post-orogenic intrusions. Figures 1.2 and 1.3 show the geological features and two cross sections traversing almost all of the exposed rock units in the Um El Tuyor area. The following is a detailed description of field observations and petrography of each of these litho-tectonic units.

1.5.1 The ophiolitic rocks

The ophiolitic rocks exposed in the study area include mainly serpentinite (still contains fresh peridotite remnants), amphibolite, metabasalt, and less commonly metagabbro. These ophiolitic units occur together in spatial association and form detached sheets embedded in a highly tectonized matrix. The ophiolitic sequence, which forms a structurally complex elongate belt in the central and south-western parts of the Um El Tuyor area, is made up of imbricate thrust sheets and slices of allochthonous, dismembered remnants of oceanic crust. The tectonized ultramafic rocks are characterized by pervasive serpentinization. However, a lherzolite and/or dunite composition is inferred in the less serpentinized rocks. The protolith mineralogy likely includes olivine, pyroxene, tremolitic amphibole, chlorite, chromite and magnetite.

1.5.1.1 Serpentinite

The serpentinite rocks occupy large areas and form conspicuous mountainous ridges with steep slopes (Figs. 1.4, 1.5). They occur also as lenses (~ 10 m long) embedded in a talc carbonate/talc schist matrix. The rock samples from summits are massive, while those collected from the topographically lower horizons are intensively deformed vuggy talc ankerite-serpentinite. Near thrust zones, the serpentinite rocks are listwanitized and contain sulphide minerals (i.e. pyrite). Weathering of the listwanitized serpentinite produces a distinctive bright orange color and a hackly surface, on which, quartz and carbonate veins forming a positive relief relative to the carbonate matrix. Relics of the less-tectonized ultramafic rocks are essentially composed of olivine, diopside and hypersthene with antigorite partially replacing olivine, and bastite replacing pyroxene (Figs. 1.6a,b). Pods or tectonic slivers of dunite and lherzolite are most likely the protoliths of these serpentinite rocks.

Fig. (1.4): Gebel Um El Tuyor El Foqani (looking SE): the hill in the background consists mainly of serpentinite, whereas the low relief foothills are composed of garnet-biotite schist.

Fig (1.5): Meshed serpentinite, partly replaced by talc and carbonate minerals. East of G. Um El Tuyor El Foqani (Looking W)

Petrographically, serpentinite is composed mainly of antigorite and subordinate chrysotile, talc, bastite and carbonate minerals. The antigorite occurs as large plates, fibrous and scaly aggregates. In places, antigorite forms interlocking meshes, enclosing cores of weakly birefrengent cryptocrystalline serpentine minerals (Fig. 1.6c,d). However, in some samples, the polygonal meshes are occupied by olivine or enstatite relics and fine magnetite grains. Chrysotile, if present, occurs as veinlets traversing the serpentinite. These veinlets are commonly less than 3 mm wide, but may reach up to 1 cm thickness. They account for less than 3 vol.% of the rock. The serpentine minerals, in general, are partially replaced by an association of talc, calcite, chlorite, magnetite and/or fibrous tremolite (Fig. 1.6e). The opaque minerals are commonly chromite (Fig. 1.6f) and iron oxides, occurring as shapeless aggregates and fine streaks.

1.5.1.2 Metagabbro

The metagabbro is exposed only in few, limited locations in the western part of the investigated area, south of Gebel Um El Tuyor El Tahtani. It occurs as small isolated masses of medium to fine-grained, mesocratic to melanocratic rocks. In places, these rocks show rhythmic graded layering. The metagabbro in the study area occurs also as coarse-grained cumulate rocks, particularly in spatial association with amphibolite. The metagabbro unit has tectonic (thrust) contacts against the underlying serpentinite. Generally, the metagabbro is deformed and metamorphosed under regional metamorphism of the greenschist facies conditions.

Microscopically, samples of the investigated metagabbro are composed essentially of actinolite, plagioclase, subordinate clinopyroxene, ilmenite, apatite and rutile. Plagioclase occurs as large poikilitic plates replaced almost completely by intergrown albite and epidote. Actinolite occurs as light green laths replacing more or less completely the clinopyroxene. Ilmenite and apatite occur as euhedral crystals enclosed in the large plagioclase and pyroxene plates, whereas rutile forms irregular blebs dispersed in the altered domains.

This metagabbro unit is comparable with the "Older Metagabbro" in Egypt, observed elsewhere and described by many authors (e.g. Basta and Takla, 1974; El Sharkawy & El Bayoumi, 1979; Shackleton et al., 1980; Takla et al., 1981; El Gaby, 1994; Abdel Khalek et al. 1992, etc.).
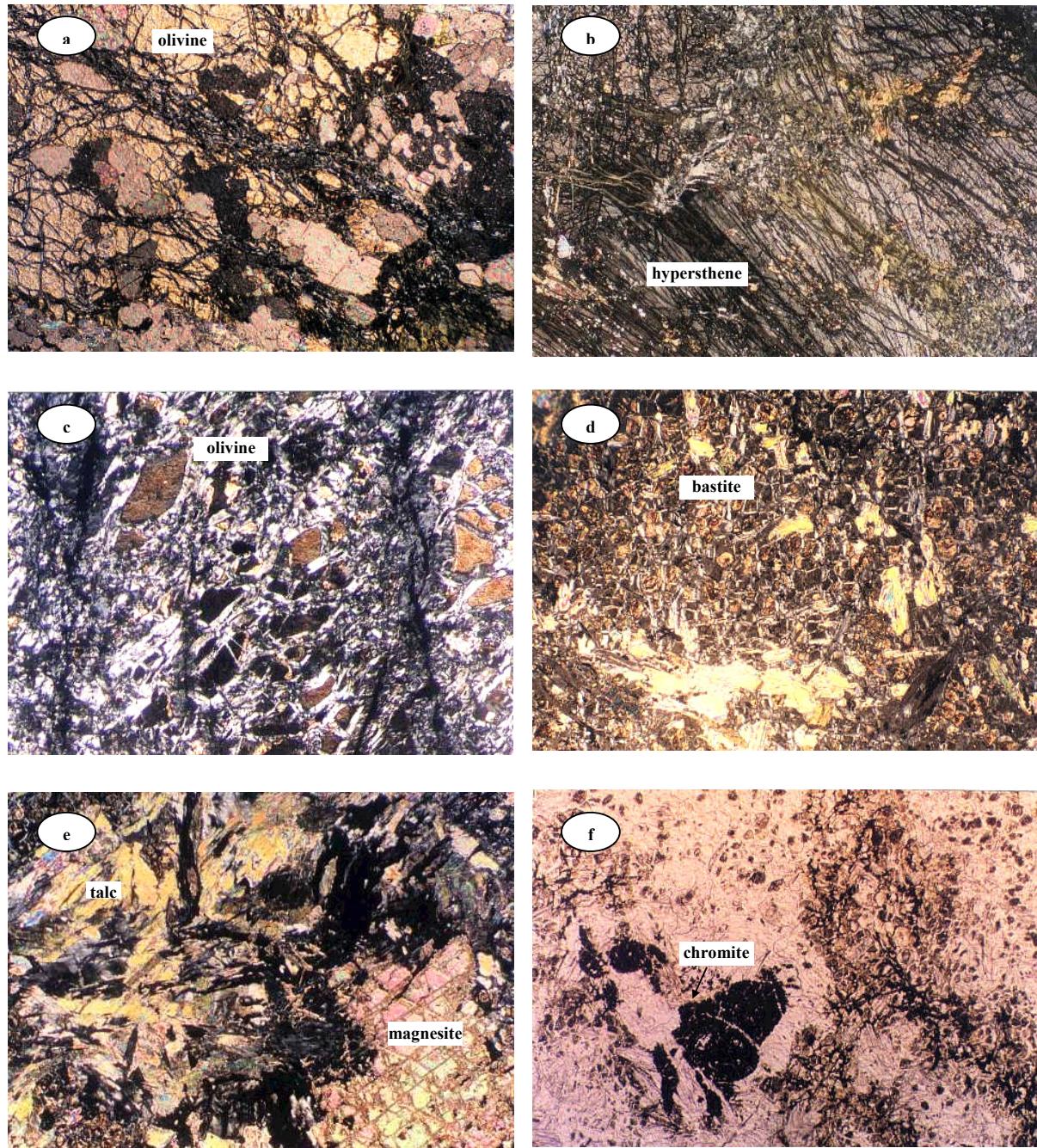
Fig. (1.6): Photomicrographs of the ultramafic rocks exposed in the Um El Tuyor area showing: a) deformed olivine porphyroblasts embedded in a groundmass of talc and subordinate chlorite, in a sample representing the preserved relics of ultramafites (XPL, crossed polarized light, field of view ~5.93 mm across); b) strongly deformed, cleaved hypersthene porphyroclast replaced partly by antigorite and talc (XPL, wide of view ~3.03 mm); c) meshed serpentinite with relics of olivine still preserved (XPL, wide of view ~3.03 mm); d) bastite and talc replacing serpentine and filling the interspaces between the antigorite laths (XPL, wide of view ~5.93 mm); e) talc flakes with anomalous birefringence colors, and white magnesite exhibiting the characteristic cleavage pattern replacing the serpentine minerals in highly tectonized serpentinite (XPL, wide of view ~5.93 mm); f) large chromite grain traversed by acicular talc flakes. The very fine magnetite streaks delineate the meshed texture (PPL, plane polarized light, wide of view ~5.93 mm).

1.5.1.3 Amphibolite

Amphibolite occurs as voluminous thrust-bounded sheets in association with the serpentinite and metabasalts units (Fig. 1.7). Sporadically, it occurs as extensional boudins, ~1–2 m thick and 2–4 m long embedded in a matrix of talc carbonate and talc schist along the thrust zones. The amphibolite rocks are, in general, fine- to medium-grained, and commonly foliated. Foliation is the result of preferred alignment of amphibole minerals and the alternating amphibole and plagioclase-quartz rich layers. Actinolite and tremolite are the dominant mineral phases, occasionally associated with chlorite and relics of hornblende. The actinolite plates are weakly pleochroitic from pale green to pale brownish green, whereas, and tremolite is colorless to pale grey (Fig. 1.8a). Plagioclase (An_{55-65}) constitutes ~10 vol. % of the rock, occurring as interstitial prismatic plates or occasionally as recrystallized ribbons. Some plagioclase crystals are partially replaced by epidote and calcite. Along contacts with the sheared serpentinite rocks, the amphibolite rocks are talcose, and enclose some serpentinite shear pods.

Fig. (1.7): Sharp contact between the amphibolite and talcose serpentinite along Wadi Defeit. (Panoramic view, looking NW).

1.5.1.4 Metabasalt

The metabasalt rocks form several prominent hills in the central and south-western parts of the Um El Tuyor area. It occurs as grey green, fine-grained, aphanitic rocks with massive or slightly foliated appearance. Locally brecciated and amygdaloid flow structures are present in places. Plagioclase (An_{50-60}) constitutes less than 3 vol.% of the rock (Fig. 1.8b). Near and along the thrust contacts with the underlying metasediments, this metabasalt unit is transformed into chlorite and tremolite-actinolite schists.

1.5.1.5 Highly sheared ophiolitic rocks (derivatives)

The highly sheared ophiolitic rocks are mainly ankerite-rich talc carbonate and quartz carbonate rocks. They occur at the lower horizons of the ophiolitic masses, commonly within thrust zones. Locally, they enclose some pure talc bands and elongate amphibolite boudins (Fig. 1.8c). Microscopically, the highly sheared ophiolitic rocks are grouped into: a) Fine-grained, yellowish brown talc schists, made up mainly of very small laths of talc with minor chlorite (Fig. 1.8d), b) Porphyroblastic talc carbonate rocks, composed of large calcite and magnesite patches in a schistose groundmass of fibrous talc grains (Fig. 1.8e), and c) Quartz carbonate (listwanite) rocks, composed essentially of quartz with bands of talc and carbonate (Fig. 1.8f).
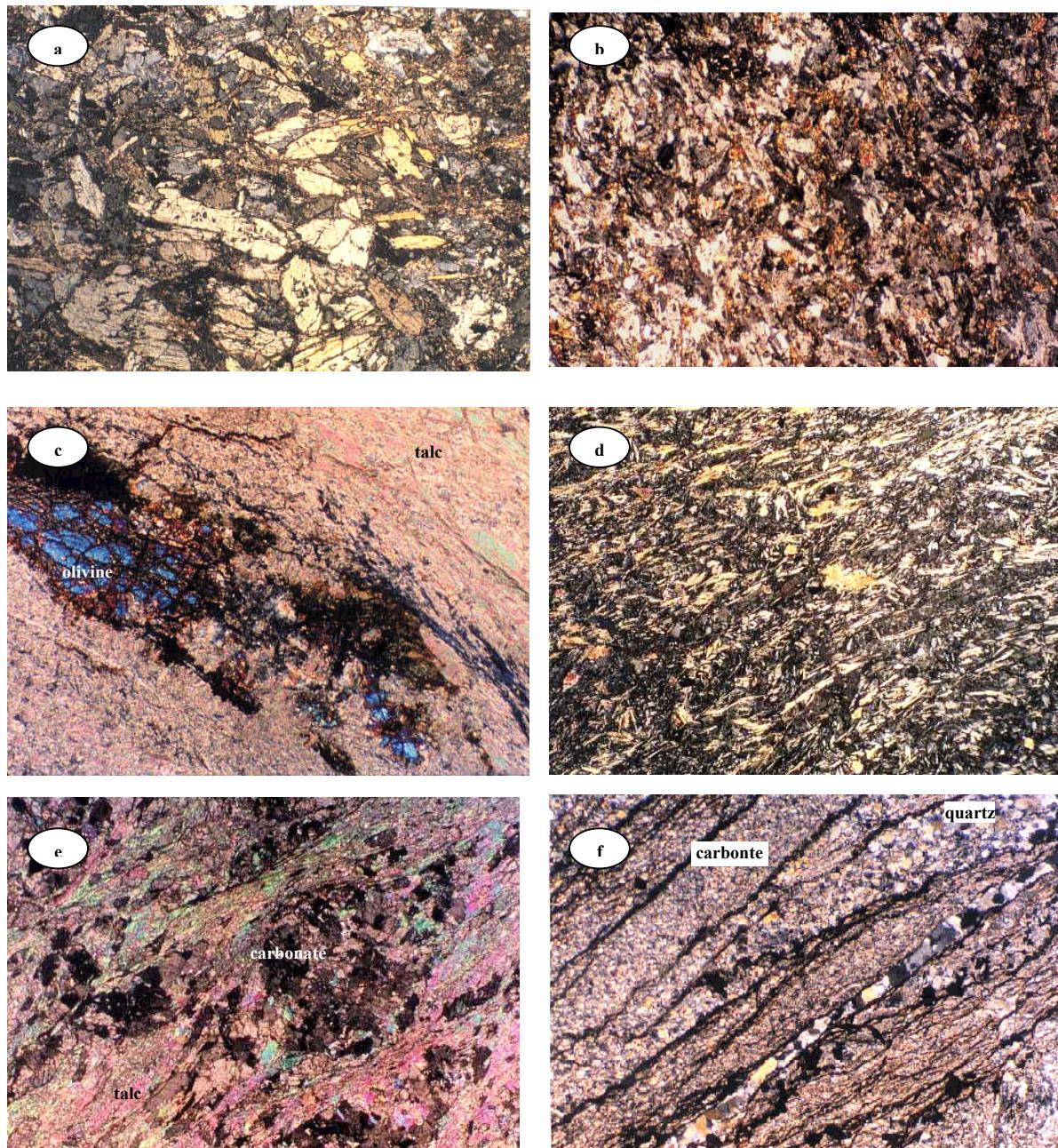
Fig. (1.8): Photomicrographs of the ophiolitic rocks exposed in the Um El Tuyor area showing: a) aligned actinolite, tremolite, and chlorite plates constituting the chief components in amphibolite exposed along Wadi Defeit (XPL, wide of view ~5.93 mm); b) metabasalt with greenschist mineralogy, i.e. albite, chlorite and epidote (XPL, wide of view ~5.93 mm); c) tectonized ultramafic rocks with olivine porphyroblasts replaced partly by talc and chlorite (XPL, wide of view ~5.03 mm); d) talc schist made up of flamenous talc and chlorite flakes (XPL, wide of view ~5.93 mm); e) a snow ball-like shaped carbonate mosaic surrounded by very fine talc laths indicating a dextral sense of shear (XPL, wide of view ~3.03 mm); f) quartz carbonate sample displays alternating quartz-rich and carbonate-rich bands. Disseminated opaque sulphides are concentrated at the boundaries separating the alternating bands (XPL, wide of view ~5.93 mm).

1.5.2 The island arc assemblage

The island arc-related assemblage consists of metasedimentary and metavolcanic-volcanoclastic layered units, and actinolite-hornblende metagabbro. Rocks of this assemblage are intensely deformed and form the footwall of the major thrusts in the eastern part of the study area.

1.5.2.1 The metasediments

The metasedimentary sequence forms a low to moderate topography in small tracts beyond the frontal slices of the ophiolites. In the eastern part of the study area, the metasedimentary rocks are unconformably overlain by ophiolithic rocks, with thrust contacts in-between (Figs. 1.9a,b). The metasedimentary sequence consists mainly of garnet-biotite schists, locally contain intercalations of metasiltstones or quartzite bands. Mineralogy of these rocks includes mineral phases pointing out to medium or high grade metamorphism (biotite±hornblende, staurolite, almandine garnet+rare sillimanite).
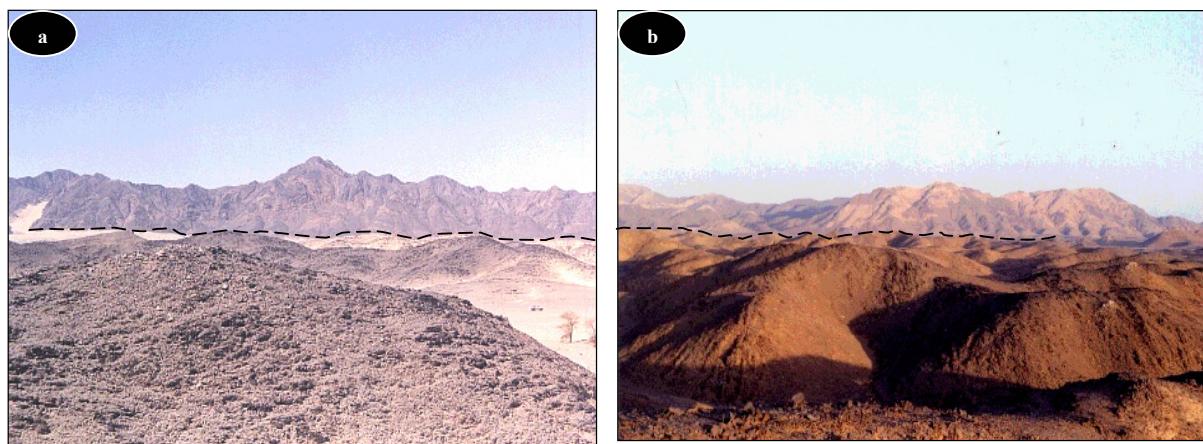
Fig. (1.9): G. Al Adrag. (a) and El Tuyor El Foqani (b) (looking west): moderately elevated hills of garnet-biotite schist overlain by the ultramafic rocks.

The garnet-biotite schist covers extended areas in the eastern part of the study area, and occurs as fresh (hard) or intensively weathered rocks. These rocks are fine-grained, porphyroblastic in texture, with xenomorphic garnet and staurolite crystals embedded in a schistose matrix of mainly biotite and less commonly chlorite (Figs. 1.10a→c). Hornblende occurs in places, and is assumed to have been developed at the expense of biotite, since some relics of biotite tabular inclusions are observed in the hornblende crystals (prograde feature). Chlorite is subordinate and, if present, occurs as elongate flakes in association with biotite in the matrix and. Quartz occurs as anhedral grains displaying undulose extinction, and form ~30 vol. % of the groundmass.

The metasiltstones are mainly exposed in the western part of the study area. They are pelitic to psammetic in composition. They contain alternating quartz-rich and clay minerals-rich bands (Figs. 1.10d to f). They are composed essentially of quartz, andesine, subordinate orthoclase and biotite crystals or fragments embedded in a fine grained matrix of quartz, feldspar and chlorite. The matrix grain fabric (bedding/foliation) is wrapped around the xenomorphic garnet porphyroblasts, which have asymmetrical quartz- and chlorite pressure shadows. Some large quartz grains occur also as porphyroblasts and generally stretched at their ends. In some places, sillimanite is associated with garnet and muscovite, occurring as fine grained cleaved plates, particularly in the refolded rocks (Fig. 1.10f).
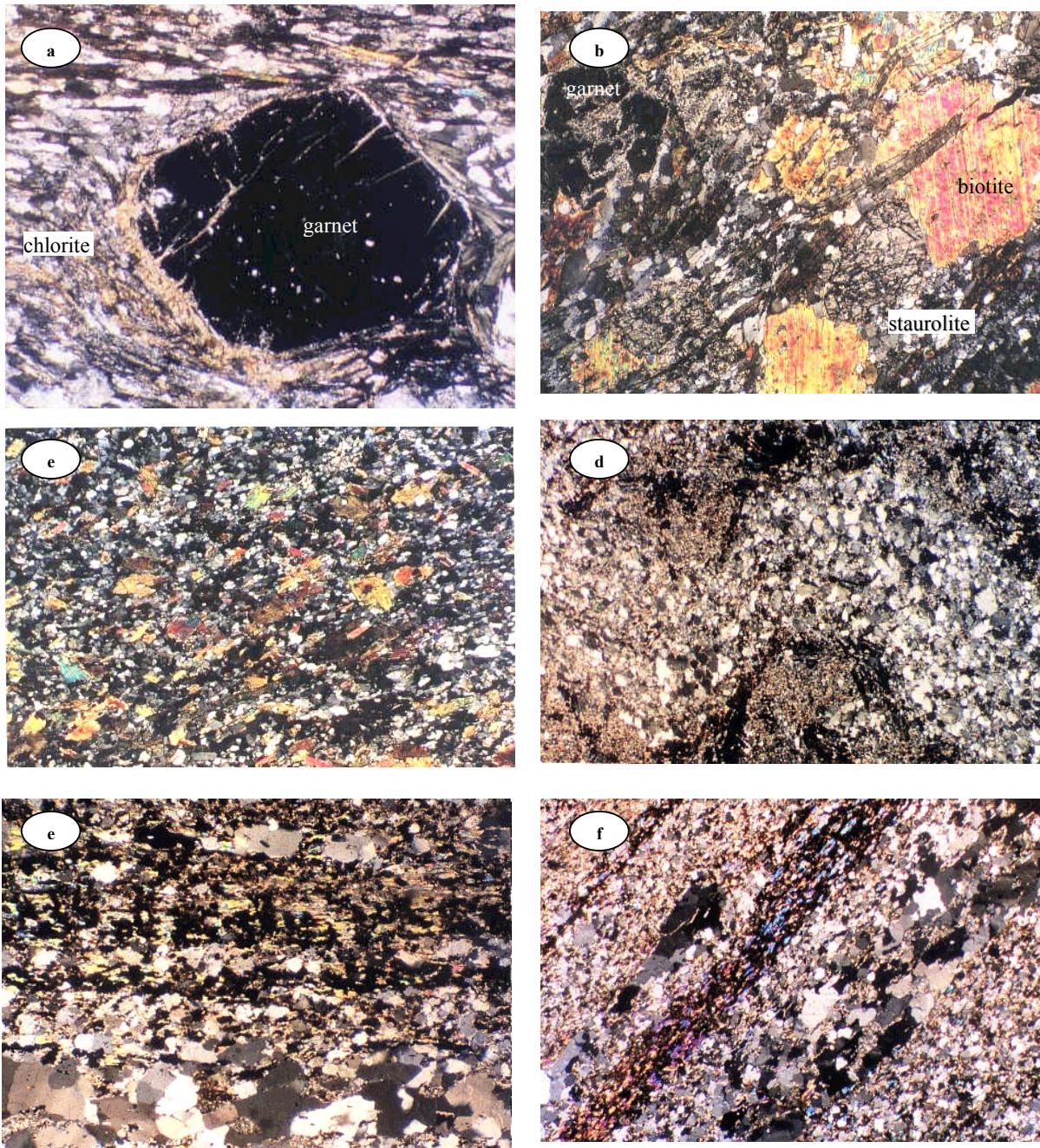
Fig. (1.10): Photomicrographs of the metasedimentary rocks exposed in the Um El Tuyor area showing: a) garnet biotite schist with foliation-parallel staurolite and chlorite flakes wrapped around a large garnet porphyroclast (XPL, base of photo ~2 mm); b) staurolite replacing biotite and garnet in a typical sample of the staurolite-bearing garnet biotite schist in Um El Tuyor area (XPL, wide of view ~3.03 mm); c) fine-grained sub-parallel biotite and hornblende plates in highly deformed garnet biotite schist (XPL, wide of view ~5.93 mm); d) folded alternating quartz-rich and argillaceous bands in sample representing the metasiltstones of Um El Tuyor area. The argillaceous bands are made up dominantly of kaolinite, chlorite, and iron oxides (XPL, wide of photo ~5.93 mm); e) alternating recrystallized quartz-rich and sericite/muscovite-rich laminations in recrystallized/segregated metasiltstones from the western part of the study area (XPL, wide of photo ~3.03 mm); f) sillimanite-bearing bands (blue-colored) in a sample of the metasiltstones (XPL, wide of view ~5.93 mm).

1.5.2.2 The metavolcanic rocks

The island arc metavolcanic rocks are exposed mainly in the central and southern parts of the study area. They are generally metamorphosed basalts/basaltic andesites as inferred from their mineralogy, and display variable degrees of schistosity. On basis of their field and microscopic criteria, the metavolcanic rocks exposed in the study area have been classified into metabasalt, hornblende-plagioclase schist, and chlorite schist. The metabasalt occurs as fine-grained recrystallized and segregated rocks. These rocks exhibit evidence of metamorphism under upper greenschist to epidote-amphibolite facies conditions. Near thrust faults (Fig. 1.11), the metabasalts are usually converted into talc-tremolite and chlorite schists. Generally, these rocks are composed essentially of plagioclase, epidote, chlorite and less common hornblende (Fig. 1.12a). In places, epidote, chlorite and albite replace completely the original mineralogy.
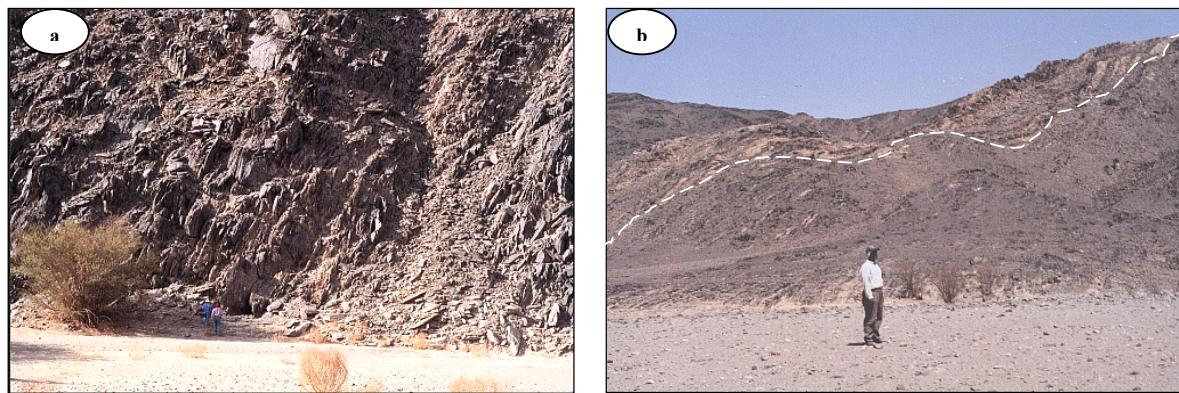
Fig. (1.11): Exposure of the metavolcanic rocks in the southern part of the Um El Tuyor area: a) massive to strongly foliated metabasalt. The green color is due to the enrichment in chlorite and tremolite minerals (looking SW); b) thrust contact (detached line) between the metavolcanic rocks and the ultramafites (looking NE).

The hornblende-plagioclase schist is usually exposed in areas at some distance from the thrust contacts and occurs as dark rocks. Rocks of this unit are composed essentially of green hornblende, plagioclase and quartz grains, preferentially aligned within the main foliation (Fig. 1.12b). Hornblende occurs as prismatic porphyroblasts with stretched ends parallel to the main foliation and locally replaced in part by epidote and chlorite. These crystals are rich in inclusions of quartz, iron oxides and less commonly plagioclase laths (Fig. 1.12c). Plagioclase (An_{35-50}) occurs as elongate porphyroblasts and as fine sub-rounded grains in the matrix. Plagioclase porphyroblasts exhibit deformational twinning and usually associated with quartz ribbons in the highly deformed domains (e.g. fold hinges, crenulated rocks, etc.). The chlorite schist occurs as medium-grained rocks exposed mainly in association with the metabasalt but commonly near the thrust contact. These rocks are typically porphyroblastic in texture, and composed essentially of faint green chlorite flakes usually associated with tremolite and/or actinolite (Fig. 1.12d). Fine saussuritized plagioclase grains are common in the groundmass. It is noticed that the rocks in the thrust zones and their nearby are markedly enriched in tremolite and talc.

1.5.2.3 The metavolcanoclastic rocks (meta-tuffs)

Sequences of metavolcanoclastic rocks are commonly exposed in the strongly deformed cores of synclines in the southern part of the study area (Fig. 1.13). They are mainly dark colored, massive to strongly foliated, chiefly mafic, graded welded crystal tuffs. These rocks show a wide range of grain size, and are composed essentially of epidote, quartz, chlorite, and subordinate calcite and opaque minerals (Figs. 1.14a,b). In places,

these tuffs contain elongated schistose, mostly felsic/lithic fragments that are oriented parallel to the fabric of the enclosing rocks.
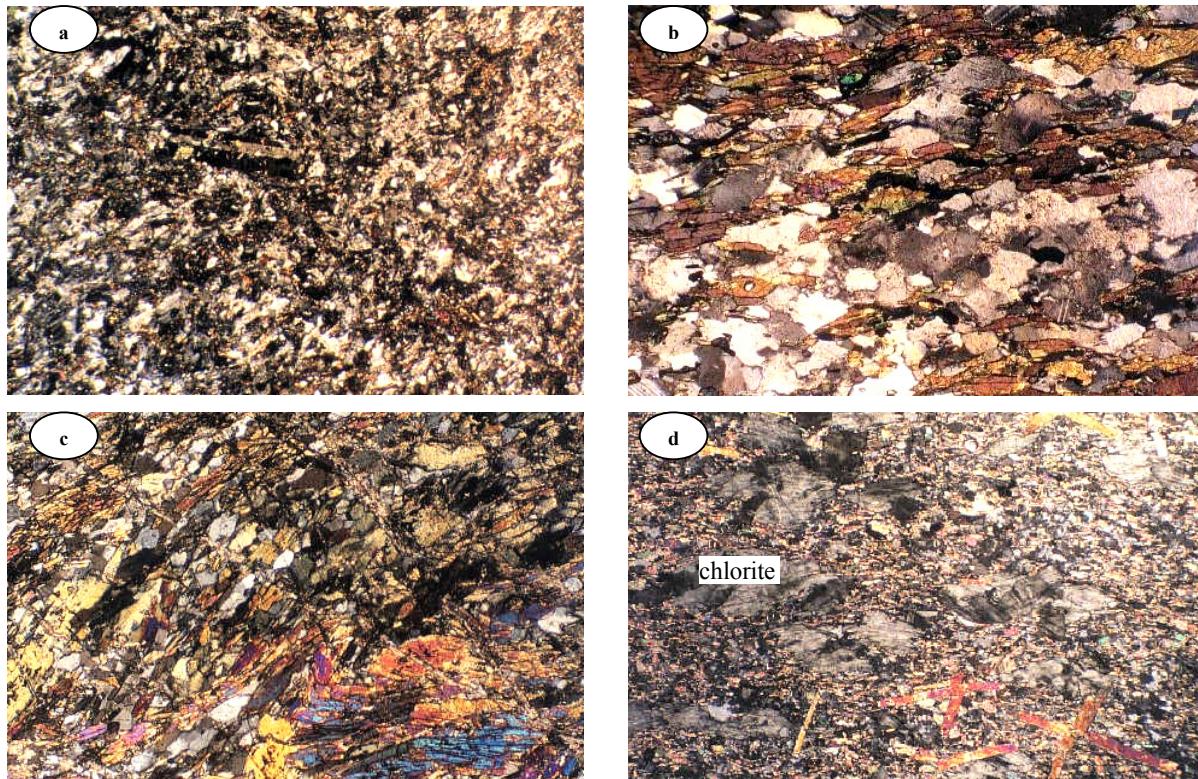
Fig. (1.12): Photomicrographs of the metavolcanic rocks exposed in the Um El Tuyor area showing: a) porphyritic metabasalt enriched in recrystallized quartz and epidote in the matrix (XPL, wide of view ~5.93 mm); b) preferably oriented hornblende, actinolite, plagioclase crystals and elongated quartz ribbons in hornblende schist exposed in the southern part of the study area (XPL, wide of view ~5.93 mm); c) poikilitic hornblende porphyroblasts traversed by calcite-bearing veinlets and microfissures and enriched in recrystallized quartz (XPL, wide of view ~3.03 mm); d) aligned chlorite flakes and randomly oriented tremolite plates embedded in a very fine-grained matrix of the same components in tremolite chlorite schist (XPL, base of photo is 5.93 mm).

Fig. (1.13): Meta-tuffs exposed in a core of an anticline structure cropping out in the southern part of the study area (looking N).

1.5.2.4 The island arc metagabbro

The island arc metagabbro forms subcircular or irregular plutons intruding the ophiolitic and the island arc-related metasedimentary/metavolcanic assemblages. On aerial photographs, the circular to subcircular plutons intrude the metavolcanic rocks, whereas irregular shaped masses occur in the metasediments. These metagabbro domains are, in turn, intruded by granodiorite masses. Coarse grained gabbro patches commonly occur along contacts with granite.

The island arc-metagabbro is generally massive, and heterogeneous in terms of both grain size and

proportions of mafic and felsic minerals. Petrographically, it is a hornblende-bearing gabbro (Fig. 1.14a), showing a granoblastic texture. It is composed essentially of plagioclase, hornblende, chlorite and subordinate biotite. Plagioclase (An_{50-60}) forms subhedral crystals, constituting ~45 vol. % of the rock. Large plagioclase crystals have commonly quartz, apatite and biotite inclusions in their cores. A few plagioclase crystals show epidotization in their centres. Hornblende (~30 vol. %) occurs as green prismatic crystals, which are more or less aligned and commonly clustered. Interstitial chlorite (~5 vol. %), clinozoisite (<2 vol. %) and tremolite replace the original pyroxene (~3 vol. %) almost completely, and hornblende partially (Fig. 1.15b). Subordinate, light brown biotite flakes (~5 vol. %), with corroded rims, are spatially associated with hornblende. Quartz, forming elongate grains and oriented ribbons, constitutes about 10 vol. % of the rock.
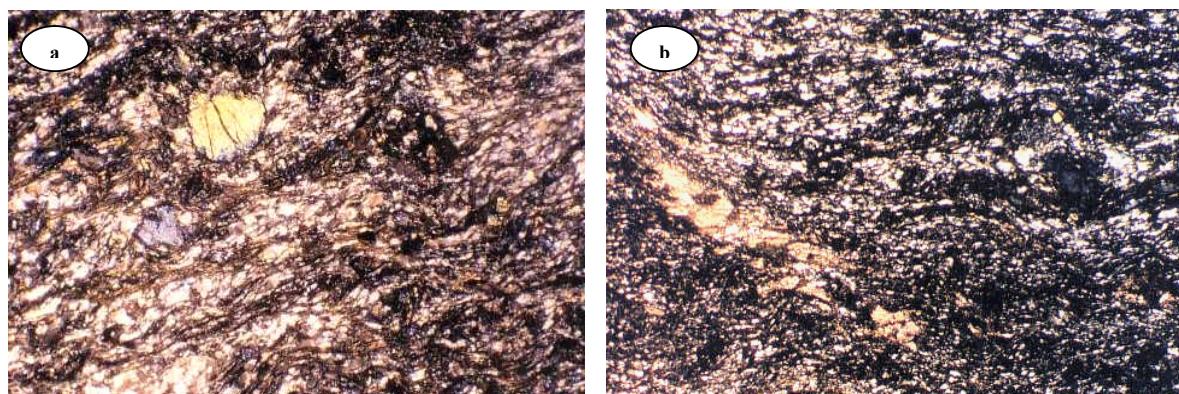
Fig. (1.14): Photomicrographs of the metavolcanoclastic rocks exposed in the Um El Tuyor area: a) crystal tuff containing epidote porphyroblasts embedded in a welded matrix of plagioclase, chlorite and iron oxide-bearing groundmass (XPL, wide of view ~3.03 mm); b) alternating microscopic to sub-microscopic quartz-rich and chlorite-rich tuffs with epidote and calcite patches (XPL, wide of view ~5.93 mm).

1.5.3 Syn-orogenic granitoids

The syn-orogenic granitoids are large, grey colored, medium-grained plutons. They occur as low-land cones and ridges, covering extended areas in the northern part of the study area. The sheared appearance and local schistosity of these granitoids suggests that they are syn-orogenic plutons.

These granitoids are either undeformed, hornblende-bearing or foliated with dominant biotite and less common hornblende. Structural investigations revealed low angle to sub-horizontal intrusive contacts delimit these plutons, suggesting that magma injection took place along the pre-existing oblique to flat-lying structures including foliation planes and thrust surfaces. In places, they contain abundant mafic xenoliths of gabbroic composition, and variable sizes. In the northern part of the study area, these granitoids are commonly traversed by 0.5 to 2.5 m wide, NE-trending orthoclase-muscovite pegmatites. Along their contacts with the ophiolitic rocks in the western part of the study area, these granitoids show strong NNE foliation.

Microscopically, they are granodiorite to granite in composition, with granular texture. They are composed essentially of plagioclase (An_{30-35}), quartz, biotite, subordinate hornblende, chlorite (3 vol. %), accessory sphene, and apatite. Plagioclase forms about 65 vol. % of the rock. It occurs as commonly as zoned prismatic crystals showing carlsbad and/or polysynthetic twinning (Fig. 1.15c). Interstitial quartz grains (~25 vol. %) occupy spaces among feldspar crystals and exhibits straight extinction. Euhedral to subhedral hornblende crystals, if present, show simple twinning and may contain euhedral opaque minerals and sphene. Aligned biotite flakes (~6 vol. %) are locally chloritized, and contain sphene along the cleavage planes. (Fig. 1.15d).

Subordinate euhedral sphene crystals (<1 vol. %) with rhombic outlines usually associated with biotite.
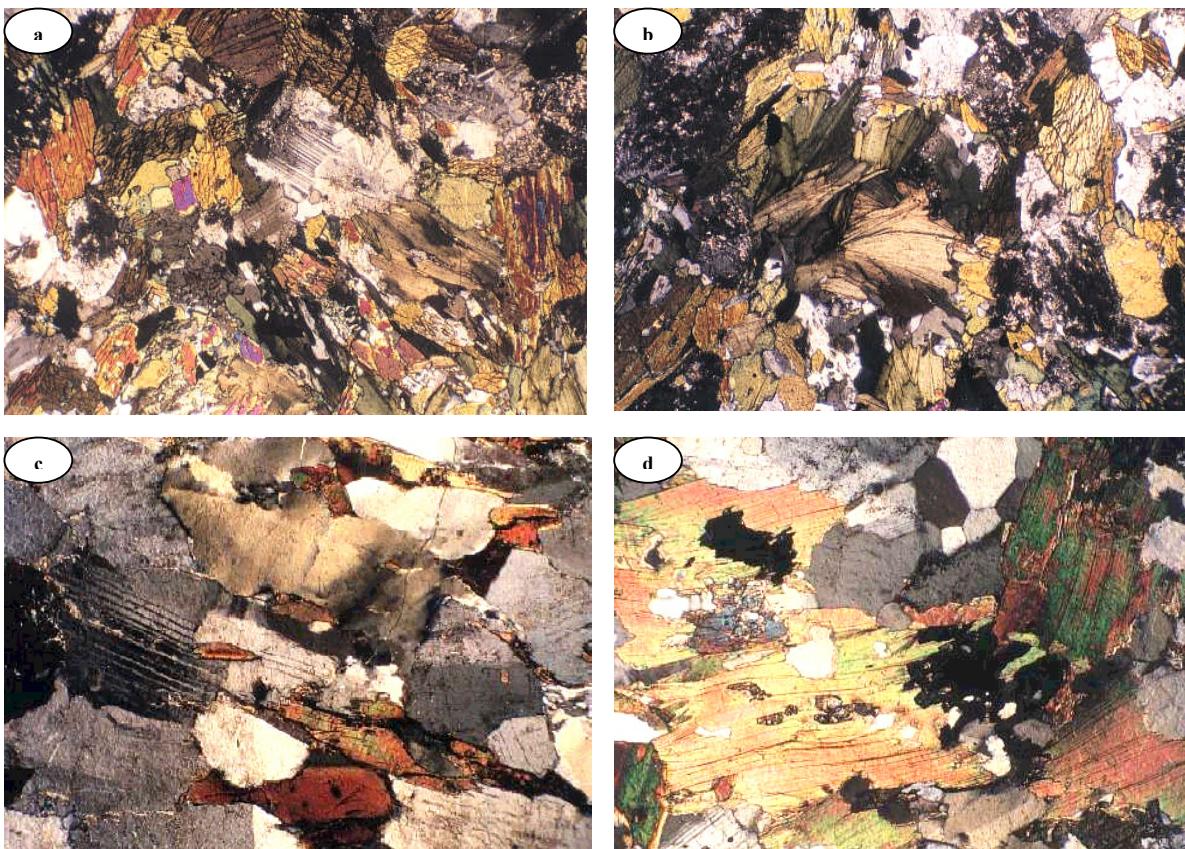
Fig. (1.15): Photomicrographs showing: a) island arc metagabbro with albite intergrows with chlorite and occupying the intergranular spaces between hornblende laths. In places, diopside and hornblende are completely replaced by chlorite (XPL, wide of view ~5.93 mm); b) chloritized, albitized island arc metagabbro with chlorite, albite and quartz replacing hornblende and plagioclase (XPL, wide of view ~5.93 mm); c) aligned biotite and albite plates defining the shearing direction in deformed syn-orogenic 'grey' granite from the northern part of the study area. Quartz is also elongated and displays undulose extinction (XPL, long dimension is 3.03 mm); d) syn-orogenic granite with biotite flakes, bent and replaced by sphene and iron oxide nodules along the cleavage planes (XPL, wide of view ~3.03 mm).

1.5.4 Post–orogenic intrusions

Plutons displaying no foliation and intruding the metasedimentary, metavolcanic, and ophiolitic rocks are interpreted in the present work as post-orogenic magmatic manifestations. They distributed over the entire study area, commonly occurring in small exposures. On the aerial photographs and Landsat (TM) images, these plutons are circular to subcircular (see Figs. 7.1.1 & 7.1.2, Appendix A). They include olivine gabbro and muscovite-biotite granite rocks.

1.5.4.1 Olivine gabbro

The olivine gabbro is granular, coarse-grained, and melanocratic in hand specimen. They have sharp intrusive contacts against the country rocks. They are exposed only in few locations in the study area. Commonly, they form low land ridges. Microscopically, they show sub-ophitic texture consisting essentially of plagioclase, olivine, clinopyroxenes and accessory iron oxides (Fig. 1.16a). Plagioclase (~70 vol. %) is mainly bytownite (An_{80-85}), occurring as long prismatic crystals forming coarse inter-granular texture (Fig. 1.16b). Poikilitic olivine (~27 vol. %) and plagioclase in pyroxene host crystals are evidence for co-genetic crystallization.

Subordinate augite (<3 vol. %) occurs as equant to short prismatic crystals commonly with simple twinning.
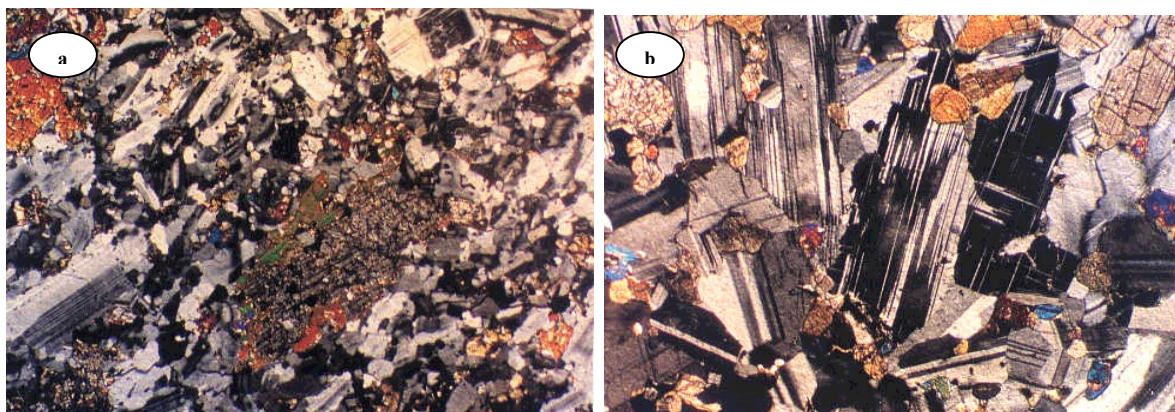
Fig. (1.16): Photomicrographs of the post-orogenic (olivine) gabbro exposed in the Um El Tuyor area showing: a) subophitic texture among bytownite tabular crystals and augite porphyrocrysts, with hornblende rims (XPL, wide of view ~5.93 mm); b) olivine, augite and bytownite forming the main constituents of the younger gabbros (XPL, wide of view ~5.93 mm).

1.5.4.2 Muscovite-biotite granite

The muscovite-biotite granite is a pink-colored medium-grained rock. It forms generally high topographic circular to irregular plutons (Fig. 1.17). The spatial association of exposures of this unit with regional-scale strike slip-faults, and the densely jointed nature of the pluton margins are interpreted as evidence for preferential emplacement along the fault surfaces. In places, intrusions of the muscovite-biotite granite are associated with local alteration halos. These rocks are coarse to medium-grained, generally have granular texture, but locally show micrographic and myrmekitic intergrowths (Fig. 1.18a). They are composed mainly of large microperthitic microcline (~45 vol. %) and subordinate perthite (< vol. 5%), and quartz (15 vol. %). Additionally, there are large subhedral albite crystals (<2 vol. %) with well-developed twinning and euhedral biotite inclusions (Fig. 1.18b). Quartz (~23 vol. %) is commonly associated with potash feldspars and occurs as anhedral crystals. Biotite constitutes ~10% and occurs as brown flakes usually accompanied by iron oxides and sphene.

Fig. (1.17): Field photograph showing exposure of the muscovite-biotite granite intruding the 'older' syn-orogenic (low land) granite in the southern part of the study area (looking S).
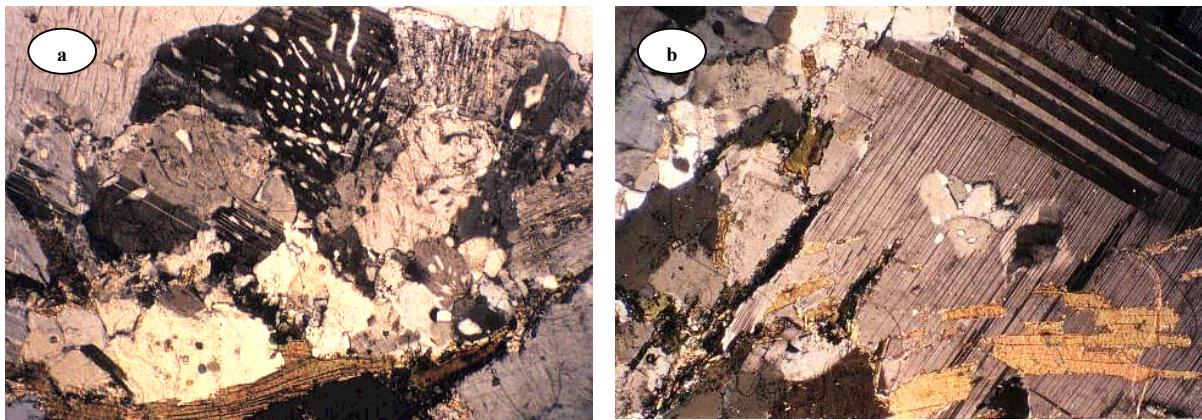
Fig. (1.18): Photomicrographs of the post-orogenic granite exposed in the Um El Tuyor area, showing: a) myrmeketically intergrown microperthite and quartz (XPL, wide of view ~3.03 mm); b) tabular biotite inclusions in a large albite plate. Quartz occupying the interstitial spaces among feldspar crystals (XPL, wide of view ~3.03 mm).

1.5.5 Dikes

Numerous dike sets traverse the metasedimentary and metavolcanic rocks in the Um El Tuyor area. Generally, they are abundant in the western part of the study area, particularly where intersecting strike slip faults are observed. On basis of their field and microscopic relationships, they are categorized into felsic and mafic dikes.

The felsic dikes form ENE-trending sets, and commonly occur near exposures of the post-orogenic granite in the study area. In hand specimen, they are pink colored porphyritic, with feldspar phenocrysts embedded in a fine-grained quartz, sericite and chlorite-rich groundmass. In places, these dikes are displaced or exhibit some evidence of deformation. In the Um El Tuyor mine area, numerous sheets of dacite dissect the host rocks. They are mostly conformably with the foliation planes, and hence considered sills. They are varying in width from some decimeters to more than two meters. Flow texture is represented by abundant brown mica flakes, aligned commonly parallel to the sill margins. Some are sulphide-bearing, especially at deeper levels and in close spatial association with the auriferous lodes.

The mafic dikes are common in the western part of the study area, traversing the island arc metavolcanic and metasedimentary rocks. They occur as WNW-ESE and/or NW-SE striking swarms dissecting the metasediments and the gabbroic rocks. These dikes are associated with hematized halos in the north-western part of the study area. In thin sections, they are basaltic to andesitic in composition, and consist of essential plagioclase, calcite, epidote and chlorite, and minor quartz and iron oxides. Plagioclase occurs as fine acicular laths showing multiple twinning but many crystals are severely altered into kaolinite. The laths entrap very fine chlorite and epidote crystals that replace the original ferromagnesian minerals. Calcite occurs as fine interlocked crystals commonly form microbands or filling the polygonal spaces among the plagioclase laths.

On basis of the aforementioned field observations, a tentative chronological sequence for the basement rocks cropping out in the Um El Tuyor area can be constructed, as follows:

- Dikes   (Youngest)
- Muscovite-biotite granite
- Olivine gabbro   } Post-orogenic intrusions
       - Syn-orogenic granitoids   (granites to granodiorites)
          - Island arc metagabbro
          - Meta-volcanoclastic rocks   } Island-arc assemblage
          - Metavolcanic rocks
          - Metasediments (pelitic to psammopelitic)
               - Highly sheared rocks (e.g. talc carbonate,
                  talc schist and quartz carbonate)
               - Metabasalt
               - Amphibolite   Ophiolites
               - Metagabbro
               - Serpentinite (with relict ultramafics)   (Oldest)

The proportional surface distribution of the different rock types is shown in Figure (1.18). The latter shows that the ophiolitic rocks occupy the largest terrane area among others. On the other hand, a considerable proportion of the territory is covered by recent stream (alluvial) sediments.

9 Alluvial deposits (Wadi fillings)
8 Muscovite-biotite granite
7 Olivine gabbro
6 Syn-orogenic granitoids
5 Island arc metagabbro
4 Meta-volcanoclastic rocks
3 Metavolcanic rocks
2 Metasediments
1 Ophiolitic rocks
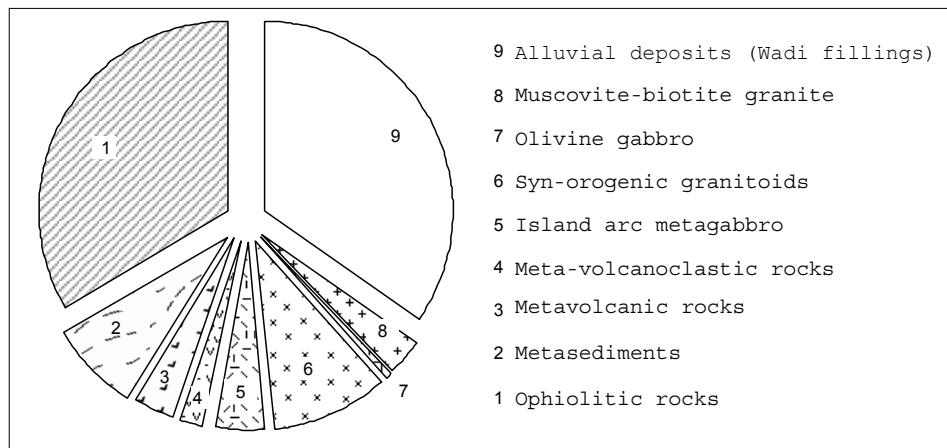
Fig. (1.19): Proportional distribution of the different lithologies exposed in the Um El Tuyor area.

CHAPTER 2

STRUCTURE & METAMORPHISM

2 STRUCTURE & METAMORPHISM

2.1 Introduction

The basement rocks exposed in the Um El Tuyor area display intense superimposed faulting, folding and shearing, implying polyphase deformation. In order to understand the deformation history of the area, structural elements of map, meso- and microscopic scales have been studied.

2.2 Structural elements

2.2.1 Faults and thrusts

The study area is dissected by numerous fault sets, varying from reverse (moderate to low angle thrusts) to almost vertical strike-slip faults. The thrust faults strike mainly in NE-SW to ENE-WSW directions, whereas most of the strike-slip fault trends follow NE-SW, NNW-SSE, NW-SE, and NNE-SSW directions. Interpretation of field relationships and Landsat TM images suggest that the NE-SW trending faults are the oldest structural element in the study area.

The NE-SW trending, 35-55°NW-dipping, thrust faults mark the tectonic contacts between the ophiolitic slabs and the underlying metasedimentary/metavolcanic sequences (Figs. 2.1a,b). They are commonly associated with highly sheared talc carbonate and listwanite rocks. NE-SW trending strike slip faults traverse the ophiolitic and the arc-related rocks in the central part of the study area with left lateral off-set. Locally, intense decimeter- to meter-thick sheared talc schist and talc carbonate rocks are developed where these faults dissect margins of the ophiolitic units. The NE-SW trending strike slip faults are commonly associated with the thrust faults, especially in the eastern part of the study area.
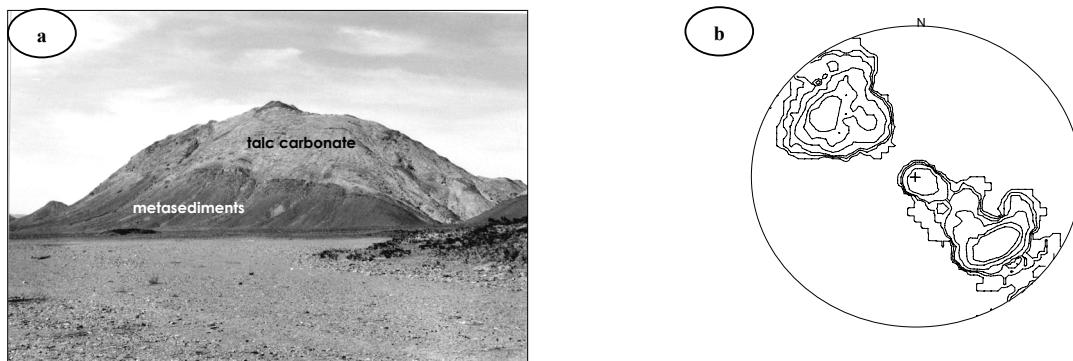
Fig. (2.1): a) Thrust contact between the metasediments (dark rocks at bottom) and talc carbonate (looking SW). b) Equal-area, lower hemisphere stereographic projections of poles to the thrust planes in the western side of the study area (contours at 2, 4, 6, 8, 10 and 12 points per unit area).

The NW-SE trend is manifested by a major strike slip fault detached and displaced the ophiolitic blocks in the central part of the study area. The exposures of the post-orogenic muscovite-biotite (pink) granite and olivine gabbro are mostly aligned along these faults.

The NNW-SSE faults are right-lateral strike slip faults can be traced for up to 9 km. These faults mainly dissect the island arc metavolcanic rocks in the western part of the study area, and commonly represent the contacts with the ophiolitic units. They are characterized by sub-vertical planes and commonly associated with slickensides.

Sets of WNW-ESE and NNW-SSE trending faults dissect the post-orogenic granite, commonly in the southern part of the study area. The lateral displacement along these faults is limited and cannot be shown at map scale (see Fig. 1.2). NNE-SSW and N-S joint systems dissect the metavolcanic rocks in the south eastern part of the area, and attributed to a late shear reactivation. These joint systems dissect also the syn- and post orogenic granites with no obvious lateral displacement.

2.2.2 Thrust-related minor structures

Within and near the thrust zones, numerous thrust-related meso- and microscopic fabrics have been observed. These fabrics are predominated by mylonitization cleavage (N 35-55° E/35-60° NW, Figs. (2.2a,b) and down-dip stretching lineation. The latter is distinguished by preferentially oriented biotite, chlorite and wedge-shaped quartz porphyroblasts. As a result of development of decimeter-scale folds, the stretching lineation exhibits dispersion in many directions on the mylonitization cleavage planes. However, in the north-eastern part of the study area, where folding was less intense, the stretching lineation is consistently NW-directed and pitch gently to the north. Geometry of this N-dipping stretching lineation and the mylonitization cleavage together with other kinematic indicators, such as rotating porphyroblasts, mesoscopic duplexes, groves and slickensides, indicate a SSE-directed emplacement of the thrust sheets.
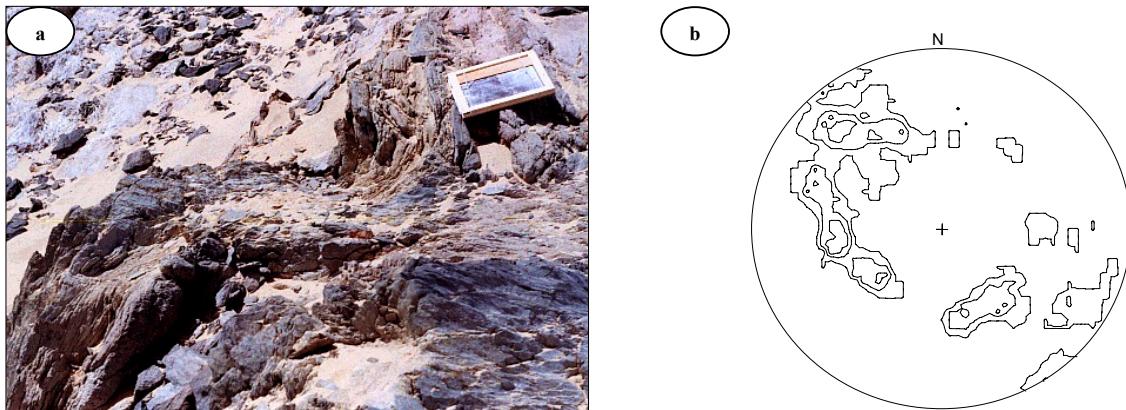
Fig. (2.2): a) Slickensides on surfaces of folded talc schist within a thrust zone in the northern part of the study area. Gliding and groves are seen in the down-right side of the photo (scale dimensions are ~20 cm). b) Equal-area, lower hemisphere projection of poles to mylonitization foliation (S_m), in the eastern part of the study area (contours at 3, 6, 9%).
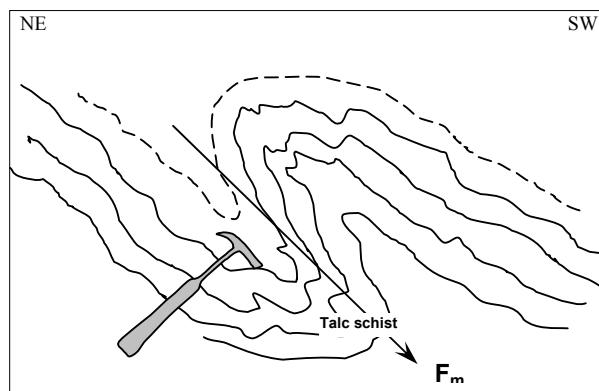
Fig. (2.3): Sketch drawing illustrating the superimposition of F_m folds on the mylonitization cleavage in the south-western part of the study area.

Locally, the thrust zones are affected by meter-scale tight isoclinal 'sheath' folds, with commonly sinistral asymmetry and their axes strike sub-parallel to the stretching lineation (Fig. 2.3). Along the thrust planes, shear

bands (C surfaces) are inclined less steeply than the mylonitization cleavage. The kinematic analysis of shear sense indicators, such as asymmetric folds, asymmetric augens, fractured and rotated porphyroblasts, etc., suggests a sinistral shearing that was coeval with thrusting of the ophiolitic slices. In addition, the occasionally observed sub-horizontal slickensides on the steeply NW-dipping thrust planes, and sheath folds with sinistral asymmetry suggest left-lateral transpression accompanying the thrusting in the study area. The basal domains of the thrust slabs and the pre-dating structures are deformed and distorted by later deformation (Fig. 2.4).
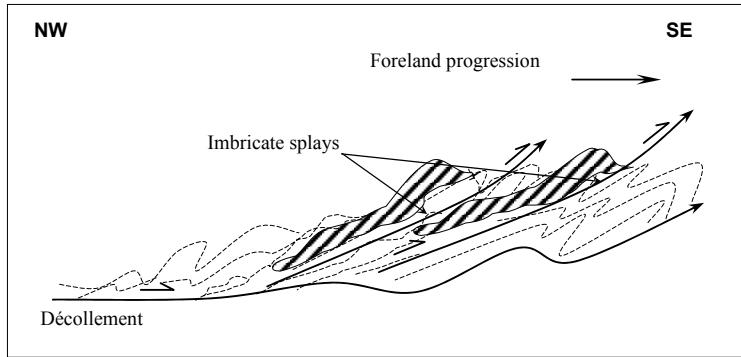
Fig. (2.4): Geometry of the thrust faults in the Um El Tuyor area. Sketch drawing based on field and microscopic observations. The section shows the thrust splays emanating from the main thrust plane.

2.2.3 Folds

Regional folding is recognized in the Um El Tuyor area by numerous map-scale asymmetric tight to recumbent plunging syncline and anticline folds. These folds are attributed to three folding events, namely F_m, F_2, and F_3. Commonly, refolding of F_2 by F_3 is recognized, especially in the western part of the study area (Figs. 2.5a).

The F_m folds have NE-SW-striking axes, plunging gently or moderately towards the SW. In the present work, this generation of folds has been given the symbol F_m owing to their assumed spatial and genetic relationship to the thrusts, and related mylonitization zones. The F_2 folds have NW-SE trending axes and plunge steeply to the NW (Fig. 2.5b). They are superimposed by a system of non-coaxial F_3 folds. The F_3 folds are NNW-trending folds and crenulations, plunging to the NW. F_3 folds are less tight if compared with the F_2 folds.

2.2.4 Foliations

In coincidence with the three fold generations, three generations of foliation are developed in the deformed rocks cropping out in the Um El Tuyor area. These three generations are namely; S_m, S_2 and S_3 foliations. The S_m foliation is principally a mylonitization cleavage striking NE-SW or ENE-WSW and dipping moderately to the NW. it well-developed in the thrust zones. In places distal from the thrust faults, S_m is, however, represented by non-penetrative cleavage planes and/or aligned inclusion trails in garnet porphyroblasts in the metapelites. S_2 is axial planar foliation, and concordant to axes of the F_2 folds. It is defined by preferably oriented micaceous minerals in the metasedimentary and amphiboles in the metavolcanic rocks. It strikes commonly NW-SE and dips at moderate to steep angles to the NE or SW. In the eastern part of the study area, the S_2 foliation is weak or less pervasive than in the western part. S_3 foliation is generally a crenulation cleavage coaxial with the F_3 fold axes, and has a NNW-SSE strike and a SW or NW dip (Fig. 2.5c). The crenulation cleavage is dominant in the high strain domains, i.e. near fold closures, and commonly traverses the metasedimentary rocks.
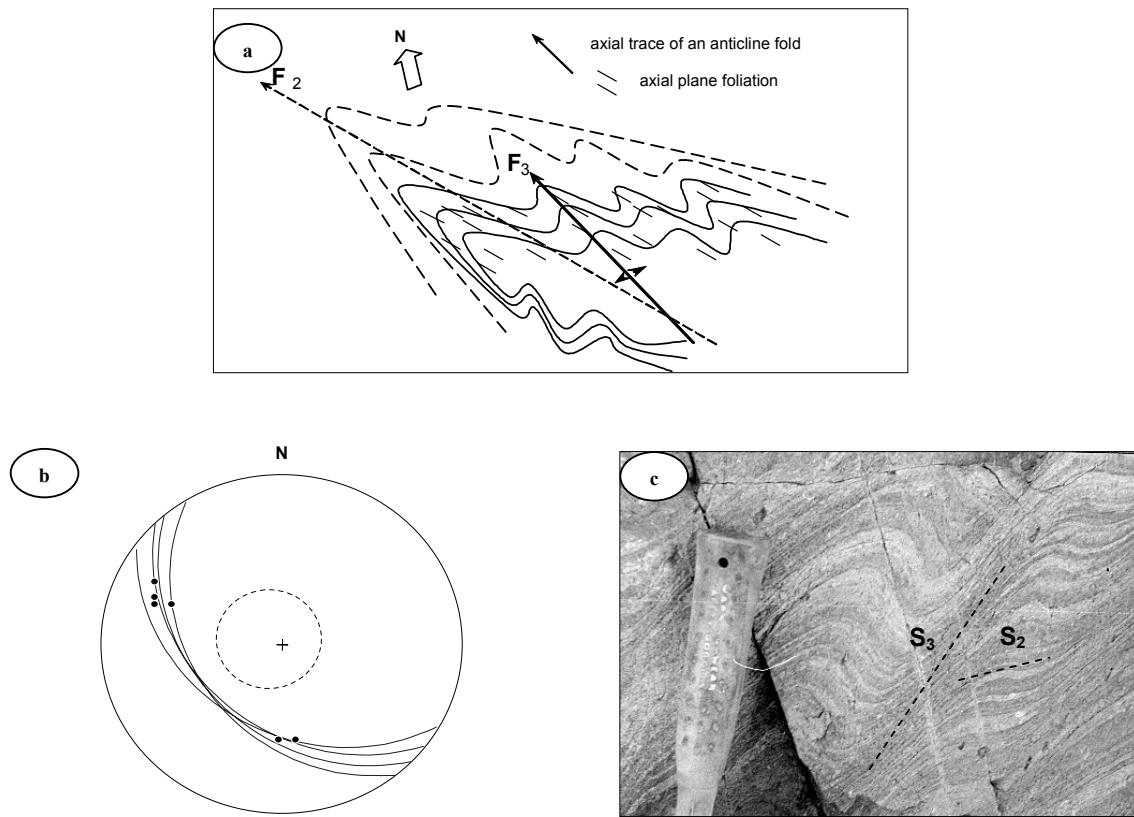
Fig. (2.5): a) Refolding model of F_2 by F_3 folds. This geometry is drawn from structures developed in the metasedimentary and metavolcanic rocks in the central part of the study area. b) Equal-area, lower hemisphere stereographic projections of the axial planes (great circles) and fold axes (dots) of the major F_2 folds in the south-western part of the study area. Plotting of S_2 foliation yielded a girdle (broken-line circle) with a moderately W-plunging major fold. c) Crenulation cleavage (S_3) superimposed on S_2 cleavage palnes (S_m) in the metasedimentary rocks exposed in the Um El Tuyor mine area.

2.2.5 Lineations

L_m is WNW-ESE to NW-SE trending stretching lineation associated with the planar mylonitic fabrics along and near the thrust zones. It is expressed in striation, groves, and amphibolite boudins in the talc carbonate and talc schist and in aligned tremolite and chlorite in the underlying island arc metavolcanics. If present, the L_2 lineation is defined by NNW-SSE stretched biotite flakes mainly in the hinge zones of the F_2 folds. It pitches generally at 20-38° to the NNW. The L_3 lineation is a down-dip mineral lineation, defined by aligned chlorite and mica flakes, and staurolite plates in the metasedimentary rocks. On the other hand, it is manifested by pencil-like and kink fabrics in the metavolcanic rocks.

2.2.6 Shear zones

In the present work, zones in which the cleavage is more intensively developed, and mortar textures and brecciation have been observed are defined as shear zones. In these zones, abundant meso- and microscopic shear fabrics are aligned in sub-parallel directions (Figs. 2.6a→d). The sense of shear has been determined by using markers in the wallrocks and the deflected foliation cleavages into the shear zone. A major, 5 km long, shear zone traverses the arc-related metasediments and the ophiolites in the central part of the study area. In this zone, various NW-SE sinistral 'left lateral' shear elements cut by NNW-SSE dextral shear fabrics. The sinistral shearing is attributed to movement along planes of the older NW-SE strike slip faults. On the other hand, elements define the

dextral sense of shear are attributed to a dominant non-coaxial simple shear within the ductile-brittle to brittle-ductile zones, i.e. the principal axes of finite strain do not lie parallel to those of successive strain increments.

In the Um El Tuyor mine area, the dextral sense of shear is inferred from the sigmoidal quartz porphyroblasts developed in the wallrocks. This dextral shear component seems to be coeval with the main auriferous quartz veining and coincides with the NNW-trending faulting. The most prominent shear fabrics include S-C structures, tension gashes, inclusion trails, mantled porphyroblasts, undulose extinction and microfractures. The direction of shear is assumed to lie sub-parallel to striations, slickensides, mineral lineation, and to the mortar textures, if present.

Evidence for crystal-plasticity in the quartz porphyroblasts is expressed in the undulating extinction and the recrystallized grains along healed planes. On the other hand, brittle deformation is manifested by the abundant microfractures and the serrate boundaries of quartz porphyroblasts.
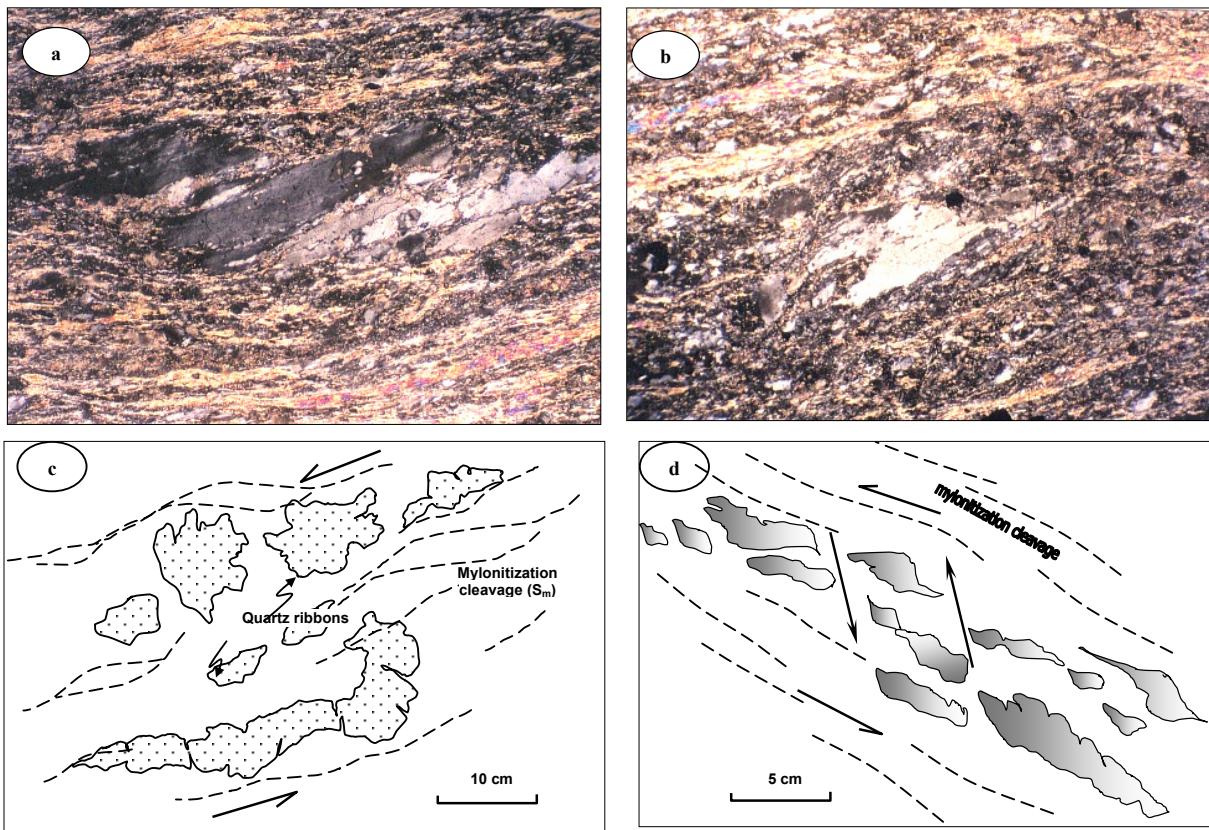
Fig. (2.6): a) Photomicrograph showing an advanced stage of shearing manifested by dispersion of quartz δ-type porphyroclast and associated microfractures and sub-grains. Fracturing favours fluid access and sericite, mica growth within the S-planes (XPL, wide of view ~2 mm). b) Photomicrograph of alternating sericite-rich and chlorite-rich bands in hydrothermally altered, deformed wallrocks. Patchy wedge-shaped quartz porphyroblast (in the centre) has stretched ends. The latter imply sinistral sense of shearing. The crystal also shows partial kinematic replacement by sericite from matrix (XPL, wide of view ~3.03 mm). c), d) Mesoscopic sheared quartz ribbons in listwanite exposed in the eastern thrust zone of the study area. The stretched ends and geometry of the ribbons suggest left-lateral shear.

2.3 Structural evolution (Deformation history)

Based on the aforementioned and considering the crosscutting relationships, the structural evolution of the Um El Tuyor area can be chronologically subdivided into five consecutive deformation phases (Table 2.1).

Thrust faulting (D1 or Dm)

The presence of gently to moderately NW-dipping thrust faults separating the ophiolitic rocks from the underlying island arc sequences, and related internal fabrics is suggestive for a regional tectonic thickening and crustal shortening along a NW-SE direction (Dm). During this deformation event, various deformational fabrics, including thrust segments, co-axial sheath folds (F_m), mylonitization cleavage, and stretching lineation developed. Regionally, the ophiolitic slices and their underlying metasedimentary and metavolcanic rocks are incorporated into synforms. Similar features have been explained by the tendency of the dense ophiolites to sink unequally into the underlying lighter rocks forming an array of subcircular synforms (Shackleton, 1988). Left-lateral transpression movement was coeval with, or subsequent to the thrusting event.

Early folding (D2)

The development of tight, asymmetric small scale and regional F_2 folds, with wavelength of ~2-8 km, is attributed to the early NE-SW compressional stress regime (D2). Development of these 2nd generation folds was accompanied by the formation of penetrative fine-grained schistosity in the island arc metasedimentary and metavolcanic rocks. This S_2 cleavage is by far the most common minor structure in the study area. As a result of local cleavage/bedding intersection, less common intersection lineation is superimposed on the S_2 surfaces. The resulting line (L_2 lineation) is parallel to F_2 axial planes and pitches in the same direction of the fold plunge. Related extensional shear fractures are subsidiary and mainly confined to the hinge zones of the F_2 folds, especially the anticlines. Orientation of the major D2 fabrics at high-angles to the regional Dm-related structures implies a change in direction of the compressional regime during D2.

Third generation folding (D3)

A third deformation increment is considered as a manifestation of a non-coaxial continuation of the early NE-SW compressional stress regime. During this deformation episode, the early (F_2) folds, related (S_2) cleavages, and the thrust faults were affected by a series of open F_3 folds and crenulations. The deformation represented by the F_3 folds led to general uplift of the central part of the study area. Folding through the D3 phase was accompanied by formation of strike slip faults (with a dextral sense of shear) extending in a NNW-SSE direction, parallel or sub-parallel to the axial planes of F_3 folds.

Transcurrent shearing (D4)

The transcurrent shearing (D4-related) structures are best developed in the central part of the study area, and are mainly NW to NNW-trending brittle-ductile shear zones cut through the early developed structures. This fourth increment of deformation generally records an episode of transcurrent deformation resulting largely in slip reactivation of the pre-existing NW-trending faults and formation of discrete shear zones, of which, one is hosting the presently investigated gold mineralization.

Tensile deformation (D5)

Tensile deformation (D5) is a late shearing event indicated by WNW-ESE and NNE-SSW trending fault and joint/fracture systems, mainly in the southern part of the study area. These fault and joint systems traverse the post-orogenic granite and the shear zones with no obvious lateral displacement.

Table (2.1): Schematic compilation of the deformational phases and magmatic activities in the Um El Tuyor area

Magmatic activity &sedimentation	Deformation	Structures	Evidence (Fabrics)
	Weak tensile shear (D5)	- WNW-ESE and NNE-SSW fault trends with no obvious transpression	- WNW-ESE, NNE-SSW and N-S joint/fracture systems traverse the syn- and post-orogenic granites and the pre-existing rocks.
	Transcurrent compressional shear (D4)	- Discrete shear zones, generally NNW-trending, commonly traversing the ophiolitic and island arc rocks	- Local shear fabrics, S-C structures, mortar texture, pressure-shadows, etc
Post-orogenic intrusions			- Oval-shaped structures on (TM) Landsat images - Sharp irregular (intrusive) contacts against the country rocks in the field
	Third generation folding (D3)	- F_3 major and minor syncline and anticline structures developed in the ophiolitic and island arc rocks - Right-lateral strike slip faults crosscutting the former fabrics and dislocate the ophiolitic blocks	- S_3 (NNW-SSE) crenulation cleavage and kinks, coaxial with F_3 axial planes - Meso- and microscopic S-C fabrics and mantled garnet and staurolite porphyroclasts
	Early folding (D2)	- F_2 asymmetric folds, tight and frequently overturned	- Early, penetrative slate foliation (S_2) strikes roughly NW-SE, and considered the commonest meso- to micro-structure in the Um El Tuyor area - Rotated garnet, and stretched biotite and staurolite porphyroclasts with sinistral asymmetry
Emplacement of the syn-orogenic intrusions (mainly granodiorite)			- Marginal sub-horizontal intrusive contacts along pre-existing flat-lying structures including schistosity planes and thrust faults. Aligned hornblende tabular crystals and biotite flakes parallel to the main shear direction
	Regional thrusting (Dm=D1)	- Transposition of primary bedding into mylonitic cleavage planes - Narrow continuous high strain zones (thrust zones) - Frequent major sheath folds ($F_m=F_1$), occasionally recumbent, with axes parallel or sub-parallel to thrusts planes	- Penetrative mylonitization cleavage S_m (ENE to NE-SW) common near thrust zones. - Intrafolial sheath folds and NE to NNE mineral elongation lineation - Asymmetric amphibolite boudins and talc pockets elongated parallel to mylonitization foliation - Sinistral sense of shear inferred from the σ-type quartz porphyroblasts, detached quartz ribbons and development of intergranular sub-grains
Extrusion of island arc basalt and basaltic andesite and related tuffaceous equivalents		- Bedded metavolcanic and metavolcanoclastic units	- Poorly to well-preserved lamination and graded bedding in the meta-tuffs (S_o)
Deposition of pelites and psammopelites		- Successions of pelitic and psammo-pelitic rocks (highly deformed)	- Primary textures and planar fabrics, bedding planes (S_o)
Generation of an oceanic crust (elsewhere, then transportation)		- Slabs of ophiolitic units covering extended terrains	- Primary differentiation banding in the ophiolitic metagabbro

Time

2.4 Metamorphism

The Um El Tuyor crustal collage underwent three phases of regional metamorphism (M1→M3), and a late stage of local hydrothermal alteration (metasomatism). M1 is manifested by serpentinization and uralitization of the ophiolitic units. Further, the transformation of serpentinites into talc carbonate rocks along the thrust contacts is evocative for diaphthoresis of the ophiolitic units during thrusting. On the other hand, the M1 metamorphism affected the island arc rocks non-uniformly. The M1 mineral assemblage is represented by inclusions of chlorite, less commonly biotite, and elongate quartz within the large garnet porphyroblasts in the metasedimentary rocks. These inclusions form trails parallel to the S_m cleavage planes and almost perpendicular on the matrix foliation (S_2). In the metavolcanic rocks, M1 assemblage includes actinolite, chlorite, epidote, and albite.

M2 is considered coinciding with the development of S_2 cleavage. It is indicated by the development of intermediate to high grade metamorphic mineral phases, e.g. hornblende, garnet and staurolite, and by growth of the matrix minerals in the arc-related metasedimentary rocks. Development of almandine garnet rims and staurolite ($\pm$sillimanite) in the metasedimentary rocks marks the peak of regional metamorphism. Similarly, the metavolcanic rocks show a mineralogical assemblage including biotite, hornblende(paragasite), quartz defining S_2 and indicating a prograde metamorphism.

Development of chlorite and less commonly biotite traversing the staurolite and garnet porphyroblasts in the examined metapelites, and replacement of hornblende by epidote and iron oxides in the metavolcanic rocks suggests a third metamorphic event in the study area, M3. This phase is considered as a result of non-coaxial deformation associated with formation of the third generation folds and crenulations (D3). This low-grade association is attributed to a phase of exhumation followed the peak metamorphism.

Locally, reactivation along previous discontinuities was accompanied by invasion of large amounts of fluids manifested by widespread alteration and veining. Retrograde metamorphic reactions took place during shear zone formation caused high plasticity, which enhanced the permeability of the host rocks and provided sites of dilation.

The occasional development of epidote and some inclusion-free garnet porphyroblasts indicates a post-crystallization metamorphic phase. This is interpreted as contact metamorphism related to the emplacement of the post-orogenic granite. Relationships among the metamorphic phases and deformation episodes are illustrated in Fig. (2.7).
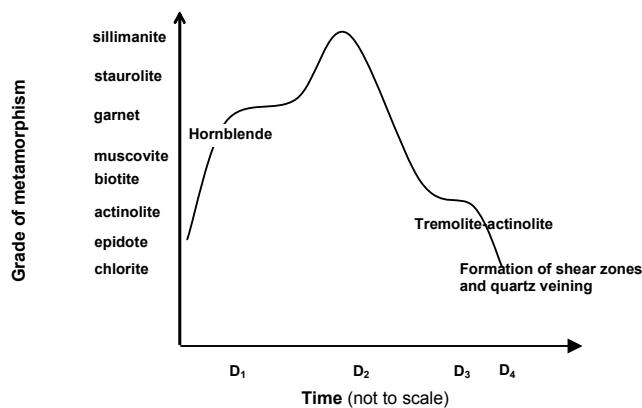
Fig. (2.7): Schematic diagram illustrating the metamorphic history of the Um El Tuyor basement. Grade of metamorphism plotted against time.

2.4.1 The metamorphic fabrics; porphyroblast-matrix textural relationships

To examine and assign the significance of the regional and macroscopic structures in relation to the microscopic fabrics, numerous thin sections of the pelitic metasediments have been prepared. The metasedimentary units exposed in the study area are characterized by foliations of different generations and porphyroblastic minerals such as garnet, staurolite and biotite. Commonly, these porphyroblasts contain foliation traces defined by quartz and biotite inclusion trails. The relationship between the internal foliation (S_i) within the porphyroblasts and the matrix foliation (S_e) outside the porphyroblast was used to determine the relative timing of porphyroblasts growth with reference to foliation of a particular generation. This is in accordance with the criteria described by Spry (1969), Ghosh (1993), and Passchier & Trouw (1996).

In this context, rocks from the highly tectonized zones (e.g. near fold-closures and in refolded horizons) are given the term high-strain zone rocks. Whereas, low-strain zone rocks represent samples collected from the less deformed zones.

Matrix fabrics

Generally, a moderately or steeply dipping, penetrative foliation is defined in the matrix by biotite, chlorite and elongate quartz grains. However, in the high strain zones, crenulation cleavage is typically developed, and a heterogeneous strain is inferred. The main difference in matrix fabrics of rocks in the high- and low-strain zones is defined by quartz and biotite orientation and presence or absence of hornblende. In the high-strain zone rocks, quartz occurs as polycrystalline aggregates forming ribbons parallel to the crenulation cleavage. Biotite forms stretched, pulled apart bladed-shaped flakes. Locally, some biotite flakes are internally crenulated and exhibit sinistral asymmetry. Hornblende, if present, is developed at the expense of biotite but commonly poorly oriented. In contrast, quartz occurs as slightly elongated grains dispersed in the matrix of rocks in the low-strain zones. Biotite flakes are oriented within the matrix foliation and display some degrees of orientation dispersion. Hornblende is absent.

Porphyroblast fabrics

Garnet occurs commonly as euhedral to subhedral xenomorphic porphyroblasts, 0.5 to 6 mm in diameter, and occasionally has quartz-, chlorite- and biotite-dominated pressure shadow tails, which are best-developed in the high strain domains. In rocks from the high-strain zones, garnet porphyroblasts vary from inclusion-poor (~3 vol. %) to inclusion-rich (up to 40 vol. %, Figs. 2.8a,b). In the inclusion-rich porphyroblasts, quartz inclusions define a discontinuous straight foliation (S_i), coinciding with S_m, and typically inclined on the matrix foliation (S_e).

The staurolite porphyroblasts are generally euhedral to subhedral and range from mm to cm in size (Figs. 2.8c,d). They are generally aligned within the crenulation cleavage. It is assumed that this alignment might be the result of either static or mimetic growth or dynamic rigid-body rotation during flattening strain. The staurolite porphyroblasts define a stretching lineation associated with the crenulation cleavage, suggesting that alignment of the staurolite was influenced by the matrix strain. On the other hand, similar to garnet porphyroblasts in the same section, S_i in the staurolite porphyroblasts is consistently inclined on the matrix foliation. This observation suggests that porphyroblasts could not have grown statically after deformation had ceased. Instead, growth of the porphyroblasts was completed before the end of matrix deformation (c.f. Passchier & Trouw, 1996, and Bell et al.

1986). Therefore, metamorphism and deformation interpreted to have been coeval, and the investigated microstructures are syn-kinematic.
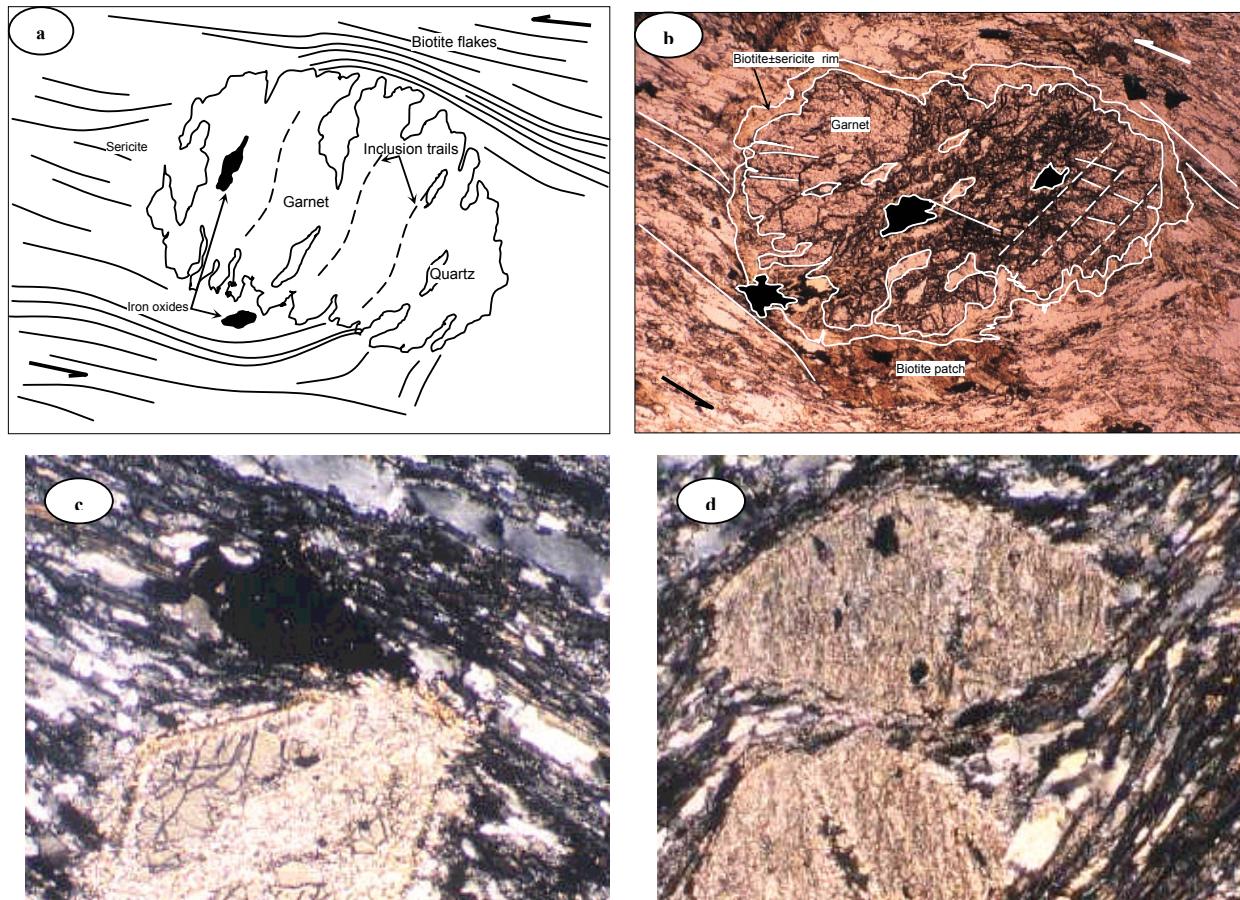
Fig. (2.8): a) Sketch draw of a microscopic relationship between a garnet porphyroblast with quartz inclusion trails and the matrix foliation (wide of view is ~4 mm). b) Photomicrograph of quartz-dominated, tectonically controlled inclusions in garnet crystal exhibit strong deformation and replaced by sericite and biotite at fractures. Notice the high angle between inclusions straight foliation (S_i) and matrix foliation S_e (XPL, wide of view is ~2 mm). c) Staurolite porphyroblast developed within the S_2 planes. d) Biotite, chlorite-rich laminations wrapped around two staurolite porphytoblasts along the matrix foliation (c and d are foliation parallel, lineation-perpendicular views, XPL, wide of view ~2 mm).

2.4.2 Mineral chemistry

The purpose of obtaining mineral compositions is to use the data for geothermobarometry of the metamorphic events affected the basement complex in the study area. Electron microprobe technique was employed in analysing chlorite, biotite, garnet, muscovite, staurolite, and feldspar for their major elements. The analytical conditions, parameters and data are given in Appendix B.

Chlorite, occurring as flakes dispersed in the rock and inclusion trails within garnet porphyroblasts in the metapelites, shows uniform octahedral sheet composition, expressed in Fe/(Fe+Mg) ratios of 0.42 to 0.45 (see Cathelineau, 1988). The Fe^{+3} contents in chlorites from the studied metapelites (calculated according to the procedure adopted by Droop, 1987) are relatively low. The Si/Al ratios are slightly variable, from a minimum of 0.75 in chlorite inclusions in garnet porphyroblasts to a maximum of 0.94 in chlorite flakes parallel to the matrix foliation. Slightly higher MgO contents are shown by chlorite inclusions in garnet porphyroblasts, whereas, dispersed chlorite flakes have higher FeO contents (Table B.1; Appendix B).

The biotite flakes are non-zoned, with $Mg/(Mg+Fe^{2+})$ ratios range from 0.41 to ~0.44. Biotite inclusions in the large garnet and staurolite porphyroblasts have higher MgO%. Whereas, the highest TiO_2 content was observed in biotite flakes adjacent to rims of the large garnet porphyroblasts.

The analyzed garnet porphyroblasts are generally almandine-rich. The large garnet porphyroblasts have Ca-Mn-rich cores, and Fe-Mg-rich rims (Tables B.1, B.2; Appendix B). The composition of the cores can be expressed as $Py_{2.6}Alm_{67}Sp_{20.7}Gro_{9.4}$, whereas the rims are $Py_6Alm_{80}Sp_6Gro_7$. This growth zoning (Fig. 2.9) indicates that the examined garnet did not homogenize its interior, but added successive shells of materials whose composition reflects equilibria processes in the rock matrix (see Spear & Daniel, 1998).

For most of the analyzed muscovite grains, the structural formulae is generally identical, containing 6.56 - 6.672 Si atom per formula unit, and having X_{Ms} in the range of 0.96-0.99. Composition of the individual plagioclase crystals is homogenous, with anorthite (An) content of 25 mol %, on average. However, plagioclase coexisting with the garnet porphyroblasts is richer in the anorthite component (An_{30}).

In the investigated metapelites, staurolite is generally iron-rich. Some representative microprobe data of fresh, non-sericitized, staurolite porphyroblasts in the studied metapelites is given in Table B.2 (Appendix B).
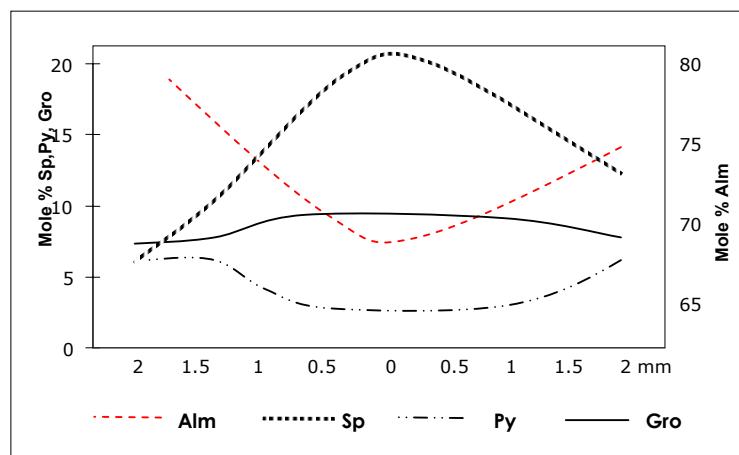
Fig. (2.9): Average compositional variation along three profiles traversing three garnet porphyroblasts in the garnet-biotite schist.

2.4.3 Geothermobarometry

The composition of garnet porphyroblast cores, with minimum Mn and Fe/(Fe+Mg), were combined with chlorite and biotite inclusions to obtain information on the early metamorphic episode (M1). The garnet-chlorite thermometry (Dickenson and Hewitt, 1986; Kranidiotis & McLean, 1987) suggests a temperature range of 380±50°C for cores of the large garnet porphyroblasts and chlorite inclusions. Formation temperature range of 353 to 409°C is estimated for the investigated chlorite flakes and inclusion trails in the metapelites. However, the limited mineral phases constraining the M1 assemblage, along with the absence of suitable barometer prevent pressure estimation of this metamorphic event.

The geothermometric conditions of M2 metamorphism are estimated using the biotite-garnet thermometry with calibration of Kleemann and Reinhardt (1994).

$$KMg_3AlSi_3O_{10}(OH)_2 + Fe_3Al_2Si_3O_{12} \Leftrightarrow KFe_3AlSi_3O_{10}(OH)_2 + Mg_3Al_2Si_3O_{12}$$

    Mg-biotite   Fe-garnet   Fe-biotite   Mg-garnet
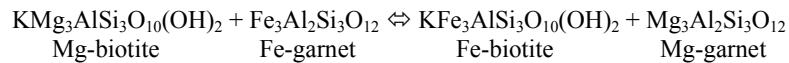
This thermometry is based on a reaction, common in metapelites of medium to high grade metamorphism, virtually independent of pressure, but strongly dependent on temperature (Ferry & Spear, 1978). Calculations according to Bhattacharya et al. (1992) on the obtained microprobe data yield a temperature range of 534°- 561°C for the peak metamorphic conditions during M2 (Table B.3; Appendix B). The used garnet activity model is that of Berman (1990). Pressure is estimated using the plagioclase-biotite-muscovite-garnet geobarometer of Powell and Holland (1988), originally calibrated by Ghent and Stout (1981). A pressure range of 5.26 - 6.20 kbar is indicated for the prograde path during M2. As temperature and pressure rose, the stable mineral assemblage (garnet-chlorite-biotite-muscovite-quartz) became unstable and staurolite started to form (Lasaga, 1986).

$$Mg_3(Mg,Si)_2(SiO_4)_3 + (Fe,Mg,Ti)_5Al_2Si_3O_{10}(OH)_8 + 2KAl_3Si_3O_{10}(OH)_2 \rightarrow (Fe,Mg)_2Al_9(Si,Al)_4O_{22}(OH)_2$$

    garnet   chlorite   muscovite   staurolite

$$+2K(Fe,Mg,Ti)_3AlSi_3O_{10}(OH)_2 + SiO_2 + H_2O$$

                           biotite   quartz
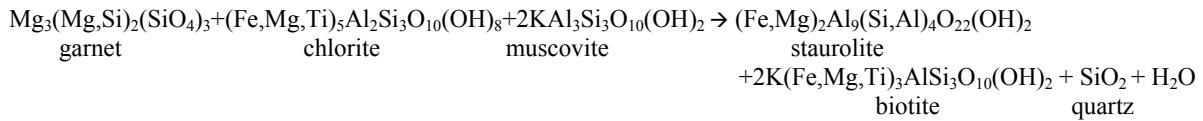
Various textural relationships (e.g. replacement, overgrowth, reaction rims, etc.) suggest the development of staurolite at the expense of chlorite and garnet, emphasizing the prevalence of the above mentioned reaction during metamorphism. Staurolite started to form during the earlier stages of the prograde path (M2). However, it is thought that the metamorphism reached its peak only when both sillimanite and staurolite were stable. Temperature estimates (Table B.4; Appendix B), according to the method of Koch-Müller (1997) give similar values as obtained from the garnet-biotite geothermometer of Bhattacharya et al. (1992).

CHAPTER 3

GEOCHEMISTRY & TECTONIC EVOLUTION

3 GEOCHEMISTRY & TECTONIC EVOLUTION

Geochemical data can be used for rock characterization and to decipher the tectonic environment in which the rock unites exposed in the Um El Tuyor area were formed. The analytical data and techniques are given in Appendix C. Further, the tectonic evolution model is constructed on basis of the inter-relationships among units of different tectonic settings in coincidence with the present field observations.

3.1 The ophiolitic rocks

3.1.1 Serpentinite

According to the classification and nomenclature of peridotites and pyroxenites proposed by Streckeisen (1976) and Le Bas & Streckeisen (1991), the analyzed serpentinite resembles peridotite (lherzolite and dunite) in composition (Fig. 3.1a). Samples assumed to be originally dunite are typically characterized by their higher Mg# (MgO/[MgO+FeO+MnO] molar ratio) and normative olivine values compared to those considered as metamorphosed lherzolite (Table C.1; Appendix C). On the AFM diagram of Coleman (1977), data points of the analyzed serpentinite samples plot in the field of metamorphic peridotites and overlap with the ultramafic cumulate field (Fig. 3.1b). The investigated serpentinite rocks are depleted in Al_2O_3, if compared with the primordial mantle rocks (c.f. Hofmann, 1988), and there is a positive correlation between Al_2O_3 and CaO (Fig. 3.1c). On the CaO vs. MgO variation diagram (Fig. 3.1d), plots of the analyzed serpentinite samples overlap with the abyssal peridotites field (c.f. Dick, 1989).

The REE profiles of the analyzed serpentinite samples (Fig. 3.1e) show generally high abundances of the REE relative to chondrite, with particular enrichment in the light REE (LREE). Although $(La/Lu)_N$* ranges from 3.81 to 6.75 and $(Tb/Yb)_N$ from 0.84 to 1.67, most of the samples show sub-parallel trends irrespective of their litho-geochemical or geographic association. The general absence of positive Eu anomaly in any of the analyzed samples suggests that plagioclase was not a major fractionating mineral phase. Similarly, the primitive mantle-normalized multi-element patterns of the investigated serpentinite (Fig. 3.1f) show an overall slope from left to right, that is, enrichment in Th, Rb, Ba, Sr, and depletion in HFSE (i.e. Cr. Ni, Zr and Zn). These patterns indicate a slightly positive Nb anomaly, which is characteristic of the enriched mantle tectonites (see Weaver and Tarney, 1981).

3.1.2 The ophiolitic metagabbro, amphibolite and metabasalt

The geochemical data of the studied ophiolitic metagabbros, amphibolite and metabasalt are given in Table C.2 (Appendix C). Plots of the normative pyroxene (px), plagioclase (pl) and olivine (ol) values of the analyzed metagabbro, amphibolite and metabasalt samples on Streckeisen (1976) diagram classify them as gabbro-norite and olivine gabbro-norite (Fig. 3.2a). The Zr/Ti vs. Nb/Y and the P_2O_5 vs. Zr discrimination diagrams (Winchester and Floyd, 1977) indicate a subalkaline-tholeiitic affinity of these rocks (Figs. 3.2b,c). Plots of the investigated amphibolite and metabasalt scatter within the MORB field and overlap with the island arc tholeiites (Fig. 3.2d,e). A kind of evidence for back arc setting for these rocks is indicated by Fig. (3.2f). Plots of data points of ophiolitic metagabbro, amphibolite and metabasalt rocks roughly follow the partial melting curve I in Fig. (3.2g), which correlates to Archaean mantle sources with 60% olivine + 20% orthopyroxene + 10% clino-

(* normalized to chondrite using reference data of Sun and McDonough (1989)

pyroxene +10% plagioclase (Drury, 1983; Sun and Nesbitt, 1977). The latter observation suggests low to moderate degrees of partial melting of a garnet-free mantle source for the studied ophiolites (see Dick, 1989; Drury, 1983). The MORB character of the investigated metagabbro, amphibolite and metabasalt is consistent with their association with tectonized serpentinites. However, MORB signatures from accreted oceanic terranes are relatively rare. Dewey (1976) gave an explanation for similar situations, that, it is mechanically more feasible to obduct young buoyant supra-subduction zone oceanic crust (SSZ) than to obduct mature oceanic crust generated at a mid-ocean ridge.
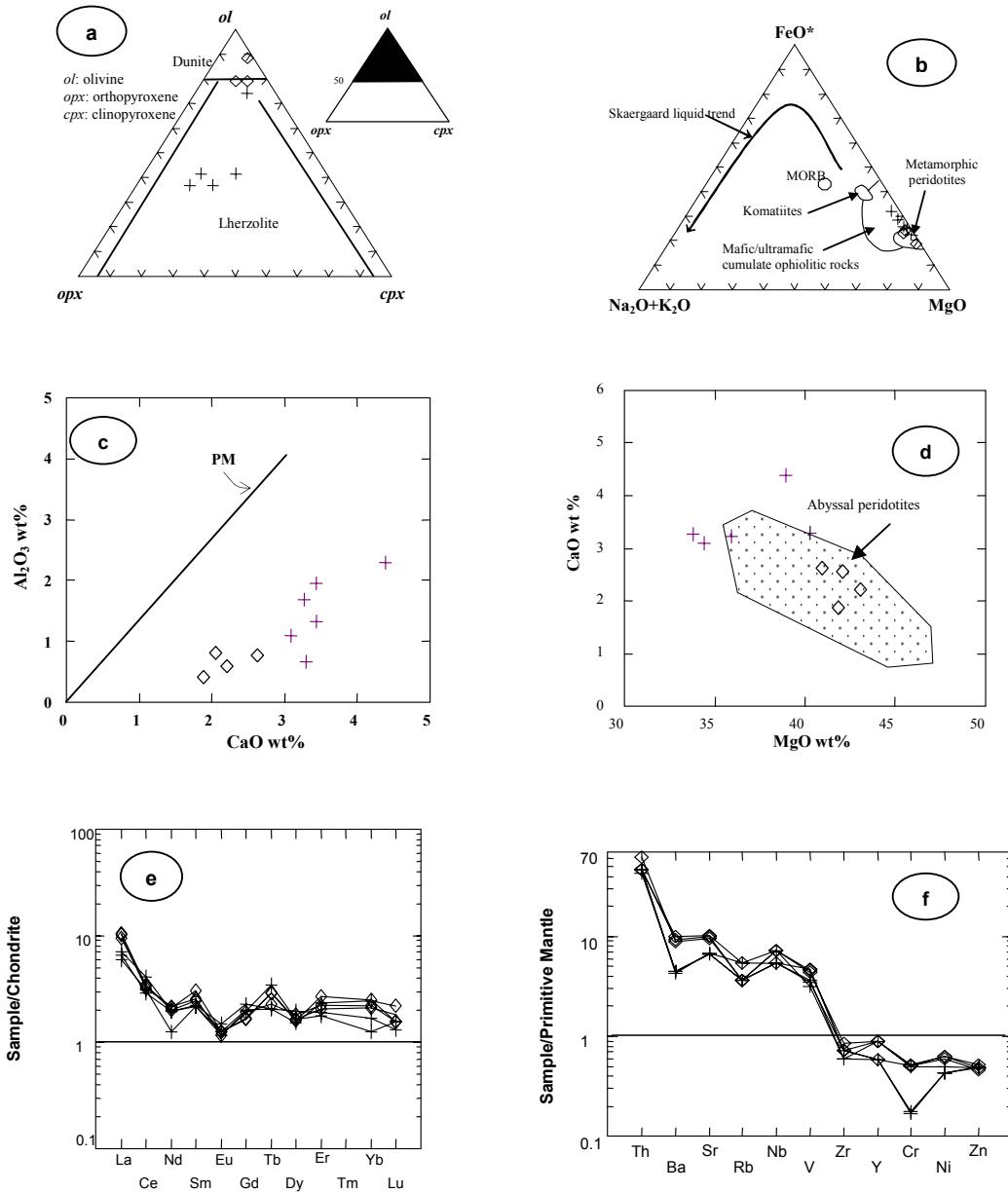
Fig. (3.1): a) Classification and nomenclature of the analyzed serpentinite samples (diagram after Streckeisen, 1976); b) AFM diagram (after Coleman, 1977) with data points of the investigated serpentinites; c), d) Al₂O₃ vs. CaO, CaO vs. MgO variation diagrams. PM= primordial mantle (Hofmann, 1988), abyssal peridotites field is drawn according to Dick (1989); e) Chondrite-normalized RRE patterns; f) Primitive mantle-normalized trace element patterns for the studied serpentinite. Normalizing values from Sun and McDonough (1989). Samples of assumable lherzolite composition are given the plus symbol and those retain dunite in composition are represented by rhombi. Major oxide contents are recalculated on anhydrous basis.
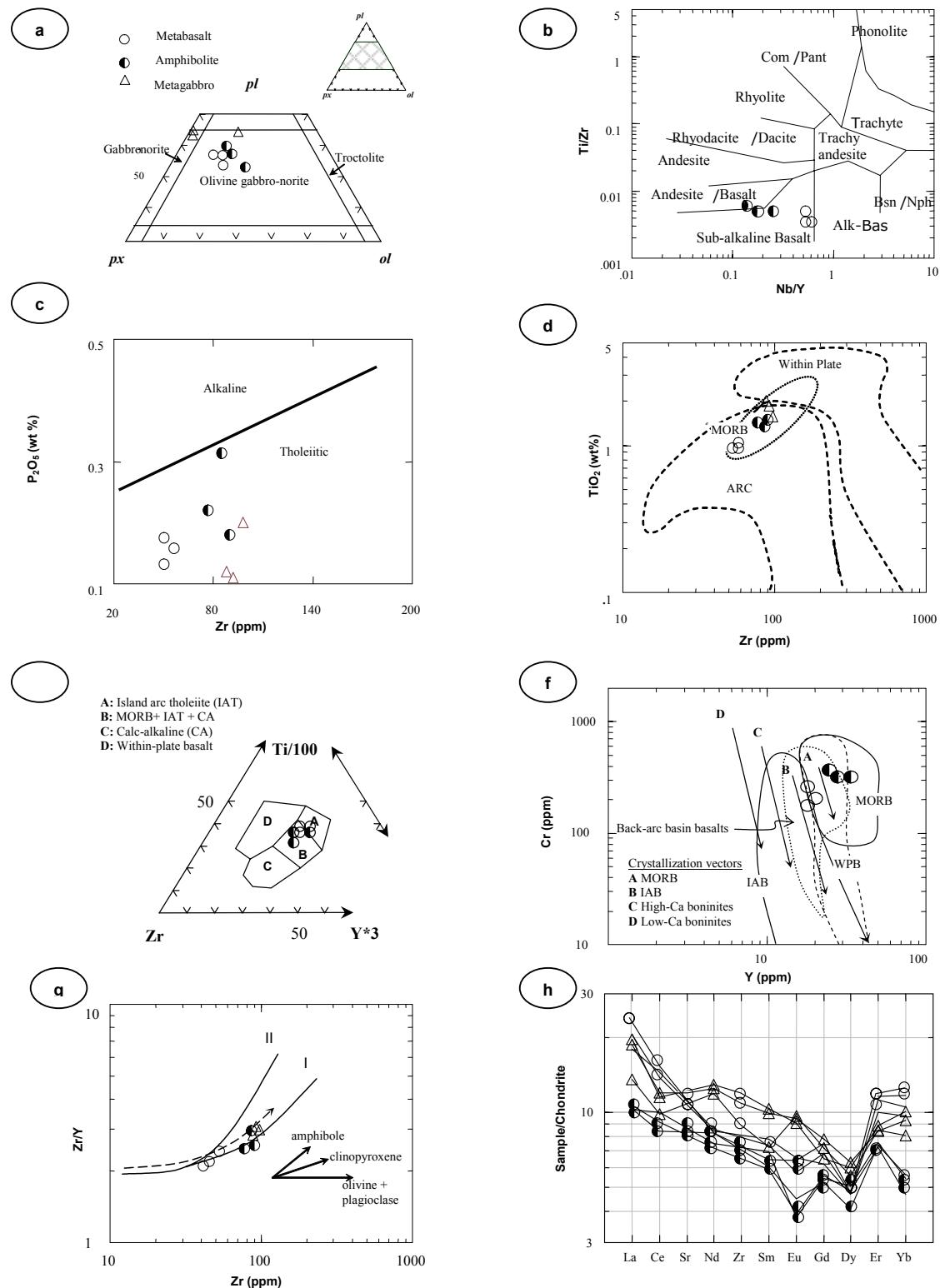
Fig. (3.2): a) Plots of the normative px (pyroxene), pl (plagioclase) and ol (olivine) values of the studied metagabbro, amphibolite and metabasalt on Streckeisen (1976) diagram. b) Nb/Y–Zr/Ti discrimination diagram (Winchester and Floyd, 1977) for the studied ophiolites. c) Zr- P₂O₅ diagram for the invesigated rocks after Winchester and Floyd (1976). d) TiO₂- Zr diagram for the investigated metagabbro and amphibolite (after Pearce, 1980). e) and f) Plots of the analyzed metagabbro, amphibolite and metabasalt samples on the Ti-Zr-Y discriminating diagram of Pearce and Cann (1973) and Y- Cr discriminating diagram of Pearce et al. (1984b) respectively. IAB: island arc basalt, MORB: mid ocean ridge basalt, WPB within plate basalt. The field of back-arc basin basalts is after Hawkins et al. (1990). g) Zr/Y vs. Zr diagram for the investigated rock. Melting curves (I and II) are after Drury (1983) and vectors for fractional crystallization after Floyd (1993). h) Chondrite-normalized REE patterns of the investigated ophiolitic rocks.

Bloomer et al. (1995) suggested that after the initiation of a subduction zone, infant arc volcanism with exceptionally high production rates (equivalent to slow spreading ridges) replaces the thinned (pre-existing) oceanic crust during formation of a supra-subduction zone ophiolite. Thus, both MORB and depleted volcanic arc chemistries can be expected.

The extended (REE, Sr and Zr) spidergrams show LREE-enrichment of the analyzed samples (Fig. 3.2h). Because Sr may be mobile during metamorphism and weathering, the Sr/Sr* (see Appendix C for definition) is used as a comparison with the Eu contents. Rocks with plagioclase accumulations (i.e. metagabbro) exhibit positive Eu/Eu* and Sr/Sr* anomalies, whereas, rocks that have had plagioclase removed (i.e. metabasalts) show negative Eu/Eu* and Sr/Sr* anomalies. The analyzed metagabbro samples have strong positive Sr/Sr* anomaly (2.65-3.35), which is typical of plutonic cumulate rocks having plagioclase in their mineralogy (c.f. Smith Nagihara and Casey, 2001). The investigated amphibolite samples show steeper REE patterns (higher La/Yb) if compared to the metagabbro. Also, they indicate no significant positive Eu/Eu* and Sr/Sr* anomalies, therefore, assumed to have not derived from cumulate rocks (see Seifert et al., 1996).

The studied amphibolite and metabasalt are assumed to have been derived from basaltic protolith with incompatible trace element–enriched composition rather than accumulations of fractionated minerals from a magma chamber or conduit system. Emplacement of the basaltic magma might have promoted crystallization of plagioclase and clinopyroxene, whereas, metamorphism produced the observed mineral assemblages and grain-coarsening.

3.2 The island arc assemblage

3.2.1 The metasediments

On basis of their mineralogy, the studied metasediments are categorized into metapelite (garnet±staurolite biotite schists), meta-psammite (quartz+garnet+biotite-muscovite bearing metasiltstones) and subordinate quartzite. Similarly, the major and trace elements data of the analyzed samples indicate three distinct groupings coinciding with the three dominant lithologies of the Um El Tuyor metasediments. The metapelite and quartzite samples show contrasting geochemical characteristics, while the meta-psammite samples typically have intermediate compositions between these two lithologies (Table C.3; Appendix C). In comparison with the quartzite, the metapelite samples have significantly lower SiO_2 and higher Fe_2O_3, K_2O, MgO, Al_2O_3, TiO_2, Zr, Na_2O, Rb, Ba and V contents.

The ternary molecular A-CN-K plot after Nesbitt and Young (1984) has been used to investigate possible chemical effects of weathering in the Um El Tuyor metasediments. In Figure (3.3a), the metapelite and quartzite samples plot in the right side of the weathering trend of the Precambrian metapelites (Nesbitt and Young, 1982) near the A-K join, indicating that some of these samples have been affected by K-metasomatism. Values of the chemical index of alteration (CIA) for these samples, calculated following the method of Fedo et al. (1995), are varying from 37.97 to 57.68, which indicate that the region was subjected to low or moderate chemical weathering. In the A-CNK-FM diagram of Nesbitt and Young (1989), all the data points plot along a mixing line between illite(muscovite) and chlorite (Fig. 3.3b). The latter observation suggests the existence of mafic rocks in the source region at the time of deposition of the metasediments and metasomatic introduction of K_2O (Nesbitt and Young, 1989).

On the ACF diagram (Fig. 3.3c) proposed by Winkler (1976), plots of the analyzed metasediments indicate derivation from argillaceous graywacke. Miyashiro (1973) used the ACF diagram to distinguish between rocks of sedimentary and igneous origins. Shale and graywacke parentages are assumed for the metasedimentary rocks exposed in the study area (Fig. 3.3d).
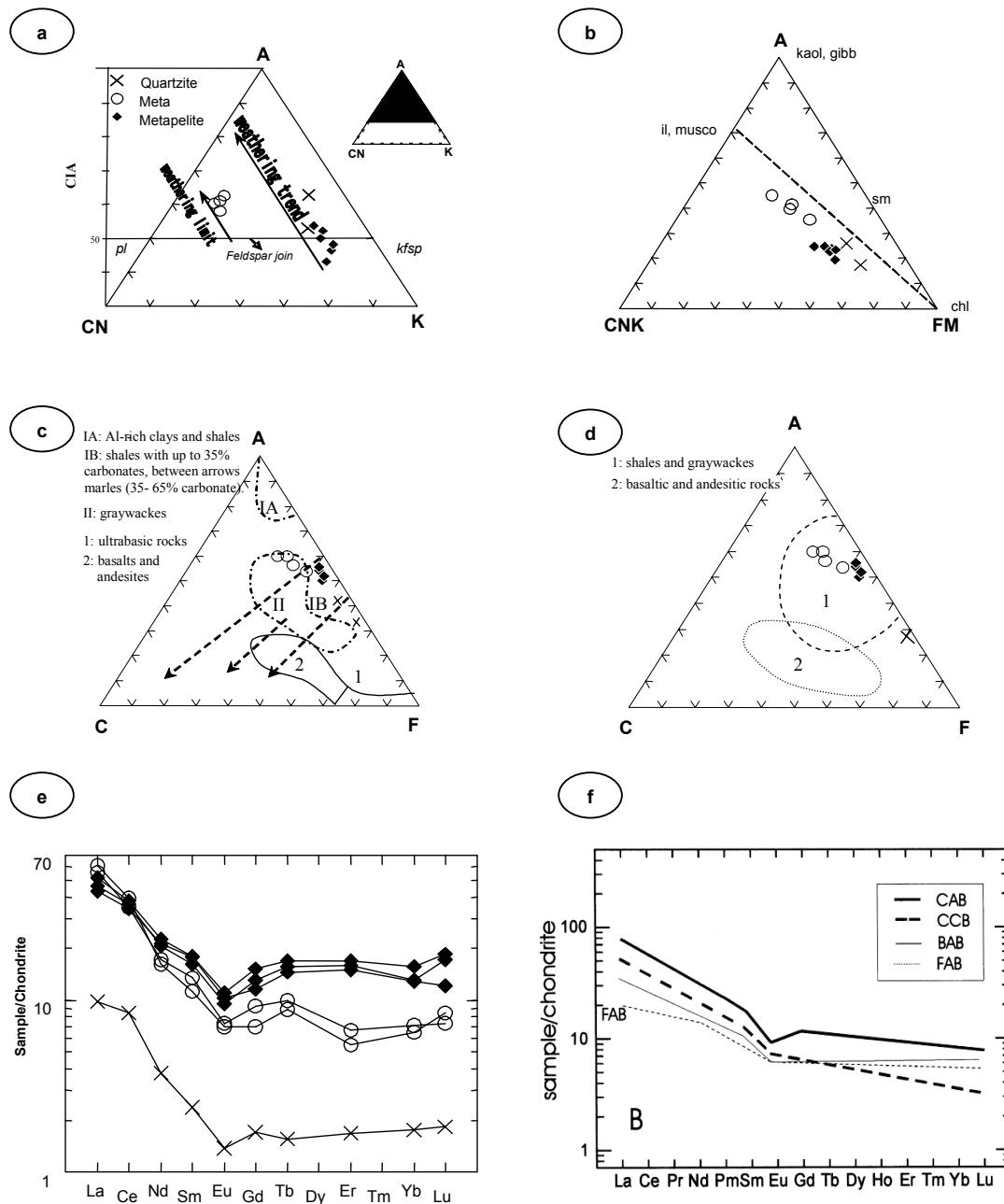
Fig. (3.3): a) A-CN-K diagram of Nesbitt and Young (1984) for the Um El Tuyor metasedimentary rocks. b) A-CNK-FM diagram for the studied metasediments. kaol, kaolinite; gibb, gibbsite; chl, chlorite; sm, smectite; il, illite; kfsp, potash feldspar; pl, plagioclase and musc; muscovite. c) ACF diagram for the studied metasediments (after Winkler, 1976). d) ACF diagram with field boundaries after Miyashiro, 1973. A= Al_2O_3, C= CaO, N= Na_2O, K= K_2O, F= Fe_2O_3*, M= MgO. e) Chondrite-normalized rare earth element (REE) profiles for representative samples of Um El Tuyor metasediments. Normalizing values from Sun and McDonough (1989). f) Typical chondrite-normalized REE profiles for clastic rocks in arc-related basins (after McLennan et al. 1990). CAB= continental arc basin, CCB= continental collision basin, BAB= back-arc basin , FAB= fore-arc basin.

The high MgO, Fe_2O_3 and TiO_2 concentrations, the low abundances of Ni, Cr, V, and the LREE enrichment in most of the metapelite samples suggest a significant contribution from a differentiated mafic source. On the other hand, the presence of quartzite bands within the metapelite sequence suggests a contribution from a continental source. The low La/Th (5.22–8.42) and intermediate Ti/Zr (33.2- 49.5) ratios are typical of a mixed felsic-mafic crustal source (e.g. Bhatia and Crook 1986).

The total sum of the rare earth elements (ΣREE) of the Um El Tuyor metasediments (ranges from 16.61 to 90.06 ppm) correlates positively with their Al_2O_3 contents. The chondrite-normalized REE profiles of the analyzed samples indicate fractionated patterns (Fig. 3.3e), with $(La/Yb)_N$, ranging from 3.26 to 9.46. Also, these samples show LREE enrichment and flat HREE, $(La/Sm)_N$ ranging from 2.82 to 5.43 and $(Gd/Yb)_N$ ranging from 0.89 to 1.28. The quartzite contains significantly lower ΣREE than the metapelites and the metapsammites, reflecting surface processes (e.g., McDaniel et al. 1994). On the other hand, the REE profiles of the metapelite and metapsammite are similar to profiles of the back arc sedimentary basins (Fig. 3.3f; McLennan et al. 1990), while their negative Eu anomalies (Eu/Eu* ratio ~0.10 to 0.59) are attributed to the presence of an Eu-depleted felsic rock in the source region.

3.2.2 The island arc metavolcanic rocks

Data of the bulk chemical composition of the island arc metavolcanic rocks are summarized in Table C.4 (Appendix C). Based on Figures (3.4a to d), the investigated metavolcanic rocks are geochemically classified as basalt and basaltic andesite derived from alkaline to sub-alkaline magma in arc and/or back arc tectonic settings. The Large Ion Lithophile elements-to-High Field Strength elements ratios (LILE/HFSE, e.g. K/Ti, K/Zr and K/Nb), the negative Ti anomalies, and the slightly negative Nb anomaly displayed by data points of the analyzed samples indicate a subduction-related petrogenesis for the studied metavolcanic rocks (c.f. Ewart, 1982; Hole et al. 1984). The Ti/V ratios in the studied metavolcanic rocks (30.47–61.69) are similar to those in the oceanic basalts extruded at mid-ocean ridges and back-arc spreading centres (see Shervais, 1982, for reference values). On the other hand, data of the studied metavolcanic rocks are roughly similar to data of the ocean island basalt (Sun and McDonough, 1989).

The investigated metavolcanic rocks are characterized by moderate enrichment in LREE relative to HREE (Fig. 3.4e), with $[La/Yb]_N$=3.5–5.37, $[Ce/Yb]_N$=2.2–3.82, and $[Tb/Yb]_N$=0.73–1.28. All of the analyzed samples have Th/Yb ratios higher than 1, which is typical of the calc-alkaline island arc rocks (Pearce, 1983). The low to moderate concentrations of the incompatible elements (Y<40 ppm; Nb<20 ppm; Zr<250 ppm; Hf<5.5 ppm; Th<7 ppm) and many inter-element ratios (e.g. Nb/Y=0.1–0.8; Th/Yb=1.2–2.0; Zr/Nb mostly 10–25) indicate that the studied metavolcanic rocks represent a calc-alkaline arc suite (Barrett and MacLean, 1997). However, the Zr/Y ratio (>60) of the analyzed metavolcanic rocks indicates a weakly tholeiitic affinity (Pearce, 1983; Barrett and MacLean, 1997; Condie, 1986; Harris et al., 1986).

The primitive mantle-normalized immobile elements profiles of the studied metavolcanic rocks (Fig. 3.4f) show depletion in Sr and Nb relative to Th–U and La–Ce, and a prominent trough at Nd, consistent with a subduction-associated petrogenesis (Hildreth and Moorbath, 1988; Hawkesworth et al., 1993; Brenan et al., 1994).
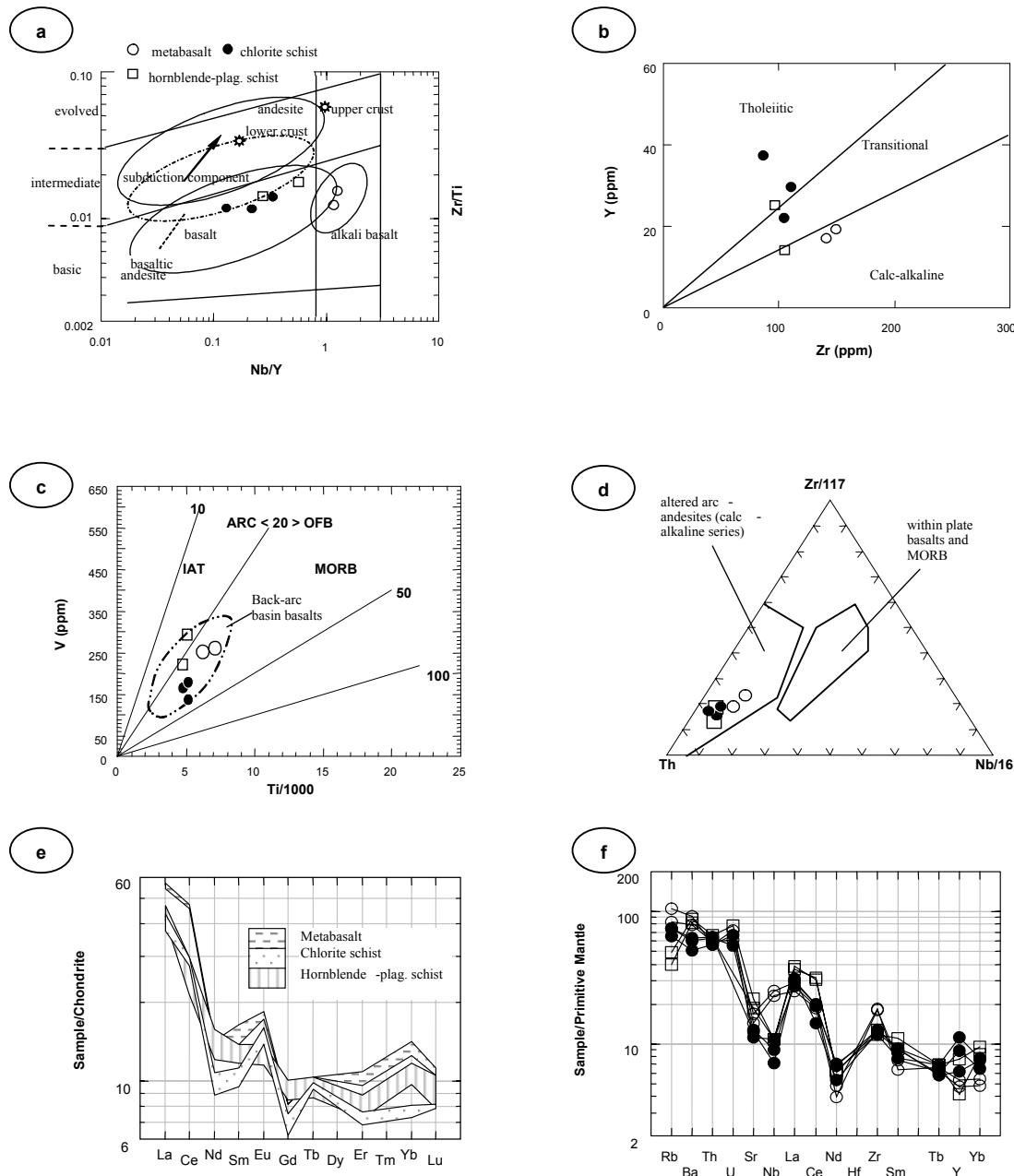
Fig. (3.4): a) Nb/Y versus Zr/TiO2 diagram (after Winchester and Floyd, 1977) for the studied metavolcanics with 10% probability ellipses and subduction component arrow after Pearce (1996). b) Zr/Y diagram for the investigated metavolcanics, field boundaries after Barrett and MacLean (1997). c) Tectonic setting discriminant diagram (Shervais, 1982) for the studied metavolcanics. Field of the back-arc basin basalts after Pearce et al. (1984b) and Hawkins et al. (1990). d) Th-Zr-Nb tirnary plot of the studied metavolcanics with fields after Wood (1980). e) Chondrite-normalized REE patterns of the Um El Tuyor metavolcanic rocks. f) Primitive mantle-normalized immobile elements plot of the investigated metavolcanic rocks. Normalization values from Sun and McDonough (1989).

3.2.3 The island arc metagabbro

The arc-related metagabbro displays a wide range of whole rock composition (Table C.4; Appendix C). Abundances of the most incompatible trace element (Nb, Zr and Y) in the analyzed samples indicate a volcanic arc tectonic setting (Fig. 3.5a). The limited range of Cr and Ni concentrations in the studied metagabbro, relative to their bulk rock chemistry indicates that magmatic differentiation was the main process (Murck and Campbell, 1986). In order to estimate the amount of the partial melting and the path of differentiation, the approach outlined by Pearce (1980) has been used. The partial melting curve for the C3 chondrite which closely represents the primordial mantle is modelled on a Cr vs Y plot since these elements do not seem to be affected by variations in the mantle composition (Pearce, 1980). The data points of the representative samples suggest ~ 20 to 40% melt fraction of basaltic magma in a back arc setting (Fig. 3.5b). Very similar

Because Zr is more incompatible if compared with Y and Ti in the mantle phases, Zr/Y and Zr/Ti ratios increase if magma evolved by fractional crystallization from basic to acidic composition. A plot of Zr (ppm), as a fractionation index (Pearce and Norry, 1979), versus Zr/Y ratio shows a large variation in Zr/Y ratios with increasing Zr abundance (Fig.3.5c). Olivine and plagioclase fractionation will not change the Zr/Y ratio, whereas, clinopyroxene and amphibole fractionation may slightly raise the ratio with increasing the Zr content (see Floyd, 1993). The observed trend for the investigated metagabbro rocks shows a concomitant increase in Zr/Y ratio with higher Zr concentrations. This relationship reflects the onset of amphibole fractionation which led to a decrease in Y and enrichment in Zr, typical of calc-alkaline volcanic arc lavas (Brown et al., 1977). Samples of the studied metagabbro rocks closely follow curve II, indicating moderate to high degrees of partial melting of a garnet-bearing mantle source (c.f. Drury, 1983).

A striking chemical signature of the volcanic arc rocks for the investigated metagabbro is the depletion in HFSE (e.g. Nb, Zr and Y) relative to the LILE (e.g. K, Sr and Ba; Pearce, 1982; McCulloch, 1993). The chondrite- and primitive mantle-normalized REE patterns of these rocks are characterized by convex-downward profiles (Figs. 3.5d,e). These patterns are characterized by enriched LREE [average $(La/Sm)_N$ = 2.03], slightly enriched middle REE (patterns are convex upward), virtually flat HREE [average $(Gd/Yb)_N$ = 1.09] and very slight positive Eu anomalies (Eu/Eu*= 0.93 to 1.07). Positive Eu anomalies, characteristic of samples that have high modal concentrations of plagioclase, suggest that plagioclase contributed to the abundances of Eu and the lightest REE and helped in diluting the intermediate and heavy REE abundances (e.g. Hassanipak et al. 1996). The MORB-normalized geochemical pattern of the analyzed samples of the metagabbro rocks (Fig. 3.5f) suggests a close resemblance to the calc-alkaline volcanic arc basalt.
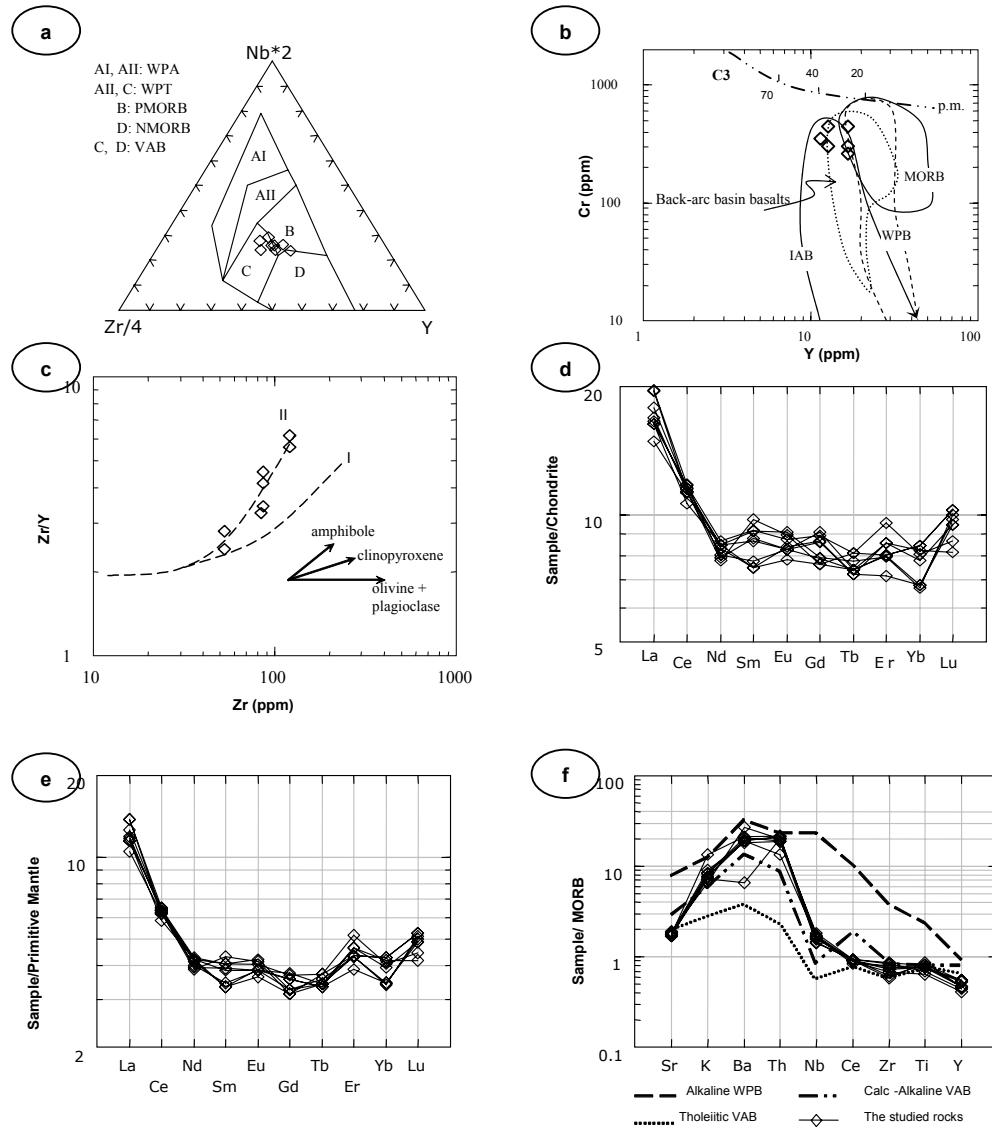
Fig. (3.5): a) Zr-Nb-Y diagram for the investigated island arc metagabbro (Meschede, 1986); WPA: within plate alkali basalts, WPT: within plate tholeiites, MORB: mid ocean ridge basalt, and VAB: volcanic arc basalt. LKT = low-potassium basalt, OFB = ocean-floor basalt, BAB = back-arc basalt, OIB = oceanic-island basalt, VAT = volcanic-arc tholeiite. CFB = continental-floor basalt. b) Cr vs Y plot for the studied island arc metagabbro showing the evolution path of magma (according to Pearce, 1980). The p.m.-line is the partial melting curve of C3 chondrite. MORB=mid-oceanic ridge basalt, IAB=island arc basalt, WPB=within plate basalt (Pearce et al.1984b and references therein). c) Binary plots of a Zr/Y vs. Zr for the studied metagabbro. Melting curves I and II after Drury (1983), and vectors for fractional crystallization after Floyd (1993). d), e) Chondrite- and primitve mantle-normalized REE pattern of the metagabbro. Normalization vlaues from Sun and McDonough, (1989). f) MORB-normalized incompatible element patterns of the studied metagabbro. Data used for comparison are: the average composition of tholeiitic and calc-alkaline volcanic arc basalt and within plate basalt (Pearce, 1982).

3.3 The syn- and post-orogenic intrusive rocks

3.3.1 The granitic rocks

The syn-orogenic granitoids and post-orogenic granite are discussed here together to depict differences in their chemical characteristics and tectonic setting. Characteristically, the syn-orogenic granitoids have higher Al_2O_3, MgO, CaO, Fe_2O_3, TiO_2, Ba, Zr, and V, but lower total alkalis, SiO_2, Th, U, and REE, compared to the post-orogenic granite (Table C.5; Appendix C). Using the diagram of Hunter et al. (1978), the representative granitoids data points plot in the granodiorite field, whereas the post-orogenic granite samples indicate a quartz-

monzonite composition (Fig. 3.6a). The post-orogenic granite is normal or strongly differentiated as shown in Fig. (3.6b). On the other hand, the syn-orogenic granitoids are strongly per-aluminous calc-alkaline rocks, whereas data points of the post-orogenic granite distribute between the calc-alkaline and alkaline peraluminous to metaluminous fields (Figs. 3.7a,b). Further, the trace element data are also commensurate with fractional crystallization, with lower Sr, REE and transitional metals (i. e. Ni, Co), and higher Rb and Ba relative to SiO_2 wt. %. Discrimination in the Nb vs. Y diagram of Pearce et al. (1984a) revealed that the granitoids are volcanic arc related (Fig. 3.7c), with some geochemical characteristics of the recent syn-collision granite (high Rb, low Zr, Hf and Sr contents, see Pearce et al., 1984a). On the other hand, data of the post-orogenic granite indicates a calc-alkaline nature, and a within-plate setting (WPG). The diagram of Maniar & Piccoli (1989) indicates strikingly different tectonic environment of the syn- and post-orogenic granitic rocks (Fig. 3.7d). The alumina saturation index of Shand (1947) calculated for the syn- and post orogenic granitic rocks (mol% $A1_2O_3$ /[Na_2O+K_2O+CaO]) is less than 1.1. The latter is typical of I-type granites according to Vetter and Tessensohn (1987). Although both of the syn-and post orogenic granitic rocks in the Um El Tuyor area are I-type granites, the syn-orogenic granitoids are assumed to have been derived from deeper sources, as indicated by Fig. (3.7e). The high Rb/Sr (>2.6) and low Sr/Ba (<0.4) ratios in the post-orogenic granite samples are consistent with plagioclase fractionation during their crystallization.

Samples of the post-orogenic granite have higher Rb/Sr values (2.29 to 3.79) if compared with the syn-orogenic granitoids (maximum 0.41). The positive Sr/Sr* anomalies, negative Eu anomalies and non-fractionated HREE in the syn-orogenic granitoids suggest presence of plagioclase and absence of garnet in the source magma (c.f. Jung et al., 1999). The per-aluminosity combined with the negative Nb anomalies, low Ti/P ratios, and strong negative Eu anomalies of the post-orogenic granite suggest contribution from a crustal source (c.f. Opiyo-Akech et al., 1999).

Chondrite-normalized REE patterns (Fig. 3.7f) show that the syn-orogenic granitoids have enriched LREE (La_N/Yb_N =6.05–7.23) and less fractionated HREE (average Gd_N/Yb_N =1.04), and display negative Eu anomalies (Eu/Eu* =0.61-0.75). On the other hand, samples of the post-orogenic granite are more enriched in the LREE (La_N/Yb_N=6.19-10.03) and show much pronounced negative Eu anomaly (Eu/Eu* reaches 0.52).
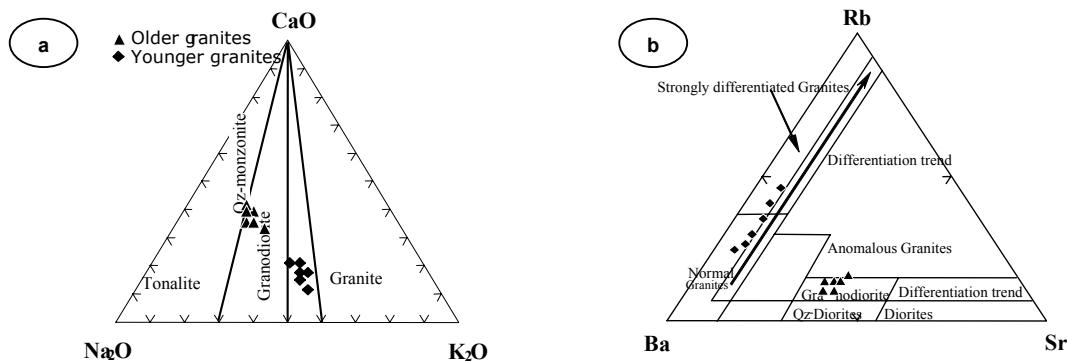
Fig. (3.6): a) Nomenclature of the granitic rocks exposed in the Um El Tuyor area (after Hunter et al., 1978). B) Ba-Rb-Sr diagram for the studied granitic rocks. Discrimination fields after El Bouseily and El Sokkary (1975).
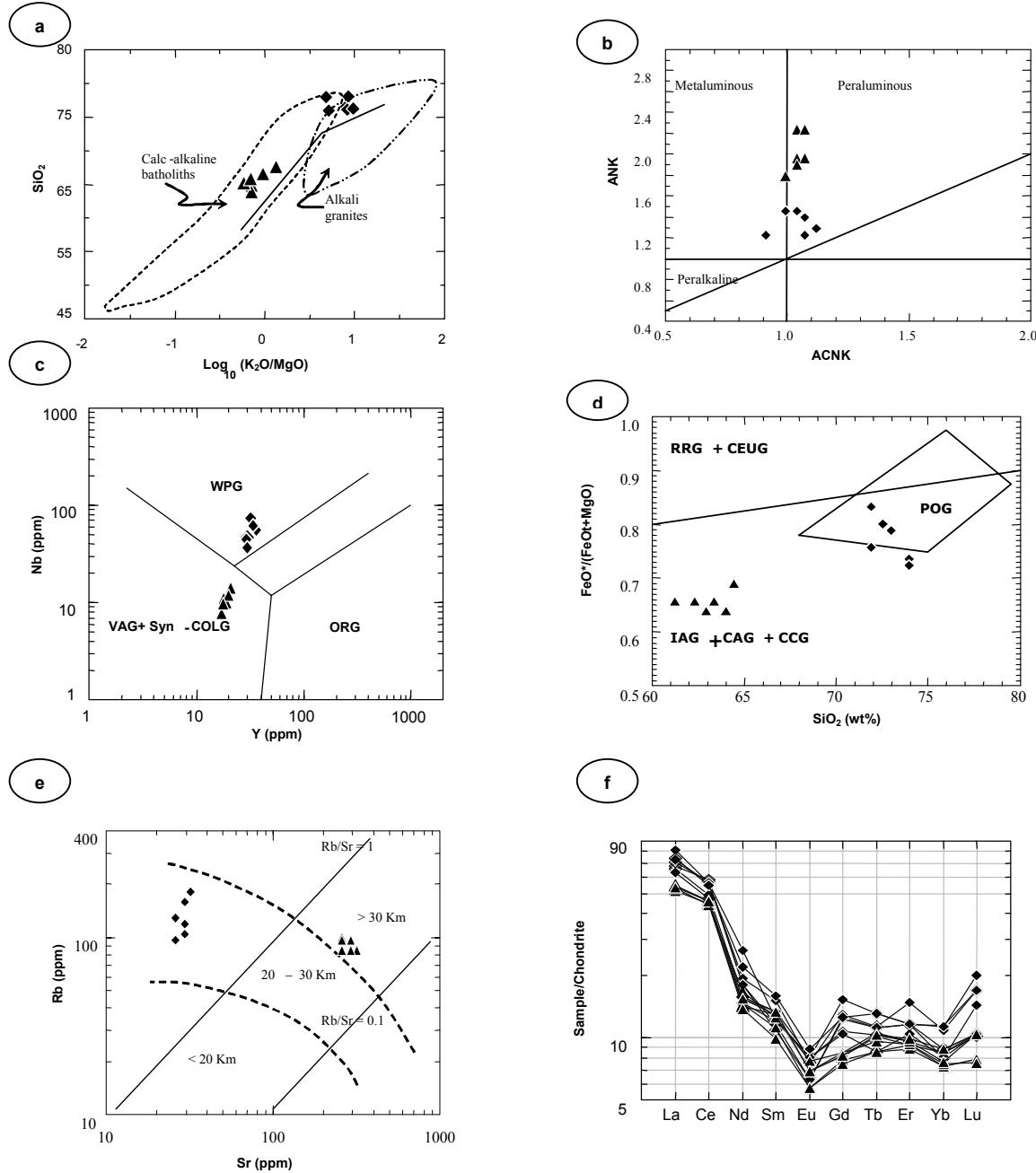
Fig. (3.7): a) Rogers and Greenberg (1981) discriminating diagram for the studied granitic rocks. b) Molar Al₂O₃/(Na₂O+K₂O) plotted against molar Al₂O₃/(CaO+Na₂O+K₂O), diagram of Maniar & Piccoli (1989). c) Discrimination diagram for tectonic affinity of granites (after Pearce et al., 1984a). d) Discrimination diagram for the studied granitic rocks (after Maniar & Piccoli, 1989). IAG: island arc granitoids; CAG: continental arc granitoids; CCG: continental collision granitoids; RRG: rift-related granitoids; CEUG: continental epiorogenic uplift granitoids; POG: post orogenic granite. e) Rb- Sr crustal thickness index (after Condie, 1973). f) Chondrite-normalized REEs patterns of the granitic rocks exposed in the Um El Tuyor area.

3.3.2 The post-orogenic, olivine gabbro

The geochemical data of a number of representative samples of the studied post-orogenic, olivine gabbro are given in Table C.5 (Appendix C). The data show that these rocks exhibit low K tholeiitic magmatic affinities (Fig. 3.8a), have nearly MORB character, and assumed to have been evolved in within-plate setting (Figs. 3.8b,c). These rocks display depleted HFSE (e.g. Ti, Zr and Nb) when compared to LILE (e.g. K, Sr and Ba), an intrinsic feature in the upper mantle as a result of melting events of the mantle wedge (Gill 1981). The chondrite-normalized REE patterns are characterized by convex-downward profiles (Fig. 3.8d), revealing enriched LREE [average $(La/Sm)_N$=1.83] and virtually flat HREE [average $(Gd/Yb)_N$=1.04]. Positive Eu anomalies (Eu/Eu*=1.06-1.17) and the enriched LREE suggest that plagioclase contributed to the abundances of Eu and the lightest REE (Hassanipak et al., 1996). The marked positive Eu anomalies with lower total REE values may be attributed to a protracted fractionation history, low-pressure fractionation of plagioclase and olivine (c.f. Hawkesworth et al., 1977).
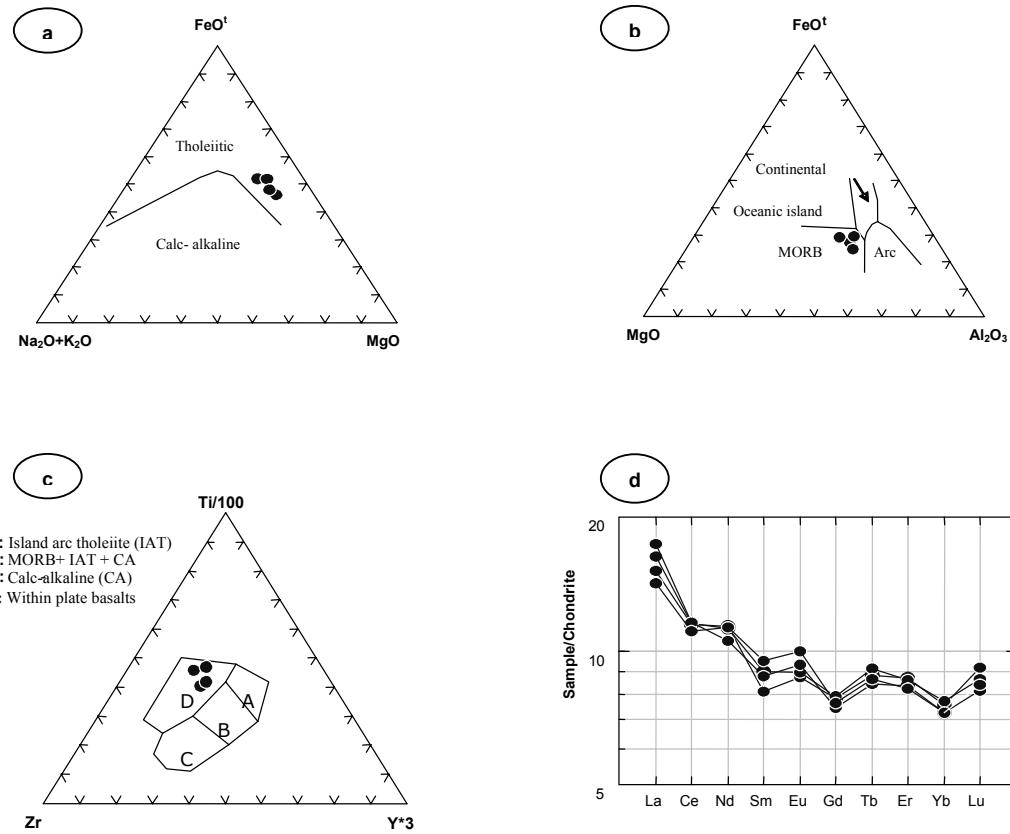
Fig. (3.8): a) Geochemical discriminating AFM diagram for the post-orogenic, olivine gabbro exposed in the Um El Tuyor area (the boundary line after Irvine and Baragar, 1971). b) MgO-FeOᵗ- Al₂O₃ ternary diagram for the studied gabbro (discrimination boundaries after Pearce et al., 1977). c) Ti-Zr-Y diagram (Pearce and Cann, 1973). IAT: Island arc tholeiite, MORB: mid-oceanic ridge basalt, CA: calc-alkaline. d) Chondirte-normalized patterns of the studied gabbro. Normalizing values from Sun and McDonough (1989).

3.4 Tectonic evolution

Understanding the geologic/tectonic evolution of the study area is based on its structural set-up and different petrographic and geochemical relationships. Rocks exposed in the Um El Tuyor area display abundant superimposed deformational fabrics indicating several successive deformational episodes. Thrust and mylonitization fabrics identify zones of tectonic boundaries separating different lithological domains. Pervasiveness of the mylonitization cleavage is a function of proximity to thrust zones.

The tectonic evolution of the area comprises arc-back arc deformation manifested by the obducted ophiolitic slices onto the island arc sequences, thrust structures and crustal shortening fabrics, along with coeval subduction-related magmatism. Penetrative deformation of the imbricate ophiolite and arc-assemblages constrains compressional regime post-dating the obduction. Calc-alkaline magmatism expressed in the emplacement of arc-gabbros and syn-tectonic granites considered more or less contemporaneous to the outlasted deformation, suggesting intra-plate origin for subduction shortening. This evolutionary sequence is consistent with data derived from the geochemical studies. Figs. (3.9a, b, c) are three-dimensional illustrations of the tectonic evolution of the basement complex exposed in the study area.
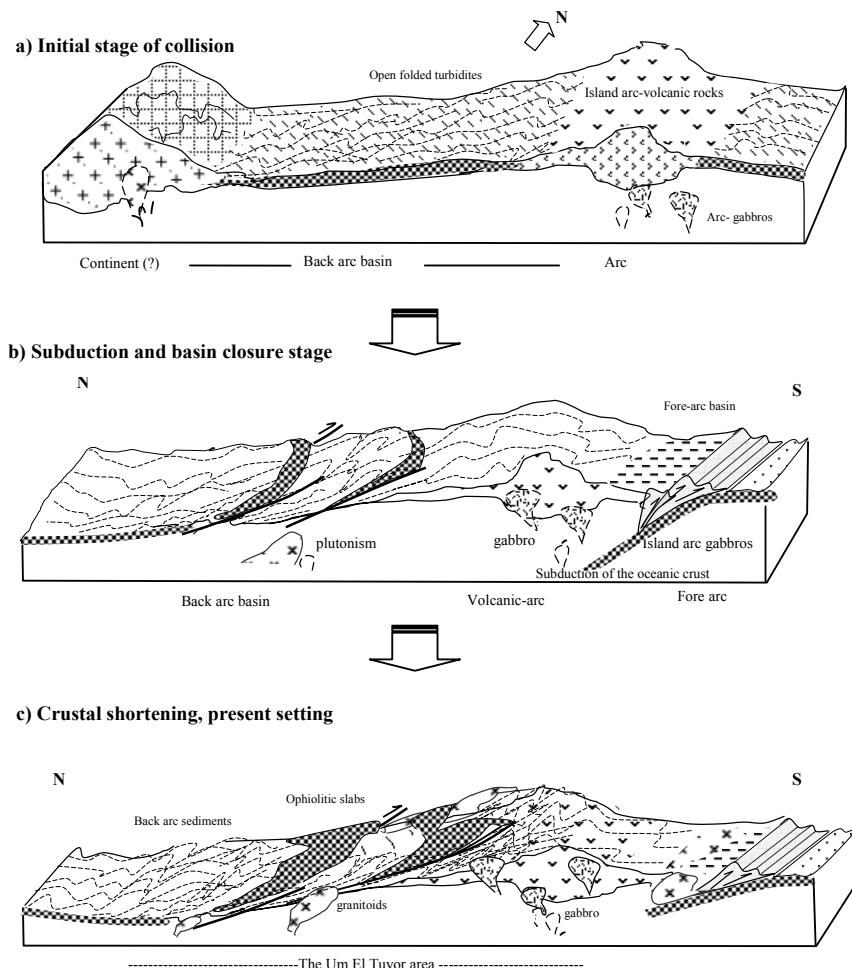
Fig. (3.9): Schematic block diagrams illustrating the tectonic evolution of Um El Tuyor area: a) initial stage of collision; b) subduction and back arc basin closure stage; c) crustal shortening (thrusting) stage.

CHAPTER 4

THE UM EL TUYOR GOLD DEPOSIT

4 THE UM EL TUYOR GOLD DEPOSIT

4.1 Introduction

The Um El Tuyor deposit is one of almost fifteen gold occurrences and deposits in the Wadi Allaqi region, which consist of gold-bearing quartz veins hosted in basement rocks, and which have been formed during the Late Proterozoic "Pan-African" orogeny (Hume, 1937; Pohl, 1988; Abdel Tawab, 1992). The Um El Tuyor gold mine is located at lat. 22° 18´ 15"N and long. 34° 38´ 00"E, 1 km to the south of the main Wadi Defeit, ~5 km west-north-west of the peak of Gebel Um El Tuyor El Foqani. The location can be reached from the Red Sea coast, taking Bir Iseala track (entrance at ~34 km south of the Shalatin Village) with a total distance of ~175 km, or from Aswan along the main Wadi Allaqi.

Remains of mining work in the Um El Tuyor mine area are confined to auriferous quartz vein arrays traversing the rugged hills of metasedimentary rocks. Numerous excavations and openings to milky quartz veins in the small tributaries surrounding the mine area are witnessing of old mining activities, probably dated back to the Arab times. However, it is likely that the deposit has been most actively exploited at the beginning of the 20th century, i.e. 1904-1925 (Fig. 4.1a, see also Jenkins, 1925; Hume, 1937; Hunting Ltd, 1967).

Only two internal reports, dating back to 1912 and 1913 respectively, were found in the library of the Egyptian Geological Survey and Mining Authority (EGSMA). These reports are the result of early English inspections of the Um El Tuyor (Um Tiour, as written in these reports) gold mine, describing the mining work and general conditions during that time. The reports state that the mineralized veins have been stopped out through six shafts varying in depth from 36 to 88 m. Four of these shafts are vertical, whereas, the fifth is combined from vertical to underlay, and the sixth 'northern' is sunk along the dip of host rock foliation. Geometry of the shafts is compiled from details given in the aforementioned reports and illustrated in Fig. (4.1b). In 1912, the manager of the mine reported an average of gold content in the mineralized veins of ~23–25 g/t. Several dumps, small tailing heaps, and abundant ruins are still preserved. The buildings and abundant ruins of extraction and grinding tools indicate considerable mining activities.
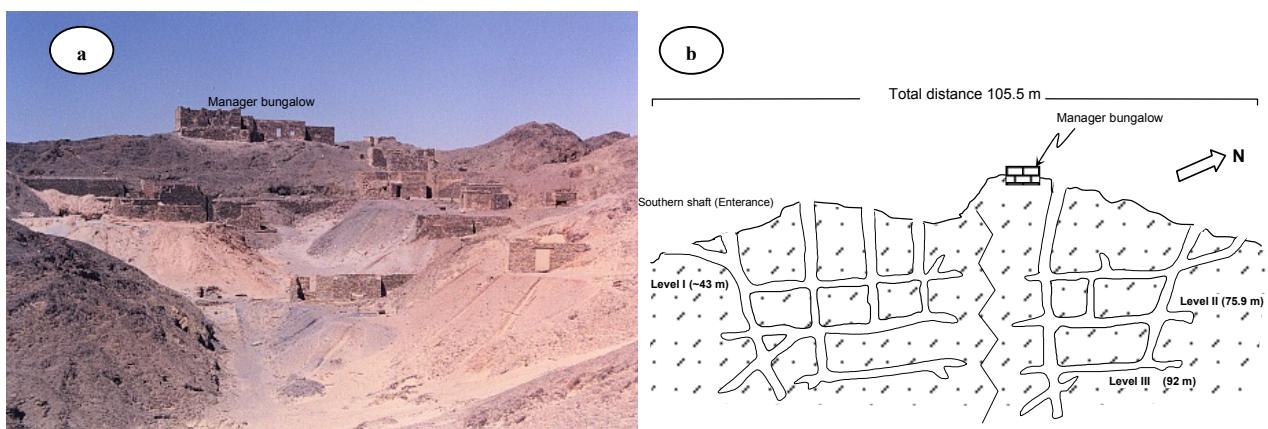
Fig. (4.1): a) The Um El Tuyor gold mine (Looking N). b) Sketch drawing showing the underground work in Um El Tuyor mine as described in reports of the English inspection campaigns (1912, 1913)

4.2 Geology of the mine area

The area around Um El Tuyor mine is covered mainly by mafic-ultramafic ophiolitic rocks, metasedimentary rocks, island arc metavolcanoclastic successions and syn-orogenic granitoids (Fig. 4.2). The area has a moderate to high relief topography of rugged mountainous terrains and intensely weathered rocks covering the frontal slices of the elevated hills. On the processed multi-channel (7/4/1) TM images, the mine area appears with a brownish white color and extends over ~ 300×200 m east of G. Um El Tuyor El Foqani.

The Um El Tuyor gold deposit occurs near the contact between metasedimentary and metabasalt units. Two small outcrops of pink-colored, post-orogenic granite (some hundred meters wide) within the metabasalt are observed east of the mine area (lat. 22° 18` 12"N, long. $34^o$ 38` 07"E and lat. 22° 18` 23"N, long. $34^o$ 38` 06"E). In the mine area, abundant dacite sills traverse the metasediments, commonly concordant with the main foliation. Towards the quartz vein system, the host rocks and the dacite sills show evidence of variable shearing and hydrothermal alteration. Zones adjacent to the auriferous veins contain bleached and brecciated wallrocks.

The gold-bearing quartz veins are confined to the intensely sheared pelitic metasedimentary rocks. These rocks are mainly pale brown to dark grey, fine-grained garnet biotite schist. Recrystallization of these rocks under conditions of amphibolite facies metamorphism resulted in a banded appearance. At a local scale, intercalations of metasiltstones are observed within the garnet biotite schist. These intercalations are composed essentially of alternating quartz-rich bands and sericite±chlorite-rich bands. Subordinate limonite occurs as very fine aggregates associated with the sericite±chlorite-rich bands staining the rock with a reddish or brownish color. The significant amount of recrystallized quartz makes these intercalations more competent compared to the garnet-biotite-rich host schist. In the vicinity of gold-bearing quartz veins, an assemblage of quartz+sericite+carbonate±albite±graphite replaced the original mineralogy of the metasediments almost completely. In the mine area, the regional metamorphism had its peak (manifested by development of a hornblende, staurolite, garnet, ±sillimanite association) early in the deformation history, during or after the development of the main foliation. Hydrous silicate phases, i.e. sericite and chlorite are attributed to a stage of retrograde metamorphism accompanied formation of the major shear zone in later deformation stages.

4.3 Structural context

The basement rocks exposed in the Um El Tuyor area experienced multiple folding and faulting events manifested by numerous brittle and ductile structural elements (see Chapter 2). The gold-bearing quartz veins are situated in a map-scale, NNW-SSE striking brittle-ductile shear zone cutting through the hinge zone of an anticline fold (F_2). The latter has a NW-SE striking axial plane and plunge to the N. Besides the shear zone, this anticline is traversed by dense NW-SE and NE-SW faults (see Fig. 4.2). Field observations and aerial photograph interpretations indicated that this shear zone cuts the NW-SE and NE-SW fault systems, and therefore is considered younger.

The S_2 foliation is the most common meso- to microscopic fabric in the mine area. This foliation strikes consistently northwest (309-320°) and dips at ~65° to the SW, roughly conformable with the primary layering of the host metasediments. Locally, the S_2 foliation is disrupted by the development of centimeter-scale crenulations (striking N18-22°W and dipping 21-34°SW) and related near-pervasive cleavages (S_3).
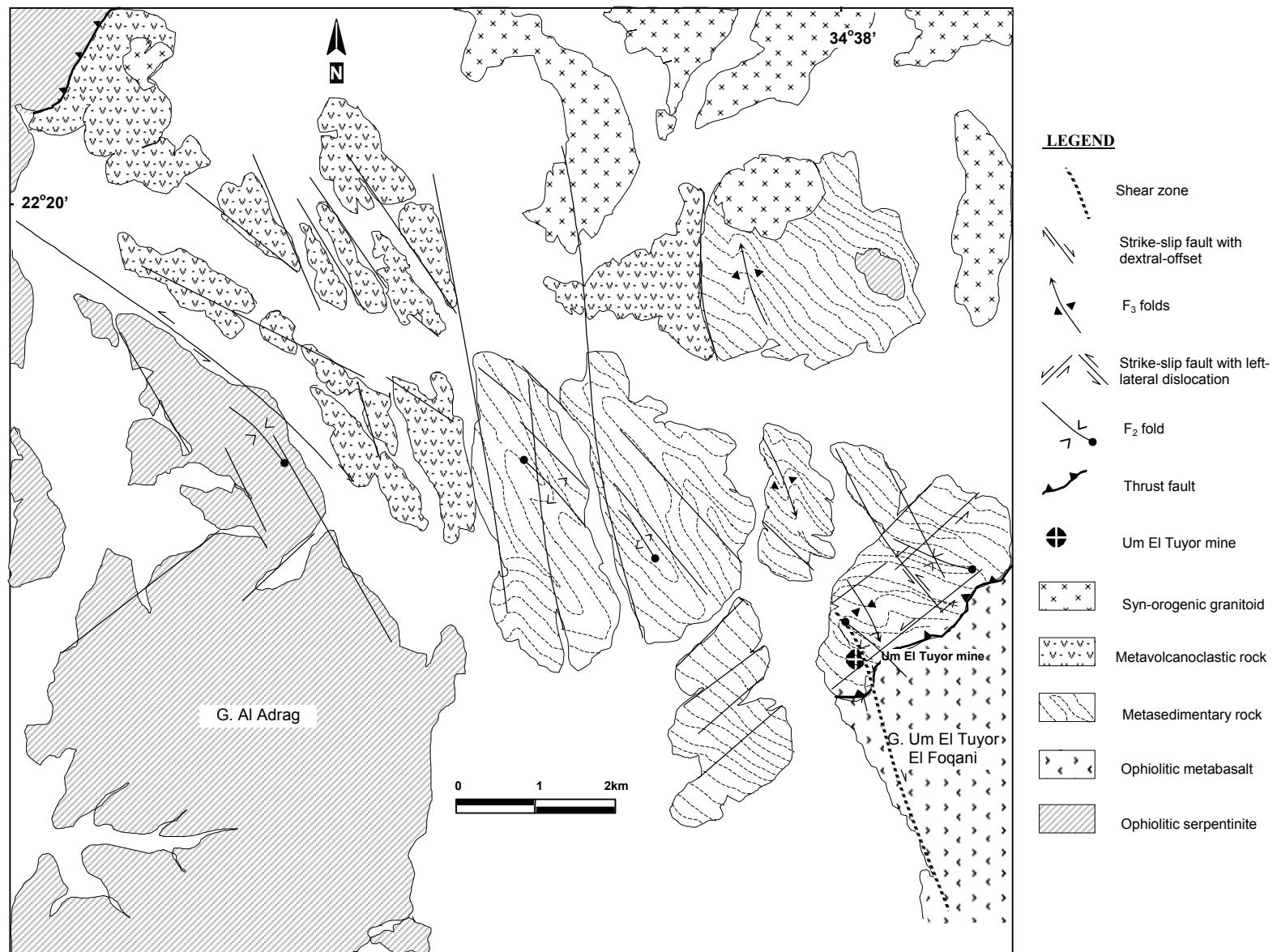
Fig. (4.2): Geology and structural elements of the Um El Tuyor mine area and its surroundings

In the mine area, mineral elongation lineation is defined by the alignment of muscovite, sericite and quartz ribbons (Fig. 4.3a). The boudinage shape of the foliation-parallel veins within the NNW-trending shear zone suggests that there was a predominant shortening normal to S_2 foliation planes during shearing (Fig. 4.3b). Other fabrics, such as intersection lineation and slickensides and/or slickenfibers are observed in the wallrocks. The intersection lineation generally plunges steeply to the S or SSW, as indicated by the steeply dipping chlorite flakes and some quartz lenses. Chlorite–muscovite slickenfibers on the cleavage planes have probably formed during a cleavage-parallel shearing. Bends and dilational jogs formed by deflection of the host rock foliation into the shear zone became favourable sites for quartz precipitation (Fig. 4.4). The local competence contrast between the host metasedimentary rocks and the dacite sills (Figs. 4.5a,b) is assumed to have produced loci for quartz precipitation.
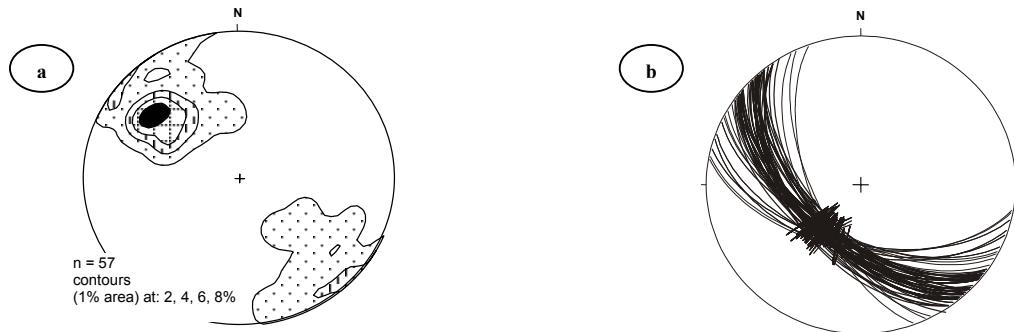
Fig. (4.3): a) Poles to the elongation lineation indicated by micaceous minerals on cleavage surfaces of the wallrocks adjacent to the auriferous quartz veins. b) Stereogram of great circles representing orientation of the foliation-parallel vein surfaces.

Fig. (4.4): Microphotograph showing quartz jogs accommodated in dilation zones created by deflection of the foliation in wallrocks into the shear zone in the Um El Tuyor mine area. (wide of view is ~5.93 mm)
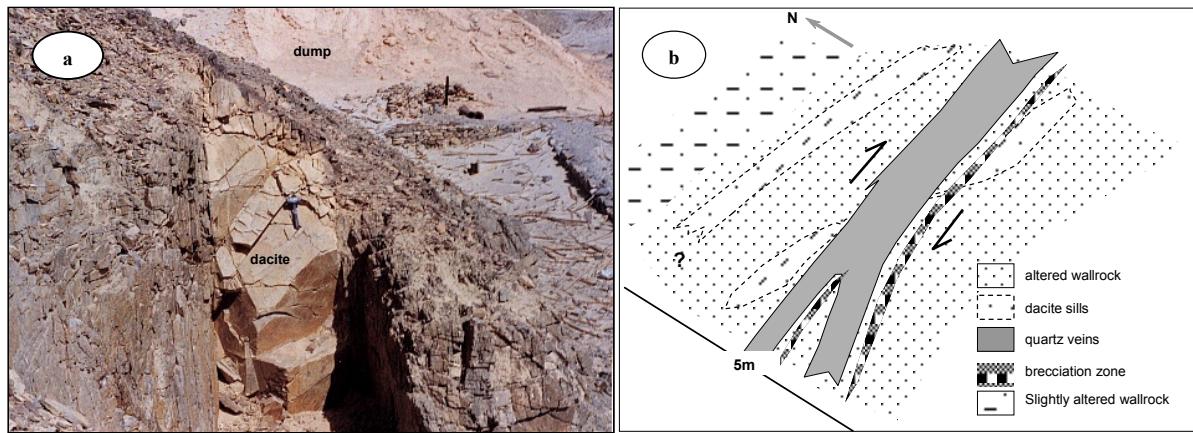
Fig. (4.5): a) Field photograph showing an 80 cm-wide dacite sill traverses the host rocks at the mine area (looking N). b) Sketch drawing (based on field observation) of the proposed geometrical relationship between quartz veins and dacite sills in the Um El Tuyor mine.
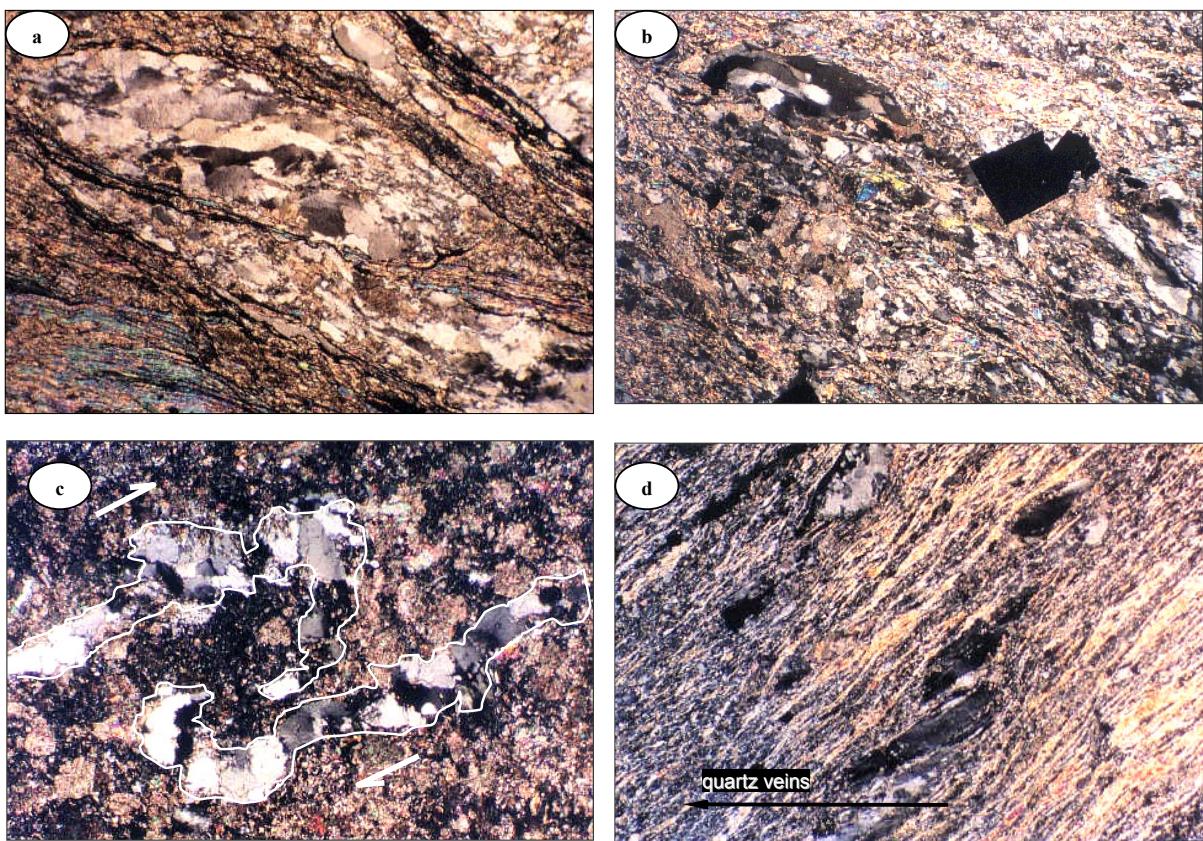
Fig. (4.6): Photomicrographs of samples collected from the Um El Tuyor mine area showing: a) quartz-dominated tension gashes along foliation planes in the host rocks. The quartz jogs are separated by laminations rich in sericite, chlorite ±graphite (XPL, base of photo is 3.03 mm); b) elongated quartz and xenomorphic pyrite occupying the dilation jogs in the sericitized rocks adjacent to the auriferous quartz veins (XPL, base of photo is 5.93 mm); c) Z-shaped bent quartz ribbon in a propylitized rock sample (XPL, wide of view ~5.93 mm); d) pervasively sericitized and silicified rock sample containing disrupted quartz ribbons. The strain partitioning and/or slippage are foliation-parallel and common in the highly sheared rocks adjacent to the auriferous veins (XPL, base of photo is 7.93 mm).

The most common shear fabrics observed in the host and wallrocks include S-C structures, Z-shaped bent quartz ribbons, partitioned quartz ribbons, tension gashes, inclusion trails, microcrakes, and undulose extinction (Figs. 4.6a→d). Evidence for crystal-plasticity in quartz is indicated by undulating extinction and tiny to sub-microscopic recrystallized grains along the healed planes. On the other hand, brittle deformation is inferred from the abundant microfractures and serrate boundaries of the large quartz porphyroblasts in the host rocks. The direction of shear is assumed to lie sub-parallel to striations, slickensides, mineral lineation, and mortar textures (if present).

Structural controls on the Um El Tuyor gold mineralization are observed at different scales. Occurrence of the main oreshoots within a NNW-trending map-scale shear zone, and their tabular geometry represent the prime control on gold distribution in the mine area. Textures of open space filling are generally absent, suggesting that the fracture walls were abruptly jacked apart by highly pressured fluid followed by rapid precipitation of quartz (c.f. Coelho & Ramboz, 1998). The field relations and internal deformation features of the veins suggest formation during different stages of shearing. In the present work, an analogous model of emplacement to the fault-valve model, which is proposed by Sibson et al. (1988) and Sibson (1992), is proposed for formation of the quartz veins in Um El Tuyor mine (Fig. 4.7).
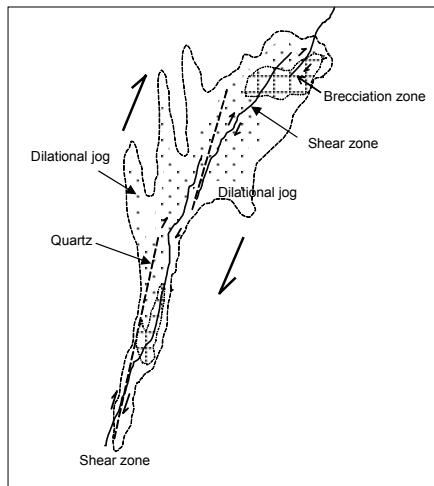
Fig. (4.7): The auriferous quartz veins in relation to shear zone in the Um El Tuyor mine. The configuration is based on field and microscopic observations, and considering the general model given by Sibson et al. (1988).

4.4 Gold mineralization

Gold mineralization in the Um El Tuyor mine is related to sets of auriferous quartz veins, lenses and veinlets, along foliation-concordant and foliation-discordant fault segments (Fig. 4.8a). Occasionally, the pervasively altered envelopes bordering the gold-bearing quartz veins are considerably auriferous. The present field and microscopic observations suggest the presence of several types of quartz veins and veinlets in the mine area, of which only two types are gold-bearing, namely the quartz-carbonate and laminated quartz veins. Formation of the quartz-carbonate veins marks the beginning of the gold mineralization in the mine area, whereas, mineralization has ceased shortly after the emplacement of the laminated quartz veins. The laminated quartz veins are notably restricted to the northern part of the mine area. Compared with the quartz-carbonate veins, their sulphide content is much higher. In the quartz-carbonate and laminated quartz veins, gold is irregularly distributed, but usually associated with sulphide minerals.

Generally, the quartz-carbonate and laminated quartz veins strike NW-SE to NNW-SSE and dip steeply to the southwest. Geometrically, the quartz-carbonate and the laminated quartz oreshoots are central shear (fault-fill) veins and lensoidal bodies, mostly associated with high-angle reverse faults and related fracture arrays (Fig. 4.8b). The laminated quartz veins are typically narrow, <30 cm wide, and spaced several decimeters apart. Based on field and microscopic observations, it is likely that the laminated quartz veins intruded into the quartz-carbonate veins by means of re-opening and re-filling of the fractures. The heterogeneous (non-uniform) deformation of these two vein types implies a syn-kinematic gold mineralization with a transcurrent shearing in the dilation segments of the shear zone. In his report, Merton (in EGSMA, 1912) mentioned that the gold grade increases with depth, especially where the wall rocks are densely quartz veinned. The northern flank of the vein was most productive, where it tends to pinch out southwards. Gold contents of up to ~29 g/t were reported in the workable parts of the northern vein. The northern flank of the vein was most productive, where it tends to pinch out southwards.

Quartz vein widths vary significantly over short distances along the strike and up and down along the dip. Variation in thickness is commonly the result of the shear plane-parallel margins of quartz veins, especially in zones where the host rock foliation deflects into the shear zone. Thinning of the veins has been observed where the shear zone influence is absent. Boudinage of the quartz-carbonate veins is ubiquitous along the shear zone, forming

the typical linear fabric in the host rocks. Hume (1937, p. 575) stated that bifurcation of the auriferous veins is common where they are less than 40 cm wide in the deeper zones. The quartz vein splays define terminations of the host rock foliation. The country rock fabrics adjacent to the vein margins display progressive changes in orientation, such that they coincide with the vein margins or intersect the veins at low angles (15-20°).
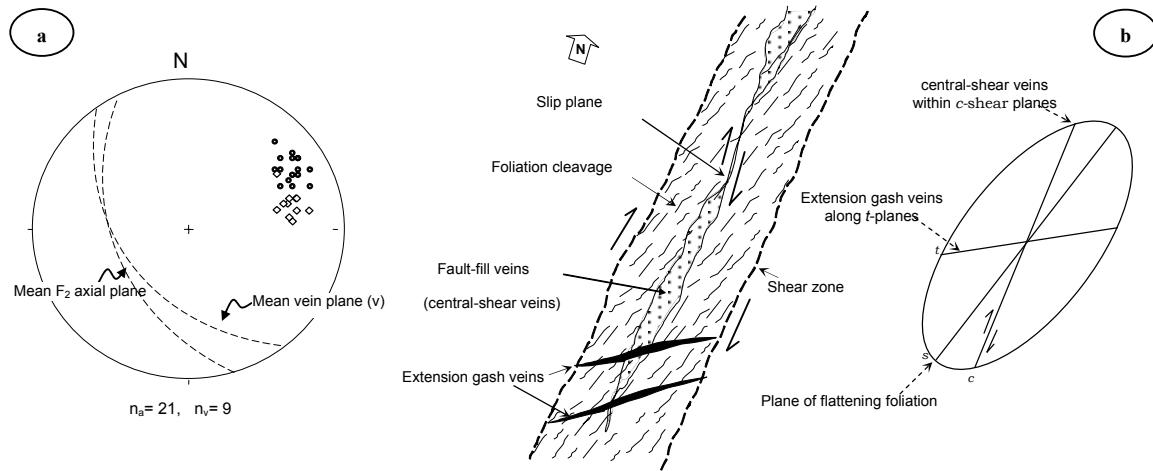
Fig. (4.8): a) Stereographic plot of structural data collected from the Um El Tuyor mine area. Poles to quartz veins represented by circles, and poles to S$_2$ planes are indicated by rhombi. b) Sketch drawing showing features of the shear zone, the associated veins, and the corresponding strain ellipse. Um El Tuyor gold-bearing quartz lodes are central shear planes veins, while the extensional gashes are barren. Strain ellipsoid reveals dilation along the c-planes (modified after Hodgson, 1989).

4.4.1 The quartz-carbonate veins

The quartz-carbonate veins are generally 75 to 120 cm thick, occurring as single tabular bodies, vein arrays, irregular swellings and pinches. In places, they occur as a series of quartz lenses or intermittent quartz and host rock stringers (Fig. 4.9). Generally, the veins cut the brecciation cleavage, but in places, lenses are buckled around it. This observation may indicate synchronous timing of vein formation and shearing. All of the quartz-carbonate veins and lenses have similar mineralogical, chemical and structural characteristics. Vein mineralogy consists mainly of quartz (~55 vol.%), carbonate (22 vol.%), muscovite/sericite (~17-11 vol.%), and 6-12 vol.% sulphides (mainly pyrite, arsenopyrite, and subordiante sphalerite, pyrrhotite, chalcopyrite and galena). Free gold and electrum occur as microscopic inclusions within the sulphide grains and filling the micro-fracture in sulphide and quartz grains. Refractory gold is indicated by the microprobe data of the arsenopyrite and As-pyrite grains.

Fig. (4.9): Densely veined wallrocks from zones adjacent to the main gold-bearing veins in the Um El Tuyor mine. The quartz veinlets are disposed along foliation planes (wide of view is ~20 cm).
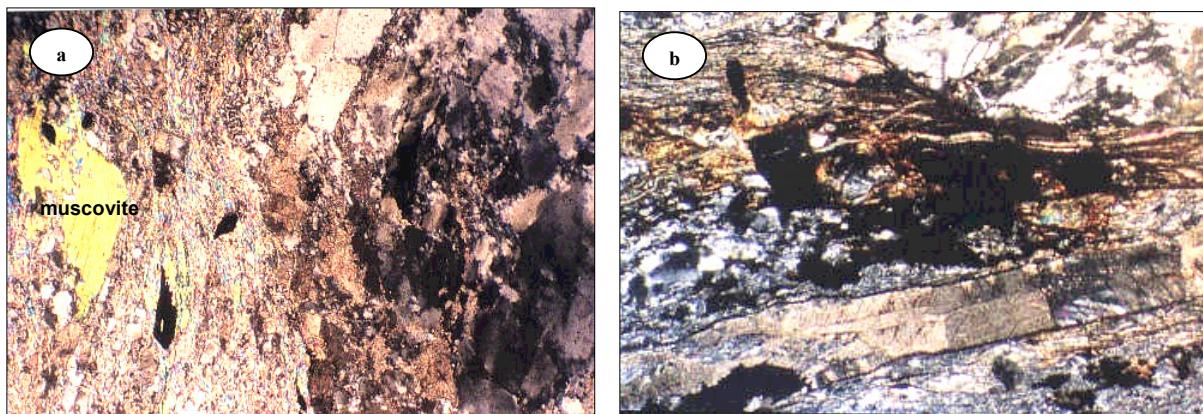
Fig. (4.10): Photomicrographs of: a) sericite and muscovite flakes surround an inner carbonatized, silicified zone in the vicinity of a quartz carbonate vein in the Um El Tuyor mine area (XPL, wide of view ~3.03 mm); b) intensively carbonatized/silicified wallrocks containing veinlets of carbonate and clay minerals±sulphude traversing the silicified wallrocks, mainly parallel to the wallrock fabric (XPL, wide of view ~5.93 mm).

The carbonate minerals are dominated by ferrodolomite, that is in general a $Ca(Fe,Mg)(CO_3)_2$ solid solution (Table D.1, Appendix D). Carbonate dominated zones are typically massive with irregular outlines. Locally, the carbonate-rich domains contain tabular grains of fluorapatite. Deposition of carbonate was synchronous with phosphorous deposition as inferred from the coexistence of carbonate and fluroapatite. Sericite commonly intermingles with carbonate, bound the quartz grains adjacent to carbonate, disseminated in a network pattern within carbonate-rich zones (Figs. 4.10, 4.11). Because of the lower FeO wt% contents (Table D.2, Appendix D), sericite exhibits less bright hue compared to muscovite in the Backscattered images (Fig. 4.11).

Muscovite occurs as plates (up to ~300 µm long) or very fine disseminated flakes (Figs. 4.11a). The large muscovite flakes display compositional zoning typifying paragonitic substitution (Figs. 4.12a,b), where Na/(Na+K+Ca) values ranging from 0.15 to 0.39 (Table D.3, Appendix D). The large muscovite plates have variable (Fe+Mn+Mg) values of 0.08 - 0.63 atoms per formula unit (a.p.f.u.). In places, large muscovite plates contain euhedral to subhedral fluorite inclusions. The fluorite inclusions show no preferential orientation, but traverse the cleavage planes, implying later paragenesis (Fig. 4.13).
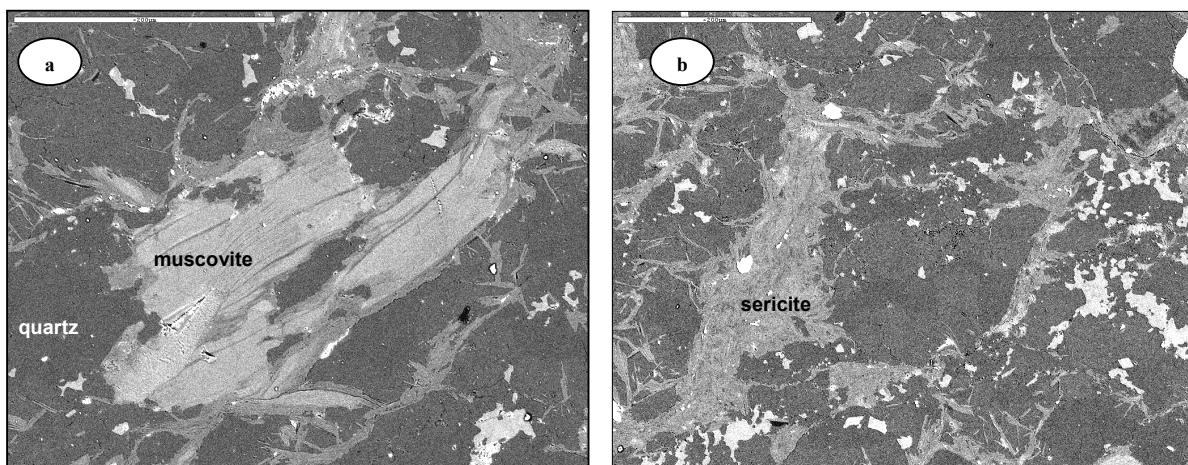
Fig. (4.11): Backscattered electron SEM images of the quartz-carbonate veins showing: a) large muscovite flakes embedded in a carbonate rich matrix and bounded by rims, mainly of sericite (bar scale is 200 µm); b) dispersed sericite flakes forming networks in a quartz-carbonate vein body (the bar scale is 200 µm).
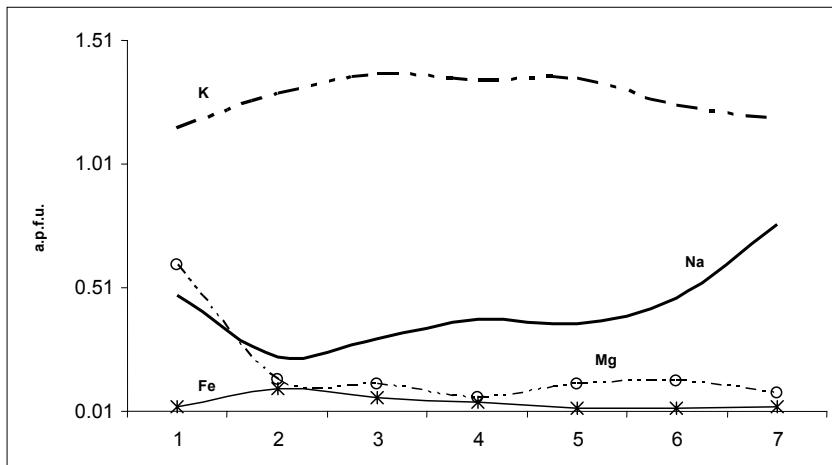
Fig. (4.12): Concentration profile across one muscovite flake (from rim to core and again to rim) from a quartz-carbonate vein of the Um El Tuyor deposit testifies paragonitic substitution at rims. (Points every 10 μm, and cations are calculated on basis of 22 oxygens).

Albite occurs as subhedral to anhedral grains intergrown with quartz and commonly embedded in a carbonate-rich matrix. Compositionally, albite is homogenous with the anorthite component of 0.0 to 0.03 mol percent (Table D.4, Appendix D). The large albite crystals are inclusions-free and exhibit simple twinning. The crystals have irregular outlines against the surrounding carbonate and quartz. Fine grained albite occurs at the interface between veins and the adjacent wallrocks. Generally, the albite grains disseminated in and adjacent to the auriferous quartz carbonate veins show similar compositions.
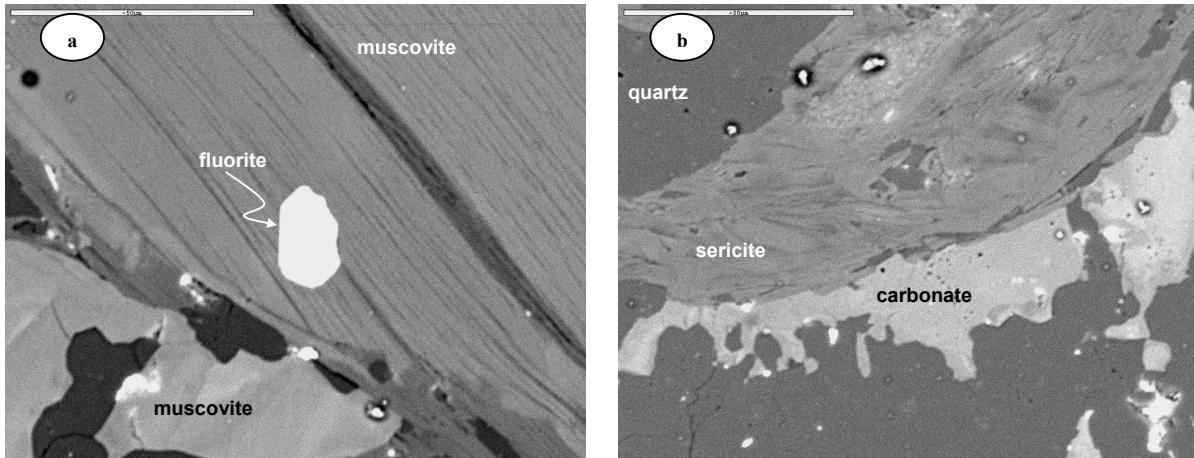
Fig. (4.13): Backscattered images of the quartz-carbonate vein from Um El Tuyor mine: a) cleaved muscovite flake enclosing a subhedral fluorite crystal, which traverses the cleavage. Notice, sericite stands as a reaction rim between muscovite and carbonate; b) coexisting sericite and carbonate. The carbonate zones display irregular outlines against quartz. Bar scale in photo (a) is 50 μm, and in (b) is 20 μm.

The trace element concentrations in quartz-carbonate veins and veinlets place some constraints on the geochemistry of the hydrothermal fluid. Information on base metals and rare earth elements of Um El Tuyor Au-bearing quartz-carbonate veins is based largely on the 42-element analyses of 6 samples (Table D.5, Appendix D). Silver values are lower than those of Au in all samples. There is a positive correlation between gold and silver contents, with Au/Ag ratios ranging between 4.23 and 5.34, suggesting a co-genetic relationship of Au and Ag (e.g. Shelton et al., 1988). The highest Au and Ag values (16.44 ppm and 3.63 ppm, respectively) occur in a sample taken from the deep-seated hematized parts of the main quartz carbonate veins. The arsenic contents range from

3251 ppm to 7746 ppm, and the As/Au ratios exceed 200 in all the analyzed samples. Sb, Hg and W are near or below the detection limit. The base-metal values are generally low, nevertheless they are consistent with the field and petrographic observations that chalcopyrite is more abundant than sphalerite and galena. Values of Co are erratic, ranging from 3 to 44 ppm. The Cr values are mostly in the range of 7 to 22 ppm. Pb concentration has a median value of 16 ppm. The maximum Pb content lies near 27 ppm and occurs in the sample containing the highest Cd value (0.8 ppm). In contrast to Cu or Pb, the Zn concentration (54 ppm maximum) shows a poor correlation with Au. Contents of Ni, Co, V, and Cr are occasionally associated with high concentrations of Au and As. The elevated Ba, Sr, Sn concentrations may be due to their enrichment in carbonate and/or in the case of Sr, through its release during feldspar alteration. Generally, the chondrite-normalized patterns of auriferous quartz-carbonate vein samples (Fig. 4.14) exhibit enriched and fractionated pattern of the LREE and low HREE concentrations.
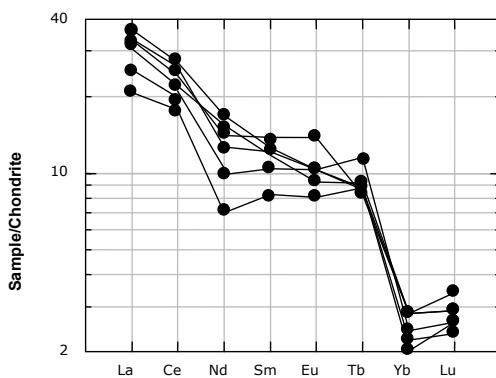
Fig. (4.14): Condrite-normalized REE patterns of the auriferous quartz-carbonate veins in the Um El Tuyor mine area. The reference normalizing values are from Sun and McDonough (1989).

4.4.2 The laminated quartz veins

The laminated quartz veins contain abundant deep grey or black-colored planar zones separated by milky quartz domains, which define the laminations (Fig. 4.15a). The laminated quartz veins occur as boudin-like bodies along the host shear zone (Fig. 4.15b), commonly of less than 50 cm width. They are composed essentially of bluish grey to white quartz, bearing pyrite, arsenopyrite, galena, ±chalcopyrite and free gold. Visible gold grains occur mainly in the dark bluish quartz domains.

Large elongated clasts of the wallrocks are commonly enclosed in these veins, generally close to their contacts. The extremities of these clasts display continuity with vein laminations. In the vicinity of vein margins, the laminations extend parallel to the vein walls and display continuity with mesoscopic fault/fracture planes in the host rock schist. These fault planes are locally parallel to the vein margins or intersect them at acute angles (up to ~25°). Study of the vein margins indicated that many laminations are initiated where the host rock protruded into the veins along the fault planes. The laminations become progressively thinner away from the host rock protrusions and commonly acquire a stylolitic character. This change in character, from laminar to stylolitic, commonly corresponds to the disappearance of carbonate and sulphides in the lamination mineralogy.
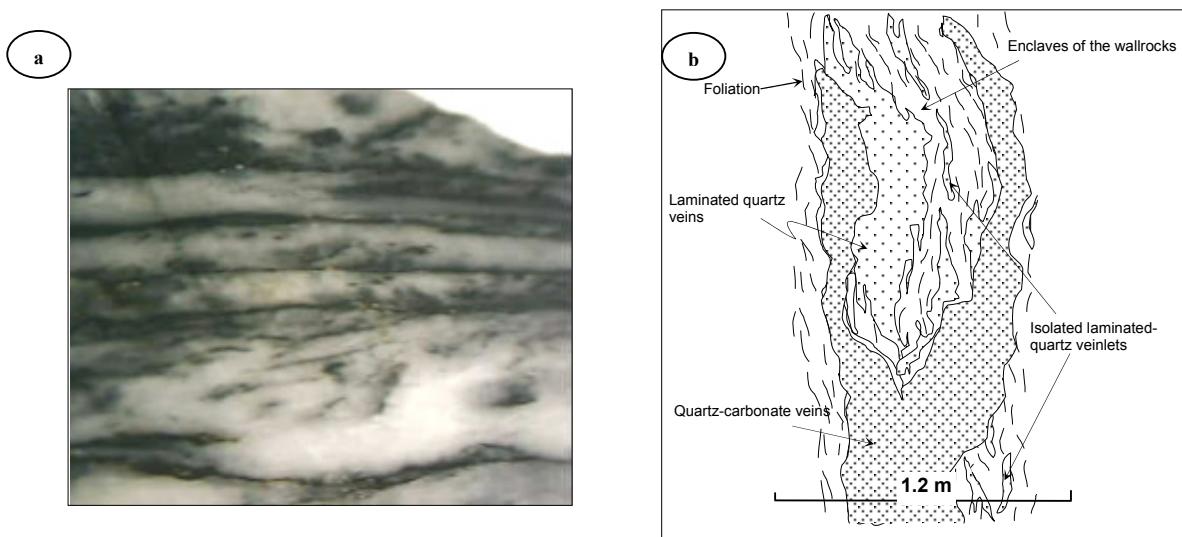
Fig. (4.15): a) Close-up view of the laminated quartz from the Um El Tuyor mine area (wide of view is ~3 cm). b) Sketch drawing showing the relationship between the quartz carbonate veins and laminated veins milky and grey quartz.

Difference in grain size across the individual lamination suggests that these laminations represent boundaries/discontinuities of grain size reduction (generally a few millimeters wide) in the vein material (Fig. 4.16a). The formation of these laminations is attributed to a progressive shear strain associated movement on the fault planes. Shearing along the laminations is suggested by development of recrystallized quartz grains containing deformation bands and incipient sub-grains and displaying asymmetric orientation of c-axes at high angles to the lamination planes (Fig. 4.16b). As a result, strain-enhanced dissolution of quartz took place and residual graphite was enriched in the quartz veins (e.g. Bell and Cuff, 1989).
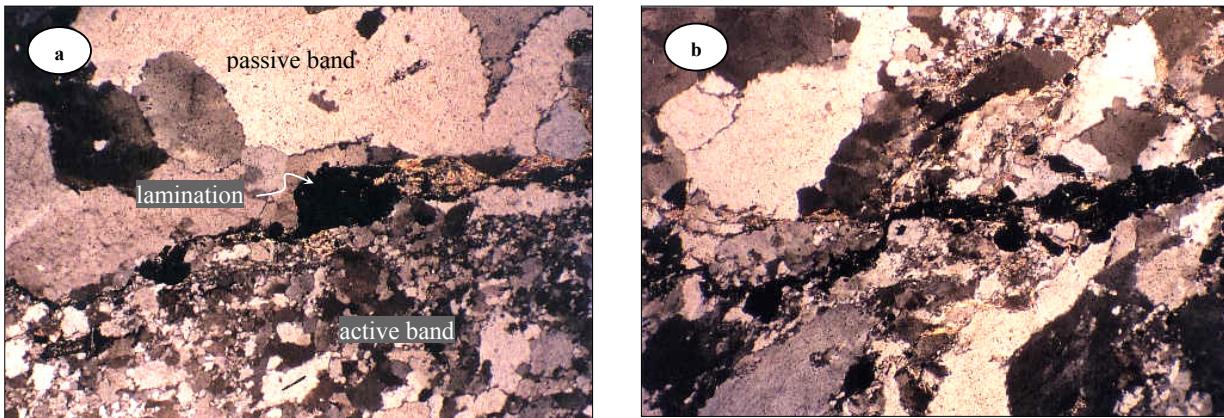
Fig. (4.16): a) Photomicrograph of graphite-rich lamination separating active and passive bands of markedly different grain sizes. Note the spatial concentration of recrystallized fine quartz near laminations (XPL, wide of view is 3.03 mm). b) Chlorite+graphite+sulphide-rich lamination along shear planes dominated by fine-grained recrystallized quartz, between two bands of coarse-grained quartz. Also, the dextral sense of shear is seen. (XPL, wide of view is 5.93 mm)

C-axes of quartz grains constituting the passive domains in laminated quartz veins (Fig. 4.17) were determined in thin sections cut perpendicular to laminations and/or vein walls, using a Zeiss 5-axes Universal Stage. The crystallographic orientation of the large polygonal aggregates reflects the orientation of the original quartz grains and growth. These grains (crystals) commonly contain deformation bands and incipient subgrains, indicating their formation synchronously with deformation (dynamic recrystallization).
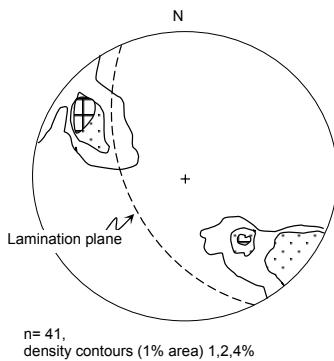
Fig. (4.17): Stereographic, equal area, lower hemisphere projection of poles to c-axes of quartz grains in the laminated quartz veins, and great circle of the average lamination plane.

The fine-grained bands are composed of recrystallized polygonal grains corresponding to shear bands in which the fault offset was accommodated. These fine grained bands are herein referred to as active bands (see Fig. 4.16), in regard to their behaviour during lamination initiation (in analogy with Davis and Hippertt, 1998). In contrast, the passive bands correspond to the relatively non-deformed domains between the shear bands. Formation of polygonal quartz grains, abundant in the active bands, is attributed to plastic deformation and recrystallization under temperatures of ~250°C (see Hickey and Bell, 1996). The lamination mineralogy contains Fe-dolomite, sericite, sulphide minerals, ±chlorite, ±calcite, ±graphite (Table D.6, Appendix D). Very fine gold grains are confined to the quartz sub-grain boundaries. Gold grains occur preferentially in zones of relatively coarse grained quartz adjacent to the shear planes. Gold may have been introduced with quartz, but redistributed within the veins and concentrated in the laminations by the effects of synchronous progressive deformation (see Davis and Hippertt, 1998).

4.4.3 Barren quartz veins

Excluding the quartz-carbonate and laminated veins, quartz veins and veinlets in the mine area are barren. The barren veins are ~15 cm up to 2 m wide and follow NNW, NE and NNE directions. Although no direct relationship between the auriferous and barren quartz veins is observed in the mine area. However, some of the barren quartz veins are hosted by fault/fracture planes that are virtually dissecting the gold-bearing veins on surface. Structurally, most of the barren veins are in tension gashes (see Fig. 4.8) and fracture-fillings. A major barren quartz vein, ~2 m wide, is observed in the southern part of the mine area. This vein exhibits vuggy structures and contains kaolinite pockets. The other barren quartz veins are varying from white to grey, and generally do not exceed few decimeters wide. In the south-western part of the mine area, dense milky quartz veinlets, mostly less than 20 cm wide, dissect the intensely fractured/jointed host rocks.

4.4.4 Quartz textures

The gold-bearing quartz veins at the Um El Tuyor area display variable degrees of shearing and dynamic recrystallization related to bulging recrystallization described by Drury et al. (1985) (Figs. 4.18, 4.19). In the large quartz grains, the undulose extinction is moderate to strong and mortar texture and deformation lamellae occur locally to widespread. These criteria indicate that ductile deformation and recrystallization processes were variable (c.f. Poirier and Guillope, 1979). In the quartz-carbonate veins, quartz porphyroblasts are dissected by conjugate

sets of shear bands and large irregular subgrains (Figs. 4.18). Small bulges are developed along the older grain boundaries, indicating recrystallization by local boundary bulging (e.g. Vollbrecht et al., 1999). In the laminated quartz veins, quartz clasts show different but coexisting deformation fabrics. These fabrics include plastic recrystallization and brittle brecciation. The curved boundaries of the quartz porphyroclasts are attributed to corrosion produced by percolation of aqueous fluids during shearing.

Extinction bands (undulose extinction) are assumed to have been formed by bending of the lattice in response to heterogeneous slip, whereas the mortar texture is an expression of an increase in rock deformation (e.g. Vernon, 1976). The quartz grains are commonly coarsely crushed (granulated) and surrounded by a matrix of smaller grains. However, many large grains are completely transformed into an aggregate of small grains. The non-recrystallized cores of the large quartz grains are sutured and exhibit smooth undulose extinction. With increasing strain the 'original' large grains become flatter and more elongate. Under the microscope, abundant aligned trails of fluid inclusions mark the original fractures that have been healed.
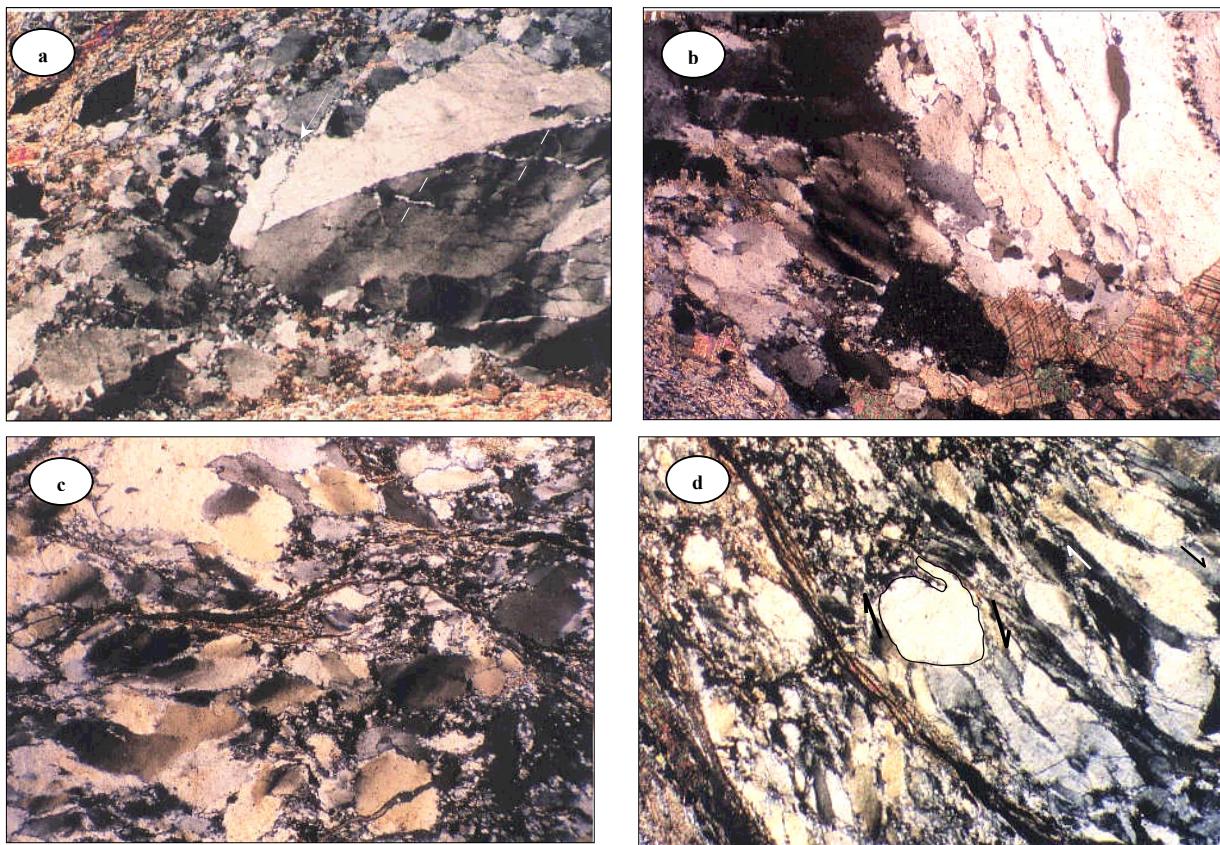
Fig. (4.18): Photomicrographs of samples representing the quartz-carbonate veins showing: a) large quartz porphyroblast displaying signs of brittle and ductile deformation (XPL, wide of view ~5.93 mm); b) incipient recrystallization defined by small polygonal quartz grains and sub-grains occupying intergrain planes, mainly parallel to the grain boundaries, and in turn, vein margins (XPL, wide of view ~ 5.93 mm); c) quartz vein with shear planes filled with carbonate+clay minerals (XPL, wide of view ~5.93 mm); d) elongate quartz ribbons and rotated grains indicate a dextral since of shear (XPL, wide of view ~3.03 mm).
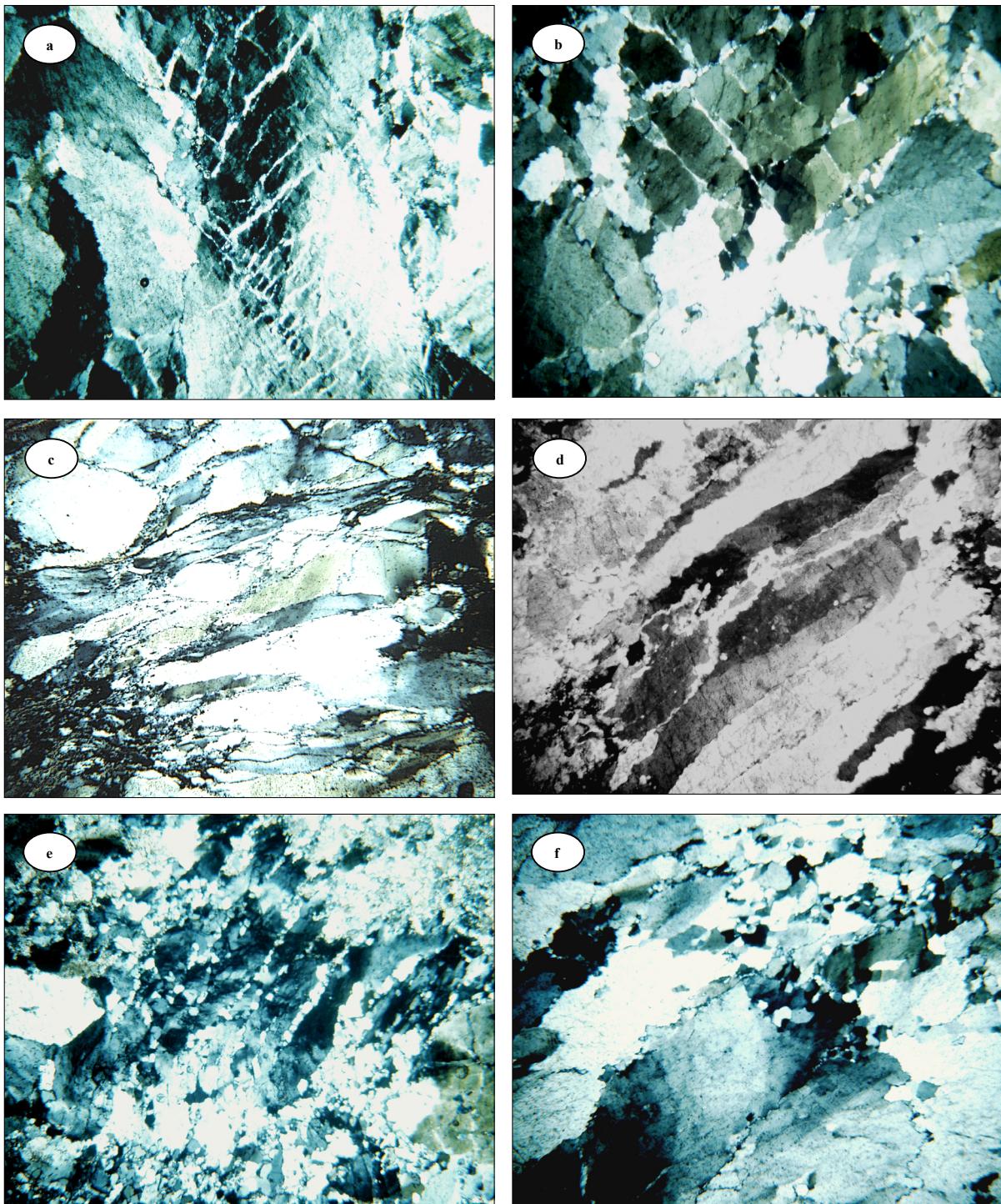
Fig. (4.19): Photomicrographs showing: a), b) vein quartz grains display undulose extinction and crossed extensional planes, within which later hydrothermal quartz has been invaded (XPL, wide of a and b views are 2 mm, 0.95 mm respectively); c), d) gliding recrystallized slabs (lamellae) in quartz prophroclasts refer to relatively high temperature (~370- 400°C) and associated with some components of bulging recrystallization. (XPL, widths of views is ~4 mm and 2 mm respectively); e), f) intensively recrystallized quartz porphyroclasts with serrated grain boundaries and recrystallized bulges along grain boundaries and cracks reveal dynamic recrystallization at 350°C (XPL, wide of view is 2 mm). Textural temperatures are roughly estimated in sense of Stipp et al. (2002).

4.5 Ore mineralogy and paragenesis

4.5.1 Petrography

Textures in the mineralized veins and wallrocks, together with data obtained from the microanalyses suggest the presence of at least two generations of sulphide minerals assemblages in the investigated deposit. An early generation includes arsenopyrite+pyrite+chalcopyrite±pyrrhotite ±subordinate sphalerite, and is characteristically associated with gold and/or electrum. This assemblage occurs commonly in the quartz-carbonate veins as disseminations or clustered in quartz veinlets traversing the carbonate aggregates. In contrast, the late assemblage, dominated by pyrite+arsenopyrite±subordinate galena, is most common in the laminated quartz veins, occurring as disseminated fine prismatic grains or overgrowths on the former (early generation) pyrite and arsenopyrite grains. These two sulphide assemblages occur exclusively in the wallrocks. Pre-ore stage opaque minerals in the host rocks include cobaltite, magnetite and/or hematite. On the other hand, marcasite and less abundant diginite are reported in the altered wallrocks, considered post ore-stage in regard to their textures.

Ore microscopic studies of several polished sections showed that arsenopyrite, pyrite, chalcopyrite, pyrrhotite and sphalerite are the main sulphide minerals associated with gold mineralization. Arsenopyrite is the most abundant ore mineral (>50 vol.% of sulphides) in the auriferous quartz veins. It occurs mainly as large euhedral to subhedral aggregates, up to 4 mm in size. Along the quartz-carbonate vein margins, arsenopyrite, pyrite and carbonate occur as veinlets and/or crude bands.

The early arsenopyrite occurs commonly as individual or clustered rhombic grains disseminated in the quartz-carbonate veins, and displays notable concentration in the carbonate-rich domains. This arsenopyrite variety is intergrown with euhedral arsenian pyrite (with ~3 atom.% As) and locally exhibits serrate or interlocking mineral boundaries (Fig. 4.20a). The large, individual arsenopyrite grains are often zoned with inclusion-rich cores and/or porous margins (Fig. 4.20b). Inclusions within this arsenopyrite variety include chalcopyrite, pyrrhotite, sphalerite and gold/electrum. Silver inclusions are less common, but if present, usually occur as triangular inclusions near margins of the host arsenopyrite grains. Where arsenopyrite juxtaposes with pyrite, gold inclusions occur commonly near the separating contact. Intergrowth of euhedral arsenopyrite and pyrite, and arsenian nature of the early generation pyrite is suggestive of co-precipitation.

The idiomorphic arsenopyrite rhombic crystals have margins with higher arsenic and relatively lower concentrations of Ni and Co. The compositional zoning is also seen in back-scattered electron images (Fig. 4.20b). Typically, variation in arsenic content within a single grain (<1.5 atom.%) is less developed than the variation among different grains from the same polished section (up to 3 atom.%). The chemical composition of arsenopyrite grains show a consistent relationship between arsenic and sulphur, and mineral assemblage as well (Table D.7, Appendix D). Arsenic and sulphur are negatively correlated (Figs. 4.21a,b), following roughly the classical substitution ($FeAs_{1\pm x}S_{1\pm x}$).

On the other hand, arsenopyrite of the late sulphide assemblage occurs as small grains (<150 μm), commonly in the chlorite-sericite±graphite-bearing laminations within the laminated quartz veins. It has lower As and higher S atom.% if compared to arsenopyrite belongs to the early sulphide assemblage (Table D.8, Appendix D). This late assemblage-related arsenopyrite variety is optically homogenous and devoid of inclusions.
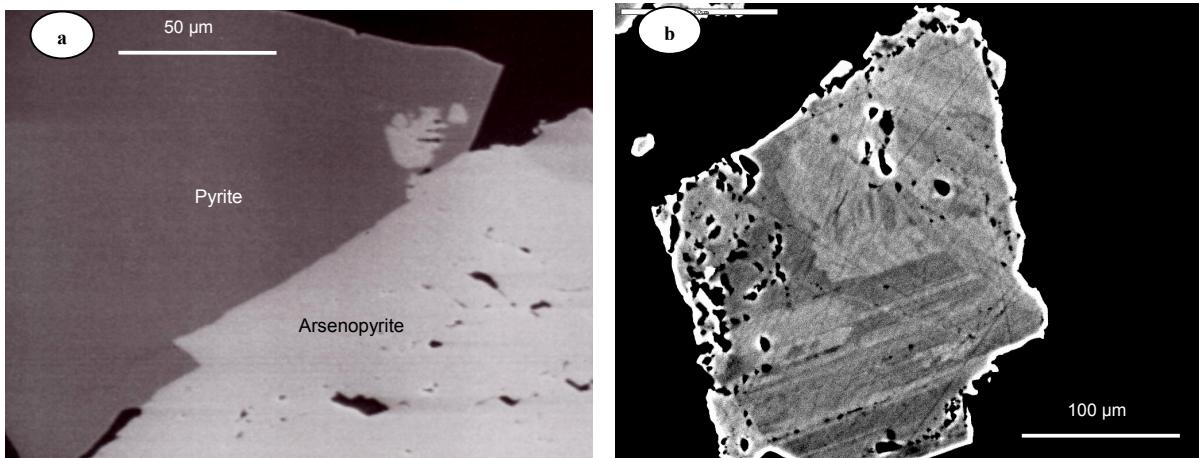
Fig. (4.20): Photomicrographs showing: a) reflected light image of juxtaposing pyrite/arsenopyrite in the quartz-carbonate veins; b) back-scattered electron image of fine oscillatory growth zonation in arsenopyrite disseminated in the quartz-carbonate veins. As/S ratios generally increase from centre to rim.
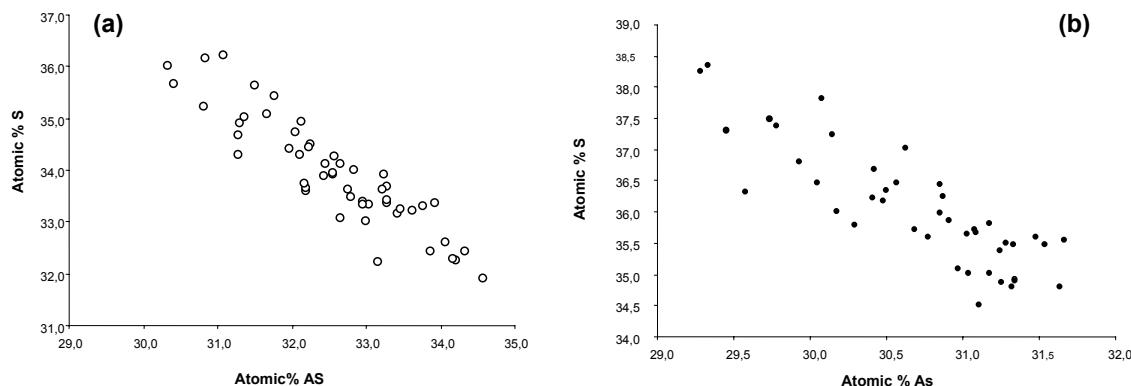
Fig. (4.21): Binary correlation between S and As atom. % in arsenopyrite disseminated in: a) the quartz-carbonate veins, and b) the laminated quartz veins.

Pyrite is the second most abundant sulphide mineral and gold carrier in Um El Tuyor Au-deposit. Pyrite constitutes almost 45 vol.% of the total sulphide minerals content in the deposit. Morphologically, it occurs as coarse to microcrystalline, hypidiomorphic or xenomorphic grains. Locally, it is the most abundant sulphide phase, particularly in and adjacent to the quartz-sericite-carbonate zone. Pyrite, in the intensively altered wallrocks, is inclusion-free and associated with chalcopyrite and sphalerite. In contrast, pyrite grains disseminated in the auriferous quartz-carbonate veins are euhedral (≤3mm) and contain abundant sphalerite, chalcopyrite and gold inclusions. The coarse-grained pyrite occurs typically as subhedral equant crystals, whereas the fine-grained pyrite variety occurs as euhedral to irregular granules, pyritohedrons or framboids.

Similar to arsenopyrite, the presence of two distinct generations of pyrite is supported by data derived from the microanalyses. The early variety is heterogeneous (arsenian) pyrite with low contents of Co, Ni (max. 0.15 wt% Co) and 0.18 to 2.35 wt.% As (Table D.9, Appendix D). This pyrite type is intergrown with euhedral to subhedral arsenopyrite in the quartz-carbonate veins. In the coarse-grained pyrite, As (and Au if present) contents are higher near arsenopyrite inclusions and/or contacts with the neighbouring arsenopyrite grains (Figs. 4.22a,b). A positive correlation between Au and As is commonly inferred.
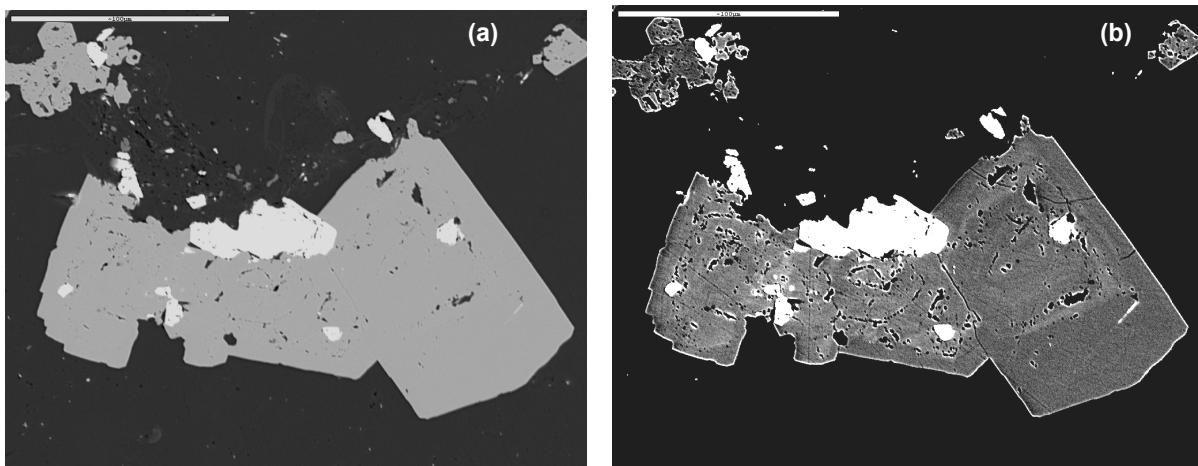
Fig. (4.22): Photomicrographs showing: a) reflected light, and b) back-scattered electron images of intergrown pyrite-arsenopyrite pair. Zoning of pyrite euhdera emphasized by the increasing As content towards arsenopyrite (wide of both views is 250 μm).

On the other hand, the late pyrite variety is expressed mainly in fine-grained subhedral aggregates, usually with low arsenic contents (Table D.10, Appendix D) and no gold or pyrrhotite inclusions. Pyrite of this variety is most common as individual disseminated in the laminated quartz veins, and occurs as overgrowths on the earlier arsenic-rich framboids in the quartz-carbonate veins.

The euhedral arsenopyrite and pyrite grains are commonly fractured and healed by recrystallized quartz and galena or chalcopyrite (Fig. 4.23a). In some sections, pyrite is altered into goethite, particularly along its margins. Mineral inclusions of pyrrhotite, chalcopyrite, ilmenite and/or rutile and sericite are common in pyrite grains in the highly altered horizons (Fig. 4.23b).

Sphalerite is subordinate, occurring typically as anhedral inclusions intergrown with chalcopyrite and pyrrhotite in pyrite and/or arsenopyrite host crystals. Occasionally within the large arsenopyrite crystals, sphalerite inclusions are associated with or envelop gold and/or electrum inclusions (Fig. 4.23c). Sphalerite occurs also as individual grains disseminated in the quartz-carbonate veins. Chemical compositions of sphalerite inclusions and individual grains are summarized in Table D.11 (Appendix D).

Pyrrhotite occurs mainly as patchy inclusions, commonly in the large euhedral pyrite and arsenopyrite crystals (Fig. 4.23d) but they are less abundant if compared to sphalerite inclusions. Composition data of some pyrrhotite inclusions are given in Table D.12 (Appendix D).

Chalcopyrite occurs as very fine (~30μm) dispersed anhedral grains in the altered and less-altered rocks in the mine area. It occurs also as tiny inclusions intergrowing with sphalerite in the coarse-grained pyrite, or occupies spaces between aggregated pyrite and arsenopyrite grains in quartz veins. Microprobe data of some chalcopyrite inclusions are given in Table D.13 (Appendix D).

Cobaltite fine subhedral grains (~50 μm) are disseminated in the carbonate-rich domains within the quartz-sericite-carbonate±chlorite altered rocks (Fig. 4.23e). The micro-analytical data revealed that some grains have typical cobaltite composition, whereas others are in the (Fe-Co-Ni-As-S) system (Table D.14, Appendix D). Monazite (~20 μm) occurs in the auriferous quartz veins and in the altered rocks in association with fluorapatite and carbonate minerals. The spatial association of monazite, fluorapatite and carbonate (with more than 3 wt.% P_2O_5) suggests that formation of phosphorous-bearing minerals was contemporaneous with carbonate precipitation in the Um El Tuyor mine (see paragenesis below) .

Marcasite is associated with pyrite in the sericite-carbonate rich zones near quartz veins. It occurs as large irregular grains and laths (Fig. 4.23f). Marcasite replaced some pyrite grains almost entirely. Where marcasite replaces arsenopyrite, patches with an As-bearing unidentified phase (OH-arsenate?) are observed. Chemical composition data of some marcasite are given in Table D.15 (Appendix D). In the laminated quartz veins, intergrown diginite and galena are commonly associated with free gold grains in secondary sites (such as microfracutres).
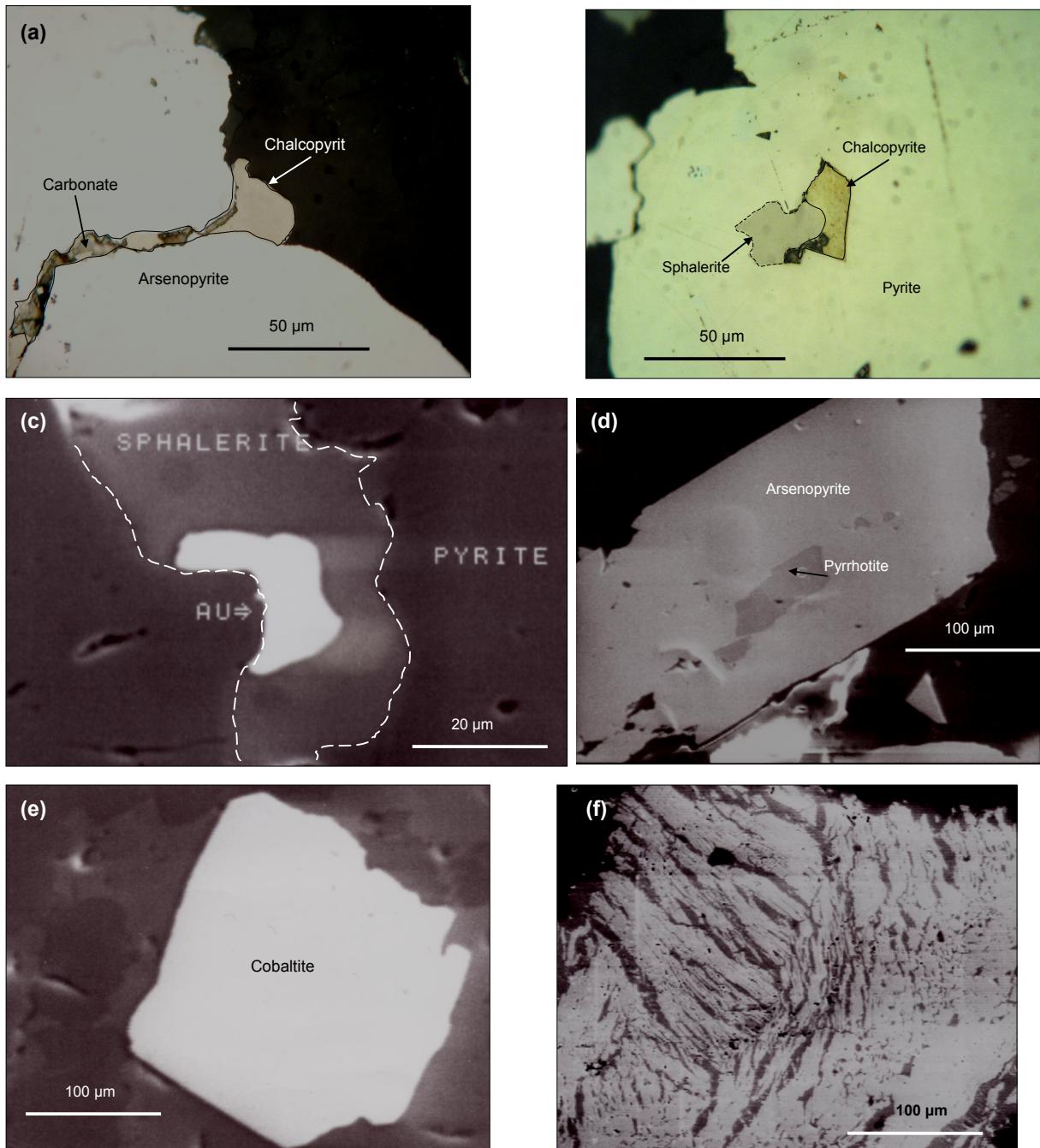
Fig. (4.23): Photomicrographs showing reflected light images of: a) chalcopyrite and carbonate occupying microfissures in deformed arsenopyrite grains; b) intergrowing chalcopyrite and sphalerite inclusions in pyrite; c) sphalerite and gold inclusions in a large pyrite crystal. d) pyrrhotite inclusions in a large euhedral arsenopyrite crystal; e) subhedral cobaltite crystal disseminated in the least altered zones in the mine area; f) large marcasite in the sericite -rich wallrocks in the Um El Tuyor mine area.

4.5.2 Modes of gold occurrence

4.5.2.1 Gold/electrum inclusions

Ore microscopy of the investigated samples detected abundant sub-mesoscopic to sub-microscopic gold grains, with free gold to Ag-poor electrum (~20 wt.% Ag) compositions (Table D.16, Appendix D). These grains occur as inclusions in arsenopyrite crystals (Fig. 4.24a), at pyrite-arsenopyrite contacts (Fig. 4.24b), as isolated grains dispersed in the quartz-carbonate domains, as free gold stringers and irregular grains occupying microfissures in vein quartz, and/or as fine wires within the rhythmic zones in goethite grains (oxidized after sulphides).

Variation in modes of occurrence is considered as indicative of multiple gold mineralizing events in the mine area. The occurrence of gold as inclusions within pyrite and arsenopyrite crystals and/or as tiny grains on sulphide grain surfaces and corners (Figs. 4.24c,d,e) suggests formation during earlier hydrothermal phases. According to distribution, two types of primary gold have been observed in the auriferous sulphides. They are categorized as: Au grains (inclusions) closely related to the well developed rhombdohedral growth zones in the host arsenopyrite (Fig. 4.24a), and Au-rich patches and lenticular zones that display no relation to any obvious growth zones.

On the other hand, the native gold grains are attributed to a remobilized phase 'secondary' refined during the late hydrothermal stages. The free (native) gold occurs commonly as individual dispersed grains, or associated with sulphides in the chlorite-sericite±graphite-bearing laminations in the laminated quartz veins.

Remobilization of gold is inferred from the presence of free gold blebs, globules, and wires in intensively oxidized sulphide grains (Fig. 4.24f). In the laminated quartz veins, the amount of disseminated gold grains decreases sharply with distance from the laminated domains and a zone of maximum concentration located at 0.4-1 mm from the lamination planes. Gold grains and wires are usually associated with galena and very fine (~30 - 50 μm) arsenopyrite. The presence of a 0.4 mm wide, gold-absent zone adjacent to laminations is suggestive for lateral migration of gold-bearing fluids through microfractures and grain boundaries leading to nucleation and growth of gold particles between pre-existing quartz grains in the passive domains (see also Davis and Hippertt, 1998). Electrum is absent in the laminated quartz veins.

Morphologically, gold grains are straight-edged to subrounded particles (10 - 100 μm), but globules, stringers, films and scales are also common in the examined samples. In color, gold grains from the Um El Tuyor deposit range from strong yellow with a red tint to creamy yellow. The variation in color is probably due to the presence of silver as an alloy.

4.5.2.2 Structure-bound Au in arsenopyrite [Fe (As$_{1\pm x}$ S$_{1\pm x}$)] and arsenian pyrite [Fe(S,As)$_2$]

On basis of electron-probe microanalysis (EPMA), Johan et al. (1989) proposed a substitution mechanism in arsenopyrite: [2As[Fe]⇔(Au,Sb)+Fe], where As[Fe] is As in Fe sites. Marcoux et al. (1989) detected an inverse correlation between Au and Fe in the auriferous arsenopyrite in two French deposits. Similarly, Wu & Delbove (1989) reported a negative correlation between Fe and Au in synthetic arsenopyrite, suggesting substitution of Fe by Au. Their synthetic arsenopyrite crystals were found to be zoned, with Au-rich rims and Au-poor cores. Fleet & Mumin (1997) provided a review of earlier work on arsenopyrite and suggested that invisible Au in arsenopyrite represents Au removed from ore fluids by chemisorption at As-rich, Fe-deficient surface sites which was then incorporated as a metastable solid-solution.
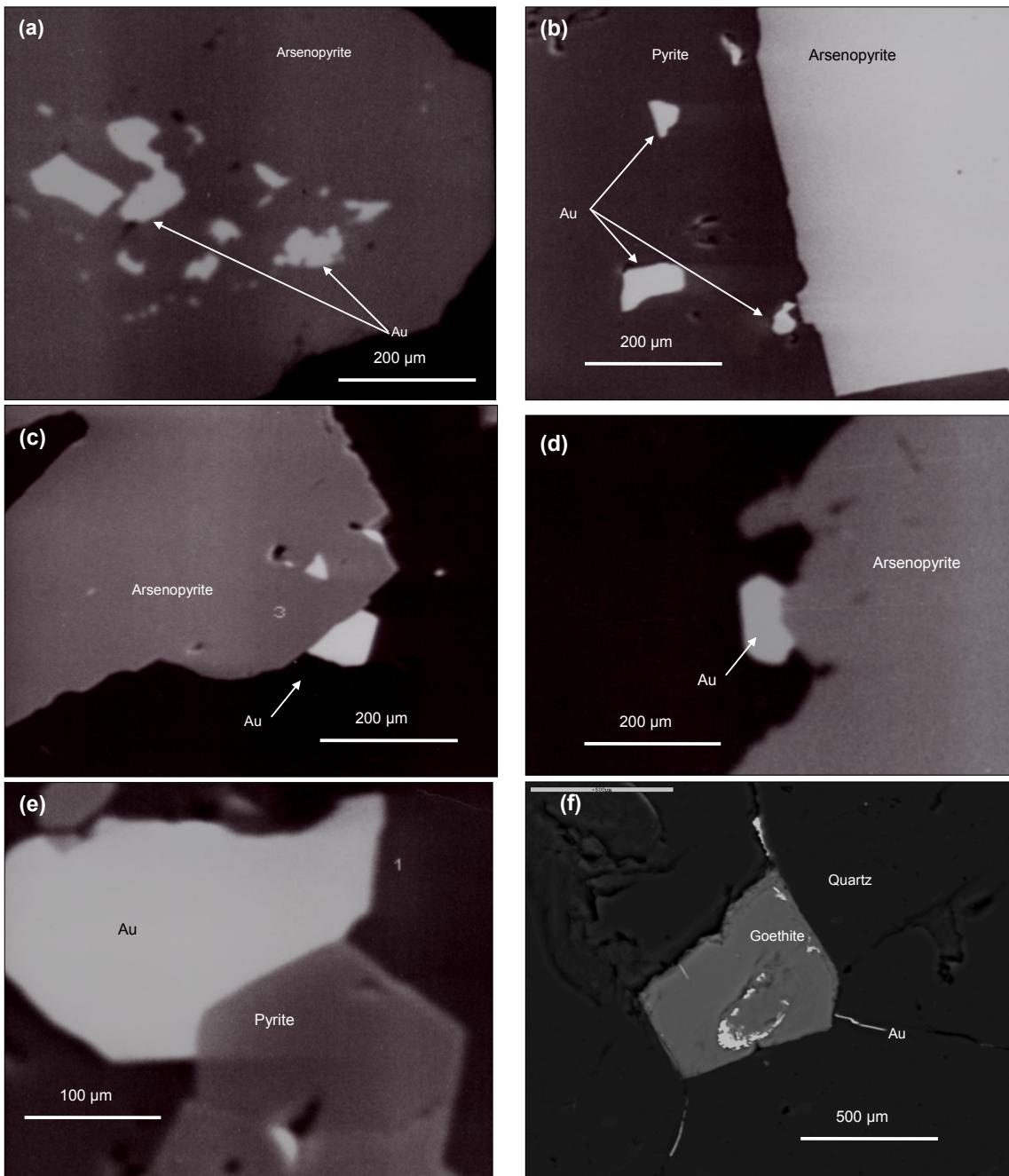
Fig. (4.24): Reflected light photomicrographs showing modes of gold occurrence in the Um El Tuyor gold deposit: a) shapeless gold inclusions distribute in a pattern similar to the margin of the host arsenopyrite grain; b) gold inclusions near contact between intergrown pyrite and arsenopyrite; c); d) euhedral gold crystals at surfaces of arsenopyrite grains; e) euhedral gold and pyrite grains in the auriferous quartz veins; f) remobilized (oxidized) gold rims within goethite (after pyrite).
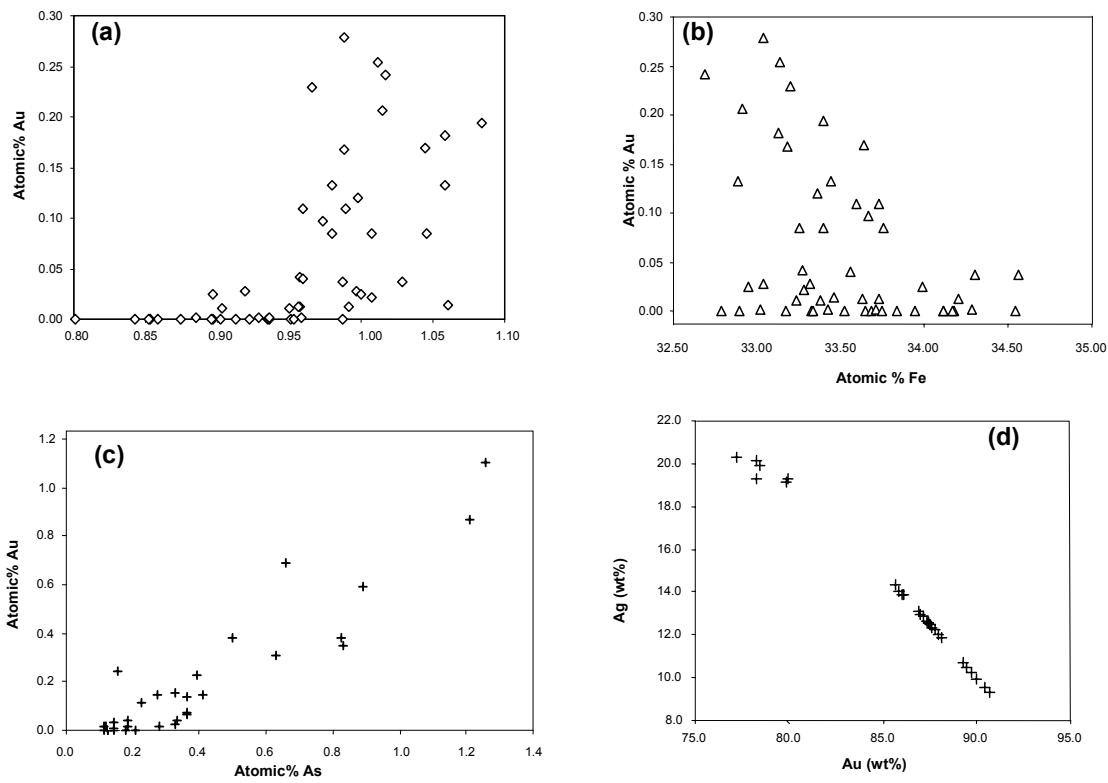
Fig. (4.25): Binary diagrams showing relationships between a) Au and As/S atomic %; b) Au and Fe atomic % in earlier arsenopyrite; c) Au and As atomic % in pyrite coexist with arsenopyrite of the earlier sulphide assemblage; d) Au wt% vs. Ag wt% of (primary) gold and electrum particles in quartz carbonate veins in Um El Tuyor Au-deposit.

In arsenopyrite from Um El Tuyor gold deposit, the (As+S) atomic % values are relatively constant at ~66. The EPMA data showed that Au, if present, is positively correlated with the atomic % As/S ratios and inversely correlated with Fe concentration (atomic %) in the auriferous pyrite and arsenopyrite of earlier mineralization (Figs. 4.25a to c). The most appealing interpretation is that gold replaces iron in both arsenopyrite and pyrite. Composition of gold grains and inclusions in arsenopyrite and pyrite of the first generation assemblage shows a negative correlation between gold and silver concentrations (Fig. 4.25d).

4.5.3 Paragenesis

Mineral paragenesis of Um El Tuyor gold deposit is determined on basis of the microscopic overgrowth and replacement textures displayed by the ore and gangue minerals. The concentration and textural relationships of the ore minerals do not vary significantly in the studied ore bodies, but generally can be distinguished as two mineralization phases. The early mineralization phase is expressed in disseminated auriferous pyrite and arsenopyrite with subordinate sphalerite, pyrrhotite and gold/electrum grains. On the other hand, the later mineralization phase is manifested by pyrite, arsenopyrite, galena±chalcopyrite, and free gold grains disseminated in the laminations and occupying fractures in the laminated quartz veins. Late supergene phases expressed in marcasite, diginite, goethite, and rutile are exclusively disseminated in and adjacent to the auriferous veins. The observed textural features reveal more or less simultaneous precipitation of all ore minerals. Gold and FeS_2 precipitation should have lasted over the entire event. However, later remobilization of earlier pyrite, arsenopyrite, and gold grains is assumed. The early disseminated arsenian pyrite and arsenopyrite, both variably auriferous,

associated with the prime hydrothermal and gold deposition event. In contrast, free gold grains are associated with later fine-grained arsenopyrite and As-poor pyrite. A schematic paragenetic sequence of the ore and gangue minerals in the Um El Tuyor mine area is summarized as follows:

Pre-ore stage

      - garnet, staurolite, biotite, ilmenite, magnetite ±hematite ±cobaltite ±chalcopyrite

Ore stage

Early ore stage   - biotite, chlorite, quartz, Fe-Mg carbonate, arsenopyrite, pyrite, chalcopyrite, gold and/or electrum ±spahlerite ±pyrrhotite ±cobaltite

Late ore stage   - monazite + fluorapatite + carbonate

    - quartz + sericite + pyrite + arsenopyrite + galena + free gold ±graphite ±chalcopyrite

Post ore stage

      - marcasite, diginite, rutile, goethite ±OH-arsenate

4.5.4 Temperature and sulphur fugacity based on sulphide assemblages

Assuming conditions under equilibrium, and since composition of arsenopyrite (Fe-As-S) is a function of sulphur fugacity and temperature, it is possible to estimate the conditions of arsenopyrite formation in the Um El Tuyor deposit. The method of temperature and sulphur fugacity calculation is based on the Fe-As-S mineral assemblage and the As atom.% in arsenopyrite (Barton 1969; Kretschmar and Scott 1976; Scott 1983; Sharp et al. 1985).

The chemical compositions of the arsenopyrite and the coexisting sphalerite were determined by an electron-microprobe. The analytical data and techniques are given in Appendix D. In order to detect any zonation within the individual grains, points from centres and margins of the large arsenopyrite crystals were routinely analyzed. In some samples, arsenopyrite grains are compositionally more variable than others. The conspicuous presence of pores in margins of some grains is interpreted as subsequent chemical overprinting. This textural evidence reflects varying degrees of retention of equilibrium. Data of such grains are considered not reliable for geothermometric purposes.

Arsenopyrite of the early sulphide assemblage (early-ore stage, see above), coexisting with pyrite and pyrrhotite, shows a range of ~31.29 to 32.03 at.% As. This arsenopyrite is also associated with electrum (with 18–27 Ag atom.%) and sphalerite (X_{FeS} mole% ≈0.16-18). This assemblage implies a temperature range of 382 to 429°C (Fig. 4.26). On the other hand, arsenopyrite of the later assemblage (late-ore stage) has 29.76 to 31.02 at.% As, assuming a formation temperature range of 338 to 365°C for the late mineralization phase. Fugacity of sulphur (-log f S$_2$) in the earlier mineralization phase was between 6.6 and 7.5 bars, whereas a range of 7.8-8.6 bars is estimated for the later mineralization (Figs. 4.26, 4.27). The results indicate that the ore fluids evolved progressively toward lower temperatures and sulphur fugacity with time.

Decrease of sulphur fugacity, through sulphide precipitation and/or H$_2$S loss might have favoured gold deposition through destabilization of gold bisulphide complexes such as Au(HS)$_2$ (Seward, 1984; Drammond and Ohmoto, 1985; Bowers, 1991).
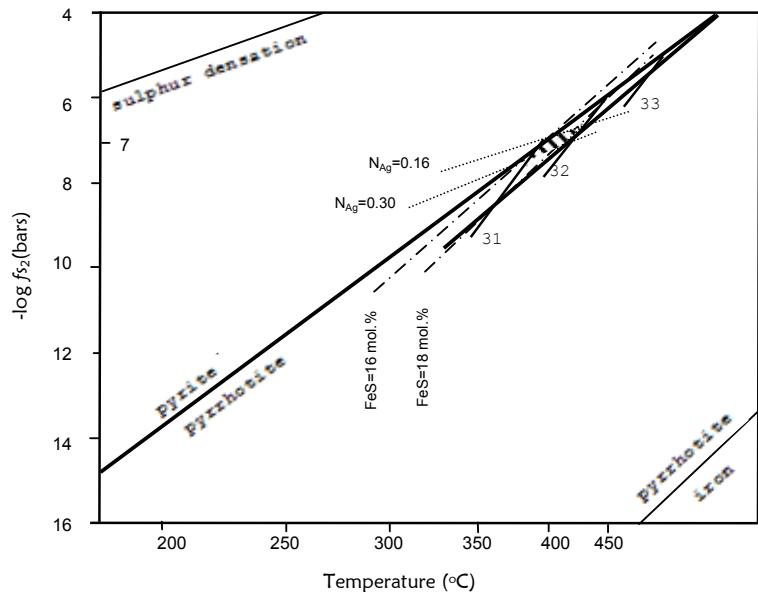
Fig. (4.26): The Fe–Zn–As–S system at low pressure adapted from Scott 1983. Hatched area reflects deposition conditions of electrum and sphalerite, and the doted area indicates deposition of arsenopyrite+pyrite±pyrrhotite (early sulphide assemblage in the Um El Tuyor deposit). Stability field of arsenopyrite (Barton, 1969), and arsenopyrite-buffered curves at.% As 31, 32 and 33 (from Kretschmar and Scott,1976), stability curves of silver; N_{Ag} in electrum (Barton and Toulmin, 1964), isopleths of sphalerite (Barton and Skinner, 1979) are shown. As: arsenic, aspy: arsenopyrite, bn: bornite, cpy: chalcopyrite, l: liquid, lö: loellingite, po: pyrrhotite, py: pyrite.

Fig. (4.27): The Fe–Zn–As–S system at low pressure, adapted from Scott 1983. The broken lines depict formation temperature range and fS_2 conditions of the late sulphide assemblage in the Um El Tuyor gold deposit. Stability field of arsenopyrite (Barton, 1969), and arsenopyrite-buffered curves (from Kretschmar and Scott,1976) are shown. As: arsenic, aspy: arsenopyrite, bn: bornite, cpy: chalcopyrite, l: liquid, lö: loellingite, po: pyrrhotite, py: pyrite.
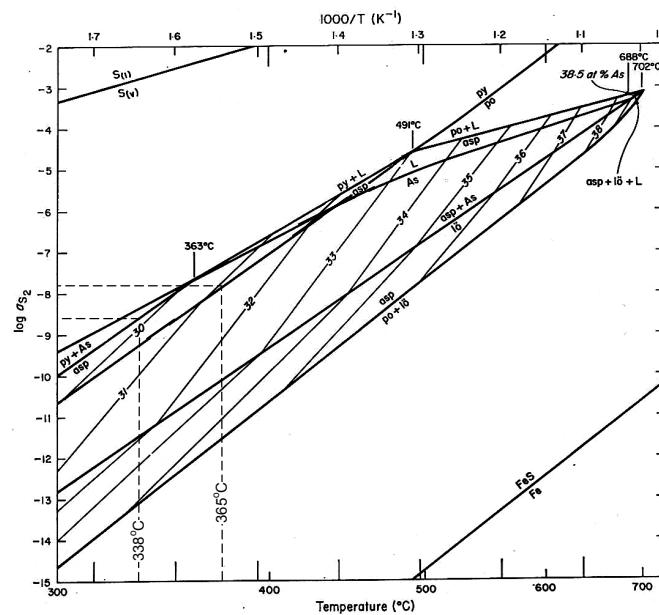
If arsenopyrite and sphalerite are buffered with respect to sulphur, the As/S ratio of arsenopyrite is mainly a function of the temperature, whereas the content of FeS in sphalerite (ZnS) depends on the confining pressures (Kretschmar and Scott, 1976). Clark (1960) suggested that As/S in arsenopyrite coexisting with pyrite and pyrrhotite decreases as a function of the total pressure. In such case, some kind of linear relationship should be expected between the concentration of FeS in sphalerite and As content in the coexisting arsenopyrite.

Sphalerite is present in the auriferous quartz veins mainly as fine inclusions intergrown with chalcopyrite in xenomorphic arsenopyrite, or as disseminated subhedral grains in quartz+siderite±chlorite rich domains in the adjacent wallrocks. The FeS content of the sphalerite inclusions in arsenopyrite is less variable or rather constant. FeS mol% contents in sphalerite inclusions are positively correlated with the As atom% in the host arsenopyrite crystals (Fig. 4.28). The FeS mol% contents are in the interval 15.75-18.19, which, according to Scott (1983), corresponds to a confining pressure range of 3.87-1.86 kb, respectively. Although sphalerite is a pressure sensitive mineral, sphalerite composition may be affected by deformation and alteration. Similarly, pyrrhotite is a non-refractory mineral, which means that it is rather easily affected by retrograde metamorphism and deformation. It is therefore possible that some of the FeS in sphalerite exsolved by decrease in temperature (Scott, 1983). This means pressure estimates are higher than the real conditions that might be expected if sphalerite barometry is used.

Fig. (4.28): Mole % FeS in sphalerile inclusions versus atomic % As in the host arsenopyrite crystals.
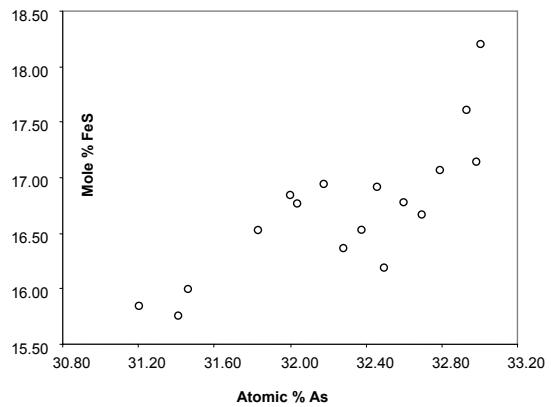
CHAPTER 5

HYDROTHERMAL ALTERATION

5 HYDROTHERMAL ALTERATION

5.1 Introduction

Chemical interaction between rocks and the hydrothermal solutions is certainly a major factor in precipitation of many ores (Rose and Burt, 1979, Susak, 1994). An understanding of the hydrothermal alteration processes is therefore important to obtain information on the physico-chemical conditions in the hydrothermal system (Reed, 1997). Commonly, a regular zoned pattern of alteration occurs around the mineralized veins. This zonation reflects changes in composition of the fluid with time or extent of interaction with the host rocks (Meyer and Hemley, 1967). The hydrothermal alteration zones around the ore (e.g. vein arrays) are therefore manifestation of the extent to which the original wallrocks were out of chemical equilibrium with the mineralizing fluids (Lindgren, 1895).

In the Um El Tuyor mine area, pervasive silicification, sericitization, carbonatization and sulphidation are major signs of fluid circulation. Pervasiveness of alteration is concomitant with the intensity of shearing in the vicinity of the auriferous veins. Alteration halos around quartz veinlets are symmetric if veins are parallel to the foliation, but indented if veins are oblique. These observations suggest that fluid percolation was guided by the host rock foliation anisotropy.

Hydrothermal alteration in the Um El Tuyor mine area has been modelled using a sample map (Fig. 5.1). Three main alteration zones are distinguished: a) a quartz-carbonate-sericite/muscovite-sulphide±graphite±albite-rich envelope around the auriferous veins, b) an intermediate selectively pervasive chlorite-sericite-carbonate-quartz-sulphide±biotite zone, and c) a distal zone of biotite-chlorite±sericite alteration (Fig. 5.2). Boundaries among alteration zones are gradational over centimeter to decimeter-scales. Generally, the degree of quartz veining, gold and base metal enrichment increases from the outer towards inner alteration zones. The inner zone presents the highest gold grade, especially where it is traversed by the laminated quartz veins.

In the following section, alteration mineralogy, style, and intensity of the three alteration types in the Um El Tuyor gold mine area are discussed.

5.2 Alteration zones

5.2.1 The distal zone (biotite-chlorite±sericite alteration)

In the mine area, the distal alteration zone is characterized by preferential replacement of the original garnet-biotite-staurolite±hornblende mineralogy by an association of biotite-chlorite±sericite. In the pervasively altered zones, chlorite replaces biotite entirely. The chlorite-dominated alteration produced alternating chlorite-rich and sericite-rich bands (Figs. 5.3a,b). The chlorite-rich bands contain very fine magnetite±hematite acicular shreds. In places, sericitic alteration overprints the biotite+chlorite (±minor rutile) alteration. Few veinlets of vuggy quartz (<2 cm wide), enclosing thin chlorite selvages, traverse the chlorite±sericite alteration.

Replacement of large brown biotite plates by fine-grained aggregates of green biotite is distinguished. The brown biotite is assumed to be of metamorphic 'primary' origin. The term metamorphic denotes crystallization during regional metamorphism of the host rocks. The metamorphic biotite occurs as preferentially oriented subhedral to anhedral flakes, with irregular and ragged edges in places. In contrast, the green biotite is observed only in the altered rocks, mainly in association with sericite and quartz, therefore, considered hydrothermal.
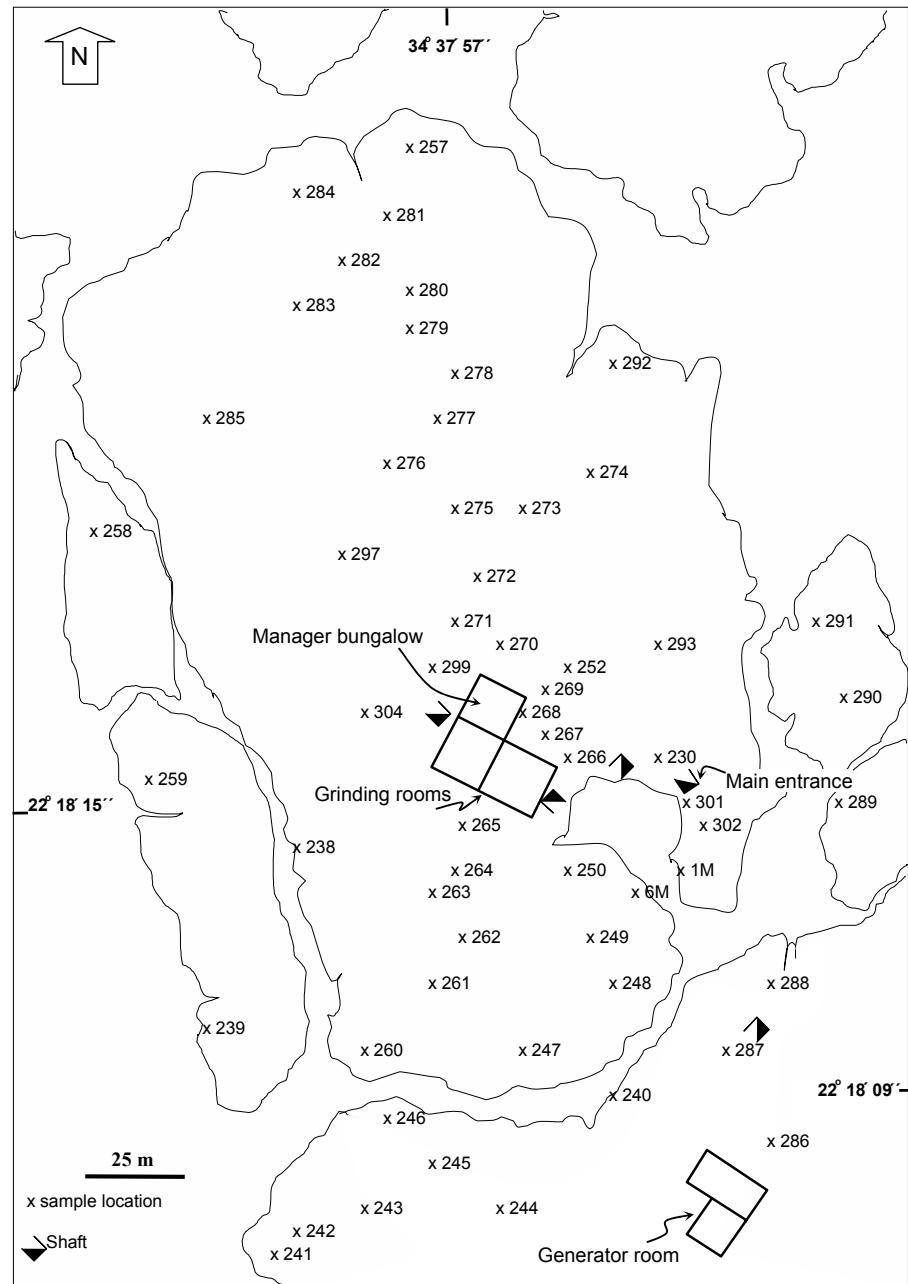
Fig. (5.1): Sample map of the Um El Tuyor gold deposit
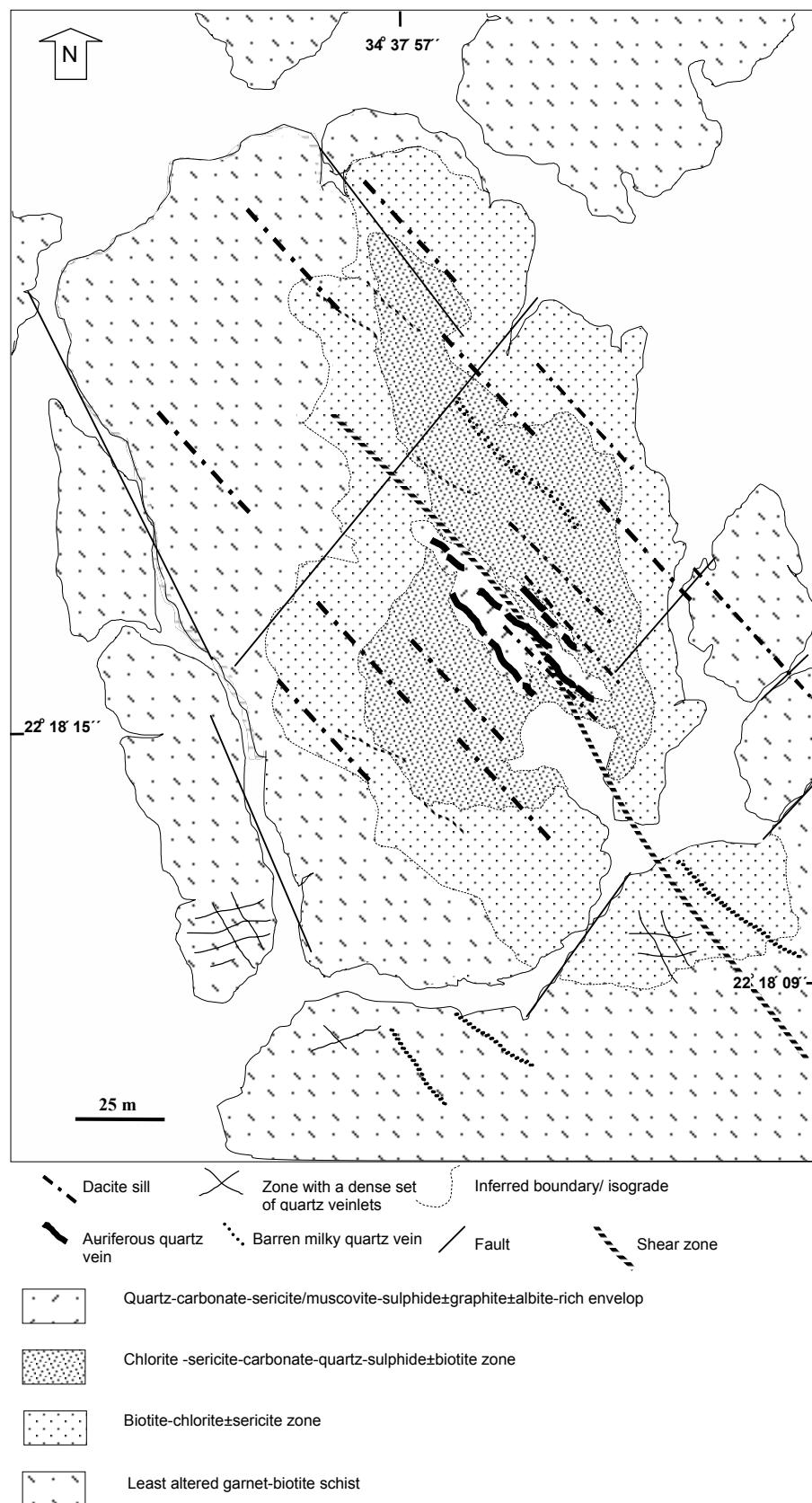
Fig. (5.2): Alteration map of the Um El Tuyor gold deposit

The hydrothermal biotite forms patchy aggregates of weakly pleochroic, pale green flakes. It is characterized by its small size (typically 50 to 300 μm long) and occurrence as randomly oriented aggregates. A distinction between the two biotite varieties is possible on basis of their microscopic appearance, mode of occurrence and also on their different geochemical characteristics.

The chemical composition and calculated structural formulae of both biotite varieties (Table E.1; Appendix E) show that the X_{Mg} value is the most significant factor in distinction between the metamorphic and hydrothermal biotite varieties. The metamorphic biotite is phlogopite-rich (average FeO/MgO=1.4), whereas, the hydrothermal biotite is annite-rich (average FeO/MgO=1.9). Compared to the metamorphic biotite, the hydrothermal biotite is impoverished in Al_2O_3, MgO and enriched in SiO_2, K_2O and FeO (Fig. 5.4a). A plot of Al (total) versus Fe/(Fe+Mg) ratios provides another distinction between the investigated hydrothermal and the metamorphic biotite varieties (Fig. 5.4b). The X_{Fe} ratios are higher in the hydrothermal biotite relative to those in the metamorphic biotite.
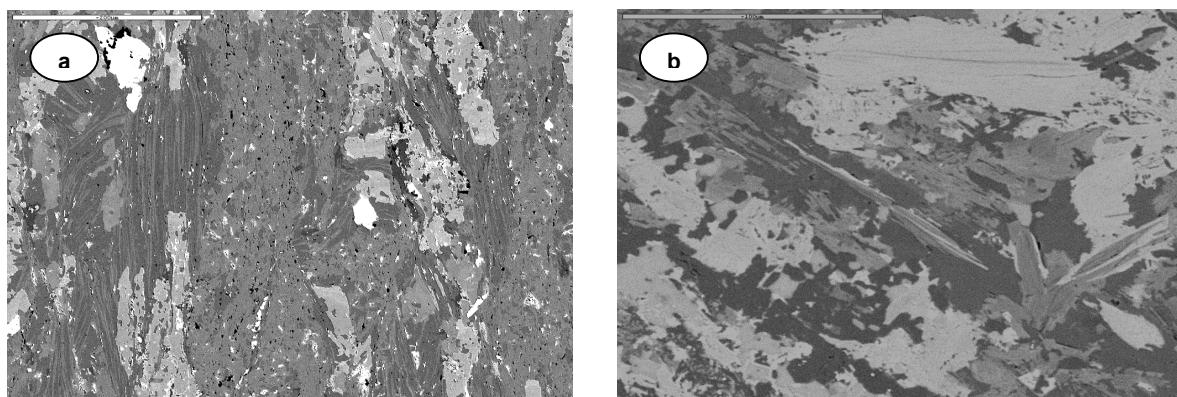
Fig. (5.3): Backscattered electron images of the hydrothermally altered samples from the Um El Tuyor mine showing: a) Aligned flaky minerals are sericite, chlorite and minor biotite. b) Patchy intergrown chlorite and carbonate traversed by sericite flakes in the intermediate alteration zone. The bar scale on both images is 200 μm.
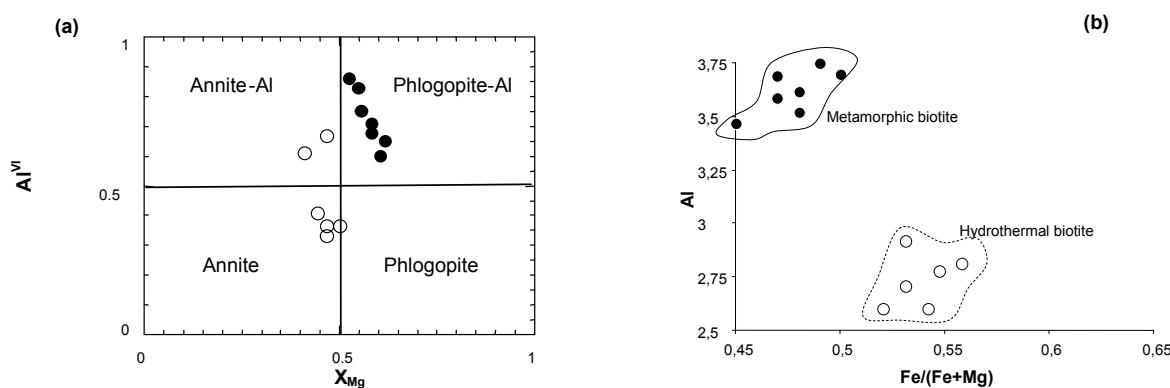
Fig. (5.4): a) Biotite classification, diagram after Guidotti (1984). b) Binary plot of Al^{total} versus Fe/(Fe+Mg) ratios in the metamorphic and hydrothermal biotite varieties in host rocks of the Um El Tuyor gold deposit.

Although some biotite flakes have entirely transformed into chlorite (ripidolite or pycnochlorite, Fig. 5.5), some biotite flakes are only partly replaced, along cleavage planes and fractures. The developed chlorite lamellae inherited their crystallographic directions from the original biotite. Scattering of element concentrations in the analyzed chlorite grains is evocative of variable contribution of hydrothermal fluids. The analytical data of the

chlorites are used for temperature estimates based on the chlorite geothermometer of Cathelineau (1988) and taking into account the Al^{IV} correction proposed by Kranidiotis & McLean (1987). Calculated chlorite formation temperatures in the distal alteration zone range from ~221 to 261°C (Table E.2; Appendix E).
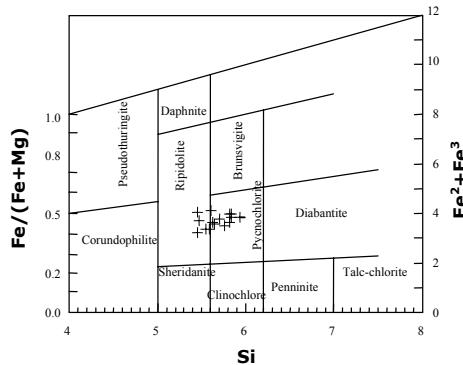
Fig. (5.5): Representative data of chlorite composition in the distal alteration zone in the Um El Tuyor mine area. Classification of Hey (1954).

5.2.2 The intermediate zone (chlorite-sericite-carbonate-quartz-sulphide±biotite alteration)

The intermediate alteration zone is represented by rocks enriched in chlorite, sericite, carbonate, quartz, pyrite, arsenopyrite, and less abundant galena. Due to the presence of chlorite±iron oxides, this zone is characterized by a green or reddish colour. This zone is typically developed in the sheared rocks. It is traversed by a dense set of barren quartz-hematite and quartz±sericite veins, averaging 3 to 12 cm in width.

In the intermediate alteration zone, relics of fine-grained green biotite are still preserved. Chemically, they are annite-rich with almost constant Si a̲toms p̲er f̲ormula u̲nit (a.p.f.u), but erratic Al^{vi} contents (Table E.3; Appendix E). If compared with the hydrothermal biotite in the distal alteration zone, biotite in the intermediate zone has lower SiO_2, Na_2O and K_2O and higher CaO, Al_2O_3, FeO^t, MnO and MgO contents. This feature may be attributed to the propylitization.

Chlorite forms colourless to olive green aggregates with a rosette morphology, and fills in the interstices between the porphyroblasts. The microprobe analytical data show that chlorites in the intermediate alteration zone have pycnochlorite/rhipidolite compositions (Fig. 5.6a, Table E.4; Appendix E). Given the observation of compositional uniformity, lack of correlation between the Fe/(Fe+Mg) and the Si/Al, Al^{iv}, and Al^{iv}/Al^{total} ratios, the low concentration of alkaline oxides ($Na_2O+K_2O+CaO<0.5$ wt.%), and the lack of correlation between Na+K+2Ca and octahedral vacancy (T2; Fig. 5.6b), no intergrowths of smectite and/or illite with flakes of this chlorite type is indicated (see Foster, 1962). The calculated chlorite formation temperature (geothermometer of Cathelineau, 1988, and Al^{IV} correction after Kranidiotis & McLean, 1987), range from 278 to 346°C, with noticeable increase towards the auriferous veins (Table E.4; Appendix E). These temperatures are higher than those calculated for chlorite in the distal alteration zone, as shown in Fig. (5.7).

In the intermediate alteration zone, the carbonate minerals are mainly iron-bearing dolomite (ferroan dolomite) and less common calcite, replacing partially or completely chlorite and biotite. Chemically, the Fe-bearing dolomite is nearly $Ca(Fe,Mg,Mn)(CO_3)_2$ solid solution, with a rhodochrosite component, which does not exceed 2 mol% (Table E.5; Appendix E).
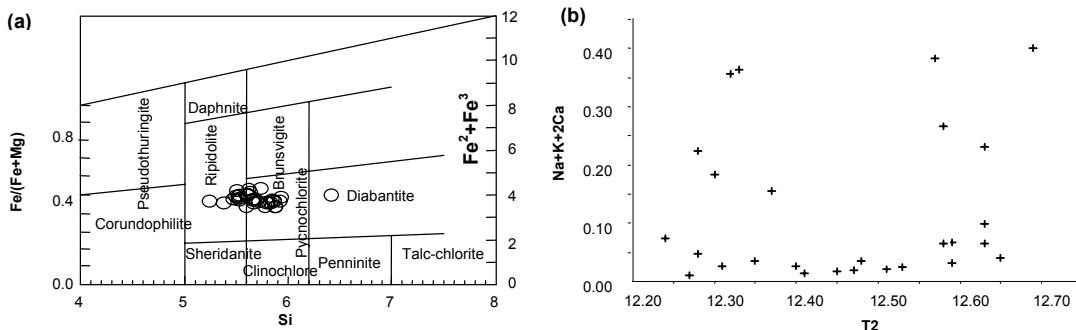
Fig. (5.6): a) Composition of chlorite in samples from the intermediate alteration zone in the Um El Tuyor mine area. Classification of Hey (1954). b) Na+K+2Ca versus T2 in chlorites disseminated in the intermediate alteration zone in the Um El Tuyor mine area.
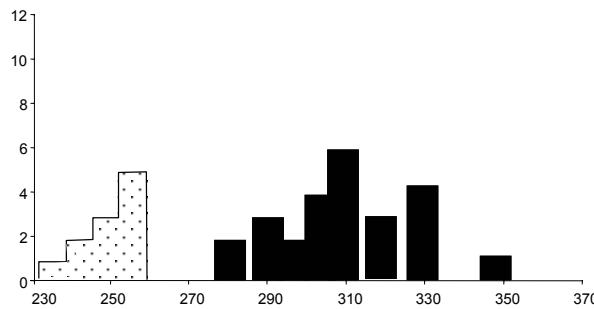
Fig. (5.7): Frequency histogram showing ranges of the estimated formation temperatures for chlorites from the distal (dotted blocks) and intermediate (dark blocks) alteration zone in the Um El Tuyor mine area. Data calculated after the Al^{IV} cation site occupancy method of Cathelineau (1988).

Sericite occurs as medium- to fine-grained grains, commonly associated with chlorite. The chemical composition of sericite in the intermediate alteration zone (Table E.6; Appendix E) is similar in to composition of the secondary muscovite of Miller et al. (1981). The compositional variation might have been controlled by phengitic substitution of Si for Al in the tetrahedral sheet composition and octahedral Fe, Mg for Al tschermakite-type substitutions (Fe$^{(VI)}$, Mg$^{(VI)}$ + Si$^{(IV)}$ ⇔ Al$^{(VI)}$+ Al$^{(IV)}$). This feature might be indicated from the negative correlation between (Si+Mg+Fe^{2+}) versus (Al^{IV}+Al^{VI}) (Fig. 5.8). Compositional differences between cores and rims of the sericite flakes are observed. At the individual grain- scale, grain cores show higher celadonite content relative to the margin (Fig. 5.9). This observation, together with the enrichment in Al^{VI} and K in grain margins is attributed to some degrees of paired substitution of (Mg,Fe) for Al, and Si for Al.

Subhedral crystals of fluorapatite commonly occur in association with carbonate minerals in the intermediate alteration zone. Chemical compositions of some fluorapatite crystals are given in Table E.6 (Appendix E). Euhedral fluorite inclusions are occasionally observed in the large muscovite plates, especially in samples exhibit massive alteration.
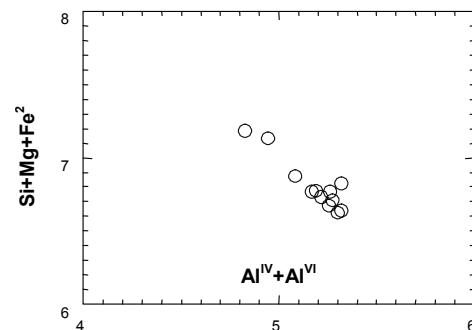
Fig. (5.8): Chemical composition of sericite in samples from the intermediate alteration zone in the Um El Tuyor mine area. Data plotted as Si+Mg+Fe^2 vs. Al^{IV}+Al^{VI}. Cation are calculated based on 22 oxygens per formula unit.
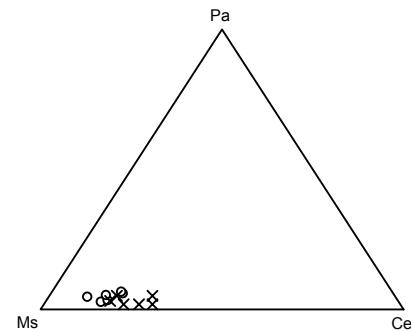
Fig. (5.9): Classification of sericite disseminated in the intermediate alteration zone in terms of muscovite (Ms=KAl$_3$Si$_3$O$_{10}$(OH)$_2$), paragonite (Pa=NaAl$_3$Si$_3$O$_{10}$(OH)$_2$) and celadonite (Ce=K(Mg,Fe)(Fe^{3+},Al)-Si$_4$O$_{10}$(OH)$_2$) end members. Crosses indicate cores and circles represent rims of the analyzed flakes.

5.2.3 The quartz-carbonate-sericite/muscovite-sulphide±graphite±albite envelop

Although not extensive, the quartz-carbonate-sericite/muscovite-sulphide±graphite±albite assemblage is the most conspicuous hydrothermal alteration in the Um El Tuyor mine area. The width of this alteration envelops is proportional to the width of the quartz veins, but rarely exceeds few meters. Commonly, fine anhedral quartz grains are disseminated in the wallrocks, and their abundance increases towards the main quartz veins.

Within and adjacent to quartz veins, carbonate intermingle with the fine-grained hydrothermal quartz and sericite or form dense veinlets traversing the silicified wallrocks and the quartz veins (Fig. 5.10a). In this alteration type, carbonate occur principally as Fe-dolomite and/or ankerite (Fig. 5.10b, Table E.7; Appendix E). However, in places, calcite constitutes a minor component among the hydrothermal phases, and traverses the massive Fe,Mg carbonate-rich domains. In thin sections, calcite is commonly white to yellowish brown, and exhibits twinning lamellae. In contrast to the earlier carbonate, the analyzed calcite grains exhibit very low MgO, FeO and MnO wt% (Table E.7; Appendix E).

Higher contents of sulphide minerals are common in zones where carbonate (i.e. ankerite) become a substantial constituent of veins and the adjacent wallrocks. Backscattered electron images point to some sort of spatial relationship between sulphides and zones rich in carbonate with a relatively high siderite component.
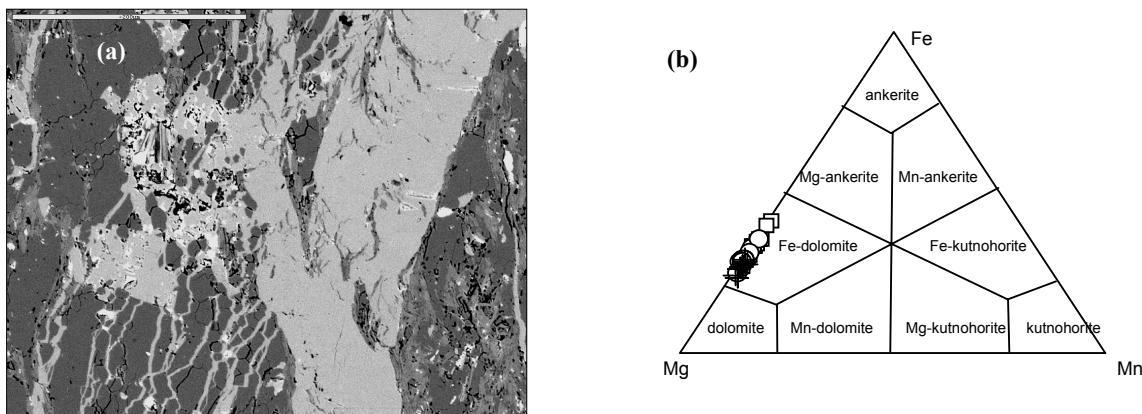
Fig. (5.10): a) Backscattered electron image showing 10-150 μm-wide carbonate veinlets traversing the silicified wallrocks in the mine area. The bar scale is 200 μm. b) The FeCO$_3$-MgCO$_3$-MnCO$_3$ triangular classification diagram of Trdlička & Hoffman (1976) showing compositions of carbonate of the dolomite-ankerite series in samples of the auriferous veins and wallrocks. Cross symbols: carbonates from intermediate zone, circles: carbonate from proximal zone, squares: carbonate from quartz carbonate veins. The carbonates in quartz-carbonate veins are more enriched in Fe than in the alteration zones.

Sericite occurs as weakly oriented fine-grained flakes and aggregates, intermingling with carbonate minerals and rimming muscovite flakes (Fig. 5.11a). Sericite displays a darker hue than muscovite in the backscattered

electron images. The Na$_2$O content is higher in sericite compared with that of muscovite, whereas the contents of TiO$_2$ and MgO are higher in muscovite. Due to the very fine grain size of sericite, compositional differences between cores and margins of the sericite flakes have not be examined. Generally, the examined sericite has typical muscovite composition (Fig. 5.11b, Table E.8; Appendix E). Sericite in the alteration envelops around the veins is rich in Na$^+$ and poor in K$^+$ and phengite content (atomic Fe+Mg per formula unit) compared with sericite in the intermediate alteration zone.

Albite is confined to the contact zones of quartz veins and the quartz-sericite-carbonate-rich wallrocks (Fig. 5.12). It occurs as fine-grained, subhedral crystals dispersed in and adjacent to the main gold-bearing quartz-carbonate veins. Albite grains exhibit compositional zoning with Na-rich rims around cores with relatively higher K/Na atomic ratios (Table E.9; Appendix E). Discrete tiny gold grains along with arsenopyrite, pyrite and less common chalcopyrite are observed in the vicinity of the auriferous quartz veins.

Graphite occurs as tiny laths commonly associated with sericite in zones enriched in sulphides, and zones around the laminated quartz veins.
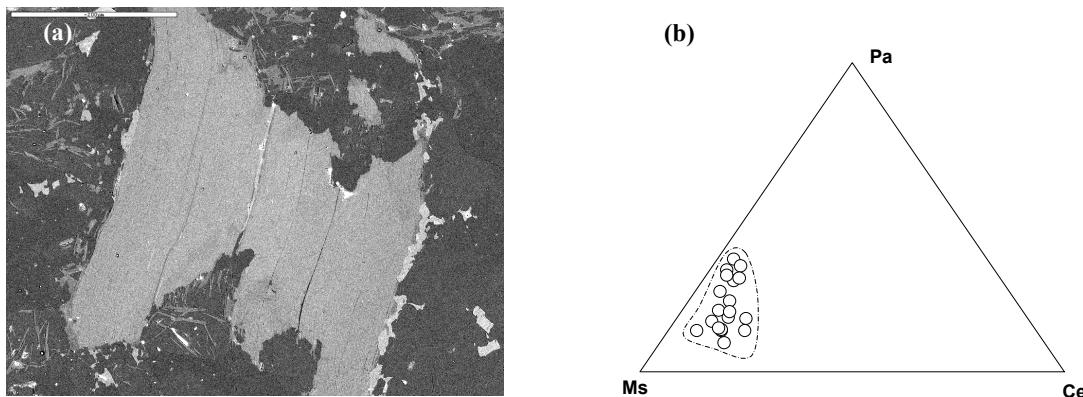
Fig. (5.11): a) Backscattered electron image showing a large muscovite plate with carbonate minerals along the cleavage planes and dispersed sericite flakes near margins. Bar scale is 50 µm. b) Classification of the analyzed sericites from the proximal alteration zone in terms of muscovite (Ms=KAl$_3$Si$_3$O$_{10}$(OH)$_2$), paragonite (Pa=NaAl$_3$Si$_3$O$_{10}$(OH)$_2$) and celadonite (Ce=K(Mg,Fe)(-Fe,Al)Si$_4$O$_{10}$(OH)$_2$) end members.
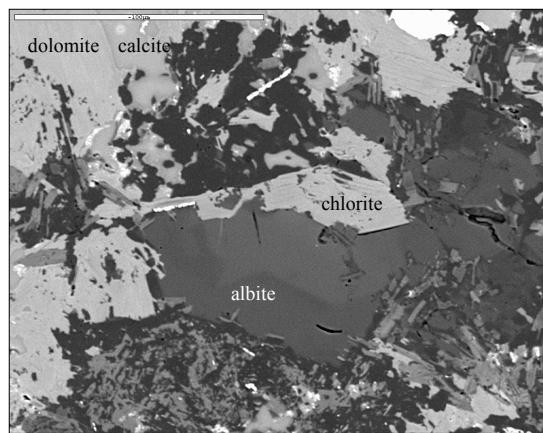
Fig. (5.12): Backscattered electron image of a zoned albite crystal rimming relics of chlorite and intergrown with carbonate and sericite.

The geographic distribution of the hydrothermal phases and mineralogical changes throughout the three alteration types is summarized in Table (5.1).

Table (5.1): Schematic geographic distribution of the hydrothermal alteration types the Um El Tuyor mine area

Primary phases	ALTERATION ZONE AND ASSEMBLAGE					Hydrothermal phases
	Distal zone	Intermediate zone		Ore zone		
	bio-chl±ser	chl -ser-qz-py-rut±bio	ser-py-apy-cp-dol-qz	qz-ser-alb-ank-py-apy-envelop	Qz veins (main lodes)	
Biotite	unstable, partly replaced by hydrothermal biotite, sericite chlorite±epidote,		completely replaced by chlorite, carbonate, sulphides,	Absent		Hydrothermal biotite, chlorite, Sericite
Staurolite	unstable, replaced by sericite.	altered into sericite, rutile and iron oxides	absent	Absent		
Hornblende						
Garnet	unstable, partly replaced by sericite, quartz and iron oxides	completely altered into sericite, quartz, and partly replaced by sulphides		absent		Carbonate
Apatite	less common (accessory), stable	partly replaced by rutile, carbonate and frequently with monazite		replaced by carbonate and fluorapatite		
Feldspar	unstable, partly replaced by sericite or occasionally by epidote	completely replaced by sericite and/or albite				
Quartz	stable, locally augmented	fairly developed	hydrothermal quartz more or less recrystallized and redistributed			Quartz
	absent			little amount of very fine graphite associated carbonate and milky quartz.		Graphite
Total opaques%	accessory magnetite, pyrite and cobaltite, commonly associated with biotite and sericite, < 1	mainly sulphides, ~1– 3		3 – 5	~7.5	Sulphides
	absent		fine blebs disseminated in the chlorite-carbonate rich zones	electrum and free gold inclusions in sulphide grains and infill in microfissures within quartz		Gold

Unstable = phase undergoes partial or complete alteration (minor alteration products given in parentheses)
Stable = phases not affected by alteration
Abbreviations:
bio = biotite, kaol = kaolinite, ser = sericite, chl = chlorite, ep = epidote, qz = quartz, rut = rutile, dol = dolomite, ank = ankerite, py = pyrite, apy = arsenopyrite, and cp = chalcopyrite.

5.3 Geochemistry of alteration

In this section, a geochemical study is intended to characterize the chemical changes which might have been undertaken by the host rocks during hydrothermal alteration. Mass balance calculation is used to evaluate the mobility of elements during alteration and in an attempt to understand chemical modifications associated with the hydrothermal alteration, and therefore, chemistry of the mineralizing fluids. Theoretically, chemical changes occurred during the fluid-rock interaction associated with hydrothermal alteration of the host rocks can be appreciated by comparing the chemical analyses of the least and most altered rock types. A number of bulk-rock chemical analyses of the hydrothermally altered wallrocks as well as the least altered country rocks has been done.

Generally, the hydrothermally altered wallrocks have higher K_2O, $Fe_2O_3^*$ and lower MgO contents if compared with the least altered host rocks (Table E.10; Appendix E). Enrichment in K_2O may be attributed to invading of aqueous hydrothermal fluids. The high iron content in the altered samples is probably caused by sulphidation and chloritization overprints. The wt% loss on ignition (LOI) is raised considerably in samples display intense alteration, which could be ascribed for the flux of an external fluid. In the altered and unaltered rocks, contents of the LIL elements, e.g. Rb, Ba and Sr are low to moderate. The Rb/Sr, Rb/Ba, and K/Rb ratios are low, and almost identical in many of the analyzed samples. However, the Ba/La ratios are generally higher in the intensively altered rocks if compared to those in the unaltered rocks.

Assuming that the HFS elements, particularly Al and Ti, were immobile during alteration, or their mobility was not significant, correlation between their concentrations in the analysed samples might be used to estimate the mass gains and losses for each alteration type relative to the least or unaltered samples. A single alteration trend is obtained by plotting TiO_2 vs. Al_2O_3 contents in the altered samples and average of the least or un-altered precursor. This single trend is considered as indicative of an initially homogeneous precursor (Fig. 5.15). The sericitized rocks show a widespread mass loss, whereas a net mass gain can is recognized in samples from the propylitized (chloritized/carbonatized) zones compared to the least or un-altered precursor.
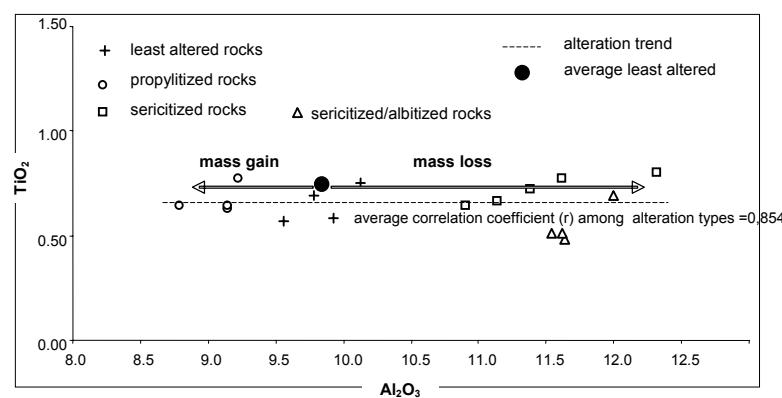
Fig. (5.13): TiO₂ vs. Al₂O₃ binary plot of the altered samples and average of the least-altered precursor. The correlation coefficient (r) is calculated using all the altered samples, with significance value of <0.01 in all cases.

5.3.1 Characterization of the immobile elements

Direct comparison between chemical analyses of least-altered and intensively altered rocks using oxide weight percentages of the major constituents are not useful, as it does not take into account the volume changes that accompany mass transfer. Therefore, a reference frame is needed to convert variations in chemical composition into units of mass transfer (Gresens, 1967). Grant (1986) modified the equations given by Gresens (1967) to develop the isocon method for calculation of absolute and relative mass or volume changes associated with alteration. This method requires the selection of immobile elements to define an isocon with which estimation of mass gains and losses of the 'mobile' elements in the altered rocks can be carried out. An isocon with slope of 1 will represent a net mass change of zero, whereas elements plotting below or above the isocon refer to mass loss or gain, respectively.

Gresens (1967) suggested the use of Al, Ti, Zr, Y, Nb and Sc to monitor volume changes. These elements have been considered as relatively immobile in most hydrothermal systems by many authors (Floyd & Winchester, 1978; Finlow-Bates and Stumpfl, 1981; Lesher et al., 1986; MacLean and Kranidiotis, 1987; Gemmell and Large, 1992; MacLean and Barrett, 1993). The HFS elements Al, Ti and the LREE (La and Ce) are used in the present study to monitor mass transfer in the isocon calculations. Their use to define the isocon has permitted calculation of the net mass changes in the altered wallrocks. For each alteration type, convergence among the concentrations of Al, Ti and LREE in the least or un-altered rocks and in the hydrothermally altered rocks defines a straight line. The latter is considered as the best fit isocon. Obtaining a single isocon for each alteration type confirms the assumption that the used elements (Al, Ti and LREE) have been effectively inert during all types of alteration.

5.3.2 Mass balance calculation

The isocon approach of Grant (1986) is mathematically similar to that of Gresens (1967), but different in the graphical representation of the data. In the method of Gresens, the components that are likely to have been immobile during alteration can be used to identify any volume change, which may have taken place. Assuming that volume change is a factor common in the behaviour of all components, it is possible to calculate gains or losses of the other components. Mass gains and losses are calculated using the following relationship (equation 1):

$$X_n = [F_v(S^b/S^a)C_n^b - C_n^a]*100 \qquad ………(1)$$

where X_n is the mass gain or loss for component n, F_v is the volume factor, S^b is the specific gravity of the altered sample, S^a is the specific gravity of the unaltered (original) sample, C_n^b is the concentration of component (n) in the altered sample, and C_n^a is the concentration of component (n) in the unaltered sample. In the isocon method of Grant (1986), equation (1) is reformulated as:

$$DX_n = 100(M^b/M^a)X_n^b - X_n^a \qquad ………(2)$$

where M^b/M^a is the mass ratio between the altered sample and the unaltered sample. This ratio is calculated by plotting the concentration of components in the altered wallrocks versus those in the unaltered precursor. X_n^b is the concentration of component (n) in the altered sample, and X_n^a is the concentration of component (n) in the unaltered sample The components that are immobile will fall on a line with a slope of $M^b=M^a$, that is the isocon.

Components that lie above the isocon have been augmented, whereas those which are below the line have been depleted during the alteration. The slope of the isocon (mass factor) can be determined graphically, and then used to calculate the mass gains and losses of the remaining components by applying equation (2).

Estimation of the mass factor may be doubtful if the metasedimentary rocks vary in their composition with laterally and vertically in the sequence. However, the convergence between compositions of each of the four representative samples with the median of these four samples yielded isocons having mass factor very close to the value 1, which suggests a very similar composition for the chosen precursor samples. Based on the latter observation, the median of the four representative samples of the un/least-altered host rocks has been found so far reliable to represent the precursor for comparison with the altered wallrocks.

In order to calculate the mass changes undergone by host rocks during hydrothermal alteration, chemical comparisons have been made among the respective medians of the unaltered (respectively least altered) and altered rocks in the mine area. The use of this statistical parameter (median) instead of the absolute concentration in a specific sample of the altered and least-altered rocks minimizes the error introduced by heterogeneity which might be expected in the host metasedimentary rocks. In many cases, the median values are similar to the chemical analyses corresponding to the most representative samples of each group, selected on basis of petrographic observations. Mass changes in every alteration type, with respect to the selected least-altered precursor, are summarized in Table E.11 (Appendix E) and shown in the isocon plots (Figs. 5.16 to 5.18).

*Fig. (5.14): Isocon diagram comparing median composition of samples from the **biotite-chlorite±sericite alteration (distal) zone**, and median composition of samples representing the least-altered rocks. The dashed line (isocon) is drawn for the largest number of potentially immobile elements. The best constraints on mass changes are given by TiO_2, Al_2O_3, P_2O_5, Ni and Ce. The inset histogram shows the distribution of mass factors calculated for each element.*
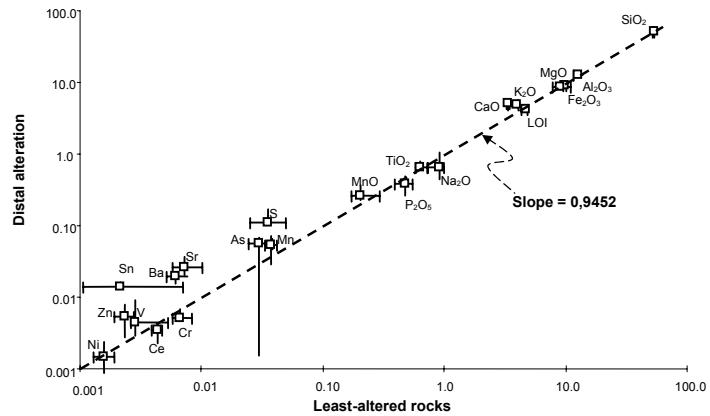
*Fig. (5.15): Isocon diagram comparing median composition of samples from the **chlorite-sericite-carbonate-quartz-sulphide±biotite (intermediate) zone** and median composition of samples representing the least-altered rocks.*
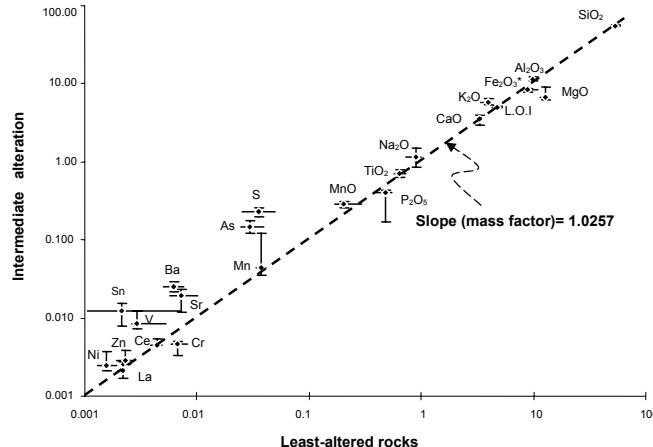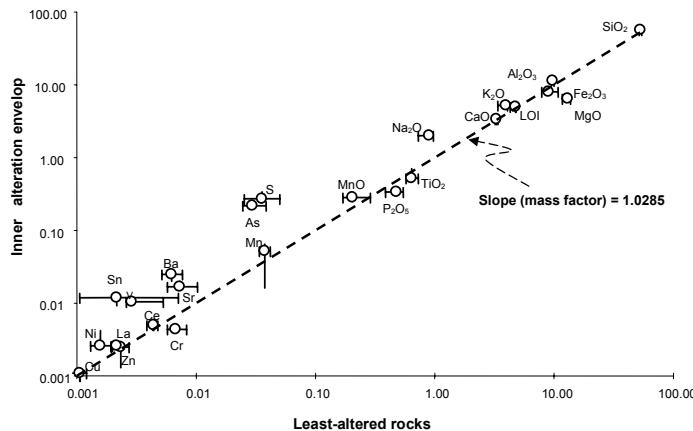
*Fig. (5.16): Isocon diagram comparing median composition of samples from the **quartz-carbonate-sericite/muscovite-sulphide±graphite±albite-rich envelope** and median composition of samples representing the least-altered rocks.*

Although aluminum (as Al_2O_3) shows severe percentage variation in the altered and least-altered rocks, the apparent variations might be mainly the result of a modal increase in other phases (such as $Fe_2O_3^*$, MgO or LOI), therefore may not be directly related to alteration. Compared with composition of the least-altered rocks, the most striking differences indicate enrichment in SiO_2, K_2O, Na_2O and LOI, and decrease in the P_2O_5 and MgO contents. In addition, many trace elements (e.g., Zn, Cu, As and Sn, as well as S, Sr, Rb and Ba) are significantly variable within each alteration type and among the different types (Table E.10; Appendix E).

Based on mass balance calculations and isocon diagram, a common loss of SiO_2, Al_2O_3, Na_2O and P_2O_5, and addition of $Fe_2O_3^*$, MnO, MgO, CaO, K_2O, SO_2 and LOI characterize the major chemical changes in the altered rocks in distal zones. The isocon slope of these rocks indicates a net mass gain of ~5.5% (Fig. 5.16). Samples from the intermediate alteration zone exhibit a noticeable addition of SiO_2, Al_2O_3, K_2O and SO_2, and loss of MgO and $Fe_2O_3^*$. Slope of their isocon reveals a slight net mass loss of about 2.5% for these rocks (Fig. 5.17). Finally, rocks from the inner alteration envelop undertook enrichment in SiO_2, Al_2O_3, Na_2O, K_2O and SO_2, and depletion in MgO. Slope of the isocon indicates a slight net mass loss of ~2.8% for these rocks (Fig. 5.18).

Generally, introduction of SiO_2, H_2O, CO_2, K_2O, and S (Figs. 5.19a to c) is evidenced from the mass balance calculation and accentuated by the widespread association of chlorite, carbonate, sericite, and sulphides. The most appealing interpretation is that these components were added from hydrothermal solutions. The addition of CO_2, together with H_2O and to a lesser extent K_2O and SO_2 resulted in carbonatization, sulphidation and sericitization. For a similar muscovite-carbonate alteration associated gold deposits, Kishida and Kerrich (1987) have proposed that the alteration would result in the release of H^+ from the fluid which decreases the fluid pH, probably reducing the solubility of gold.
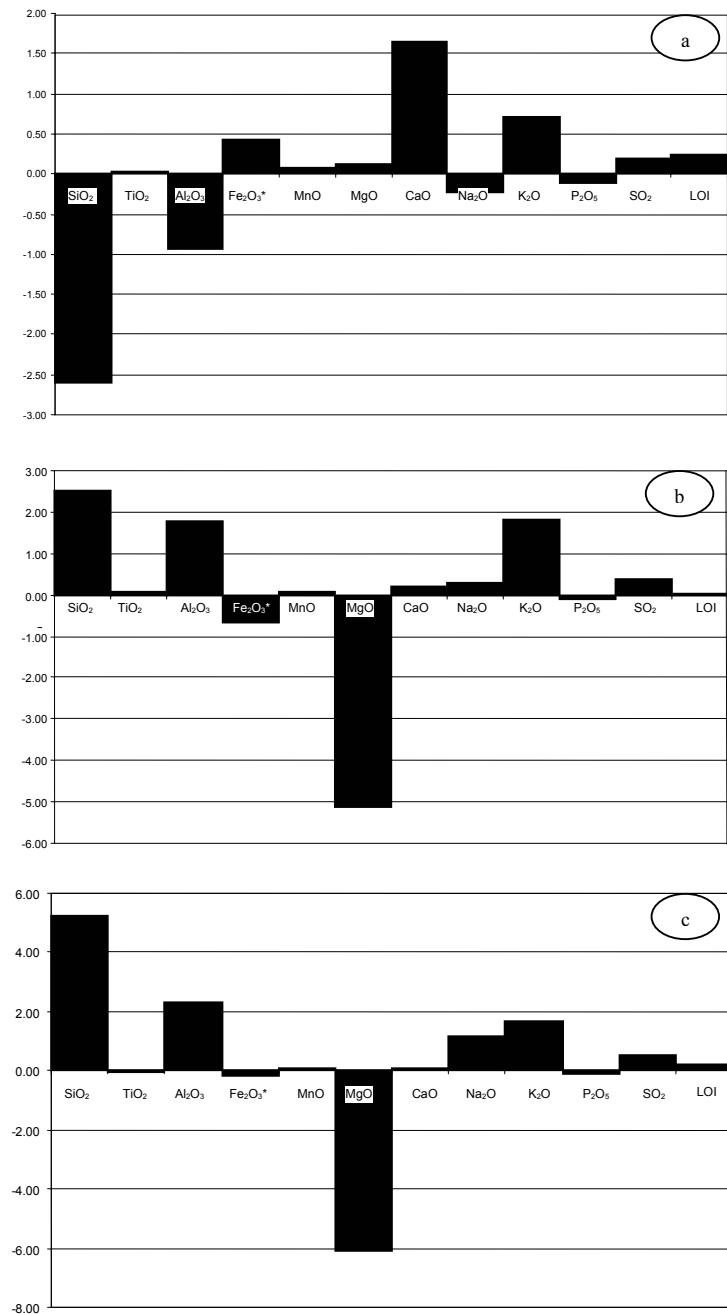
Fig. (5.17): Profile-histograms (hildreth-type) showing the mass changes (grams added or removed per 100 gram country-rock) in major element oxides during alteration based on median of the least altered samples as a reference for calculations, and the averages of mass changes in the hydrothermally altered samples from the three alteration types in the Um El Tuyor mine area. (a: outer zone, b: intermediate zone and c: inner alteration envelop)

5.4 Alteration model

A genetic relationship between the hydrothermal alteration and gold mineralization is suggested by the presence of the auriferous quartz veins within a volume of altered rocks and increasing intensity of wallrock alteration and density of the quartz veining towards the gold-quartz veins. These observations suggest a variable degrees of fluid-rock interaction through emplacement of the quartz veins. Changes in the host rock composition, mineral microanalyses and modal mineralogy are used also to decipher the type and extent of fluid-wallrock interactions during alteration. The gradational contacts between the auriferous quartz veins and wallrocks and among the alteration zones imply progressive interactions during and after infiltration of the ore-forming fluids into the host rocks. A paragenetic sequence of mineral phases associated with the Um El Tuyor gold deposit, based on the microscopic and field relations, is illustrated in Fig. (5.20).
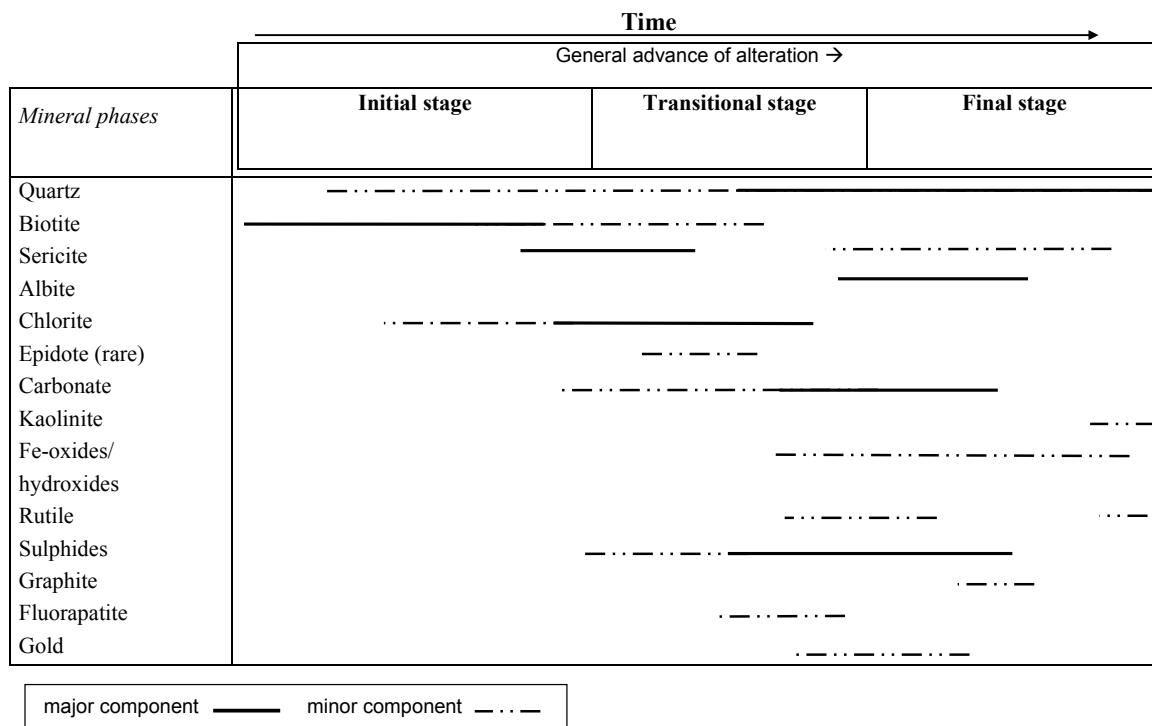
Fig. (5.18): Simplified paragenetic sequence of the hydrothermal mineral species in the Um El Tuyor gold deposit.

In an attempt to present, in simplified way, the main mineral transformations that might have taken place during hydrothermal alteration/mineralization in the Um El Tuyor mine area, a group of chemical equations is given in the following section, taking into consideration the investigations given by Meyer and Hemley (1967), Mueller & Saxena (1977), Kishida and Kerrich (1987), Groves and Forst (1991), and Barton and Skinner (1979). Noteworthy, the proposed reactions are based on conditions of equilibrium, which practically does not occur in geothermal systems.

The chemical and mineralogical changes observed in the Um El Tuyor mine area involve hydration, cation exchange, dissolution, replacement and redox reactions. The following is a tentative chronology of the metasomatic events and reactions as inferred from the petrographic observations and the microprobe data.

5.4.1 The initial stage

The incipient mineralogical transformations in the host rocks are typified by the almost complete conversion of Fe-Mg-silicates into chlorite and muscovite by means of hydrolysis, probably according to one or more of the following reactions:

$(Fe^{++},Mg)_2Al_9(Si,Al)_4O_{20}(O,OH)_4 + 2K(Fe,Mg,Ti)_3AlSi_3O_{10}(OH)_2 + 2SiO_2 + 6H^+ + K^+ + 4O^{2-} \rightarrow (Fe,Mg,Ti)_5Al_2Si_3O_{10}(OH)_8 + 3KAl_3Si_3O_{10}(OH)_2 + TiO_2 +$
staurolite   biotite   fluid   chlorite   muscovite   rutile
$3(Fe,Mg)^{2+}_{(aq.)}$ ......(1)

$2K(Fe,Mg,Ti)_3AlSi_3O_{10}(OH)_2 + 4H^+ + 12O^{2-} \rightarrow (Fe,Mg,Ti)_5Al_2Si_3O_{10}(OH)_8 + 3SiO_2 + 6TiO_2 + (Fe,Mg)^{2+} + 2K^+$ ......(2)
biotite   fluid   chlorite   quartz   rutile   (aq.)

$2Ca_2(Mg,Fe,Al)_5Si_8O_{22}(OH)_2 + 6H_2O + 4CO_2 + 3O_2 \rightarrow 2(Fe,Mg)_5Al_2Si_3O_{10}(OH)_8 + 4CaCO_3 + 10SiO_2$ ....(3)
hornblende   fluid   chlorite   calcite   quartz

$(Fe,Mg)_3Al_2(SiO_4)_3 + 2K(Fe,Mg,Ti)_3AlSi_3O_{10}(OH)_2 + H^+ + 2O^{2-} \rightarrow (Fe,Mg,Ti)_5Al_2Si_3O_{10}(OH)_8 + 3KAl_3Si_3O_{10}(OH)_2 + 3SiO_2$ ....(4)
garnet   biotite   fluid   chlorite   muscovite   quartz

The hydrothermal biotite might be derived from original metamorphic phases by means of fluid-rock interaction. Such derivation suggests introduction of CO_2-bearing fluids, as follows:

$2Ca_2(Mg,Fe,Ti)_4Al_2Si_7O_{22}(OH)_2 + 2(Fe,Mg)_3Al_2(SiO_4)_3 + 8CO_2 + 2H_2O + 4K^+ + 7O_2 \rightarrow$
hornblende   garnet
$2K(Fe,Mg,Ti)_3AlSi_3O_{10}(OH)_2 + 2KAl_3Si_3O_{10}(OH)_2 + 4CaMg(CO_3)_2 + 2TiO_2 + 4Fe_2O_3 + 8SiO_2$ ......(5)
biotite   sericite   dolomite   rutile   hematite quartz
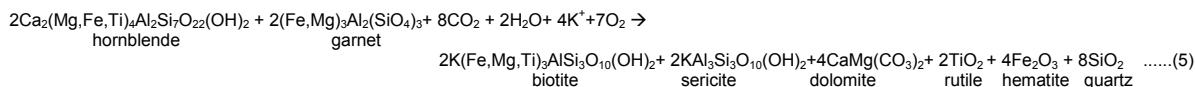
Accordingly, the subordinate occurrence of the hydrothermal biotite in the alteration zones can be explained by the limited abundance of hornblende in the host rocks. The iron released by such reactions might be fixed by the formation of ferro-dolomite, and sulphide minerals.

5.4.2 The transitional stage

The transitional stage is characterized by carbonatization and sulphidation of the ferromagnesian silicates in the host rocks. Time relationship between sulphidation and carbonatization is not clear, since sulphides and carbonate-rich domains intermingle and overlap with each other. However, the occasional presence of sulphide-rich veinlets traversing the carbonate domains suggests that carbonatization is probably earlier.

$4CaAl_2Si_2O_8 + Ca_2(Mg,Fe)_4Al_2Si_7O_{22}(OH)_2 + 4CO_2 + 3H_2O \rightarrow 2Ca_2(Fe,Mg)Al_2Si_3O_{12}(OH) + 2Ca(Fe,Mg)(CO_3)_2 + Fe_2O_3 + 9SiO_2 + 6Al(OH)^{2+} + 2O_2$
plagioclase   hornblende   fluid   epidote   Fe-dolomite   hematite quartz   (aq.)
....(6)
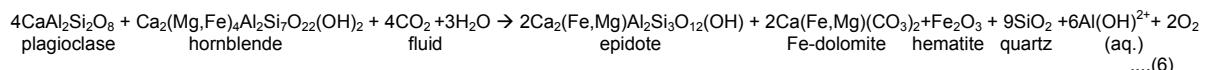
The association of chlorite and iron sulphides with hydrothermal quartz is consistent with the following chloritization reaction:

$2K(Mg,Fe)_3(AlSi_3O_{10})(OH,F)_2 + 4H^+ + 2H_2S^- \rightarrow (Mg,Fe)_5Al(AlSi_3O_{10})(OH)_8 + 3SiO_2 + FeS_2 + 2K^+ + 4F^-$ ....(7)
biotite   fluid   chlorite   quartz   pyrite   aq.
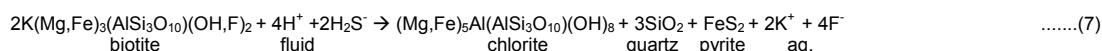
The change from chlorite or chlorite-calcite (products of reaction 3) to sericite+ankerite is consistent with microscopic observations, and can be inferred as a result of reactions involving addition of CO_2 and K^+ and release of H^+:

$3(Fe,Mg)_5Al_2Si_3O_{10}(OH)_8 + 15CO_2 + 2K^+ + 8H_2O \rightarrow 2KAl_3Si_3O_{10}(OH)_2 + 15Ca(Mg,Fe)(CO_3)_2 + 3SiO_2 + 32H^+$ (aq.) ....(8)
chlorite   fluid   sericite   ankerite   quartz

$3(Fe,Mg,Ti)_5Al_2Si_3O_{10}(OH)_8 + 15CaCO_3 + 15CO_2 + 2K^+ + 14.5O_2 \rightarrow 2KAl_3Si_3O_{10}(OH)_2 + 15Ca(Mg,Fe)(CO_3)_2 + 15TiO_2 + 3SiO_2 + 8H_2O + 4H^+$
chlorite   calcite   fluid   sericite   ankerite   rutile   quartz   fluid
........(9)
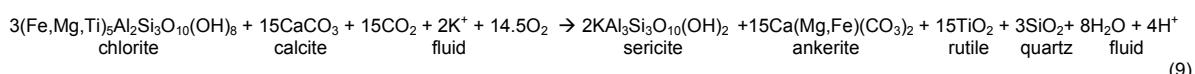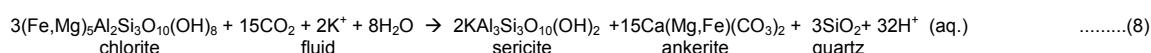
The presence of biotite relics in the intermediate alteration zone implies incomplete transformation, if chloritization has taken place according to the following paragenesis:

$$K(FeMg)_3AlSi_3O_{10}(OH)_2 + (Mg, Fe)_5Al_2Si_3O_{10}(OH)_8 + 8CaCO_3 + 8CO_2 \rightarrow 2KAl_3Si_3O_{10}(OH)_2 + 8Ca(Fe,Mg)(CO_3)_2 + 3SiO_2 + 4H_2O$$
biotite   chlorite   calcite   sericite   ankerite   quartz
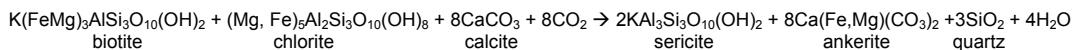
Formation of occasional fluorapatite is likely the result of remobilization of phosphorus in the host rocks and addition of fluorine from the fluid (reaction 7):

$$(Fe,Mg)_5Al_2Si_3O_{10}(OH)_8 + 10CO_2 + 10Ca^{2+} + 3PO_4^{3-} + F^- \rightarrow Ca_5(PO_4)_3F + 5Ca(Fe,Mg)(CO_3)_2 + 3SiO_2 + 3H_2O + 6O_2 + 2Al(OH)^{4+} \quad ....(10)$$
chlorite   fluid   fluorapatite   carbonate   quartz   (aq.)
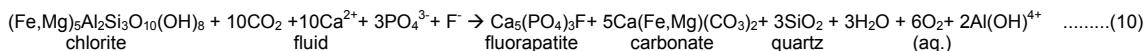
Sulphidation may be attributed to the conversion of biotite to sericite in presence of H_2S, which is evident by the presence of thin envelope of sericite-chlorite adjacent to the sulphide-rich/carbonatized zones, and around the quartz-pyrite veinlets. These relationships may be expressed as follows:

$$3K(Fe,Mg,Ti)_3AlSi_3O_{10}(OH)_2 + 18H_2S + 10O_2 \rightarrow KAl_3Si_3O_{10}(OH)_2 + 9FeS_2 + 3SiO_2 + 9TiO_2 + 9Mg^{2+} + 2K^+ + 20H_2O \quad ....(11)$$
biotite   fluid   sericite   pyrite   quartz rutile   (aq.)
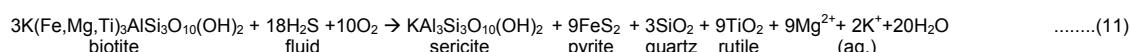
Sulphidation might also has taken place by oxidation of chlorite or magnetite by H_2S-bearing solutions.

$$(Fe,Mg,Ti)_5Al_2Si_3O_{10}(OH)_8 + 10H_2S + 8O_2 \rightarrow 5(Fe,Mg)S_2 + 3SiO_2 + 5TiO_2 + 10H_2O + 2Al(OH)^{2+} \quad ......(12)$$
chlorite   fluid   pyrite   quartz rutile   (aq.)

$$2CaMg(CO_3)_2 + 4Fe_3O_4 + 4H_2S \rightarrow 2Ca(Fe,Mg,Mn)(CO_3)_2 + 2FeS_2 + 4Fe_2O_3 + 4H_2O \quad ....(13)$$
dolomite   magnetite   ankerite   pyrite   hematite
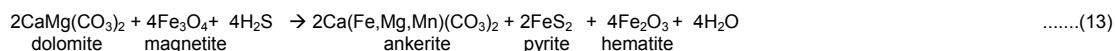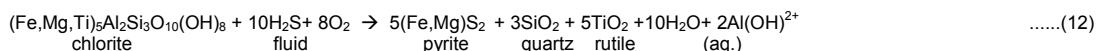
Alternatively, if HS^- was the main sulphur species in the solution instead of H_2S, the pyrite forming reaction may directly involve acid-base equilibria:

$$3K(Fe,Mg,Ti)_3AlSi_3O_{10}(OH)_2 + 18HS^- + 5.5O_2 \rightarrow KAl_3Si_3O_{10}(OH)_2 + 9FeS_2 + 3SiO_2 + 9TiO_2 + 11H_2O + 9Mg^{2+} + 2K^+$$
biotite   fluid   sericite   pyrite   quartz rutile   (aq.)

$$(Fe,Mg)_5Al_2Si_3O_{10}(OH)_8 + 10HS^- + 3.5O_2 \rightarrow 5FeS_2 + 3SiO_2 + 5TiO_2 + 9H2O + 5Mg^{2+}$$
chlorite   fluid   pyrite   quartz   rutile   (aq.)
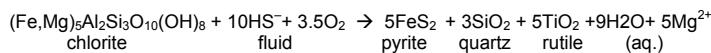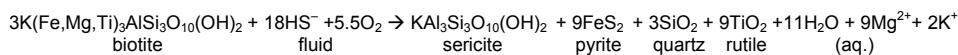
The last two equations are redox reactions (i.e. S^{2-} is oxidized to S^-) and, therefore, tend to reduce the interacting fluids particularly where the fluid/rock ratio is low, thus providing a favourable conditions for gold deposition (Phillips and Groves, 1983). However, the abundance of CO_2 in the solution, represented by widespread carbonate suggests H_2CO_3, CO_3^{2-}, $H_2CO_3^-$ and not H_2S, HS^-, S equilibria controlled the pH. In such case, Phillips and Groves (1984) considered that pyritization is not directly affect the gold solubility via pH changes, but may operate through redox reactions. The result is a bleached ankerite+sericite+quartz-rich zone with discrete gold blebs. A zone with these characteristics has been identified in the vicinity of the auriferous quartz veins in the Um El Tuyor mine area.

5.4.3 The late (advanced) stage

A sericite-ankerite-albite-quartz assemblage is typical for the advanced hydrothermal stage in the Um El Tuyor mine area. Sericitic alteration is indicated by the complete substitution of chlorite and biotite by sericite and quartz. This substitution can be explained by a reaction involves H^+ release:

$$3(Mg, Fe)_5Al_2Si_3O_{10}(OH)_8 + 2K^+ + 2H_2O \rightarrow 2KAl_3Si_3O_{10}(OH)_2 + 3SiO_2 + 15(Fe, Mg)^{++} + 26H_2O + 3H^+ \qquad ....(14)$$
$$\text{chlorite} \qquad\qquad \text{fluid} \qquad\qquad \text{sericite} \qquad\qquad \text{quartz} \qquad (aq.)$$
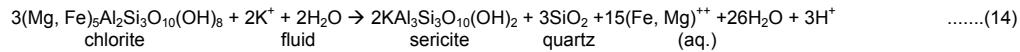
or if Al^{3+} cations were present in the fluid, the reaction can balanced as follows:

$$Mg_5Al_2Si_3O_{10}(OH)_8 + K^+ + Al^{3+} + 6H^+ \Leftrightarrow KAl_3Si_3O_{10}(OH,F)_2 + 5Mg^{2+} + 6H_2O$$
$$\text{chlorite} \qquad\qquad \text{fluid} \qquad\qquad \text{sericite} \qquad\qquad (aq.)$$
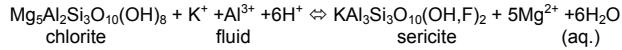
Locally, cation-exchange reactions between K-bearing mineral species (i.e. sericite) and the circulating fluids promoted deposition of albite, favoured by the relatively high $a_{Na}+ / a_K+$ in the fluid at higher temperature (Audétat et al. 1998). A chemical reaction for albitization of a K-bearing mineral species can be expressed as follows:

$$2KAl_3Si_3O_{10}(OH)_2 + Fe_3O_4 + 6H_2S + 4SiO_2 + 2Na^+ + 2O_2 \rightarrow 2NaAlSi_3O_8 + 2Al_2Si_2O_5(OH)_4 + 3FeS_2 + 2K^+ + 4H_2O \qquad ....(15)$$
$$\text{sericite} \quad \text{magnetite} \qquad \text{fluid} \qquad\qquad\qquad \text{albite} \qquad\qquad \text{kaolinite} \qquad \text{pyrite} \qquad (aq.)$$

$$KAl_3Si_3O_{10}(OH)_2 + 6SiO_2 + 3Na^+ \rightarrow 3NaAlSi_3O_8 + K^+ + 2H^+ \qquad ....(16)$$
$$\text{sericite} \qquad\qquad\qquad\qquad \text{albite}$$
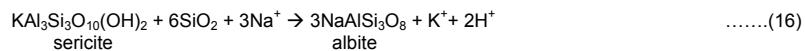
Circulation of cations released from the last two reactions would facilitate the development of additional sericite at the expense of chlorite relics (reaction no. 14).

More or less contemporaneous with the aforementioned reactions, another important process has operated side by side to form sulphides by reduction of magnetite. The latter might locally have proceeded to convert all the magnetite to pyrite, but the presence of magnetite relics in the examined samples may indicate disturbing and/or inhibiting the reaction to complete due to the presence of CO_2-fluid in the hydrothermal system.

$$2Fe_3O_4 + 3H_2S \rightarrow 3FeS_2 + 2H_2O + 0.5O_2 \qquad ....(17)$$

$$Fe_3O_4 + 2H^+ + 6HS^- \rightarrow 3FeS_2 + 4H_2O$$
$$\text{magnetite} \qquad \text{fluid} \qquad \text{pyrite} \qquad \text{fluid}$$
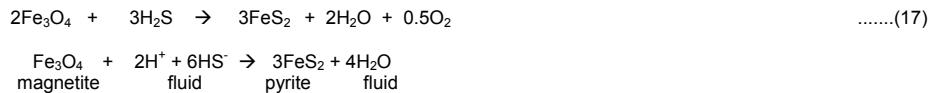
Reduction of CO_2 on the magnetite surface might have initiated precipitation of graphite.

$$4Fe_3O_4 + CO_2 \rightarrow 6Fe_2O_3 + C \qquad ....(18)$$
$$\text{magnetite} \quad \text{fluid} \qquad \text{hematite} \quad \text{graphite}$$

According to the last mentioned chemical reaction, only one molecule of graphite could be derived from four molecules of magnetite. This gives explanation for the scarcity of magnetite in the altered rocks compared to the unaltered host schists and, therefore, the abundance of graphite in the wallrocks. Further, it can explain the presence of graphite in the hematized domains in the altered rocks.

Finally, a phase of local argillic alteration produced kaolinite from albite, sericite and/or detrital K-feldspar by hydration as follows:

$$2NaAlSi_3O_8 + H_2O + 2H^+ \rightarrow Al_2Si_2O_5(OH)_4 + 4SiO_2 + 2Na^+ \qquad ....(19)$$
$$\text{albite} \qquad\qquad \text{fluid} \qquad\qquad \text{kaolinite} \qquad \text{silica} \qquad (aq.)$$

$$2KAl_3Si_3O_{10}(OH)_2 + 2H_2O + 2H^+ \rightarrow Al_4Si_4O_{10}(OH)_8 + 2SiO_2 + 2K^+ + 2Al(OH) + O_2 \qquad ....(20)$$
$$\text{sericite} \qquad\qquad\qquad \text{fluid} \qquad\qquad \text{kaolinite} \qquad \text{silica} \qquad (aq.)$$

$$2KAlSiO_3O_8 + H_2O + 2H^+ \rightarrow Al_2Si_2O_5(OH)_4 + 4SiO2 + 2K^+ \qquad ....(?)$$
$$\text{K-feldspar} \qquad \text{fluid} \qquad\qquad \text{kaolinite} \qquad \text{silica} \qquad (aq.)$$
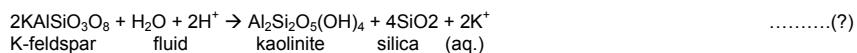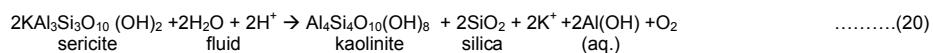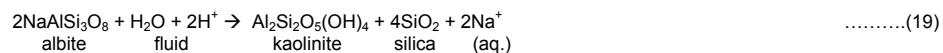
5.5 Mineral pH and redox buffers

The pH of the solution changes through rock buffer reactions in response to the exchange of ions between the solution and the primary minerals of the wallrocks. According to the aforementioned alteration reactions and stages, the present model assumes that interaction between the pelitic wallrocks and a weakly acidic solution resulted in an overall increase in pH as the rock neutralizes the solution. This pH change might have occurred when the aqueous H^+ ion consumed and Na^+ and Ca^{2+} cations released (Giggenbach, 1987, 1988):

$$3Na_2CaAl_4Si_8O_{24} + 8H^+ + 4K^+ \rightarrow 4KAl_3Si_3O_{10}(OH)_2 + 12SiO_2 + 6Na^+ + 3Ca^{2+}$$
plagioclase   sericite   quartz

$$2K(Fe,Mg,Ti)_3AlSi_3O_{10}(OH)_2 + 4H^+ +12O^{2-} \rightarrow (Fe,Mg,Ti)_5Al_2Si_3O_{10}(OH)_8 + 3SiO_2 + 6TiO_2 + (Fe,Mg)^{2+} + 2K^+$$
biotite   fluid   chlorite   quartz   rutile   (aq.)

$$2KAl_3Si_3O_{10}(OH)_2 + 2H_2O + 2H^+ \rightarrow Al_4Si_4O_{10}(OH)_8 + 2SiO_2 + 2Al(OH) + O_2 + 2K^+$$
sericite   fluid   kaolinite   quartz   (aq.)
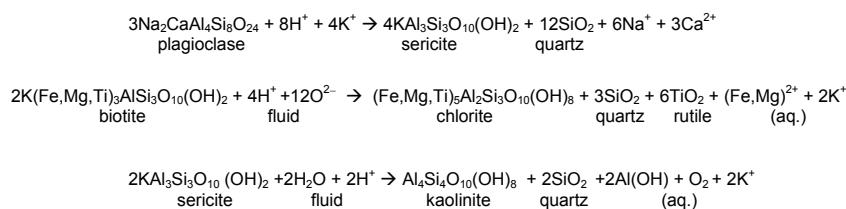
A pH increase through rock buffer reactions might have also occurred through replacement of primary hornblende by chlorite and carbonate (c.f. Scott,1988):

$$2Ca_2(Mg,Fe,Al)_5Si_8O_{22}(OH)_2 + 6H_2O + 4CO_2 + 4O_2 \rightarrow 2(Fe,Mg)_5Al_2Si_3O_{10}(OH)_8 + 4CaCO_3 + 10SiO_2$$
hornblende   fluid   chlorite   calcite   quartz
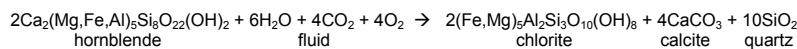
After an early increase, pH has likely decreased during the late transitional and the advanced stages of alteration. This change could be the effect of muscovite/sericite precipitation, which consumed K^+ and silica, and concentrated H^+ until muscovite saturated.

$$3(Fe,Mg,Ti)_5Al_2Si_3O_{10}(OH)_8 + 15CaCO_3 + 15CO_2 + 2K^+ + 14.5O_2 \rightarrow 2KAl_3Si_3O_{10}(OH)_2 +15Ca(Mg,Fe)(CO_3)_2 + 15TiO_2 + 3SiO_2 + 8H_2O + 4H^+$$
chlorite   calcite   fluid   sericite   ankerite   rutile   quartz   fluid

$$KAl_3Si_3O_{10}(OH)_2 + 6SiO_2 + 3Na^+ \rightarrow 3NaAlSi_3O_8 + K^+ + 2H^+$$
sericite   albite
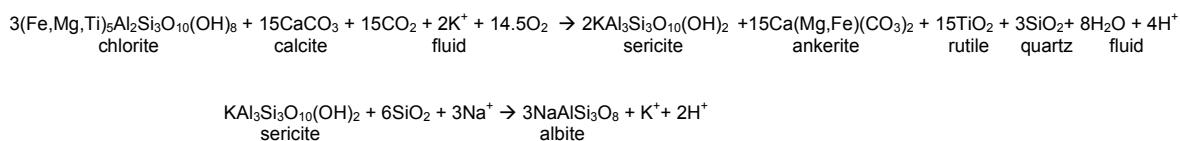
However, dissolution of muscovite and presence of CO_2 caused the failure of this buffer. As a result kaolinite formed at the final stages of alteration.

On the other hand, the redox state of the system might have been controlled by two mineral equilibria that are namely magnetite-pyrrhotite and pyrrhotite-pyrite equilibria, with decreasing water/rock ratios.

$$0.2Fe_3O_4 + 0.6HS^- = 0.6FeS + 0.3H_2O + 0.5O_2 \qquad \text{reduction of Fe (early stages)}$$

$$FeS + H_2S(g) + 0.5O_2 = FeS_2 + H_2O \qquad \text{oxidation of Fe (transitional to late stages)}$$
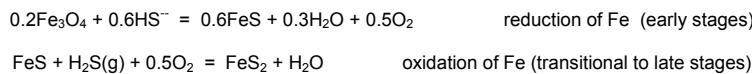
Release of more H_2O during the transitional and late alteration stages has led sericitization to proceed and the result is a pervasive, auriferous sericitic alteration.

CHAPTER 6

FLUID INCLUSION STUDIES

6 FLUID INCLUSION STUDIES

6.1 Introduction

Fluid inclusion petrography and microthermometry were carried out on seven double polished thick sections from the main auriferous quartz veins in the Um El Tuyor mine area. These studies are aimed at assessing the nature and evolution of the mineralizing fluids and to consider the physico-chemical parameters which controlled gold deposition in regard to the regional metamorphic and magmatic framework of the country rocks in the study area. The timing of fluids has been studied by examining relationships between fluid inclusions, their host mineral, geometry of the host microstructures and location of ore minerals.

Under conditions of intermediate temperatures, brittle and ductile deformation, the rates of dynamic recrystallization may exceed rates of recovery, destroying the primary depositional features and producing abundant secondary and pseudosecondary fluid inclusions along intragranular and transgranular fractures. This paragenesis is manifested in Um El Tuyor vein quartz by undulose extinction and serrated grain boundaries with variable development of sub-grains. Primary inclusions are, however, preserved in the least-deformed domains at some distance from planes of strain accommodation (e.g. Gebre-Mariam et al., 1991; Peters, 1993).

6.2 Inclusion types and modes of occurrence

Deformation and recrystallization processes in Um El Tuyor auriferous quartz veins are intensive in places or limited in others, as indicated by the moderate to strong undulose extinction, local mortar texture and deformation lamellae. As a result, a strict application of the concept of primary and secondary inclusions (after Roedder, 1984) is not simple. Deformation might have caused post-entrapment modifications, such as necking-down, partial or total leakage, selective leaching or diffusion of some components. To minimize the effect of post-entrapment modifications, inclusions suspected to have been affected by such modifications are not considered. The cores of the host quartz in quartz-carbonate veins show less deformed domains containing isolated and/or clustered randomly distributed inclusions. These inclusions are considered as the nearest to the ore fluid and the closest to the primary inclusions in the sense of Roedder (1984) and Wilkins (1990). Inclusions have these characteristics were selectively chosen for the microthermometric study.

In the auriferous quartz-carbonate and laminated quartz veins, quartz grains are typically fluid inclusion-rich. The investigated fluid inclusions are compositionally grouped into carbonic [$CO_2(\pm CH_4 \pm N_2)$-rich], aqueous-carbonic [H_2O-NaCl-$CO_2(\pm CH_4 \pm N_2)$], and aqueous [low salinity H_2O–NaCl]. The aqueous-carbonic and aqueous inclusions are commonly observed in the quartz-carbonate veins, whereas the carbonic inclusions are by far the dominant or virtually the sole fluid inclusions in most parts of the auriferous laminated quartz and quartz-carbonate veins.

Some other mono-phase carbonic inclusions are very common in both laminated and quartz-carbonate veins, occurring as planar arrays of very tiny inclusions with elongate to rounded shapes. These arrays crosscut populations of the carbonic and aqueous-carbonic inclusions, therefore considered as (later) secondary inclusions. The abundance of these inclusions is directly related to proximity to the micro-fissured domains and sealed cracks. In this approach, due to their very small size (<5 µm) and since they show no relation to the gold mineralization events, these inclusions are not further considered.

6.2.1 Fluid inclusions in the quartz-carbonate veins

In the auriferous quartz-carbonate veins, the carbonic inclusions vary in shape from regular negative crystals to irregular, and in size from ~2 to 15 µm. They are commonly two-phase inclusions (liquid and vapour) at room temperature, but occasionally mono-phase inclusions (liquid or vapour) are observed. The two-phase inclusions display mostly liquid>vapour vol. % (Figs. 6.1, 6.2). In some cases, these inclusions display sharp boundaries, which might be due to presence of a thin H_2O film along their inner walls. The degree of filling (volumetric proportion of the aqueous phase relative to the total inclusion volume: DF $=V_{H_2O}/V_t$) is mostly 0.70 to 0.80. Generally, they form intergranular clusters, in which the inclusions are randomly distributed (Fig. 6.1). These inclusions also occur as planar arrays or sharp trails commonly confined to the recrystallized domains in quartz veins. The clusters, planar arrays and trails of these inclusions situated in domains displaying less deformation are considered as earlier generations of inclusions, probably of primary or pseudosecondary origin, whereas the intragranular trails are identified as secondary in origin (c.f. Roedder, 1984).
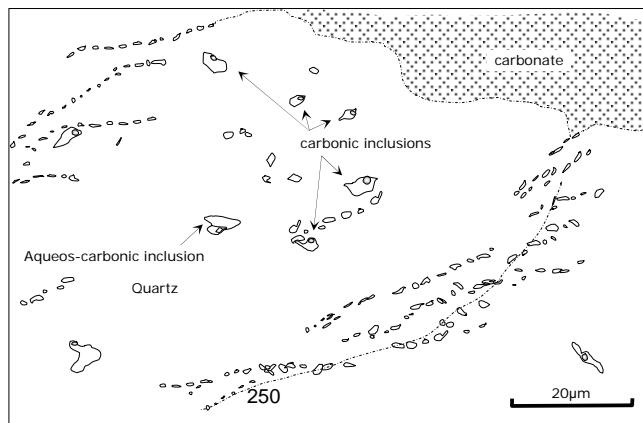
Fig. (6.1): Distribution of the carbonic inclusions in the auriferous quartz carbonate veins of the Um El Tuyor deposit. The hand-drawn sketch is based on microscopic observations.

The aqueous-carbonic inclusions have been observed only in the quartz-carbonate veins. These inclusions exhibit a variety of polygonal forms and range from 3 to 15 µm in size. They are two-phase or three-phase inclusions (vapour CO_2 + liquid H_2O ± liquid CO_2). In case of three-phase inclusions, two immiscible liquids (liquid CO_2 + liquid H_2O) and a small vapour bubble are usually observed (Fig. 6.3). The degree of filling in a single population is significantly variable (~0.45 up to 0.80), suggesting heterogeneous entrapment. In domains rich in the aqueous-carbonic inclusions, the carbonic inclusions tend to occur as sets of diffuse planar arrays or sharp trails, restricted to the interiors of quartz grains or transecting their borders.
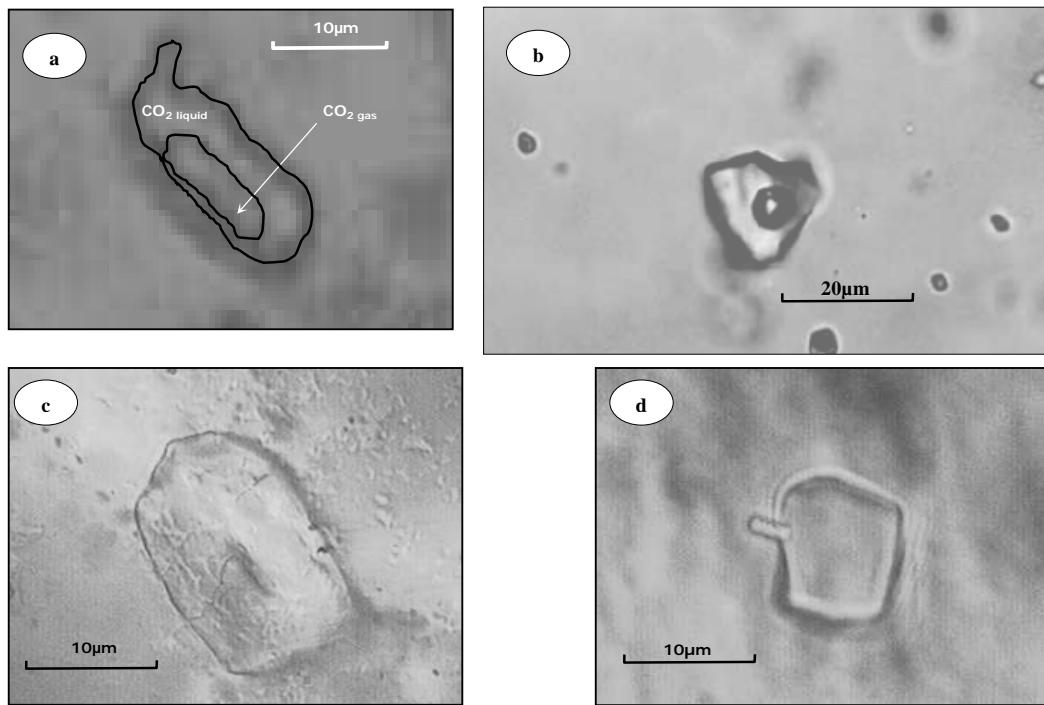
Fig. (6.2): Photomicrographs of two-phase (L>V) carbonic inclusion in quartz carbonate veins (a, b), and of monphase carbonic inclusions in laminated quartz veins (c, d).
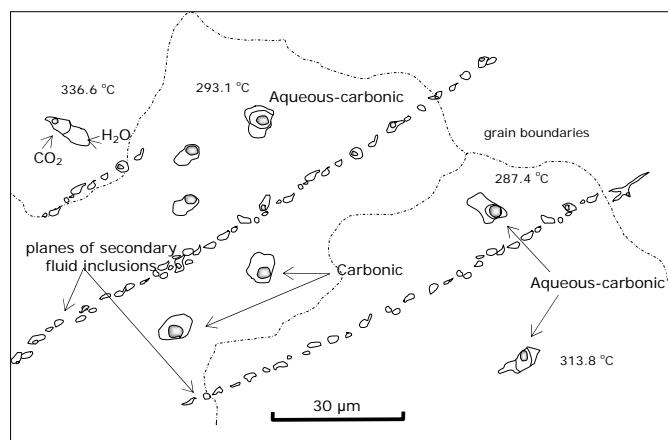
Fig. (6.3): Sketch drawing showing the distribution of the aqueous-carbonic inclusions in the auriferous quartz-carbonate veins. The given numbers indicate the total homogenization temperatures of the nearby inclusions

The aqueous H_2O–NaCl inclusions are scarce, but if present, they can easily be identified by their transparent appearance. Morphologically, they show variations from negative-crystal shapes to subhedral (especially the smaller inclusions), ovoid, spheroidal, tubular or irregular forms, and vary in size from 2 to 10 μm. At room temperature, two-phase inclusions (liquid and vapour) of this type show a range of 0.70-0.90 degree of filling (Fig. 6.4). In some cases, trapping temperatures of some of these inclusions are difficult to assess because they invariably decrepitated before total homogenization. Occasionally, non-visual fraction of CO_2 phase (less than 10 vol. %) in some of these inclusions might have been the responsible for increasing the total vapour-liquid homogenization of these inclusions.
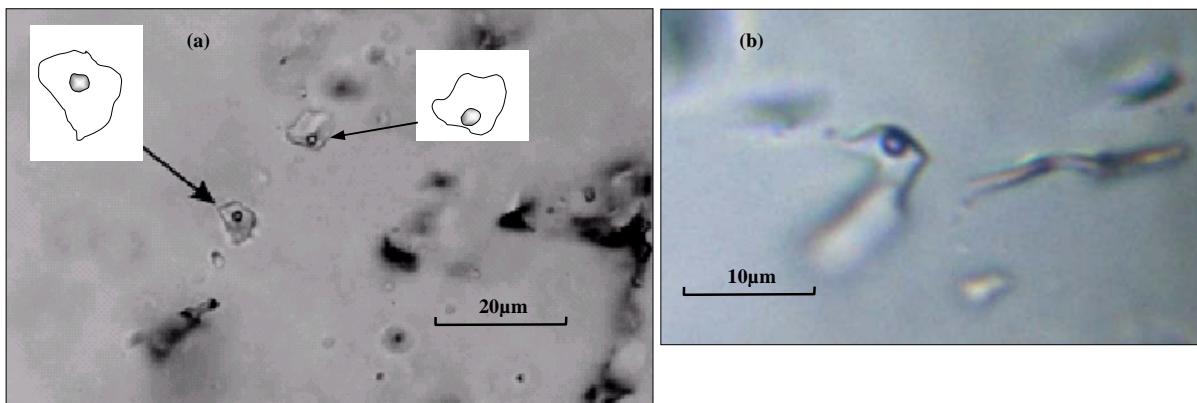
Fig. (6.4): a) & b) Photomicrographs of pseudosecondary aqueous inclusions (L>V) in the auriferous quartz carbonate veins from Um El Tuyor deposit.

6.2.2 Fluid inclusions in the laminated quartz veins

In regard to distribution and characteristics of the individual and grouped fluid inclusion planes at room temperature, there is no evidence for any pristine primary fluid inclusions in the laminated quartz veins. However, some of these inclusions show the features described for the pseudosecondary inclusions elsewhere (Roedder, 1984, Shepherd et al., 1985). The carbonic inclusions are by far the most predominant in the laminated quartz veins. They are mostly small in size (<8 µm), but some of them attain a size of 15 µm. In shape, they are mostly oval to round, but the larger inclusions are irregular. Many of these fluid inclusions are aligned sub-parallel to the shear planes in the wallrocks. These inclusions are usually two phase (liquid CO_2 > vapour CO_2) and mono-phase (liquid CO_2 or vapour CO_2) at room temperature. The mono-phase inclusions display two phases if cooled to 10^oC or below. In the two phase inclusions, the degree of fill is ~0.80 on average. These inclusions occur as planar arrays or sharp intergranular trails commonly confined to the recrystallized domains in quartz veins.

Although not primary, these pseudosecondary and secondary fluid inclusions might maintain ambient fluids entrapped when crystal growth took place during shearing. Therefore, relevant information about conditions of entrapment, and sequence of deformation events could be derived from these inclusions, especially when considering the shear-related nature of the auriferous quartz veins in Um El Tuyor mine area.

6.3 Microthermometry

After a relative chronology of fluid inclusions was established using the criteria of Roedder (1984), the microthermometric measurements have been carried out. These measurements have been achieved using a Linkam THM 600 heating/freezing stage with a thermal control unit TMS-93 mounted on an Olympus binocular microscope. The analytical details and microthermometric data are given in Appendix F.

The abbreviations used in the present context are $T_{m\ CO2}$ = carbon dioxide melting temperature (final disappearance of solid CO_2 during heating); $T_{m\ clat}$ = melting of the clathrate; $T_{h\ CO2}$ = liquid-vapour homogenization of CO_2, when vapour disappears; $T_{h\ total}$ = total homogenization of CO_2 and aqueous salt solution in the aqueous-carbonic inclusions; T_h = homogenization of the liquid+vapour aqueous inclusions; and $T_{m\ ice}$ = melting of ice in the aqueous salt solution. The latter has been distinguished only in the aqueous

inclusions, generally into liquid. The obtained data are used for identifying the gas phase, determination of the fluid salinity, composition and *P-T* conditions of entrapment.

Total freezing of the CO_2-bearing inclusions typically required supercooling to -110°C, whereas the aqueous inclusions were usually completely frozen below -60°C. Homogenization of CO_2 in the carbonic inclusions occurred mainly into the liquid phase. CO_2 final melting temperatures ($T_{m\,CO2}$) vary from 0° to ~3° C below the typical triple point of CO_2 (-56.6^{o}C) (Fig. 6.5). This depression below the triple point of CO_2 suggests the presence of small amounts of dissolved gases in addition to CO_2 in composition of the carbonic and aqueous-carbonic inclusions. If CH_4 is the dissolved gas responsible for depression of CO_2 melting point, graphical methods proposed by Heyen et al. (1982) and (Thiéry et al., 1994) suggests the presence of maximum 14 mol% CH_4 in the CO_2-bearing inclusions (Figs. 6.6a,b). Alternatively, if N_2 is the dissolved gas produced this depression, presence of a maximum of 20 mol% is estimated (Fig. 6.6c).

CO_2 homogenization temperatures ($T_{h\,CO2}$) vary from 3.4 to 28.8^{o}C. The wide range of $T_{h\,CO2}$ suggests that the density of the CO_2-rich phase was highly variable during the entrapment of fluids.

The total homogenization temperatures ($T_{h\,total}$) of some large inclusions could not be obtained due to their decrepitation prior to homogenization. Generally, $T_{h\,total}$ does not appear to vary as a function of inclusion size, and therefore the composition and density of the vein fluid were not differentially influenced by any physio-chemical effects dependent on the surface area (c.f. Binu-Lal et al., 2003).
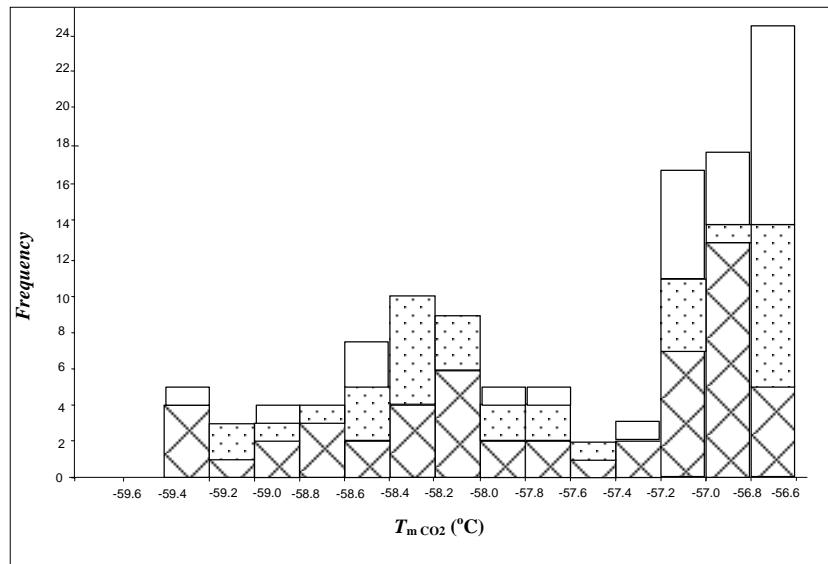
Fig. (6.5): Frequency histogram of the final CO_2 melting temperatures ($T_{m\,CO2}$) in the CO_2-bearing fluid inclusions in the Um El Tuyor auriferous quartz veins. The doted blocks represent the aqueous-carbonic inclusions, hatched boxes refer to the carbonic inclusions in the quartz-carbonate veins, and white blocks refer to the carbonic inclusions in the laminated quartz veins.
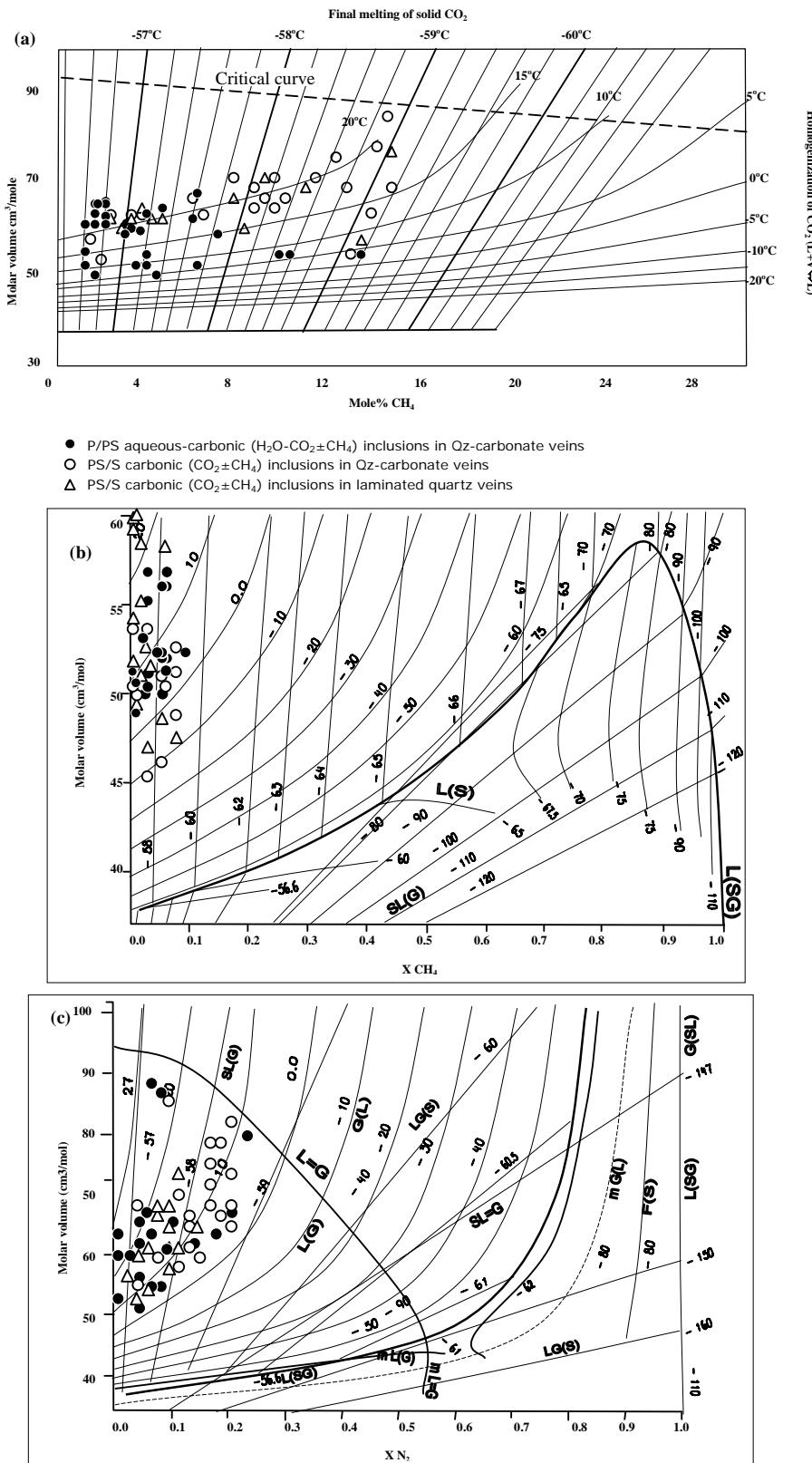
Fig. (6.6): Plots of the investigated carbonic and aqueous-carbonic fluid inclusions on a) V vs. mol % CH₄ diagram (after Heyen et al., 1982), b) VX diagram (V<60 cm³/mole, after Thiéry et al., 1994), calculated for the system CO₂–CH₄, and c) VX diagram calculated for the system CO₂–N₂ for V<100 cm³/mole after Thiéry et al., 1994. (For more details on diagrams b,c see Thiéry et al., 1994).

6.3.1 The carbonic ($CO_2 \pm CH_4 \pm N_2$) inclusions

The variable modes of occurrence (isolated, clustered and trail-bound) displayed by the carbonic inclusions in both, quartz-carbonate and laminated quartz veins in the Um El Tuyor mine, suggests a relative time difference in their formation. In the present work, the isolated and clustered inclusions are considered earlier than trail-bound inclusions (e.g. Touret, 1981).

The carbonic inclusions show a range of -56.6 to -59.3°C for the final melting temperature of CO_2 ($T_{m\ CO2}$; Fig. 6.5, Table F.1, Appendix F). As shown in Fig. 6.7, the partial homogenization ($T_{h\ CO2}$) varies between 3.7 to 28.8°C, which correspond to bulk densities ranging from 0.905 to 0.636 g/cm^3, according to the equation of state of Potter et al. (1978) and Zhang and Frantz (1987). In the investigated samples, the intragrain trail-bound (low T melting) inclusions showed higher $T_{h\ CO2}$ compared to the individual and clustered inclusions.
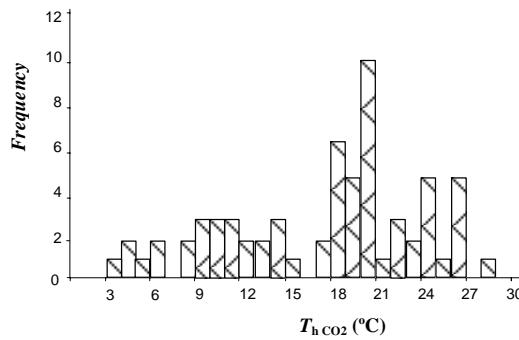
Fig. (6.7): Frequency histogram of $T_{h\ CO2}$ of the carbonic inclusions in the auriferous quartz veins in the Um El Tuyor mine area.

6.3.2 The aqueous-carbonic (H_2O–$CO_2 \pm CH_4 \pm N_2$), inclusions

The aqueous-carbonic inclusions show two, and occasionally three, phases at room temperature (liquid H_2O, vapour $CO_2 \pm$ liquid CO_2). In these inclusions, the aqueous phase, which occupies variable vol.% at room temperature surrounds a CO_2 bubble or occasionally forms a thin film along the walls of the cavity. Within a single quartz grain, the CO_2 always homogenizes into the liquid phase ($T_{h\ CO2}$) in a wide range of temperature from 3.4 to 25.6°C. This range indicates CO_2 densities between 0.907 and 0.702 g/cm^3 (Table F.2; Appendix F).

Total homogenization ($T_{h\ total}$) of the carbonic and aqueous phases in these inclusions occurred between 243.7 and 341.6°C (Fig. 6.8a). In the present work, the wide range of total homogenization temperatures is thought to reflect several episodes of CO_2 phase separation during vein formation, as indicated by textural evidence of repeated fracturing and filling of the veins. Data distribution shows a distinct mode occurs at ~287°C. For this type of inclusions, clathrate melting temperatures $T_{m\ clath}$ range from 5.2° to 9.3°C (Fig. 6.8b), which, if presence of CH_4 and/or N_2 clathrate is neglected, correspond to salinities from 8.7 to 1.4 wt. % $NaCl_{equiv.}$. Plotting of the total homogenization temperatures versus the salinities of the investigated aqueous-carbonic inclusions suggests a positive correlation (Fig. 6.9).
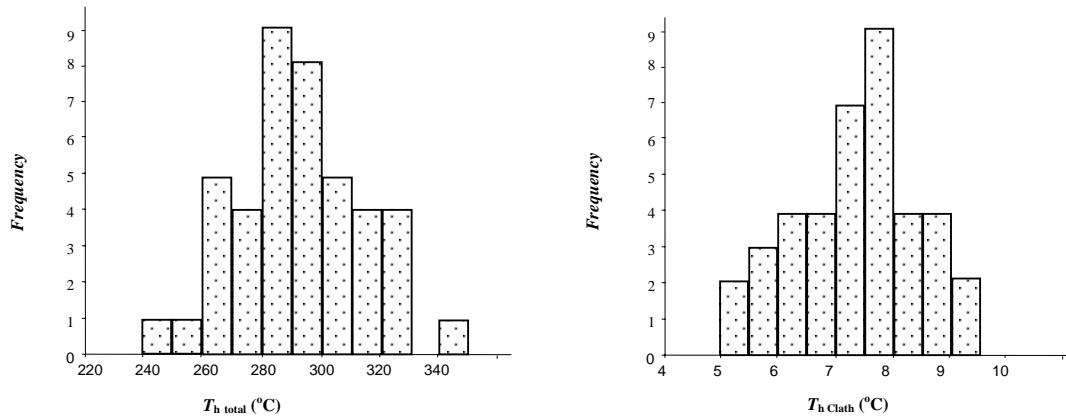
Fig. (6.8): Frequency histogram of: a) total homogenization ($T_{h\ total}$) of the aqueous-carbonic fluid inclusions (mostly L+V= L) in the quartz-carbonate veins. b) melting temperatures of clathrates in the aqueous carbonic fluid inclusions in the quartz-carbonate veins.

A positive correlation occurs between concentration of CO_2 in the aqueous-carbonic inclusions and the total homogenization temperature (Fig. 6.10). This correlation may be taken as indication of phase separation process, since miscibility of H_2O and CO_2 fluids is lower at low temperatures (c.f. Ramboz et al., 1982).
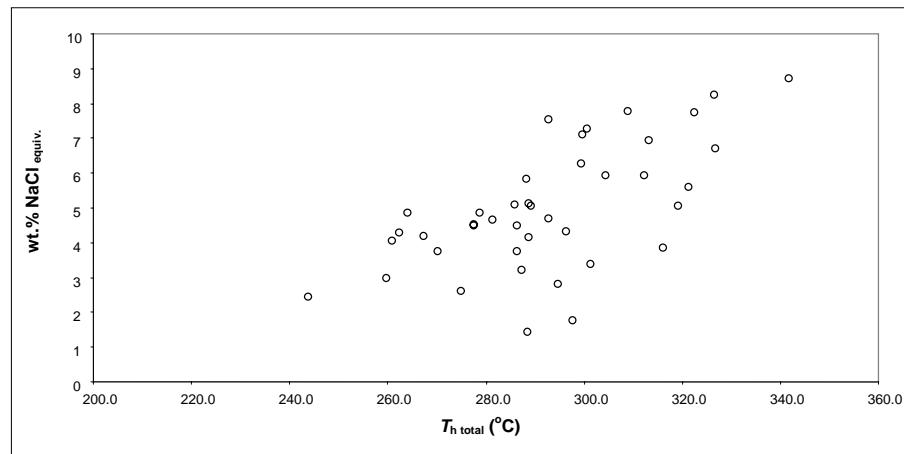
Fig. (6.9): Total homogenization temperature ($T_{h\ total}$) versus salinity diagram for the aqueous–carbonic fluid inclusions in Um El Tuyor auriferous veins.
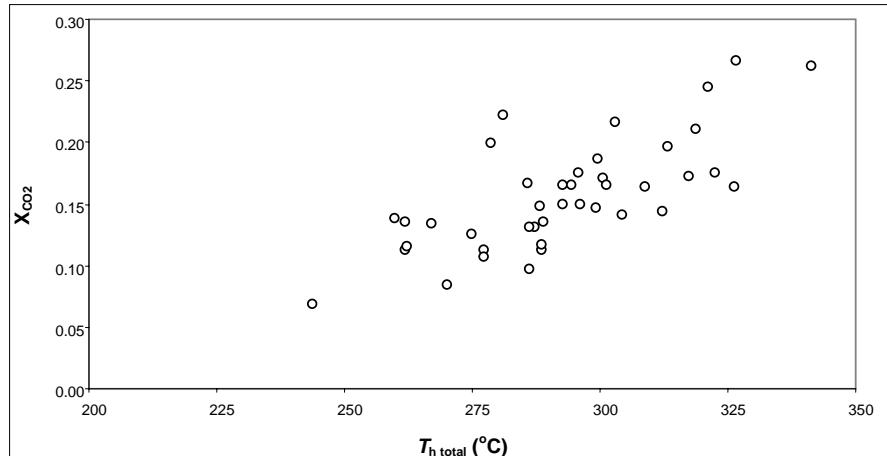
Fig. (6.10): Total homogenization temperature ($T_{h\ total}$) versus X_{CO2} diagram for the aqueous–carbonic fluid inclusions in Um El Tuyor auriferous veins.

6.3.3 The aqueous (H₂O–NaCl) inclusions

In the auriferous quartz-carbonate veins, the aqueous inclusions gave values of $T_{m\ ice}$ of -0.8 to -2.9°C (Fig. 6.11). These inclusions homogenise to the liquid phase at temperatures (T_h) between 143.6 and 254.7°C (Table F.3, Appendix F). On the basis of the equation of state by Potter et al. (1978) and Zhang and Frantz (1987), the determined ranges of $T_{m\ ice}$ and T_h correspond to salinities between 1.23 and 5.07 wt.% NaCl $_{equiv.}$, and bulk fluid densities of 0.99 and 1.02 g/cm³.

The aqueous inclusions have less variable phase proportions and their final homogenization temperatures are generally lower than those of the aqueous-carbonic inclusions. In terms of total homogenization and salinity properties, both boiling and phase separation processes may be expected to produce a spread of data on a T_h – salinity bivariate plot (Fig. 6.12). As a result of adiabatic expansion, the liquid phase may undergo cooling. The presence of dissolved gases will affect the distribution of T_h –salinity data and the trends produced by mixing and boiling processes.
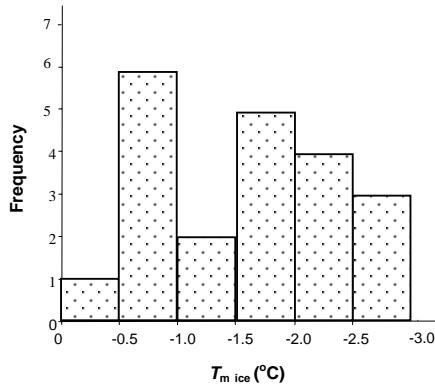
Fig. (6.11): Frequency histogram of the ice melting temperatures ($T_{m\ ice}$) in the aqueous inclusions in the auriferous quartz-carbonate veins.
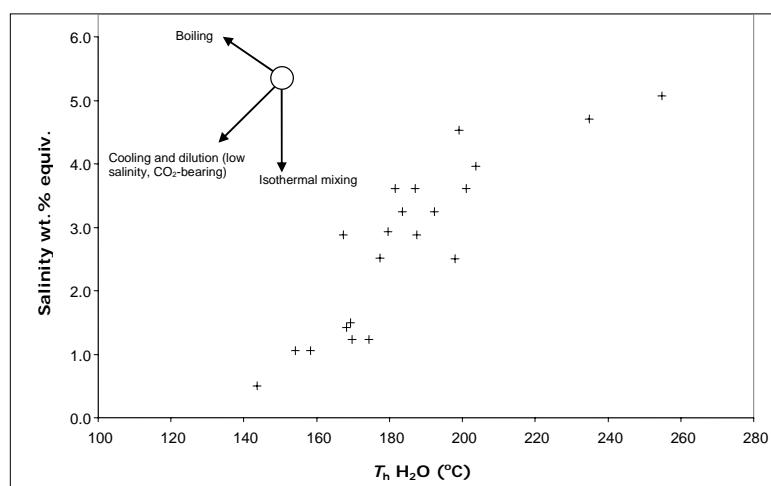
Fig. (6.12): Homogenization temperature T_h vs. salinity (wt% eq. NaCl) of the aqueous inclusions in the quartz-carbonate veins. The typical trends in T_h –salinity space due to various fluid evolution processes are indicated (after Wilkinson, 2001).

6.4 Pressure-temperature estimates

Trapping *P-T* conditions are generally obtained by assuming inclusions to be constant-volume, constant-mass systems and by determining the *P-T* path, which represents the locus of the possible pressure-temperature values at which the inclusion has been formed (Roedder, 1984). The pressure-temperature evolution of the fluid inclusion follows a univariant isochoric-isoplethic curve (isochore), which is independent from the *P-T* evolution of the host rock. This isochore can be calculated by using the appropriate equation of state if composition and density or molar volume of a fluid inclusion is known. In order to estimate the *P-T* conditions of fluid trapping, other independent pressure-temperature data such as mineral assemblages are required (Roedder and Bodnar, 1980). However, immiscibility between aqueous and carbonic fluids in the investigated inclusions derives the opportunity to calculate the pressure-temperature conditions from fluid inclusions only (e.g., Touret, 1981; Holloway, 1981). Estimating the *P–T* conditions of entrapment is made by crossing isochores for the aqueous and carbonic inclusions, assuming that these inclusions represent the end-members of the immiscible fluid. In the auriferous quartz veins of the Um El Tuyor deposit, intersection of isochores for the high density aqueous and carbonic inclusions depicts a maximum temperature of ~340°C at ~1. 5 kbar (Fig. 6.12).

Assuming that the aqueous and carbonic fluids were generated by unmixing of an initially homogeneous fluid phase, the isochores for these fluids should cross the immiscibility surface of the overall system (Pichavant et al., 1982). Figure 6.13 shows that isochores for the three types of fluid inclusions encountered meet this criterion and cross the immiscibility surface of the system (H_2O–21 mol% CO_2–6 wt.% NaCl, after Gehrig, 1980). This system is very similar to composition of the primary aqueous-carbonic inclusions in Um El Tuyor auriferous veins. Crossing is most precisely met by isochores for the high-density CO_2 and the low-salinity (low density) H_2O fluid, which intersect on the critical curve of the H_2O–CO_2-dissolved salt system. This observation, along with intersection of isochore of the aqueous-carbonic with lowest bulk density approximately at the same point, strongly suggests that the aqueous and carbonic fluids were derived from the un-mixing of a homogeneous, low salinity H_2O–CO_2 fluid (H_2O–21 mol% $CO_2(\pm CH_4 \pm N_2)$–6 wt.% NaCl mixture).
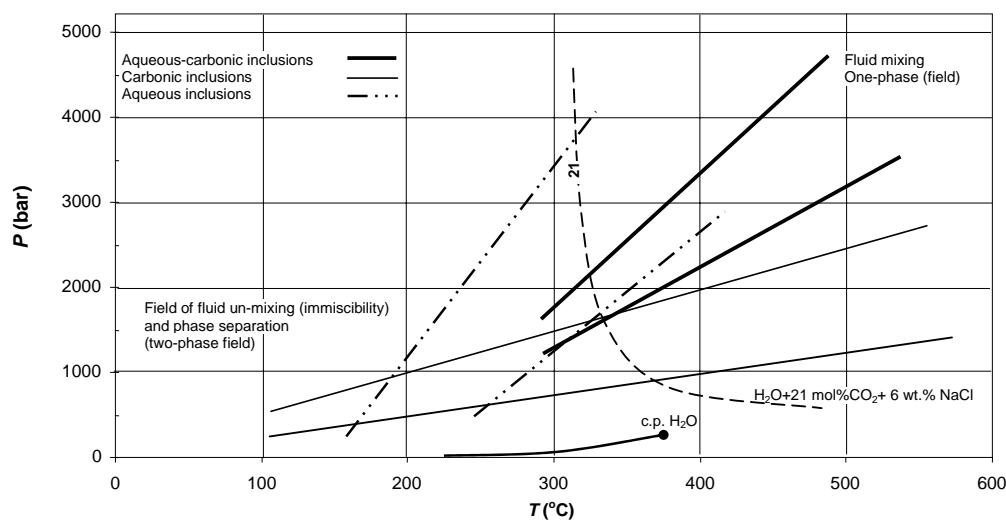
Fig. (6.13): Representative isochores for the highest and lowest density carbonic, aqueous-carbonic and aqueous inclusions in the Um El Tuyor auriferous quartz veins. Also shown is the phase boundary of CO_2-H_2O-NaCl fluids with 6 wt% NaCl and 21.0 mol% CO_2 (broken line, Gehrig, 1980). The heavy line is the liquid-vapour equilibrium curve for H_2O, c.p. is the critical point.

If the coexistence of the aqueous, carbonic and aqueous-carbonic inclusions in the Um El Tuyor auriferous quartz veins is interpreted in terms of simultaneous trapping during fluid unmixing, the point of intersection (340°C and ~1.5 kbar) should be conformable with the total homogenization conditions of the parent aqueous-carbonic inclusions, and fortunately, this is the case in the investigated fluid inclusions. On the other hand, intersection of isochores for the highest and lowest density carbonic inclusions and the isochore for low-salinity aqueous inclusions in the Um El Tuyor auriferous quartz veins define a *P-T* field between ~170-340°C at ~0.9-1.6 kbar, respectively (Fig. 6.13). This wide range of pressure probably represents the total fluid pressure regime within the shear zone from the formation of the auriferous quartz veins to periods of continuous pressure decrease during uplift. Considering the non-realistic, very low fluid entrapment temperature derived from isochores intersection, it is assumed that during the formation of the vein sudden pressure decrease occurred as a consequence of incremental opening of the fissure, followed by filling by newly deposited quartz. Similar studies have shown that this type of evolution is the rule for many hydrothermal veins (Mullis et al., 1994).

6.5 Fluid evolution and gold deposition

The coexistence of the chemically and physically contrasting fluids (e.g. carbonic and aqueous), variable CO_2/H_2O ratios, and scattering of densities and total homogenization temperature are considered as evidence of various processes, including: successive trapping of different fluids (Pichavant et al., 1982), heterogeneous trapping (Ramboz et al., 1982; Diamond, 1994), trapping of fluids during fluctuating pressure conditions (Robert and Kelly, 1987) or different structural levels (Cathelineau et al., 1991), partial mixing followed heterogeneous trapping of two unrelated homogeneous fluids (Anderson et al., 1992), necking-down of inclusions (Allibone et al., 1995), and post-entrapment modifications with variable preferential leakage of H_2O (Crawford and Hollister, 1986; Hollister, 1990; Dubessy, 1994).

Considering that the Au-mineralization in the Um El Tuyor mine area is hosted by deformed rocks, and that the wallrocks and auriferous quartz veins display abundant evidence for ductile deformation (e.g. undulose extinction, recrystallization and sub-grain development), it is doubtful that the early assemblage, carbonic and aqueous–carbonic inclusions have not undergone post-entrapment modifications and/or re-equilibration. However, a vertical trend in the T_h versus salinity bivariant plot (Fig. 6.9), which is a typical evidence for necking down and leakage under heating (Shepherd et al., 1985), has not been recognized.

The primary and secondary modes of occurrence of the carbonic inclusions, and coexistence of inclusions with variable proportions of carbonic and aqueous fluids, variable densities, partial homogenization temperatures, and variable bulk compositions are interpreted in terms of immiscibility and phase separation for the entrapped fluids in the auriferous quartz veins in the Um El Tuyor mine (Ramboz et al., 1982). Further, the occasional decrepitation before total homogenization of some of the aqueous-carbonic inclusions precluded the assumption that the H_2O and CO_2 fluids were homogenous at the time of trapping.

A common way to evaluate possible phase separation is given by Crawford and Hollister (1986) and modified by Walsh et al. (1988), where final homogenization temperatures are plotted as a function of composition (X_{CO2}) and wt.% NaCl $_{equiv}$. (Fig. 6.14). In case of immiscibility, it is expected that the carbonic and aqueous–carbonic inclusions cluster along the high and low X_{CO2} end members, respectively, and close to

the appropriate solvus of the system. The carbonic inclusions define a field in the high X_{CO2} region, along the 0 wt% NaCl $_{equiv.}$ solvus. However, dispersion is not wide. Figure 6.14 suggests that phase separation was the main process during fluid evolution.

The opposite process for producing heterogeneity, by mixing, cannot be completely discarded, but remains more difficult to be justified. In this approach, a correlation between $T_{h\ total}$ and salinity is evocative of fluid mixing in the investigated deposit (Figs. 6.9, 6.12). However, the scarcity of aqueous fluid inclusions associated with the carbonic inclusions, as a compositional continuum between these two end members, may diminish the possibility of mixing (c.f. Diamond, 1994).
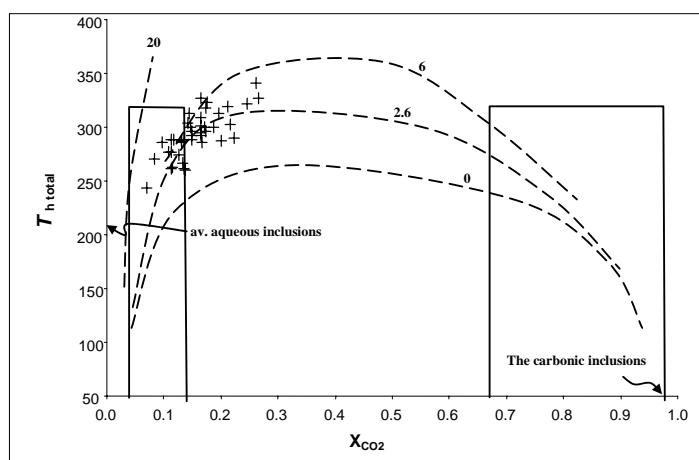
Fig. (6.14): Final homogenization ($T_{h\ total}$) vs. molar fraction (X_{CO2}) diagram of the fluid inclusions in Um El Tuyor auriferous quartz veins, showing the solvi for the CO_2–H_2O system under diverse salinity in wt% NaCl $_{equiv.}$ (references for the solvi in Crawford and Hollister, 1986). The rectangles represent the expected compositional variation in case of immiscibility (fields after Walsh et al., 1988).

Unequivocal petrographic evidences, such as variable deformation of the Um El Tuyor auriferous quartz veins and the small size of the fluid inclusions brought much difficulty in associating fluid inclusions with the fluids responsible for gold mineralization. However, in the present study, no later event with higher P–T conditions, which could have overprinted those recorded by the primary/pseudosecondary carbonic, aqueous-carbonic and aqueous fluid inclusions, was identified. This observation allowed to suggest that data derived from these fluid inclusion assemblages might be related to the gold mineralizing event, and represents the most likely physico-chemical conditions of the gold deposition.

6.6 Conditions of the gold deposition in relation to the general P–T framework of the host rocks

In order to define pressure and temperature conditions under which the fluids precipitated gold, the following constraints must be taken into account: a) Textural relationships in the ore zones demonstrate that the precipitation of the early sulphide assemblage, consisting of arsenopyrite, pyrite, pyrrhotite and sphalerite, was broadly coeval with the deposition of the primary gold. b) In the Fe–Zn–As–S system at 1 bar (Scott, 1983), the isopleths representing the As content in arsenopyrite of the early sulphide assemblage indicated a range of 382-429°C, and a range of 338-365°C for formation temperature of the late sulphide association, with fS_2 being constrained between $10^{-8.6}$ and $10^{-6.6}$ bar, respectively (see Chapter 4). c) The presence of a homogeneous parent fluid (H_2O–CO_2) indicates that P–T conditions were above the two-phase region (Fig. 6.13) for at least a

short time period during fluid entrapment. d) The chlorite geothermometer (Cathelineau, 1988) based on chlorites associated with arsenopyrite, pyrite and gold, indicates a temperature range of 278-346°C for chlorite formation (hydrothermal alteration).

Based on these constraints, it is probably realistic to regard 278°C and 429°C as the lower and upper limits for temperature of gold deposition in the Um El Tuyor mine. Combining these constraints with the *P–T* conditions defined by isochores for the carbonic inclusions with the highest density, a pressure regime of 1.4-2.1 kbar is estimated for gold deposition in Um El Tuyor auriferous quartz veins and wallrocks (Fig. 6.15). This pressure range is equivalent to depths of 5-8 km, under conditions of lithostatic overburden.

Using the temperature ranges estimated for the early and late sulphide assemblages in combination with the *P–T* conditions defined by isochores for the carbonic inclusions commonly exist in quartz intimately associated with the auriferous sulphides (den CO_2=0.82 g/cm^3), a pressure regime of 1.6-2.1 kbar is indicated for the early auriferous sulphide association, whereas the late sulphide assemblage most likely formed in a pressure range of 0.8-1.5 kbar (Fig. 6.15). Similar pressure estimates are indicated by intersection of isochores for the aqueous-carbonic and carbonic inclusions, as representatives of the early and late mineralization phases, with the critical curve of the compositional system (Fig. 6.15). Similarity between formation conditions of the early sulphides and pressures estimated for gold deposition is consistent with the auriferous nature of the early pyrite and arsenopyrite.
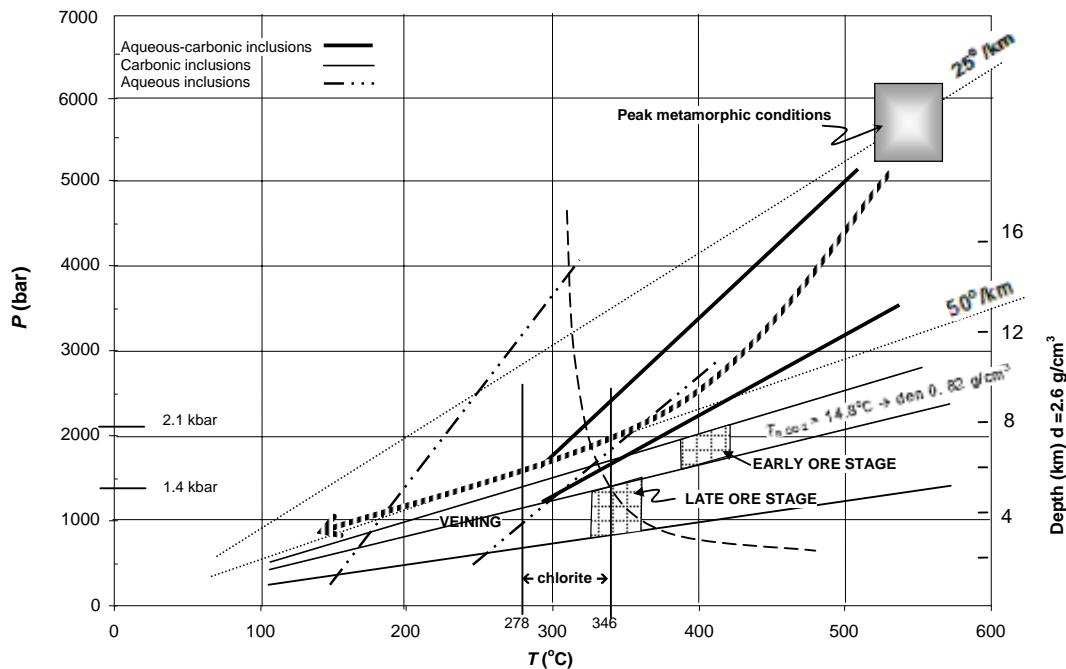
Fig. (6.15): Representative isochores for the fluid inclusions in the Um El Tuyor auriferous quartz veins. The hatched fields represent the temperature range indicated by the early and late sulphide assemblages (Kretschmar and Scott, 1976). Formation temperature range of chlorite associated with the auriferous sulphides disseminated in the mineralized wallrocks is also indicated. The shaded box represents P–T estimates for peak metamorphic conditions of the Um El Tuyor country rocks. The thick, hachured line with an arrowhead depicts a possible post-metamorphic uplift path and incremental opening of the hydrothermal veins. Also shown are the phase boundaries of CO₂-H₂O-NaCl fluids at 6wt% NaCl and 21.0 and 28.5 wt% CO₂ (broken lines, after Gehrig, 1980), and geothermal gradients of 25 and 50°C/km (doted lines). Scale on the right side refers to depth in km at the rock density of 2.6 g/cm³ for lithostatic overburden.

Destabilization of gold-sulphur complexes through interplay of cooling, redox state variation, pH changes, and decrease in sulphur fugacity probably caused the gold deposition.

The data indicate depth of 3–8 km for quartz veining and gold deposition in the Um El Tuyor mine area, which is compatible with crustal conditions of greenschist metamorphism and the brittle–ductile transition. The uplift after peak metamorphism was probably characterized by near-isothermal decompression followed by isobaric cooling (indicated by fluid inclusion textures and variable CO_2 densities).

6.7 Fluid redox state

Since solubility of the metal species in aqueous hydrothermal solutions is largely affected by oxygen fugacity (fO_2), the redox state of the ore fluid is considered critical to the transport and deposition of metals. Considering that the aqueous-carbonic fluid is the representative fluid for the Um El Tuyor gold deposit, evaluation of the C-O-H system is appropriate to address the fO_2 of the ore fluid, by using the computer program COHFLUID (Huizenga, 1995). The calculations are based on the presence of graphite in the deposit and assuming ideal mixing of the compounds. The fO_2 of the mineralizing fluids calculated for a temperature range of 278-429°C and pressures of 1.4-2.1 kbar varies from 10^{-27} to 10^{-32} bar. These values of fO_2, under the aforementioned $P–T$ conditions, plot slightly above the quartz–fayalite–magnetite (QFM) buffer and below the nickel–nickel oxide (Ni–NiO) buffer, remaining below the hematite–magnetite (HM) buffer (Fig. 6.16). Accordingly, a relatively reduced nature of the H_2O–CO_2 gold-bearing fluids is demonstrated. Such reducing conditions, together with the textural evidence for deposition of the iron sulphides concomitant with gold (at least partially) suggests that HS^--bearing or neutral HS complexes, i.e. $Au(HS)_2^-$ or $HAu(HS)_2^0$, were the predominant agents in the transport of gold in the aqueous–carbonic fluid (Hayashi and Ohmoto, 1991; Seward, 1991).
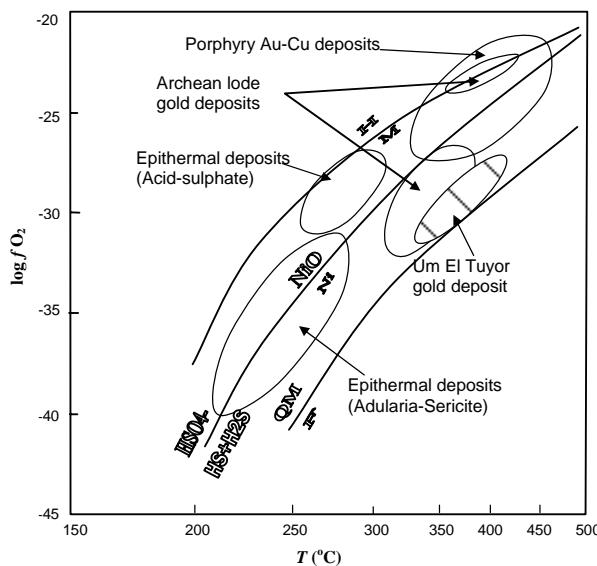
Fig. (6.16): Log fO₂ - T diagram showing the redox state of the aqueous-carbonic fluids entrapped in Um El Tuyor auriferous quartz veins (black field) with regard to with the quartz-fayalite-magnetite (Q-F-M) and hematite-magnetite (H-M) buffers. Also shown are T-fO₂ ranges of the main gold deposit types (adapted after Huston & Large 1989).

CHAPTER 7

SUMMARY AND CONCLUSIONS

7 Summary and conclusions

- Geologic context

The Um El Tuyor area is underlain mainly by Neoproterozoic ophiolites, island arc sequences and syn- and post-orogenic intrusions. The ophiolites and island arc units form a structurally complex ENE-trending elongate belt, considered as a continuation of the major Allaqi fold and thrust belt in the west of Um El Tuyor area with a general tectonic transport, roughly, from north to south (c.f. Abdelsalam et al., 2003).

The structural evolution of the Um El Tuyor area is subdivided into five deformation phases. An early period of crustal shortening (Dm) involved transportation and overriding of huge ophiolitic sheets onto sequences of island arc rocks is manifested by major thrust faults, imbricate ophiolitic thrust slices and intensely folded island arc rocks. Regional folds and pervasive foliation cleavage represent a NE-SW compressional regime (D2) superimposed on the thrust fabrics. A third deformation phase is indicated by the presence of abundant NNW-trending major folds and left-lateral faults superimposed on the older structural fabrics (D3). An episode of transcurrent deformation (D4) yielded slip reactivation of the pre-existing NW-trending faults and formation of discrete shear zones, one of which accommodates gold mineralization in the study area. Finally, a weak shear strain (D5) is indicated by the intersecting fault and joint trends traversing the post-orogenic rocks.

Microscopic investigations including a study of the microfabrics in the island arc metapelites. The observations suggest three regional metamorphic events (M1 to M3) during the evolution of the basement complex of the Um El Tuyor area. The early event was low/medium-grade metamorphism manifested by chlorite, albite and less commonly biotite inclusion trails in the large xenomorphic garnet porphyroblasts. The garnet-chlorite and chlorite geothermometries indicated a temperature range of 380±50°C for M1. On the other hand, M2 coincides with the development of S_2 cleavage. The M2 event is also manifested by the development of intermediate to high grade metamorphic mineral phases, e.g. hornblende, garnet and staurolite, and by growth of the matrix minerals in the arc-related metasedimentary rocks. Development of almandine garnet rims and staurolite (+sillimanite) in the metasedimentary rocks marks the peak of regional metamorphism. Similarly, the metavolcanic rocks show a mineralogical assemblage including biotite, hornblende(paragasite), quartz defining S_2 and indicating a prograde metamorphism. Temperatures of $534°$-$561°C$ and pressures of 5.26-6.20 kbar are estimated for the peak metamorphic conditions during M2. Development of chlorite and less commonly biotite traversing the staurolite and garnet porphyroblasts in the examined metapelites, and replacement of hornblende by epidote and iron oxides in the metavolcanic rocks suggest that a third (low-grade) metamorphic event (M3) that occurred after the peak metamorphism in the study area.

Um El Tuyor ophiolites are considered as cumulate and non-cumulus, enriched mantle tectonites with low-K oceanic tholeiite geochemistry. These ophiolites were likely formed by low to moderate degree partial melting of a garnet-free mantle source. They have field and geochemical characteristics comparable with those of several ophiolites described in the Arabian-Nubian Shield. The latter have been considered as supra-subduction zone ophiolites, whose chemistries are strongly influenced by subduction processes (e.g. Bakor et al., 1976; Price, 1984; Kröner, 1985; Pallister et al., 1988). In terms of geochemical characteristics and regional geotectonic setting, the Um El Tuyor ophiolites are similar to the G. Muqsim ophiolites, west of the

Um El Tuyor area (Sadek, 1994). Both are high-Ti ophiolites derived from enriched mantle source, and attributed to a back-arc environment and similar positions of a coeval island arc. The metapelites (garnet biotite schist) exposed in the Um El Tuyor area are most likely back arc sediments derived from a mixed felsic-mafic crustal source. They are metamorphosed under conditions of upper greenschist to upper amphibolite faices metamorphism. The island arc metavolcanic rocks are generally metamorphosed basalts with Th/Yb >1, moderate enrichment in LREE, nearly flat HREE patterns and slight negative Eu anomalies. These characteristics make them akin to the volcanic-arc basalts evolved by fractional crystallization of amphibole and clinopyroxene (c.f Floyd, 1993).

Magmatism in the Um El Tuyor basement complex is manifested by early island arc calc-alkaline hornblende gabbro, syn-orogenic I-type granitoids, and post-orogenic olivine gabbro and muscovite-biotite granite. The post-orogenic olivine gabbro shows chemical characteristics comparable with the Within Plate Tholeiites (WPT). It is depleted in the HFS relative to LIL elements. The later is an intrinsic feature of the upper mantle, as a result of the partial melting process (Gill 1981). The peraluminosity, the high Ti/P ratios, the negative Nb and Eu anomalies of the post-orogenic muscovite-bearing granite is consistent with a within-plate crustal source.

– Gold mineralization

The Um El Tuyor gold mineralization is related mainly to a set of auriferous quartz-carbonate and laminated quartz veins. These auriferous veins are closely associated with a NNW- trending brittle-ductile shear zone that, in turn, traverses regional NW-SE trending deformation fabrics in the central part of the study area. Bends and dilational jogs formed by deflection of the host rock foliation into the shear zone became favourable sites for quartz precipitation. The local competence contrast between the host metasedimentary rocks and the abundant dacite sills in the mine area is assumed to have also produced loci for quartz precipitation. Further, the crystal plasticity caused by the retrograde metamorphic reactions, which took place during shearing, enhanced permeability of the host rocks and provided sites of dilation and facilitated fluid flow through the wallrocks in the mine area (Fig. 7.1).
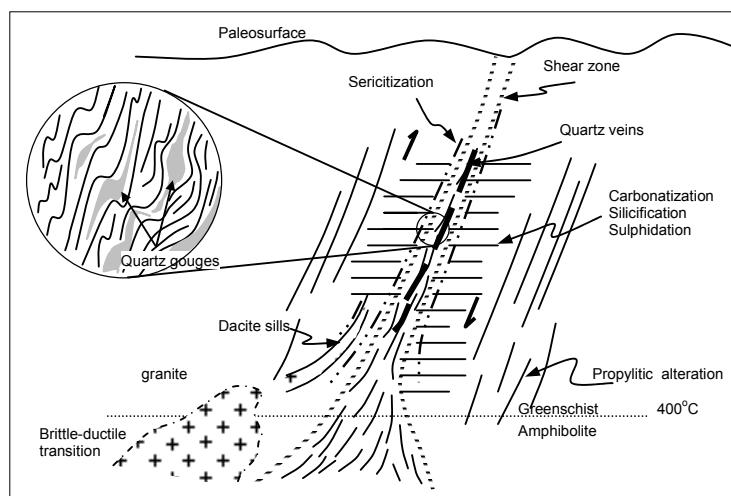
Fig. (7.1): Sketch cross section of the Um El Tuyor gold deposit, proposed on basis of the variuos field and petrographic observations (not to scale).

The typical association of the auriferous veins with hydrothermally altered rocks along the shear zone suggests a syn-shearing mineralization. Pyrite and arsenopyrite crystals cross the main fabric of the carbonaceous wallrocks or slivers of the wallrocks within quartz veins, and occasionally show incipient to conspicuous development of quartz-dominated or ankerite-dominated pressure shadows. In other places, they are variably fragmented. These features indicate that the bulk precipitation of sulphide minerals continued from syn-kinematic to late-kinematic stages of shearing in the mine area.

Where intensively altered, the host rock schists are finer grained than the less-altered portions, and the metamorphic mineralogy is almost entirely replaced by hydrothermal associations. Replacement of the metamorphic assemblage by hydrothermal mineral phases points to post-peak metamorphic hydrothermal alteration. The zoned alteration pattern around the auriferous vein system (Fig. 7.1) is attributed to temporal and lateral evolution in composition of the fluid through interaction with the wallrocks.

The formation of sericite is the most characteristic alteration process, from the incipient to the advanced stages. The generally low contents of K_2O, SO_2, As, Ba, Sr, Sn and Au in the unaltered host rocks, compared with those in wallrocks in the vein proximity, are considered indicative of addition of these elements during alteration. SiO_2 contents are either invariable or elevated, suggesting that quartz veining is derived from direct silica precipitation. CO_2 addition is inferred from the higher contents of carbonate minerals in the wallrocks relative to the unaltered host rocks.

Stages of increasing hydrothermal alteration are identified as initial, intermediate and advanced. Considering that both reactants and products are observed in the initial stage, it is suggested that the first hydrolysis reactions occurred in the presence of an acidic fluid, whose pH was buffered by the wallrocks mineralogy. The transitional stage involved also hydrolysis reactions, but was dominated by carbonatization and sulphidation besides redox reactions. The original mineralogy is almost completely replaced by hydrate minerals, i.e. muscovite and chlorite, and carbonate. The advanced stage was most likely a phase of intense sericitization, which consumed K^+, released H^+, and lowered the solution pH. Cation-exchange reactions were limited to the time when favoured $a_{Na}+/a_K+$ and temperature conditions promoted deposition of albite. Sulphidation remained operating through this stage, and the unbuffered conditions were locally attained under high fluid/rock ratios.

Gold occurs in the auriferous quartz veins as inclusions, or within the lattice in arsenopyrite and arsenian pyrite, commonly in association with subordinate sphalerite, chalcopyrite, and pyrrhotite. Another high fineness type of gold fills the microfractures in sulphide and quartz grains or occurs as dispersed blebs and globules in the intensely altered domains, particularly where sericite and carbonate are intergrown. The compositional zoning in the large arsenian pyrite crystals, from barren cores to auriferous margins, is considered as a function of redox reactions involving oxidation of Au and reduction of As (e.g. Fleet et al., 1988; Cathelineau et al., 1988; Chryssoulis, 1990; Arehart et al., 1993).

In the Um El Tuyor deposit, the auriferous vein quartz grains are typically fluid inclusion-rich. The observed fluid inclusions are compositionally grouped into carbonic [$CO_2(\pm CH_4 \pm N_2)$-rich], aqueous-carbonic [H_2O-NaCl-$CO_2(\pm CH_4 \pm N_2)$)], and aqueous [low salinity H_2O–NaCl]. In the CO_2-bearing inclusions, slight depressions in CO_2 final melting temperatures below the triple point lead to estimate presence of a maximum of 14 mol% CH_4 or 20 mol% N_2 as dissolved gases in addition to CO_2.

Fluid immiscibility, heterogeneous trapping and phase separation are evidenced in the Um El Tuyor auriferous veins by several criteria. An initial fluid system with a roughly H_2O–21 mol% CO_2–6 wt.% NaCl composition is assumed for the ore-bearing fluids. The entire gold-base metal mineralization and quartz veining event extended over conditions of 170-429°C at 0.9-2.1 kbar, respectively, equivalent to depths of 3-8 km and compatible with crustal conditions of greenschist metamorphism and brittle–ductile transition. This wide range of pressure probably represents the total fluid pressure regime within the shear zone, from the formation of the auriferous quartz veins to periods of continuous pressure decrease during uplift, including sudden pressure decrease, which occurred as a consequence of incremental opening of the fissures, followed by filling by newly deposited quartz.

- Gold deposition mechanism

The common occurrence of gold as inclusions in the sulphide minerals, and the auriferous nature of the early pyrite and arsenopyrite are consistent with the hypothesis that bisulphide complexes were responsible for the transport of gold in the Um El Tuyor mine area. Destabilization of gold-sulphur complexes through interplay of fluid-wallrock interaction, cooling, redox state variation, pH changes, and variation in sulphur fugacity probably caused the gold deposition in the auriferous veins in Um El Tuyor mine. Fluid-wallrock interaction might have provided a reducing character to the fluids, and destabilized the aurous sulphide complexes, i.e. $Au(HS)_2^-$.

$$Au(HS)_2^-{}_{(aq)} + H^+{}_{(aq)} + 1/2H_{2(aq)} = Au + 2H_2S_{(aq)} \qquad \text{(Hayashi and Ohmoto, 1991)}$$

$$K(Mg,Fe)_3AlSi_3O_{10}(OH,F)_2 + K^+ + Al^{3+} + 2Au(HS)_2^- \Leftrightarrow KAl_3Si_3O_{10}(OH, F)_2 + 2FeS_2 + 2Au + 4H^+ + Mg^{2+}$$
$$\text{biotite} \qquad\qquad\qquad\qquad\qquad\qquad\qquad \text{sericite} \qquad \text{pyrite}$$
$$\text{(Buchholz et al., 1998)}$$
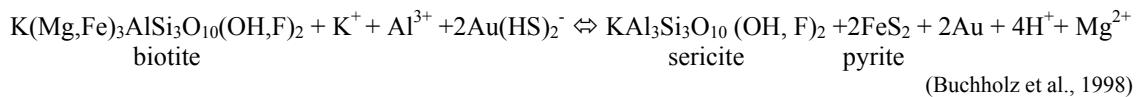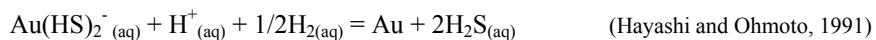
Variation in fO_2 is particularly important in case of Fe-rich host rocks. Sulphidation of Fe-rich wallrocks has been demonstrated as an efficient gold deposition mechanism (Phillips et al. 1984; McCuaig and Kerrich 1994; Mikucki, 1998). The oxidation of sulphur S^{2-} to form pyrite (S^-) provides a driving force to reduce the aurous complexes.

$$Fe_3O_4{}_{(host\ rock)} + 6H_2S \Leftrightarrow 3FeS_2{}_{(Py)} + 4H_2O + 2H_{2(g.)}$$

$$Fe_3O_4 + 6Au(HS)_2^- + 2H^+ \Leftrightarrow 3FeS_2 + 4H_2O + 6Au + 3H_2 \text{ (Raymahashay \& Holland, 1969)}$$
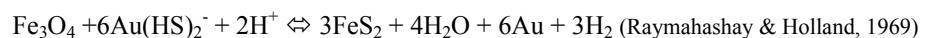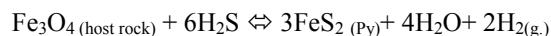
Further, at the microscopic scale, sites of increased charge density and/or conductivity polarization on the surface of grains of pyrite and arsenopyrite could also have enhanced the destabilization of the thiocomplexes, leading to gold deposition on the surface of these sulphides. This mechanism involves the physical adsorption of the charged gold species (Au^{+1}) on the fluid–sulphide interface, followed by reduction-driven chemical adsorption (Starling et al., 1989; Knipe et al., 1991, 1992).

Phase separation is recognized as an important gold precipitation mechanism in the Um El Tuyor mine area. It might have taken place when ambient conditions fell below those of the solvus for the fluid composition, through advection of the fluid to higher crustal levels (e.g. Spooner et al., 1985), or by a rapid drop in P_{fluid} due to fault-valve mechanisms (e.g. Cox et. al., 1995; Robert et al., 1995). The initially

homogenous ore fluid system was low salinity aqueous-carbonic solution (±1-2 mol% CH_4 or N_2) started to separate into two phases and precipitate gold when conditions attained ~340°C at ~1.5 kbar (at depth of ~6 km under lithostatic condition). However, the lower and upper pressure-temperature limits of gold deposition in the Um El Tuyor mine area are estimated as 278-429°C at 1.4-2.1 kbar, respectively. They are equivalent to depths of 5-8 km, under conditions of lithostatic overburden.

Possible sources of the fluid

In this context, the origin of the ore fluids is remained speculative. Nonetheless, certain trends appear relatively clear. Condition for the isochores to cross the immiscibility surface of the overall system is met by intersecting isochores for high-density carbonic and low-salinity aqueous fluid, which precisely intersect on the critical curve of the low salinity $H_2O–CO_2$ system. Further, the isochore for high-bulk density aqueous-carbonic inclusions passes through the box represents the peak metamorphic conditions on the *P–T* diagram (see Chapter 6). This observation strongly suggests that both fluids were derived from the unmixing of a homogeneous aqueous-carbonic fluid, for which an obvious candidate is the fluid generated during the metamorphic dehydration/decarbonation of the ophiolite-island arc belt. But it must also be considered that the belt has been intruded by a number of plutonic rocks, which could be a source of CO_2.

As the low-salinity, homogeneous aqueous-carbonic fluid evolved from its source (?), it is considered to have carried Au complexed with bisulphides, and at the site of trapping, underwent unmixing (phase separation) to produce H_2O and pure highly dense CO_2 inclusions. Analytical investigations of various Neoproterozoic rocks indicated gold concentration of ~200 ppb in serpentinites in the Egyptian Eastern Desert (Langwieder, 1994). This leads to the hypothesis that serpentinite is the potential source candidate for Au in the Um El Tuyor area.

REFERENCES CITED

REFERENCES CITED

- Abdel Khalek, M.L., Takla, M.A., Sehim, A., Hamimi, Z., El-Manawi, A.W., 1992. The geology and tectonic evolution of the Wadi Bitan area, southern Eastern Desert, Egypt. In: Sadek, A. [Ed.], 1st International Conference on the Geology of the Arab World. Cairo, Egypt. pp. 369-394.

- Abdelsalam, M.G., Abdeen, M., Dowaidar, H., Stern, R.J., Abdelghaffar, A. A., 2003. Structural evolution of the Neoproterozoic Western Allaqi–Heiani suture, southeastern Egypt. Precambrian Res. 124, 87–104.

- Abdelsalam, M.G., Stern, R.J., 1996. Sutures and shear zones in the Arabian-Nubian Shield. Journal of African Earth Sciences, 23, 289– 310.

- Abdel Tawab, M. M., 1992. Gold exploration in Egypt from Pharoanic to modern times. Zentralbl. Geol. Paläont. Teil 1. 1991, 2721-2733.

- Abrams, M.J., Brown, D., Lepley, L., Sadowski, R., 1983. Remote sensing for porphyry copper deposits in southern Arizona. Economic Geology 78, 591–604.

- Allibone, A.H., Cordery, G.R., Morrison, G.W., Jaireth, S., Lindhorst, J.W., 1995. Synchronous advanced argillic alteration and deformation in a shear zone-hosted magmatic hydrothermal Au–Ag deposit at the Temora (Gidginbung) Mine, New South Wales, Australia. *Econ. Geol.* 90, 1570–1603.

- Al Shanti, A.M.S., 1979. Evolution and Mineralization of the Arabian-Nubian Shield.- I.A.G. Bull. No.3, Proceedings of a Symposium, Vol. 1-4, 1-187, Oxford - New York - Toronto - Sydney - Paris - Frankfurt/M. (Pergamon Press).

- Anderson, M.R., Rankin, A.H., Spiro, B., 1992. Fluid mixing in the generation of mesothermal gold mineralization in the Transvaal Sequence, Transvaal, South Africa. Eur. J. Mineral. 4, 933–948.

- Arehart, G.B., Chryssoulis, S.L. & Kesler, S.E., 1993. Gold and arsenic in iron sulfides from sediment-hosted disseminated gold deposits: implications for depositional processes. *Econ. Geol.* 88, 171-185.

- Audétat, A., Günther, D., and Heinrich, C.A., 1998. Formation of a magmatic-hydrothermal ore deposit: insights with LA-ICP-MS analyses of fluid inclusions. Science, 279, 2091–2094.

- Bakker RJ., 1997. Clathrates: computer programs to calculate fluid inclusion V-*X* properties using clathrate melting temperatures. Comput Geosci 23: 1-18

- Bakker RJ., 1999. Optimal interpretation of microthermometrical data from fluid inclusions: thermodynamic modelling and computer programming. Habilitation thesis, Univ Heidelberg, Germany

- Bakor, A.R., Gass, I.G. And Neary, C.R., 1976. Jabal al Wask, north-west Saudi Arabia, an Eocambrian back-arc ophiolite. Earth Planet. Sci. Lett., 30, 1-9.

- Barrat, J. A., Keller, F., Amossé, J., Taylor, R. N., Nesbitt, R. W., and Hirata, T., 1996. Determination of rare earth elements in sixteen silicate reference samples by ICP-MS using a Tm addition and an ion-exchange chromatography procedure. Geostand. Newsl. 20:133-139.

- Barrett, T.J., MacLean, W.H., 1997. Volcanic sequences, lithogeochemistry and hydrothermal alteration in some bimodal VMS systems. *In:* Barrie, C.T., Hannington, M.D. (Eds.), Volcanic –Associated Massive Sulphide Deposits: Processes and Examples in Modern and Ancient Settings, Geological Association of Canada and The Society of Economic Geologists Co-sponsored Short Course Notes. Carleton University, Ottawa, 105–133.

- Barton, P.B.Jr., 1969. Thermochemical study of the system Fe-As-S. *Geochim. Cosmochim. Acta,* 33, 841-857.

- Barton, P.B.Jr., and Skinner, B.J., 1979. Sulfide mineral stabilities. Geochemistry of Hydrothermal Ore Deposits. *In:* Barnes, H.L., (Ed.), 278–403, Wiley Intersci., New York.

- Barton, P.B.Jr., and Toulmin, P., III., 1964. The electrum-tarnish method for the determination of the fugacity of sulfur in laboratory sulfide system. *Geochim. Cosmochim. Acta,* 28, 619–640.

- Basta, E.Z and Takla, M.A., 1974. Distribution of opaque minerals and the origin of gabbroic rocks of Egypt. Bull. Fac. Sci. Cairo. Univ., No.47, 346-364.

- Bell, T.H. & Cuff, C., 1989. Dissolution, solution transfer, dissolution versus fluid flow and volume loss during deformation/metamorphism. *J. Metam. Geol.* 7, 425-447.

- Bell, T.H., Fleming, P.D. & Rubenach, M. J., 1986. Porphyroblast nucleation, growth and dissolution in regional metamorphic rocks as a function of deformation partitioning during foliation development. Journal of Metamorphic Geology, 4, 37-67.

- Berman, R. G., 1990. Mixing properties of Ca-Mg-Fe-Mn garnets. *American Mineralogist*, 75, 328-344.

- Bhatia, M. R., and Crook, K. A. W., 1986. Trace element characteristics of graywackes and tectonic setting discrimination of sedimentary basins. Contrib. Mineral. Petrol. 92, 181–193.

- Bhattacharya, A., Mohanty, L., Maji, A., Sen, S.K., and Raith, M., 1992. Non-ideal mixing in the phlogopite-annite binary: constraints from experimental data on Mg-Fe partitioning and a reformulation of the biotite-garnet thermometer: Contributions to Mineralogy and Petrology, 111, 87-93.

- Binu-Lal, S. S., Wilbert Kehelpannalab, K. V., Satish-Kumara M. and Wadaa, H., 2003. Multistage graphite precipitation through protracted fluid flow in sheared meta-granitoid, Digana, Sri Lanka: evidence from stable isotopes. *Chemical Geology*, 197, 253-270.

- Bowers, T.S., 1991. The deposition of gold and other metals: pressure induced fluid immiscibility and associated stable isotope signatures. *Geochim. Cosmochim. Acta* 55, 2427–2434.

- Bowers, T.S., Helgeson, H.C., 1983. Calculation of thermodynamic and geochemical consequences of nonideal mixing in the system H_2O–CO_2–NaCl on phase relations in geologic systems: equation of state for H_2O–CO_2–NaCl fluids at high pressures and temperatures. *Geochim. Cosmochim. Acta* 47, 1247–1275.

- Brenan, J.M., Shaw, H.F., Phinney, D.L., Ryerson, F.J., 1994. Rutile-aqueous fluid partitioning of Nb, Ta, Hf, Zr, U and Th: implications for high field strength element depletions in island-arc basalts. Earth Planet. Sci. Lett. 128, 327–339.

- Brown, G.M., Holland, J.G., Sigurdsson, H., Tomblin, J.F. and Ancrulus, R.J., 1977. Geochemistry of the Lesser Antilles volcanic island arc. *Geochim. Cosmochim. Acta*, 41, 785-801.

- Buchholz, P., Herzig, P., Friedrich, G., and Frei, R., 1998, Granite-hosted gold mineralization in the Midlands greenstone belt: a new type of low-grade large scale gold deposit in Zimbabwe. Mineralium Deposita, v.33, p.437-460.

- Burke, K.C., Sengör, A.M.C., 1986. Tectonic escape in the evolution of the continental crust. In: Baranzangi, M., Brown, L. (Eds.), Reflection Seismology: The Continental Crust. Am. Geophys. Union Geodyn. Ser. 14, 41–53.

- Cathelineau, M., 1988. Cation site occupancy in chlorites and illites as a function of temperature. Clay Miner. 23, 471-485.

- Cathelineau, M., Boiron, M.C., Essarraj, S., Lespinasse, M., Poty, B., Sellier, E., 1991. Fluid density changes and gold deposition in Au quartz veins: the role of pressure fluctuations linked to multistage deformation. In: Pagel, L. (Ed.). Source, Transport and Deposition of Metals, Balkema, Rotterdam, pp. 653–656.

- Chryssoulis, S.L., 1990. Detection and quantification of 'invisible' gold by microprobe techniques, In: Hausen, D.M. (Ed.), Gold '90. SME, New York, pp. 323–332.

- Clark, L.A., 1960. The Fe-As-S system: Phase relations and applications. *Econ. Geol.* 55, Pt. I:1345-1381, Pt. II: 1631-1652.

- Coelho, C.E.S. & Ramboz, C., 1998. New Interpretation on the genesis of the Fazenda Brasileiro and Fazenda Maria Preta gold deposits, Rio Itapicuru Greenstone Belt, Bahia, revista de Ouro Preto - REM, 50 (4):42-53.

- Coleman, R.J., 1977. Ophiolilte, Springer, New York, 229 p.

- Condie, K.C., 1973. Archean magmatism and crustal thickening. Geol. Soc. Am. Bull. 84, 2981-2992.

- Condie, K.C., 1986. Geochemistry and tectonic setting of early Proterozoic supracrustal rocks in the southwestern United States. J. Geol. 94, 845–864.

- Cox, S.F., 1995. Faulting processes at high fluid pressures: an example of fault valve behaviour from the Wattle Gully Fault, Victoria, Australia. J. Geophys. Res. 100, 12841–12859.

- Crawford, M.L., Hollister, L.S., 1986. Metamorphic fluids: the evidence from fluid inclusions. *In*: Walther, J.V., Wood, B.J. (Eds.). Fluid rock interaction during metamorphism, Physical Geochemistry, Springer, Berlin, 5, 1–35.

- Davis B. K. & Hippertt J. F. M., 1998. Relationships between gold concentration and structure in quartz veins from the Hodgkinson Province, northeastern Australia. Mineralium Deposita, 33, 391–405.

- Dewey, J., 1976. Ophiolite obduction. Tectonophysics, 31, 93-120.

- Diamond, L.W., 1994. Introduction to phase relations of CO_2–H_2O fluid inclusions. In: De Vivo, B., Frezzotti, M.L. (Eds.), Fluid Inclusions in Minerals: Methods and Applications. Blacksburg, Virginia Tech, 131–158.

- Dick, H.J.B., 1989. Abyssal peridotites, very low spreading ridge and ocean ridge magmatism. In: Saunders, A.D., Norry, M.J. (Eds.), Magmatism in Ocean Basins. Geol. Soc., Spec. Publ., 42, 71– 106.

- Dickenson, M.P. & Hewitt, D., 1986. A garnet-chlorite geothermometer. Geol. Soc. Am. Abstr. Prog. 18:584.

- Dixon, T.H., Stern, R.J., Hussein, I.M., 1987. Control of the Red Sea geometry by Precambrian structures. Tectonics 6/5, 551–571.

- Drammond, S.E., Ohmoto, H., 1985. Chemical evolution and mineral deposition in boiling hydrothermal systems. Economic Geology 80, 126–147.

- Droop, G., 1987. A general equation for estimating Fe^{3+} concentrations in ferromagnesian silicates and oxides from microprobe analyses, using stoichiometric criteria. Mineralogical Magazine 51, 431–435.

- Drury, M. R., Humphreys, F. J., White, S. H., 1985. Large strain deformation studies using polycrystalline magnesium as a rock analogue. Part II: dynamic recrystallization mechanisms at high temperatures. Physics of the Earth and Planetary Interiors, 40, 208-222.

- Drury, S.A., 1983. The petrogenesis and tectonic setting of Archaean metavolcanics from Karnataka State, South India. *Geochim. Cosmochim. Acta*, 47, 317–329.

- Dubessy, J., 1994. Single components systems: phase diagrams and their application to fluid inclusions. In: De Vivo, B., Frezzotti, M.L. (Eds.), Fluid Inclusions in Minerals: Methods and Applications. Blacksburg, Virginia Tech, 95–115.

- EGSMA, 1912. Um Tiour Mine. Inspection report. Lease No. 13. Internal report, Department of Publication and Documentation.

- EGSMA, 1913. Um El Tiour Mine. Inspection report. Lease No. 12. Internal report, Department of Publication and Documentation.

- El Bouseily, A.M. and El Sokkary, A.A., 1975. The relation between Rb, Ba and Sr in granitic rocks. Chemical Geology, 16, 207-219

- El Gaby, S., 1994. Geological and tectonics framework of the Pan-African orogenic belt in Egypt. Second International Conference Geology of the Arab World, Cairo, Egypt, pp. 3–17.

- El Sharkawy, M. A. & El Bayoumi, M. A., 1979. The ophiolites of Wadi Ghadir area, Eastern Desert of Egypt, Ann. Geol. Surv. Egypt, 9, 125-135.

- El Shimi, K.A., 1996. Geology, structure and Exploration of Gold Mineralization in Wadi Allaqi area (SW, Eastern Desert, Egypt). Ph. D. Thesis (unpub.), Ain Shams Univ., 326 p.

- Ewart, A., 1982. The mineralogy and petrology of Tertiary- Recent orogenic rocks: with special reference to the andesitic- basaltic compositional range. *In:* Thorpe, R.S. (Ed.), Andesites: Orogenic Andesites and Related Rocks. Wiley, Chichester, 25–95.

- Fedo, C.M., Nesbitt, H.W., Young, G.M., 1995. Unraveling the effects of potassium metasomatism in sedimentary rocks and paleosols, with implications for paleoweathering conditions and provenance. *Geology*, 23, 921–924.

- Ferry, J.M. and Spear, F.S., 1978. Experimental calibration of the partitioning of Fe and Mg between biotite and garnet. Contributions to Mineralogy and Petrology, 66, 113-117.

- Finlow-Bates, T., Stumpfl, E.F., 1981. The behaviour of so-called immobile elements in hydrothermally altered rocks associated with volcanogenic submarine-exhalative ore deposits. Mineral Dep. 16, 319-328.

- Fleet, M.E., MacLean, P.J. and Barbier, J., 1988. Oscillatory-zoned As-bearing pyrite from strata-bound and stratiform gold deposits: an indicator of ore fluid evolution. Econ. Geol. Monogr., 6: 356-362.

- Fleet, M.E. & Mumin, A.H., 1997. Gold-bearing arsenian pyrite and marcasite and arsenopyrite from Carlin Trend gold deposits and laboratory synthesis. *Am. Mineral.* 82, 182-193.

- Floyd, P.A., 1993. Geochemical discrimination and petrogenesis of alkalic basalt sequences in part of Ankara melange, Central Turkey. J. Geol. Soc. London, 150, 541–550.

- Floyd, P.A. & Winchester, J.Á., 1978. Identification and discrimination of altered and metamorphosed volcanic rocks immobile elements. Chem. Geol, 21(3-4):291-306.

- Foster, M.D., 1962. Interpretation of the composition and a classification of the chlorites. Prof. Pap. U. S. Geol. Surv. 414A, 1–33.

- Gass, I. G., 1981. Pan-African (Upper Proterozoic) plate tectonics of the Arabian-Nubian Shield. In: Kroner, A. (ed) Precambrian Plate Tectonics. Elsevier, Amsterdam. 387-405.

- Gebre-Mariam, M., Groves, D.I., Ho, SE., McNaughton, N.J., Veamcombe, J.R., 1991. The Archaean lode-gold deposit at Racetrack, near Kalgoorlie, Western Australia: a transitional mesothermal-epithennal hydrothermal system. IX Pagel, M., Leroy, J.L. (Eds.), Source, Transport and Deposition of Metals. Balkema, Rottenhun, 661-664.

- Gebre-Mariam, M., Groves, D.I., McNaughton, N.J., Mikucki, E.J., 1993. Multiple fluid sources and depositional mechanisms at the Archean mesozonal-epizonal Golden-Kilometre gold mine, Western Australia. In: Hach-Ali, F., Torres-Ruiz, J., Gervilla, F. (Eds.), Current Research in Geology Applied to Ore Deposits, 453-456.

- Gehrig, M., 1980. Phasengleichgewichte und pVT-Daten ternärer Mischungen aus Wasser. Kohlendioxid und Natriumchlorid bis 3 kbar und 550°C. PhD thesis, Hochschulsammlung Naturwissenschaften: Chemie; Bd. 1, Freiburg, Germany, 153 p.

- Gemmell, J.B., Large, R., 1992. Stringer system and alteration zones underlying the Hellyer volcanic-hosted massive sulphide deposit, Tasmania, Australia. *Econ. Geol.* 87, 620-649.

- Ghent, E.D. and Stout, M.Z., 1981. Geobarometry and geothermometry of plagioclase-biotite-garnet-muscovite assemblages. Contributions to Mineralogy and Petrology, 76, 92–97.

- Ghosh, S.K., 1993. Structural Geology: fundamentals and modern developments. Pergamon, 598 p.

- Giggenbach, W.F., 1987. Redox processes governing the chemistry of fumarolic gas discharges from White Island, New Zealand. Applied Geochemistry 2, 143–161.

- Giggenbach, W.F., 1988. Geothermal solute equilibria: derivation of Na–K–Mg–Ca geoindicators. *Geochim. Cosmochim. Acta* 52, 2749–2765.

- Gill, J. G., 1981. Orogenic Andesites and Pate Tectonics. Springer-Verlag, Berlin. 390 p.

- Grant, J.A., 1986. The isocon diagram - a simple solution to Gresen's equations for metasomatic alteration. *Econ. Geol.* 81, 1976-1982.

- Greiling, R.O., Abdeen, M.M., Dardir, A.A., El Akhal, H., El Ramly, M.F., Kamal El Din, G.M., Osman, A.F., Rashwan, A.A., Rice, A.H.N., Sadek, M.F., 1994. A structural synthesis of the Proterozoic Arabian–Nubian Shield in Egypt. Geologische Rundschau 83, 484–501.

- Greiling, R.O., Kröner, A., El Ramly, M.F., Rashwan, A.A., 1988. Structural relationships between the southern and central parts of the Eastern Desert of Egypt: details of a fold and thrust belt. In: El Gaby, S., Greiling, R.O. (Eds.), The Pan-African Belt of Northeast Africa and Adjacent Areas. Vieweg and Sohn, Weisbaden, 121– 145.

- Gresens, R.L., 1967. Composition-volume relations of metasomatism. Chem. Geol. 2, 47-65.

- Groves, D.I., Forster, R.P., 1991. Archean lode-gold deposits. In: Fortes, R.P., (Ed.), Gold Metallogeny and Exploration, Blackie, Glasgow, 63–103.

- Guidotti, C.V., 1984. Micas in metamorphic rocks. In: Bayley, S.W. (Ed.), Micas. Reviews in Mineralogy; Vol. 13, pp. 357–456.

- Harris, N.B.W., Pearce, J.A., Tindle, A.G., 1986. Geochemical characteristics of collision-zone magmatism. *In:* Coward, M.P., Ries, A.C. (Eds.), Collision Tectonics. Spec. Publ. Geol. Soc. 19, 67–81.

- Hassanipak, A.A., Ghazi, A.M., Wampler, J.M., 1996. REE characteristics and K/Ar ages of the Band Ziarat ophiolite complex, Southeastern Iran. Canadian Journal of Earth Sciences 33, 1534-1542.

- Hawkesworth, C.J., Gallagher, K., Hergt, J.M., McDermott, F., 1993. Mantle and slab contribution in arc magmas. Annu. Rev. Earth Planet. Sci. 21, 175–204.

- Hawkesworth, C.J., O'Nions, R.K., Pankhurst, R.J., Hamilton, P.J., Evensen, N.M., 1977. A geochemical study of island-arc and back-arc tholeiites from Scotia Sea. Earth Planet. Sci. Lett. 36, 253–262.

- Hawkins, J.W., Lonsdale, P.F., Macdougall, J.D., Volpe, A.M., 1990. Petrology of the axial ridge of the Mariana Trough back-arc spreading center. Earth Planet. Sci. Lett. 100, 226–250.

- Hayashi, K.-I., Ohmoto, H., 1991. Solubility of gold in NaCl- and H2S-bearing aqueous solutions at 250–350°C. *Geochim. Cosmochim. Acta,* 55, 2111–2126.

- Hey, M.H., 1954. A new review of the chlorites. Mineralog. Mag. 30, 277-292.

- Heyen, G., Ramboz, C., Dubessy, J., 1982. Simulation des équilibres des phases dans le systè me CO_2–CH_4 en dessous de 50°C et de 100 bar. Application aux inclusions fluides. C R Acad Sci Paris 294:203–206

- Hickey, K.A., Bell, T.H., 1996. Syn-deformational grain growth: matrix coarsening during foliation development and regional metamorphism rather than by static annealing. European Journal of Mineralogy, 8, 1351-1373.

- Hildreth, W., Moorbath, S., 1988. Crustal contributions to arc magmatism in the Andes of Central Chile. Contr. Mineral. Petrol. 98, 455–489.

- Hodgson, D. J., 1989. The structure of shear-related, vein-type gold deposits: a review. *Ore Geology Reviews*, 4, 231-273.

- Hofmann, A.W., 1988. Chemical differentiation of the earth: the relationship between mantle, continental crust and oceanic crust. Earth Planet. Sci. Lett. 90, 297–314.

- Hole, M. J., Saunders, A. D., Marriner, G. F. And Tarney, J., 1984. Subduction of pelagic sediments: implications for the origin of Ce-anomalous basalt from the Mariana island. *Journal Geological Society London,* 141, 453-472.

- Holland, T. J. B. & Powell, R., 1998. An internally consistent thermodynamic data set for phases of petrological interest. Journal of Metamorphic Geology, 16, 309–343.

- Hollister, L.S., 1990. Enrichment of CO_2 in fluid inclusions in quartz by removal of H_2O during crystal–plastic deformation. J. Struct. Geol. 12, 895–901.

- Holloway, J.R., 1981. Composition and volumes of supercritical fluids in the Earth crust. In: Hollister, L.S., Crawford, M.L. (Eds.), Fluid Inclusions: Applications to Petrology. Mineralogical Association of Canada, Short Course Handbook, 6, 13–38.

- Holmes, A., 1951. The sequence of pre-Cambrian orogenic belts in south and central Africa. 18th Inter. Geol. Cong. London (1948), 14, 254-269.

- Huizenga, J.M., 1995. Fluid evolution in shear zones from the late-Archean Harare–Shamva–Bindura greenstone belt NE Zimbabwe . Thermodynamic calculations of the C–O–H system applied to fluid inclusions. PhD Thesis, Vrije Universiteit, Amsterdam, 146 p.

- Hume, W. F., 1937. The minerals of economic value associated with the intrusive Precambrian igneous rocks. Geology of Egypt. Vol. 1, 3, 689-990.

- Hunter, D.R, Barker, F. and Millard, H. T., 1978. The geochemical nature of the Archean ancient gneiss complex and granodiorite suite, Swizerland: A prelimnary study. Precambrian Res. 7, 105-127.

- Hunting Geology and Geophysics LTD., 1967. Assessment of the mineral potentials of the Aswan region, U.A.R., Photogeological Survey. Geol. Surv. Egypt.

- Huston, D.L. & Large, R.R., 1989. A chemical model for the concentration of gold in volcanogenic massive sulfide deposits. Ore Geology Reviews, 4, 171-200.

- Irvine, T.N., and Baragar, W.R.A., 1971. A guide to the chemical classification of the common volcanic rocks: Canadian Journal of Earth Sciences, 8, 523-548.

- Jenkins R. S., 1925. Note on ancient gold mine workings in Upper Egypt. Internal Report. Geol. Surv. Egypt.

- Johan, Z., Marcoux, E. & Bonnemaison, M., 1989. Arsénopyrite aurifère: mode de substitution de Au dans le structure de FeAsS. C.R. *Acad. Sci. Paris 308, Sér*. II, 185-191.

- Jung, S., Hoernes, S., Masberg, P., Hoer, E., 1999. The petrogenesis of some migmatites and granites (Central Damara Orogen, Namibia): evidence for disequilibrium melting, wall-rock contamination and crystal fractionation. Journal of Petrology 40, 1241–1269.

- Kennedy, W. Q., 1964. The structural differentiation of Africa in the Pan African (+ 500 million years) tectonic episode, Eighth Annu. Rep. Res. Inst. African Geol. Univ. Leeds, 48-49.

- Kishida, A., Kerrich, R., 1987. Hydrothermal alteration zoning and gold concentration at the Kerr Addison Archean lode gold deposit, Kirkland Lake, Ontario. *Econ. Geol.* 82, 649-690.

- Kleemann, J. & Reinhardt, J., 1994. Garnet-biotite thermometry revisited: The effect of Al^{VI} and Ti in biotite. - Eur. J. Mineral. 6, 925-941.

- Knipe, S.W., Foster, R.P., Stanley, C.J., 1991. Hydrothermal precipitation of precious metals on sulfide substrates. In: Ladeira, E.A. (Ed.), Proceedings of Brazil Gold'91: The Economics, Geology, Geochemistry and Genesis of Gold Deposits. Balkema, Rotterdam, 431–435.

- Knipe, S.W., Foster, R.P., Stanley, C.J., 1992. Role of sulphide surfaces in sorption of precious metals from hydrothermal fluids. Trans. Inst. Min. Metall. B101, 83–88.

- Koch-Müller, M., 1997. Expermentally determined Fe-Mg exchange between synthetic staurolite and garnet in the system $MgO-FeO-Al_2O_3-SiO_2-H_2O$. *Lithos*, 41, 185-212.

- Kranidiotis, P. & MacLean, W. H., 1987. Systematics of chlorite alteration at the Phelps Dodge massive sulfide deposit, Matagami, Quebec. *Econ. Geol.*, 82, 1898–1911. Lancaster.

- Kretschmar, U. & Scott, S D., 1976. Phase relations involving arsenopyrite in the system Fe-As-S and their application. Can. Mineral. 14, 364-386.

- Kröner, A., 1984. Late Precambrian plate tectonics and orogeny: a need to redefine the term Pan-African. *In:* Klerkx, J., Michot, J. (Eds.), African Geology. Royal Museum for Central Africa, Tervuren, Belgium, pp. 23-28.

- Kröner, A., 1985. Ophiolites and the evolution of tectonic boundaries in the late Proterozoic Arabian-Nubian Shield of northeast Africa and Arabia. Precambrian Res., 27: 277-300.

- Kröner, A., Greiling, R., Reischmann, T., Hussein, I. M. Ster, R. J., Durr, S., Kruger, J. and Zimmer, M., 1987. Pan-African crustal evolution in the Nubian segment of Northeast Africa. Am. Geophys. Union, Sp. Publ. 17, 235-257.

- Kusky, T. M and Ramadan, T. M., 2002, Structural controls on Neoproterozoic mineralization in the South Eastern Desert, Egypt: an integrated field, Landsat TM, and SIR-C/X SAR approach, Journal of African Earth Sciences, Volume 35, 1, 107-121.

- Langwieder, G., 1994. Die Geologie des Gebietes Wadi El-Sid/Um el Fawakhir und Geochemische Untersuchungen an Quarzgaengen des Goldlagerstaettenbezirkes El Sid/Fawakhir. Unpublished M.Sc. Thesis, Ludwig-Maximilians-Universitaet Muenchen, 122 p.

- Lasaga, A.C., 1986. Metamorphic reaction rate laws and development of isograds. Mineralogical Magazine, 50, 359-373.

- Le Bas, M.J., Streckeisen, A.L., 1991. The IUGS systematics of igneous rocks. Journal Geological Society London 148, 825-833.

- Lesher, C.M., Goodwin, A.M., Campbell, I.H., Gorton, M.P., 1986. Trace elements of ore-associated and barren, felsic metavolcanic rocks in the Superior Province, Canada. Can. J. Earth Sci. 23, 222-241.

- Lindgren, W., 1895. Characteristic features of California gold-quartz veins. Geol. Soc. Am. Bull., 6: 221-240

- MacLean, W.H., Barrett, T.J., 1993. Lithogeochemical techniques using immobile elements. J. Geochem. Expl. 48, 109-133.

- MacLean, W. H. and Kranidiotis, P., 1987. Immobile elements as monitors of mass transfer in hydrothermal alteration: Phelps Dodge massive sulfide deposit, Matagami, Quebec. Economic Geology, 82: 951-962.

- Maniar, P.D. & Piccoli, P.M., 1989. Tectonic discrimination of granitoids. *Geol. Soc. of America* Bulletin, 101: 635-643.

- Marcoux, E., Bonnemaison, M., Braux, C. & Johan, Z., 1989. Distribution de Au, Sb, As et Fe dans l'arsénopyrite aurifère du Châtelet et de Villeranges (Creuse, Massif Central français). *C.R. Acad. Sci. Paris 308, Sér.* II, 293-300.

- McCuaig, T.C., Kerrich, R., 1994. *P–T–t*–deformation-fluid characteristics of lode gold deposits: evidence from alteration. systematics. In: Lentz, D.R. (Ed.), Alteration and Alteration Processes Associated with Ore-forming Systems. Geol. Assoc. Can., Short Course Notes 11, 339–379.

- McCulloch, M.T., 1993. The role of subducted slabs in an evolving earth. Earth Planet. Sci. Lett. 115, 89–100.

- McDaniel, D. K., Hemming, S. R., McLennan, S. M., and Hanson, G. N., 1994. Resetting of neodymium isotopes and redistribution of REE's during sedimentary processes: the early Proterozoic Chelmsford Formation, Sudbury Basin, Ontario, Canada. *Geochim. Cosmochim. Acta*, 54, 2015–2050.

- McLennan, S.M., 1989. Rare earth elements in sedimentary rocks: influence of provenance and sedimentary processes. In Lipin, B.R., and McKay, G.A. (Eds.), Geochemistry and Mineralogy of the Rare Earth Elements. Rev. Mineral., 21:169-200.

- McLennan, S.M., Taylor, S. R., McCulloch, M. T., and Maynard, J. B., 1990. Geochemical and isotopic determination of deep sea turbidites: crustal evolution and plate tectonic associations. *Geochim. Cosmochim. Acta,* 54, 2015–2049.

- Meschede, M., 1986, A method of disriminanting between different types of mid-ocean ridge basalts and continental tholeiites with the Nb-Zr-Y diagram. *Chemical Geology,* 56, 207-218.

- Meyer, C., Hemley, J.J., 1967. Wallrock alteration. *In*: Barnes, H.L. (Ed.), Geochemistry of Hydrothermal Ore Deposits. Holt, Rinehart and Winston, New York, 166–235.

- Mikucki, E.J., 1998. Hydrothermal transport and depositional processes in Archaean lode-gold systems: A review. Ore Geol. Rev. 13, 307–321.

- Miller, C.F., Stoddard, E.F., Bradfish, L.J., Dollase, W.A., 1981. Composition of plutonic muscovite. Can. Miner. 19, 25-34.

- Miyashiro, A., 1973. Metamorphism and Metamorphic Belts. Allen and Unwin, London. 492 p.

- Mueller, R.F. & Saxena, S.K., 1977. Chemical Petrology, with Application to the Terrestrial Planets and Meteorites. New York, Springer-Verlag. 396 p.

- Mullis, J., Dubessy, J., Poty, B., O'Neil, J., 1994. Fluid regimes during late stages of a continental collision: physical, chemical and stable isotope measurements of fluid inclusions in fissure quartz from a geotraverse through the Central Alps, Switzerland. *Geochim. Cosmochim. Acta,* 58, 2239–2267.

- Murck B. W., Cambell J. H., 1986. The effects of temperature, oxygen fugacity and melt composition on the behaviour of chromium in basic and ultrabasic melts. *Geochim. cosmochim. Acta*, 50: 1871-1887. London.

- Nesbitt, H.W., Young, G.M., 1982. Early Proterozoic climates and plate motion inferred from major element chemsitry of lutites. Nature 299, 715–717.

- Nesbitt, H.W., Young, G.M., 1984. Predictions of some weathering trends of plutonic and volcanic rocks based on thermodynamic and kinematic consideration. *Geochim. Cosmochim. Acta,* 48, 1523–1534.

- Nesbitt, H.W., Young, G.M., 1989. Formation and diagenesis of weathering profiles. J. Geol. 97, 129–147.

- Opiyo-Akech, N., Tarney, J., Hoshino, M., 1999. Petrology and geochemistry of granites from Archean terrain north of lake Victoria, Western Kenya. Journal of African Earth Sciences, 29, 283–300.

- Pallister, J.S., Stacey, J. S., Fischer, L. B. and Premo, W. R., 1988. Precambrian ophiolites of Arabia: geologic settings, U-Pb geochronlogy, Pb-isotope characteristics, and implications for continental accretion. Precambrian Res., 38: 1-54.

- Passchier C.W. & Trouw R. A. J., 1996. Microtectonics. Springer Verlag, Berlin, 325 p.

- Phillips, G.N., Groves, D.I., 1983. The nature of Archaean gold bearing fluids as deduced from gold deposits from Western Australia. J. Geol. Soc. Aust. 30, 25–40.

- Phillips. G.N. and Groves, D.I., 1984. Fluid access and fluid-wall rock interaction in the genesis of the Archean gold-quartz vein deposit at ZHunt mine, Kambalda. Western Australia. In: R.P. Forater (Editor). Gold '82 - Proc. Int. Symp., Zimbabwe. A.A. Balkemu. Rotterdam. 389-416.

- Phillips, G.N., Groves, D.I., and Martyn, J.E., 1984, An epigenetic origin for Archean banded iron-formation-hosted gold deposits: *Econ. Geol.*, 79, 162-171.

- Pearce, J.A., 1980. Geochemical evidence of the genesis and eruptive setting of lavas from Tethyan ophiolites. Ophiolites, Proceed. Intern. Ophiol. Symp. (Panayiton A., ed.): 261-272. Cyprus.

- Pearce, J.A., 1982. Trace element characteristics of lavas from destructive plate boundaries. *In:* Andesites (Edited by Thorope, R. S) 525-548. John Wiley and Sons, Chichester.

- Pearce, J.A., 1983. The role of sub-continental lithosphere in magma genesis at destructive plate margins. In Hawkesworth, C. J., and Norry, M. J., eds. Continental basalts and mantle xenoliths. Nantwich, Shiva, 230-249.

- Pearce, J.A., 1996. A user's guide to basalt discrimination diagrams. *In* Wyman, D. A., ed. Trace element geochemistry of volcanic rocks: applications for massive sulphide exploration. Short Course Notes, vol. 12. St. John's, Geol. Assoc. Can. Mem. Univ., 79-114.

- Pearce, J.A., and Cann, J.R., 1973. Tectonic setting of basic volcanic rocks determined using trace element analyses. Earth Planet. Sci. Lett. 19:290-300.

- Pearce, J.A., Harris, N.B.W. & Tindle, A.G., 1984a. Trace element discrimination diagrams for the tectonic interpretation of granitic rocks. *J. Petrol.*, 25: 956-983.

- Pearce, J.A., Lippard, S.J. and Roberts, S. 1984b. Characteristics and tectonic significance of supra-subduction zone ophiolites. *In* Kokelaar, B. P., and Howells, M. F. eds. Geology of marginal basins. Spec. Publ. Geol. Soc. Lond. 16:77-94.

- Pearce, T.H., Gorman, B.E., Birkett, T. C., 1977. The relationship between major element chemistry and tectonic environment of basic and intermediate volcanic rocks. Earth Planet. Sci. Lett., 36, 121-132

- Pearce, J.A. and Norry, M J., 1979. Petrogenetic implications of Ti, Zr, Y and Nb variations in volcanic rocks. Contributions Mineralogy Petrology, 69, 33-47.

- Peters, S.G., 1993. Formation of oreshoots in mesothermal gold-quartz vein deposits: examples from Queensland, Australia. Ore Geol. Rev. 8, 277-301.

- Pichavant, M., Ramboz, C., Weisbrod, A., 1982. Fluid immiscibility in natural processes: use and misuse of fluid inclusion data. I. Phase equilibria analysis—a theoretical and geometrical approach. Chem. Geol. 37, 1–27

- Pohl, W., 1988. Precambrian Metallogeny of NE-Africa. In: The Pan-African Belt of NE Africa and Adjacent areas (edited by El Gaby S. And Greiling R. O.), 319-341, Earth Evolution Sci.(Vieweg), Wiesbaden.

- Poirier, J.P. and Guillope, M., 1979. Deformation induced recrystallisation of minerals; Bulletin de Mineralogie, 102, 67-74.

- Potter, R.W. II, Clynne, M.A., Brown, D.L., 1978. Freezing point depression of aqueous sodium chloride solutions. *Econ. Geol.* 73, 284–285.

- Powell, R. and Holland, T. J. B., 1988. An internally consistent dataset with uncertainties and correlations; 3, Applications to geobarometry, worked examples and a computer program. Journal of Metamorphic Geology, 6, 173-204.

- Price, R.C., 1984. Late Precambrian mafic-ultramafic complexes in northeast Africa. Ph.D. Thesis. Open University. Milton Keynes. (unpublished thesis)

- Ramboz, C., Pichavant, M., Weisbrod, A., 1982. Fluid immiscibility in natural processes: use and misuse of fluid inclusion data. II. Interpretation of fluid inclusion data in terms of immiscibility. Chem. Geol. 37, 29–48.

- Raymahashay, B. C. & Holland, H. D., 1969. Redox reactions accompanying hydrothermal wall rock alteration. *Econ. Geol.*, 64, 3, 291-305.

- Reed, M.H., 1997. Hydrothermal alteration and its relationship to ore fluid composition. *In*: H.L. Barnes (ed.) *Geochemistry of Hydrothermal Ore Deposits*. New York, John Wiley & Sons, Inc., 303-365.

- Robert, F., Boullier, A.M., Firdaous, K., 1995. Gold-quartz veins in metamorphic terranes and their bearing on the role fluids in faulting. J. Geophys. Res. 100, 12861–12879.

- Robert, F., Kelly, W.C., 1987. Ore-forming fluids in Archean goldbearing quartz veins at the Sigma Mine, Abitibi greenstone belt, Quebec, Canada. *Econ. Geol.* 82, 1464–1482.

- Robert, F., Sheahan, P.A., Green, S.B., 1991. Greenstone Gold and Crustal Evolution. Geol. Assoc. Can., Mineral Deposits Div. Publ., 252 p.

- Roedder, E., 1984. Fluid inclusions. Mineral. Soc. Am., Rev. Mineral. 12, 644 p.

- Roedder, E., Bodnar, R.J., 1980. Geologic pressure determinations from fluid inclusion studies. Annu. Rev. Earth Planet. Sci. 8, 263–301.

- Rogers, J.J.W., Greenberg, J.K., 1981. Trace elements in continental margin magmatism: Part 3 - Alkali granites and their relationship to cratonization. Geological Society America Bulletin 92, 6-9.

- Rose, A.W. Burt, D.M., 1979. Hydrothermal alteration. In: H.L. Barnes (ed.) *Geochemistry of Hydrothermal Ore Deposits*. New York, John Wiley & Sons, 173-235.

- Sadek, M. F., 1994. Geology, Geochemistry and structure of Gabal Muqsim area and environs, South Eastern Desert, Egypt. Ph. D. Thesis (unpubl.). Faculty of Science, Ain Shams University, Cairo. 274p.

- Saxena, S.K., Fei, Y., 1987. High pressure and high temperature fluid fugacities. Geochim. Cosmochim. Acta 51, 783–791.

- Scott, S.D., 1983. Chemical behaviour of sphalerite and arsenopyrite in hydrothermal and metamorphic environments. Mineral. Mag. 47, 427–435.

- Scott, G.L., 1988. The Fluid–Rock Interaction History of the Tongonan Geothermal Field, Leyte, Philippines. PhD diss., Univ. of Auckland (unpubl), 370 p.

- Seifert, K., Gibson, I., Weis, D., and Brunotte, D., 1996. Geochemistry of metamorphosed cumulate gabbros from Hole 900A, Iberia Abyssal Plain. *In:* Whitmarsh, R.B., Sawyer, D.S., Klaus, A., and Masson, D.G. (Eds.), Proc. ODP, Sci. Results, 149: College Station, TX (Ocean Drilling Program), 471-488.

- Seward, T.M., 1984. The transport and deposition of gold in hydrothermal systems. *In*: Foster, R.P. (Ed.), Gold'82. Geologic Society Zimbabwe. Special Publisher, A.A. Balkema, Rotterdam, 165–182.

- Seward, T.M., 1991. The hydrothermal geochemistry of gold. *In*: Foster, R.P. (Ed.), Gold Metallogeny and Exploration. Blackie and Son, 37–62.

- Shackleton, R. M., 1988. Contrasting structural relationships of Proterozoic Ophiolites in Northeast and Eastern Africa, In: El Gaby and R.O. Grielling (eds). The Pan-African belt of northeast African and adjacent area; Earth Evol. Sci., Veiwag and Sohn, Germany, pp. 183-193.

- Shackletan. R.M.. Ries, A.C., Graham, R.H., Fitches, W.R., 1980. Late Precambrian ophiolite mélange in the Eastern Desert of Egypt. Nature 285, 472-474.

- Shand, S.J., 1947. Eruptive Rocks. Thomas Murby and Co., London, 488 p.

- Sharp, Z.D., Essene, E.J. & Kelly, W.C., 1985. A re-examination of the arsenopyrite geothermometer: pressure considerations and applications to natural assemblages. Can. Mineral. 23, 517-534.

- Shelton, K.L., So, C.S. and Chang, J.S., 1988. Gold rich mesothermal vein deposits of the Republic of Korea: geochemical studies of the Jungwon gold area. *Econ. Geol.* 83, 1221–1237.

- Shepherd, T.J., Rankin, A.H., Alderton, D.H., 1985. A Practical Guide to Fluid Inclusion Studies, Blackie & Son, Glasgow, 239 p.

- Shervais, J.W., 1982. Ti–V plots and the petrogenesis of modern and ophiolitic lavas. Earth Planet. Sci. Lett., 59, 101–118.

- Skippen, G.B., Carmichael, C.M., 1977. Mixed-volatile equilibria. In: Greenwood, H.J. (Ed.), Application of thermodynamics to petrology and ore deposits. Mineralogical Association Canada Short Course Handbook 2, 109-l 25.

- Sibson, R.H., 1992. Fault-valve behavior and the hydrostatic-lithostatic fluid pressure interface. Earth Science Reviews, 32, 141-144.

- Sibson R.H., Robert F. & Poulsen K.H., 1988. High angle reverse faults, fluid-pressure cycling and mesothermal gold–quartz deposits. *Geology*, 16, 551–555.

- Smith, S.E., 1994. Geochemistry and petrology of basaltic and plutonic rocks from the Hayes Transform Region, Mid-Atlantic Ridge [Ph.D. dissert.]. Univ. of Houston, Houston, TX

- Smith Nagihara, S., and Casey, J.F., 2001. Whole-rock geochemistry of amphibolites and metagabbros from the western Iberia margin, Leg 173. *In*: Beslier, M.-O., Whitmarsh, R.B., Wallace, P.J., and Girardeau, J. (Eds.), Proc. ODP, Sci. Results, 173, 1–20. [Online]. Available from <http://www-odp.tamu.edu/publications/>

- Spear, F. S., & Daniel, C. G., 1998. 3-Dimensional imaging of garnet crystal size distribution and chemical zoning. I. Nucleation and growth history in the garnet zone. Geological Materials Research, 1, 48p. (http://gmr.minsocam.org).

- Spooner, E.T.C., Bray, C.J., Wood, P.C., Burrows, D.R., Callan, N.J., 1985. Grant 236 Au–quartz vein and Cu–Au–Ag–Mo– anhydrite mineralization, Hollinger–McIntyre Mines, Timmins, Ontario: $\delta^{13}C$ Values (McIntyre), fluid inclusion gas chemistry, pressure depth estimation, and H_2O–CO_2 phase separation as a precipitation and dilation mechanism. Ont. Geol. Surv. Misc. Paper 127, 229–246.

- Spry, A., 1969. Metamorphic Textures, Oxford, UK, Pergamon Ltd, 350 p.

- Starling, A., Gilligan, J.M., Carter, A.H.C., Foster, R.P., Saunders, R.A., 1989. High-temperature hydrothermal precipitation of precious metals on the surface of pyrite. Nature 340, 298–300.

- Stern, R.J., 1994. Arc Assembly and Continental Collision in the Neoproterozoic East African Orogen: Implications for the Consolidation of Gondwanaland. Annual Reviews of Earth and Planetary Sciences, 22, 319-351.

- Stern, R.J., Kröner, A., Manton, W.I., Reischmann, T., Mansour, M., Hussein, I.M., 1989. Geochronology of the late Precambrian Hamisana shear zone, Red Sea Hills, Sudan and Egypt. Journal of the Geological Society (London) 146, 1017–1030.

- Stipp, M., Stünitz, H., Heilbronner, R., Schmid, S.M., 2002. Dynamic recrystallization of quartz: correlation between natural and experimental conditions. In: De Meer, S., Drury, M.R., De Bresser, J.H.P., Pennock, G.M. (Eds.), Deformation Mechanisms, Rheology and Tectonics: Current Status and Future Perspectives. Geological Society, London, Special Publications 200, 171–190.

- Streckeisen, A. 1976. To each plutonic rock its proper name. Earth Science Review 12, 1-33.

- Sultan, M., Tucker, R.D., Gharbawi, R.I., Ragab, A.I., El-Alfy, Z., 1993. On the location of the boundary between the Nubian Shield and the old African continent: Inferences from U-Pb (zircon) and common Pb data. In: Thorweihe, U., Schandelmeier, H. (Eds.), Geoscientific Research in North-East Africa. A.A. Balkema, Rotterdam, The Netherlands, 75-77.

- Sun, S.S., Nesbitt, R.W., 1977. Chemical heterogeneity of the Archaean mantle, composition of the bulk earth and mantle evolution. Earth Planet. Sci. Lett. 35, 429–448.

- Sun, S.S., and McDonough, W. F., 1989. Chemical and isotopic systematics of oceanic basalts: implications for mantle composition and processes. *In* Saunders, A. D., and Norry, M. J., eds. Magmatism in the ocean basins. Spec. Publ. Geol. Soc. Lond. 42:313-345.

- Susak, N.J., 1994. Alteration factors affecting ore deposition. In: D.R. Lenz (ed.) Alteration and Alteration Processes Associated with Ore-Forming Systems. St. John's, Canada, Geol. Assoc. Canada, 115-130 (Short Course Notes 11).

- Takla, M. A., Basta, E. Z. and Fawzi, E., 1981. Characterization of the older and younger gabbros of Egypt. Delta Journal of Science 5, 279-314.

- Taylor, W. E., El Kazzaz, Y. A. and Rashwan, A. A., 1993. An outline of the tectonic framework for the Pan-African orogeny in the vicinity of Wadi Um Relan, SE Desert. In: Thorweihe U, Schandermeier H (eds) Geoscientific Research in NE Africa. Balkema, Rotterdam, 31-34.

- Thiéry, R., Van den Kerkhof, A.M., Dubessy, J., 1994. VX properties of CH_4–CO_2 and CO_2–N_2 fluid inclusions: modelling for T<31°C and P<400 bars. Eur. J. Mineral. 6, 753–771.

- Touret, J.L.R., 1981. Fluid inclusions in high grade metamorphic rocks. *In*: Hollister, L.S., Crawford, M.L. Eds. , Short Course in Fluid Inclusions: Applications to Petrology. Mineralogical Association of Canada, 6, 182–207.

- Trdlička, Z., Hoffman, V., 1976. Untersuchungen der chemischen Zusammensetzung der Gangkarbonate von Kutná Hora (ČSSR). -Freib. Forschungshefte, C321, 29-81.

- Unrug, R., 1997. "Rodinia to Gondwana; the geodynamic map of Gondwana supercontinent assembly." GSA Today 7(1): 1-6.

- Vail, J.R., 1983. Pan-African crustal accretion in NE Africa. J. Afr. Earth Sci. 1, 285–294.

- Vernon, R.H., 1976. Metamorphic Processes: Reactions and Microstructure Development. George Allen & Unwin, London.

- Vetter, U., Tessensohn, F., 1987. S- and I-type granitoids of North Victoria Land, Antarctica, and their inferred geotectonic setting. Geologische Rundschau 76, 233–243.

- Vollbrecht A., Stipp, M., Olesen, N. O., 1999. Crystallographic orientation of microcracks in quartz and inferred deformation processes: a study on genesis from the German Continental Deep Drilling Project (KTB). Tectonophysics, 303, 279-297.

- Walsh, J.F., Kesler, S.E., Duff, D., Cloke, P.L., 1988. Fluid inclusion geochemistry of high grade, vein hosted gold ore at the Parmour Mine, Porcupine Camp, Ontario. *Econ. Geol.* 83, 1347–1367.

- Weaver, B.L., Tarney, J., 1981. The Scourie dyke suite: petrogenesis and geochemical nature of the Proterozoic subcontinental mantle. Contrib. Mineral. Petrol. 78, 175–188.

- Wilkins. R.W.T., 1990. The relative chronology of fluid inclusions in minerals. In: Herbert, H.K., Ho, S.E. (Eds.), Stable Isotopes and Fluid Processes in Mineralization. Geology Department and University Extension, The University of Western Australia, Publ. 23, 371–382.

- Wilkinson, J., 2001. Fluid inclusions in hydrothermal ore deposits. *Lithos* 55, 229–272.

- Winchester, J.A., Floyd, P.A., 1976. Geochemical magma type discrimination: application to altered and metamorphosed basic igneous rocks. Earth Planetary Sci. Letters 28, 459-469.

- Winchester, J.A., Floyd, P.A., 1977. Geochemical discrimination of different magma series and their differentiation products using immobile elements. *Chemical Geology* 20, 325–343.

- Windley B. F., 1992. Proterozoic collisional and accretionary orogens; In Proterozoic crustal evolution, (ed) K. C. Condie (Amsterdam: Elsevier), 419-446.

- Winkler, H. G. F., 1976. Petrogenesis of Metamorphic Rocks. Springer Verlay, 334 p.

- Wood, D. A., 1980. The application of Th-Hf-Ta diagram to problems of tectonomagmatic classification and to establishing the nature of crustal contamination of basaltic lavas of the British Tertiary volcanic province; Earth Planet. Sci. Lett., 50, 11-30.

- Wu, Xin & Delbove, F., 1989. Hydrothermal synthesis of gold-bearing arsenopyrite. *Econ. Geol.* 84, 2029-2032.

- Zhang, Y., Frantz, JD., 1987. Determination of the homogenization temperatures and densities of supercritical fluids in the system NaCl-KCl-$CaCl_2$-H_2O using synthetic fluid inclusions. *Chem. Geol.* 64, 335-350

APPENDICES

Appendix A: Landsat TM images of the Um El Tuyor area

Fig. A.1: TM image of Um El Tuyor area, bands 7-4-1 (R-G-B)
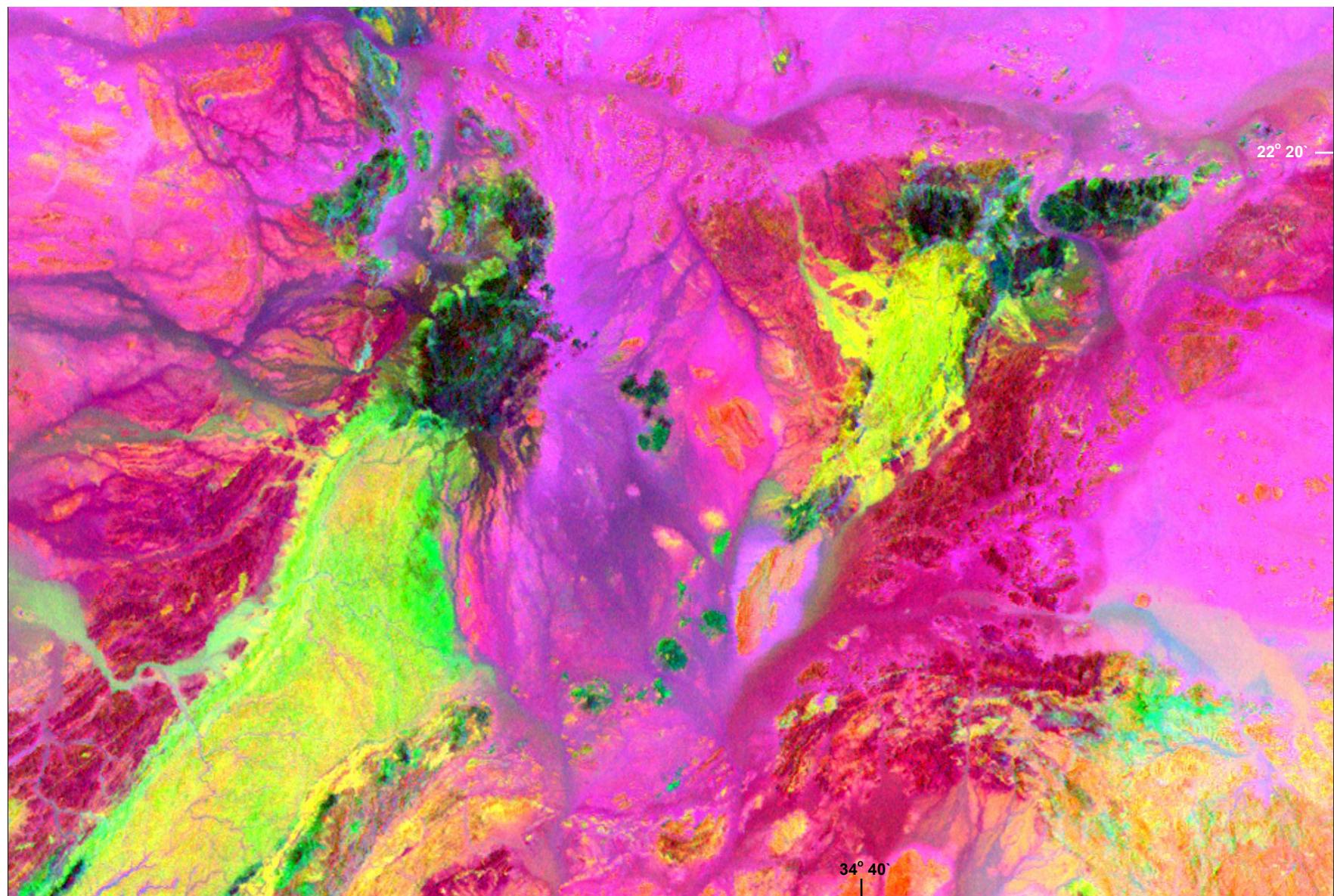
Fig. A.2: Landsat TM ratio image (5/7 as red, 4/5 as green, and 3/1 as blue) of a large part of the Um El Tuyor area (Band rationing and multiplication technique after Abrams et al., 1983)

Appendix B: The geothermobarometry data and results

Chemical analyses of the metamorphic minerals in samples representing the island arc assemblage were carried out using a Jeol JSM-6310 electron microprobe at the Institute of Geology and Mineralogy, Graz University, Austria. The measuring conditions were 15 kV, 30 *n*A, defocused electron beam with a diameter of 5-10 μm.

Table B.1: Electron microprobe data of chlorite and garnet in the metapelites rocks exposed in the Um El Tuyor area

	Chlorite inclusions in garnet porphyroclasts									Profile across a large garnet porphyroblast						
Spot no.	chl.1_2	chl.1_9	chl.1_8	chl.1_7	chl.2_incl	chl.2_incl	chl.3_incl	chl.3_incl		>>>>>>	>>>>>	>>>>>>	core	core	<<<<<<<	<<<<<<<
SiO_2	24.41	24.13	24.85	24.69	23.31	23.63	22.62	22.03	SiO_2	39.06	38.33	36.66	36.51	36.12	35.84	38.29
TiO_2	0.82	0.78	0.79	0.81	0.93	0.88	0.79	0.81	TiO_2	0.000	0.012	0.240	0.185	0.200	0.118	0.061
Al_2O_3	22.72	23.91	23.42	22.24	23.74	23.81	24.71	24.89	Al_2O_3	17.23	17.37	16.62	16.54	16.96	17.55	17.17
FeO	23.12	23.66	23.57	23.88	22.76	22.47	22.56	22.14	FeO	36.87	35.65	34.61	33.93	34.51	34.55	35.75
MnO	0.08	0.103	0.121	0.24	0.31	0.42	0.42	0.44	MnO	2.68	4.81	7.82	10.35	9.45	7.39	5.82
MgO	15.93	16.031	16.15	15.98	16.07	16.32	16.66	17.05	MgO	1.564	1.564	0.839	0.761	0.768	1.016	1.489
CaO	0.05	0.08	0.102	0.11	0.13	0.09	0.11	0.204	CaO	2.636	2.849	3.518	3.701	3.578	3.342	2.782
K_2O	0.05	0.00	0.00	0.00	0.00	0.00	0.002	0.007	K_2O	0.013	0.005	0.002	0.003	0.002	0.003	0.002
F	0.24	0.198	0.117	0.02	0.03	0.01	0.012	0.00	Totals	100.06	100.59	100.32	101.98	101.89	99.82	101.36
Total	87.16	88.69	89.01	87.94	87.25	87.62	87.87	87.57								
Formula on 28 anions (anhydrous basis)									Formula on 12 oxygens							
Si	5.123	4.984	5.106	5.158	4.894	4.929	4.716	4.610	Si	3.191	3.249	3.235	3.026	3.027	3.004	3.124
Ti	0.126	0.121	0.122	0.128	0.147	0.138	0.124	0.127	Ti	0.000	0.001	0.015	0.012	0.012	0.007	0.004
Al^{iv}	2.877	3.016	2.894	2.842	3.106	3.071	3.284	3.390	Al	1.660	1.649	1.598	1.616	1.648	1.735	1.652
Al^{vi}	2.742	2.804	2.777	2.634	2.767	2.781	2.788	2.748	Fe^{+2}	2.520	2.402	2.361	2.351	2.379	2.423	2.440
Fe^{2+}	4.057	4.086	4.050	4.172	3.995	3.919	3.933	3.874	Mn	0.186	0.192	0.333	0.727	0.660	0.525	0.402
Mn	0.014	0.018	0.021	0.042	0.055	0.074	0.076	0.078	Mg	0.191	0.188	0.102	0.094	0.094	0.127	0.181
Mg	4.984	4.936	4.944	4.977	5.029	5.075	5.178	5.319	Ca	0.231	0.246	0.307	0.329	0.316	0.300	0.243
Ca	0.011	0.018	0.022	0.023	0.029	0.020	0.025	0.046	K	0.001	0.001	0.000	0.000	0.000	0.000	0.000
K	0.013	0.000	0.000	0.000	0.000	0.000	0.001	0.002	Total	7.979	7.926	7.952	8.155	8.137	8.121	8.046
Cations	19.948	19.984	19.936	19.976	20.023	20.007	20.125	20.194	Endmembers							
CF	0.159	0.129	0.076	0.013	0.020	0.007	0.008	0.000	Alm	80.588	75.917	71.309	67.168	68.974	71.787	74.699
Fe/(Fe+Mg)	0.449	0.453	0.450	0.456	0.443	0.436	0.432	0.421	Py	6.096	5.939	3.080	2.687	2.738	3.763	5.545
Fe^{3+}	0.145	0.044	0.178	0.067	-	-	-	-	Sp	5.936	10.372	16.325	20.756	19.127	15.553	12.310
Si/Al	0.91	0.86	0.90	0.94	0.83	0.84	0.78	0.75	Gro	7.380	7.772	9.287	9.388	9.161	8.896	7.446
Al^{iv}_c	3.191	3.333	3.209	3.161	3.416	3.376	3.586	3.685								
* T(^{o}C)	**356.29**	**371.28**	**358.17**	**353.01**	**380.13**	**375.90**	**398.12**	**408.61**								

* temperature estimates calculated according to Cathelineau (1988), Al^{iv}_c =correction for the Al^{iv} after Kranidiotis & McLean (1987), Fe^{3+} calculated by means of Fe^{+3} calculated according to Droop (1987)

Table B.2: Electron microprobe data of selected garnet and staurolite porphyroblasts in the metapleites exposed in the study area

garnet

	xal1_9	xal1_1	xal1_3	xal1_5	xal1_4	xal4_3	Xal4_1
SiO_2	37.73	38.18	37.18	37.97	37.84	38.02	38.04
TiO_2	0.03	0.00	0.01	0.00	0.00	0.00	0.00
Al_2O_3	21.37	21.82	21.32	21.67	21.62	21.31	21.82
FeO	32.32	32.17	33.64	32.61	33.09	34.57	34.17
MnO	1.31	1.25	1.36	1.30	1.28	0.57	1.03
MgO	3.75	3.69	3.07	3.07	2.88	3.44	3.19
CaO	2.29	2.12	2.37	2.33	3.01	2.26	2.12
Total	98.80	99.23	98.94	98.95	99.71	100.17	100.36
Structural formula on basis of 12 oxygens							
Si	3.03	3.04	3.01	3.04	3.02	3.03	3.02
Ti	0.00	0.00	0.00	0.00	0.00	0.00	0.00
Al	2.02	2.05	2.03	2.05	2.04	2.00	2.04
$Fe^{(ii)}$	2.17	2.14	2.27	2.19	2.21	2.30	2.27
Mn	0.09	0.08	0.09	0.09	0.09	0.04	0.07
Mg	0.45	0.44	0.37	0.37	0.34	0.41	0.38
Ca	0.20	0.18	0.21	0.20	0.26	0.19	0.18
Total	7.96	7.93	7.98	7.93	7.96	7.97	7.96
T2	4.82	4.79	4.86	4.82	4.80	4.79	4.77
X_{fe}	0.83	0.83	0.86	0.86	0.87	0.85	0.86
X_{ca}	0.07	0.06	0.07	0.07	0.09	0.07	0.06
X_{mn}	0.03	0.03	0.03	0.03	0.03	0.01	0.02
Endmembers							
Py	15.45	15.40	12.56	12.91	11.82	13.89	13.04
Alm	74.70	75.28	77.29	76.92	76.30	78.26	78.35
Gro	6.78	6.36	6.98	7.06	8.88	6.55	6.23
Sp	3.07	2.96	3.16	3.11	2.99	1.30	2.38

staurolite

	stau_9	stau_7	stau_11	stau_13	stau_3	stau_4	stau_8	stau_2	stau_1	stau_16	stau_19	stau_5	stau_19
SiO_2	23.97	24.05	24.41	23.40	23.21	24.79	25.62	24.96	26.05	24.60	24.86	25.88	24.94
TiO_2	0.59	0.57	0.58	0.59	0.59	0.60	0.61	0.63	0.55	0.56	0.59	0.59	0.55
Al_2O_3	57.16	57.26	57.44	57.55	57.36	56.71	56.09	56.32	56.30	57.43	56.73	56.20	57.63
FeO	13.07	12.82	12.69	13.03	13.01	12.88	12.95	12.56	12.53	12.62	12.63	12.57	12.14
MnO	0.21	0.21	0.19	0.21	0.22	0.16	0.13	0.12	0.13	0.14	0.21	0.15	0.21
MgO	2.51	2.54	2.39	2.54	2.61	2.44	2.49	2.38	2.50	2.44	2.52	2.45	2.36
CaO	0.01	0.00	0.00	0.00	0.01	0.00	0.01	0.00	0.00	0.00	0.01	0.02	0.00
Na_2O	0.00	0.00	0.00	0.00	0.00	0.00	0.00	0.00	0.00	0.00	0.00	0.00	0.00
K2O	0.08	0.03	0.03	0.03	0.02	0.01	0.02	0.02	0.01	0.02	0.04	0.03	0.03
Total	97.60	97.48	97.73	97.35	97.03	97.59	97.92	96.99	98.07	97.81	97.59	97.89	97.86
Structural formula on basis of 48 oxygens													
Si	6.98	7.00	7.08	6.84	6.81	7.20	7.41	7.28	7.50	7.12	7.21	7.47	7.19
Ti	0.13	0.12	0.13	0.13	0.13	0.13	0.13	0.14	0.12	0.12	0.13	0.13	0.12
Al	19.62	19.64	19.62	19.81	19.82	19.41	19.12	19.36	19.10	19.58	19.40	19.11	19.59
$Fe^{(ii)}$	3.18	3.12	3.08	3.18	3.19	3.13	3.13	3.06	3.02	3.05	3.06	3.03	2.93
Mn	0.05	0.05	0.05	0.05	0.05	0.04	0.03	0.03	0.03	0.03	0.05	0.04	0.05
Mg	1.09	1.10	1.03	1.11	1.14	1.06	1.07	1.03	1.07	1.05	1.09	1.05	1.01
Ca	0.00	0.00	0.00	0.00	0.00	0.00	0.00	0.00	0.00	0.00	0.00	0.01	0.00
Na	0.00	0.00	0.00	0.00	0.00	0.00	0.00	0.00	0.00	0.00	0.00	0.00	0.00
K	0.03	0.01	0.01	0.01	0.01	0.00	0.01	0.01	0.00	0.01	0.01	0.01	0.01
Total	31.09	31.06	30.99	31.13	31.16	30.97	30.90	30.91	30.84	30.97	30.97	30.85	30.90
T2	17.50	17.49	17.42	17.55	17.62	17.45	17.37	17.52	17.29	17.38	17.43	17.34	17.33
X_{Fe}	0.74	0.74	0.75	0.74	0.74	0.75	0.74	0.75	0.74	0.74	0.74	0.74	0.74

Table B.3: Data used in and results obtained from geothermobarometry of the investigated metapelites

point no	bt_2_2	grt_2_5	mus_2_7	plag_2_6	bt_3_7	grt_3_5	mus_3_3	plag_3_6	bt_5_3	grt_5_4	mus_5_4	plag_5_8
SiO_2	28.380	38.180	46.890	62.613	29.170	37.178	47.910	62.809	29.310	38.030	48.770	62.330
TiO_2	0.360	0.000	0.822	-	0.340	0.007	0.618	-	0.352	0.000	0.723	
Al_2O_3	20.710	21.820	33.180	24.352	21.000	21.320	32.177	22.993	20.890	21.760	32.870	23.880
FeO	22.370	32.170	1.300	0.000	24.230	33.640	1.325	0.000	22.020	33.270	1.230	0.000
MnO	0.090	1.250	0.051	-	0.100	1.360	0.000	-	0.102	1.250	0.074	
MgO	17.960	3.690	1.266	-	17.460	3.067	1.629	-	16.430	3.072	0.932	
CaO	0.030	2.120	0.030	5.570	0.010	2.370	0.000	4.540	0.030	2.330	0.040	4.320
Na_2O	0.000	-	0.004	8.491	0.000	-	0.209	8.590	0.000		0.005	8.730
K_2O	4.630	-	10.962	0.018	4.670	-	10.562	0.038	5.560		9.880	0.018
Cl	0.000	-	0.000	-	0.000	-	0.000	-	0.000		0.000	
F	0.190	-	0.166	-	0.190	-	0.258	-	0.130		0.123	
TOTAL	94.073	99.230	94.024	101.000	96.523	98.946	94.041	98.971	94.177	99.712	94.000	99.278
O=F,Cl	0.080	-	0.070	-	0.080	-	0.109	-	0.055		0.052	
No Anions	22	12	22	8	22	12	22	8	22.000	12.000	22.000	8.000
Formula												
Si	4.383	3.041	6.301	2.745	4.319	3.005	6.423	2.800	4.520	3.033	6.481	2.771
Ti	0.042	0.000	0.083	-	0.080	0.000	0.062		0.041	0.000	0.072	
Al	3.769	2.048	5.255	1.258	3.840	2.031	5.084	1.208	3.797	2.045	5.147	1.251
Fe(ii)	2.889	2.143	0.146	0.000	2.969	2.274	0.149	0.000	2.840	2.218	0.137	0.000
Mn	0.012	0.084	0.006	-	0.013	0.093	0.000	-	0.013	0.084	0.008	
Mg	4.135	0.438	0.254	-	3.967	0.370	0.326	-	3.778	0.365	0.185	
Ca	0.005	0.181	0.004	0.262	0.002	0.205	0.000	0.217	0.005	0.199	0.006	0.206
Na	0.000	-	0.001	0.722	0.000	-	0.054	0.742	0.000		0.001	0.752
K	0.912	-	1.879	0.001	0.984	-	1.806	0.002	1.094		1.675	0.001
Cl	0.000	-	0.000	-	0.000	0.070	0.000	-	0.000		0.000	
F	0.093	-	0.071	-	0.081	-	0.109	-	0.063		0.052	
TOTAL	16.147	7.935	13.929	4.987	16.173	7.979	13.903	4.969	16.087	7.945	13.711	4.981
T2	9.279	4.785	8.074	2.634	9.109	4.856	8.054	-	9.266	4.791	7.983	2.671
Fe/(Fe+Mg)	0.411	0.830	0.365	-	0.428	0.860	0.313	-	0.429	0.859	0.425	

- Results Summary

Al-silicate polymorph   Sil

Garnet model used   HW

Garnet-Biotite Thermometer	T(°C)						T(°C)				T(°C)
Bhattacharya et al. 1992	**561.4**						**534.2**				**537.7**

Geobarometers	P(kbar)						P(kbar)				P(kbar)
GASP											
Grs + 2Ky/Sil + Qtz = 3 An	**5.58**						**5.98**				**6.20**

bt: biotite, grt: garnet, mus: muscovite, plag: plagioclase. Holland & Powell 1998 data set calibrations

continue

Geothermobarometry of the investigated metapelites

point no	bt_7_1	grt_7_3	mus_7_6	plag_7_7	bt_8_8	grt_8_4	mus_8_1	plag_8_7	bt_9_3	grt_9_2	mus_9_4	plag_9_5	bt_4_3	grt_4_1	mus_4_6	plag_4_4
SiO2	29.170	37.84	48.740	61.194	28.050	38.024	49.402	63.194	29.140	38.038	48.878	62.394	29.800	37.970	48.200	62.440
TiO2	0.340	0.00	0.857		0.820	0.000	0.520		0.500	0.000	0.417		0.560	0.000	0.760	-
Al2O3	21.000	21.62	32.980	24.543	22.730	21.312	30.869	23.543	20.320	21.820	30.930	23.543	20.910	21.670	32.380	24.084
FeO	24.230	33.09	1.473	0.000	21.970	34.572	1.480	0.000	23.186	34.170	1.720	0.000	23.440	32.607	1.350	0.000
MnO	0.100	1.28	0.970		0.080	0.565	0.000		0.100	1.025	2.401		0.080	1.300	1.310	-
MgO	17.460	2.88	0.158		17.140	3.443	2.320		17.880	3.190	0.360		16.930	3.070	0.027	-
CaO	0.010	3.01	0.061	6.103	0.490	2.258	0.052	5.134	0.050	2.120	0.050	5.440	0.010	2.335	0.000	5.460
Na2O	0.000		0.216	8.010	0.000	-	0.193	9.098	0.090		0.161	9.201	0.000	-	0.242	8.810
K2O	4.670		10.310	0.021	5.370	-	10.230	0.012	6.120		10.380	0.031	4.740	-	10.359	0.018
Cl	0.000		0.000		0.000	-	0.000		0.000		0.000		0.000	-	0.000	-
F	0.190		0.173		0.250	-	0.270		0.160		0.280		0.000	-	0.158	-
Total	96.52	99.71	95.29	99.80	96.25	100.17	94.69	100.98	96.89	100.36	94.93	100.61	95.82	98.95	94.14	100.81
O=F,Cl	0.080		0.073		0.105		0.114		0.067		0.118		0.000		0.067	
No Anions	22	12		8	22	12		8	22.000	12.000	22.000	8.000	22	12	22	8
Formula																
Si	4.415	3.024	6.451	2.718	4.243	3.029	6.562	2.773	4.417	3.021	6.561	2.755	4.511	3.044	6.470	2.747
Ti	0.039	0.000	0.085		0.093	0.000	0.052		0.057	0.000	0.042		0.064	0.000	0.077	-
Al	3.746	2.036	5.145	1.285	4.052	2.000	4.832	1.217	3.630	2.042	4.893	1.225	3.730	2.047	5.122	1.249
Fe(ii)	3.067	2.211	0.163	0.000	2.779	2.303	0.164	0.000	2.939	2.269	0.193	0.000	2.967	2.186	0.152	0.000
Mn	0.013	0.087	0.109		0.010	0.038	0.000		0.013	0.069	0.273		0.010	0.088	0.149	-
Mg	3.940	0.343	0.031		3.865	0.409	0.459		4.041	0.378	0.072		3.820	0.367	0.005	-
Ca	0.002	0.257	0.009	0.290	0.079	0.193	0.007	0.241	0.008	0.180	0.007	0.257	0.002	0.200	0.000	0.257
Na	0.000		0.055	0.690	0.000	-	0.050	0.774	0.026		0.042	0.788	0.000	-	0.063	0.751
K	0.902		1.741	0.001	1.036	-	1.733	0.001	1.183		1.777	0.002	0.915	-	1.774	0.001
Cl	0.000		0.000		0.000	-	0.000		0.000		0.000		0.000	-	0.000	-
F	0.091		0.072	4.985	0.120	-	0.113		0.077		0.119		0.000	-	0.067	-
TOTAL	16.124	7.958	13.789		16.156	7.971	13.861	5.006	16.315	7.958	13.860	5.027	16.018	7.933	13.811	5.005
T2	9.094	4.801	7.952	2.669	9.087	4.785	7.981	2.636	9.108	4.771	8.065	2.653	9.094	4.816	8.064	2.643
Fe/(Fe+Mg)	0.438	0.866	0.839		0.418	0.849	0.264		0.421	0.857	0.728		0.437	0.856	0.966	-

Garnet-Biotite Thermometer	T(°C)				T(°C)				T(°C)				T(°C)			
Bhattacharya et al. 1992	536.1				545.9				534.7				546.1			

Geobarometers	P(kbar)				P(kbar)				P(kbar)				P(kbar)			
GASP																
Grs + 2Ky/Sil + Qtz = 3 An	5.97				5.80				5.26				5.81			

Table B.4: Composition and temperature estimates of the garnet-staurolite pairs in the metapelites exposed in the Um El Tuyor area

	xal 1_1	str.2	xal 1_3	str_4	xal 1_4	str_7	xal 4_1	str_9	Xal 4_4	str_3	Xal 6_7	str_21	Xal 3_2	str_25	Xal 2_1	str_32	xal 1_5	str_22
SiO_2	38.18	23.97	37.18	24.41	37.84	24.79	38.02	24.96	38.04	24.41	37.29	26.05	37.40	23.21	38.74	24.05	37.18	25.88
TiO_2	0.00	0.59	0.00	0.58	0.00	0.60	0.00	0.63	0.00	0.58	0.00	0.55	0.00	0.59	0.00	0.57	0.01	0.59
Al_2O_3	21.82	57.16	21.83	57.44	21.62	56.71	21.31	56.32	21.82	57.44	21.81	56.30	21.52	57.36	21.53	57.26	21.32	56.20
FeO	32.17	13.07	32.02	12.69	33.09	12.88	34.57	12.56	34.17	12.69	32.99	12.53	32.81	13.01	32.11	12.82	33.64	12.57
MnO	1.25	0.21	0.97	0.19	1.28	0.16	0.57	0.12	1.03	0.19	1.37	0.13	1.40	0.22	1.08	0.21	1.36	0.15
MgO	3.69	2.51	3.58	2.39	2.88	2.44	3.44	2.38	3.19	2.39	3.78	2.50	3.54	2.61	3.49	2.54	3.07	2.45
CaO	2.12	0.01	2.76	0.00	3.01	0.00	2.26	0.00	2.12	0.00	2.12	0.00	2.97	0.01	1.68	0.00	2.37	0.02
Na_2O		0.00		0.00		0.00		0.00		0.00		0.00		0.00		0.00		0.00
K2O		0.08		0.03		0.01		0.02		0.03		0.01		0.02		0.03		0.03
TOTAL	99.23	97.60	98.33	97.73	99.71	97.59	100.17	96.99	100.36	97.73	99.36	98.07	99.65	97.03	98.64	97.48	98.94	97.89

Structural formulae on basis of 12 oxygen atoms for garnet and 48 oxygen atoms for staurolite (anhydrous basis)

	xal 1_1	str.2	xal 1_3	str_4	xal 1_4	str_7	xal 4_1	str_9	Xal 4_4	str_3	Xal 6_7	str_21	Xal 3_2	str_25	Xal 2_1	str_32	xal 1_5	str_22
Si	3.04	6.98	3.00	7.08	3.02	7.20	3.03	7.28	3.02	7.08	2.99	7.50	2.99	6.81	3.09	7.00	3.01	7.47
Ti	0.00	0.13	0.00	0.13	0.00	0.13	0.00	0.14	0.00	0.13	0.00	0.12	0.00	0.13	0.00	0.12	0.00	0.13
Al	2.05	19.62	2.07	19.62	2.04	19.41	2.00	19.36	2.04	19.62	2.06	19.10	2.03	19.82	2.03	19.64	2.03	19.11
Fe(ii)	2.14	3.18	2.16	3.08	2.21	3.13	2.30	3.06	2.27	3.08	2.21	3.02	2.20	3.19	2.14	3.12	2.27	3.03
Mn	0.08	0.05	0.07	0.05	0.09	0.04	0.04	0.03	0.07	0.05	0.09	0.03	0.09	0.05	0.07	0.05	0.09	0.04
Mg	0.44	1.09	0.43	1.03	0.34	1.06	0.41	1.03	0.38	1.03	0.45	1.07	0.42	1.14	0.42	1.10	0.37	1.05
Ca	0.18	0.00	0.24	0.00	0.26	0.00	0.19	0.00	0.18	0.00	0.18	0.00	0.26	0.00	0.14	0.00	0.21	0.01
Na		0.00		0.00		0.00		0.00		0.00		0.00		0.00		0.00		0.00
K		0.03		0.01		0.00		0.01		0.01		0.00		0.01		0.01		0.01
Total	7.93	31.09	7.97	30.99	7.96	30.97	7.97	30.91	7.96	30.99	7.98	30.84	7.99	31.16	7.89	31.06	7.98	30.85
T2	4.79	17.50	4.84	17.42	4.80	17.45	4.79	17.52	4.77	17.42	4.81	17.29	4.81	17.62	4.80	17.49	4.86	17.34
Xfe	0.83	0.74	0.83	0.75	0.87	0.75	0.85	0.75	0.86	0.75	0.83	0.74	0.84	0.74	0.84	0.74	0.86	0.74
Xca	0.06		0.08		0.09		0.07		0.06		0.06		0.09		0.05		0.07	
Xmn	0.03		0.02		0.03		0.01		0.02		0.03		0.03		0.03		0.03	
Endmembers																		
Py	15.40		14.86		11.82		13.89		13.04		15.37		14.23		14.97		12.56	
Alm	75.28		74.62		76.30		78.26		78.35		75.26		73.98		77.21		77.29	
Gro	6.36		8.24		8.88		6.55		6.23		6.20		8.59		5.18		6.98	
Sp	2.96		2.28		2.99		1.30		2.38		3.17		3.20		2.64		3.16	

continued

Temperature estimates

	xal 1_1 str.2	xal 1_3 str_4	xal 1_4 str_7	xal 4_1 str_9	Xal 4_4 str_3	Xal 6_7 str_21	Xal 3_2 str_25	Xal 2_1 str_32	xal 1_5 str_22
P (kbar)	5.5	5.5	5.5	5.5	5.5	5.5	5.5	5.5	5.5
XFe st=yf	0.745	0.747	0.748	0.748	0.749	0.738	0.737	0.739	0.745
YFe grt=xf	0.830	0.834	0.866	0.849	0.857	0.830	0.839	0.838	0.860
Xca grt=xCa	0.064	0.082	0.089	0.065	0.062	0.062	0.086	0.052	0.070
X Mn grt=xMn	0.030	0.023	0.030	0.013	0.024	0.032	0.032	0.026	0.032
ym	0.255	0.253	0.252	0.252	0.251	0.262	0.263	0.261	0.255
Xm	0.170	0.166	0.134	0.151	0.143	0.170	0.161	0.162	0.140
lnk	0.224	0.231	0.338	0.277	0.305	0.241	0.269	0.260	0.324
gFe	0.088	0.085	0.057	0.071	0.064	0.088	0.080	0.081	0.061
gMg	1.126	1.143	1.301	1.217	1.257	1.127	1.166	1.161	1.272
Z1	-61.110	-61.405	-61.562	-61.728	-61.755	-59.829	-59.643	-60.065	-61.105
Z2	-60.978	-61.143	-61.316	-61.890	-61.868	-59.691	-59.249	-60.164	-61.043
N	-0.072	-0.073	-0.078	-0.075	-0.077	-0.072	-0.073	-0.073	-0.077
t(K)	844.89	840.00	786.04	822.12	807.62	828.51	808.13	821.88	792.73
T(°C)	**571.69**	**566.80**	**512.84**	**548.92**	**534.42**	**555.31**	**534.93**	**548.68**	**519.53**

Calculations methods are taken from Koch-Müller, (1997)

Appendix C: The geochemical data

For major (e.g. Si, Al, Fe, Mg, K, Na and Ca) and trace (e.g. P, Ti, V, Cr, Mn, Co, Ni, Cu, Zn, Sr, Zr, Rb U, Th and Ba) element analyses, structural water was removed from sample powders by heating in a furnace at 1000°C for 30 minutes. H_2O^- was determined by weight loss of sample powders after 12 hour heating at 110°C. The H_2O^+ and CO_2 were then determined by weight the heating dry powders in a furnace at ~1070°C (for 45 minutes). The major and trace element analyses were performed on solutions in which the rock powders and the $LiBO_2$ flux had been mixed, fused, and then dissolved in 1.5 normative HNO_3. REE (La, Ce, Nd, Sm, Eu, Gd, Dy, Er, and Yb), Y, and Hf analyses were conducted on solutions in which these elements had been isolated using standard cation exchange techniques. A detailed description of sample preparation and dilution methods is given in Smith (1994). Major and trace elements were analyzed by ICP-AES and ICP-MS at the laboratories of Nuclear Material Authorities, Egypt. Accuracy for major elements is 2%, and for trace elements is 10%. In order to determine trace elements and REE of the ophiolitic rocks and the metasediments, samples were sintered with Na_2O_2, dissolved in HNO_3 and have been analyzed by ICP-MS at the Institute of geological Sciences, university of Vienna (Austria), following the procedures of Barrat et al. (1996).

Mg# $(Mg/[Mg+Fe^{2+}+Mn])$ is calculated using an assumed $Fe^{3+}/(Fe^{2+}+Fe^{3+})$ ratio of 0.14. Rare earth elements concentrations have been normalized to chondrite from Sun and McDonough (1989). Eu anomalies (Eu/Eu*) have been calculated as $Eu/Eu^*=(Eu)_N/[(Sm)_N\times(Gd)_N]^{0.5}$ and similarly calculated the Sr/Sr*, Zr/Zr*, and Ti/Ti* anomalies as $Sr/Sr^*=(Sr)_N/[(Ce)_N\times(Nd)_N]^{0.5}$, $Zr/Zr^*=(Zr)_N/[(Nd)_N\times(Sm)_N]^{0.5}$, and $Ti/Ti^*=(Ti)_N/[(Gd)_N\times(Dy)_N]^{0.5}$ (after McLennan, 1989).

Table C.1: Geochemical data and normative values of serpentinite rocks exposed in the Um El Tuyor area

Sample no.	Major oxide concentrations (wt %) and normative values								Sample no.	Incompatible trace elements and REE (in ppm)					
	5	5(e)	6(e)	7	7(e)	8	9(w)	10		5	5(e)	6(e)	7	10	9(w)
SiO_2	36,34	36,23	37,09	38,88	38,38	40,58	40,98	41,04	Ba	45	51	47	22	23	23
TiO_2	0,71	0,49	0,44	0,54	0,69	0,97	1,05	1,46	Rb	2	3	2	3	2	2
Al_2O_3	0,72	0,53	1,32	0,91	3,08	1,59	1,82	1,04	Sr	170	182	179	121	118	119
Fe_2O_3	4,64	3,84	3,34	4,77	3,00	5,41	3,58	2,72	Y	2	3	3	3	2	2
FeO	9,85	7,99	9,82	7,66	9,84	10,61	8,61	10,95	Zr	6	7	6	5	5	6
MnO	0,26	0,27	0,11	0,31	0,18	0,21	0,35	0,43	Nb	4	4	3	3	4	3
MgO	37,97	39,67	38,91	37,57	35,95	31,81	33,58	32,55	Th	4	4	3	3	2,7	3
CaO	2,05	2,13	1,47	3,09	3,12	2,14	3,01	3,7	Pb	36	38	39	19	21	22
Na_2O	0,11	0,22	0,34	0,22	0,11	0,74	0,29	0,48	Zn	24	23	26	24	25	24
K_2O	0,03	0,05	0,08	0,07	0,06	0,08	0,17	0,2	Cu	56	59	61	42	41	45
P_2O_5	0,24	0,25	0,12	0,3	0,04	0,04	0,31	0,32	Ni	1243	1201	1251	991	862	859
H_2O^+	4,32	5,29	4,35	4,88	3,31	3,54	3,34	3,04	V	584	568	599	461	402	444
H_2O^-	0,33	0,48	0,25	0,7	0,02	0,31	0,61	0,92	Cr	1524	1522	1560	510	504	532
CO_2	2,62	3,01	2,53	2,03	0,98	1,23	2,4	1,73	Ta	-	-	-	-	-	-
Total	100,19	100,45	100,17	101,93	98,76	99,26	100,1	100,58	Co	98	94	101	143	107	114
Mg#	0,79	0,83	0,80	0,82	0,78	0,75	0,79	0,74							
Normative components									REEs						
Q	0,00	0,00	0,00	0,00	0,00	0,00	0,00	0,00	La	3,5	3,9	3,8	2,6	2,2	2,4
Or	0,19	0,32	0,51	0,44	0,38	0,5	1,07	1,25	Ce	3,2	3,3	3,1	3,9	3	2,8
ab	1,00	0,81	2,97	1,97	0,98	6,64	2,61	4,28	Nd	1,5	1,43	1,52	1,38	0,9	1,38
an	1,49	0,34	1,97	1,36	8,18	0,83	3,37	0,10	Sm	0,7	0,56	0,6	0,5	0,5	0,51
Lc	0,00	0,00	0,00	0,00	0,00	0,00	0,00	0,00	Eu	0,11	0,11	0,1	0,11	0,1	0,13
Ne	0,00	0,66	0,07	0,00	0,00	0,00	0,00	0,00	Gd	0,5	0,52	0,59	0,61	0,6	0,69
-wo	3,32	4,00	2,13	5,44	3,33	4,26	4,44	7,21	Tb	0,17	0,17	0,13	0,12	0,2	0,12
Di -en	2,58	3,18	1,65	4,34	2,55	3,24	3,46	5,4	Dy	0,63	0,61	0,69	0,58	0,62	0,75
-fs	0,37	0,36	0,25	0,45	0,42	0,56	0,48	1,08	Er	0,51	0,67	0,55	0,58	0,44	0,47
Hy -en	3,38	0,00	0,00	7,85	4,46	17,33	19,93	12,33	Yb	0,52	0,62	0,55	0,61	0,51	0,42
Hy -fs	0,48	0,00	0,00	0,82	0,73	3,00	2,79	2,46	Lu	0,07	0,06	0,06	0,06	0,06	0,05
Ol -fo	67,34	73,5	72,03	61,17	61,7	44,7	46,31	47,62	Eu/ Eu*	0,57	0,62	0,51	0,61	0,56	0,67
Ol -fa	10,6	9,14	12,04	7,04	11,19	8,55	7,15	10,48	La_N/Sm_N	3,15	4,38	3,99	2,73	2,77	2,96
Mt	7,24	6,07	5,21	7,33	4,61	8,33	5,54	4,16	La_N/Yb_N	4,55	4,25	4,67	1,95	4,80	1,80
He	0,00	0,00	0,00	0,00	0,00	0,00	0,00	0,00	La_N/Lu_N	5,19	6,75	6,57	4,50	3,81	4,98
Il	1,45	1,02	0,9	1,09	1,39	1,96	2,13	2,92	Tb_N/Yb_N	1,39	1,17	1,01	0,84	1,67	1,22
Ap	0,56	0,60	0,28	0,69	0,09	0,09	0,72	0,74	- below detection limit						
Total	100,00	100,00	100,00	100,00	100,00	100,00	100,01	100,01							

Table C.2: Major, trace and REE elements data of the ophiolitic rocks exposed in the Um El Tuyor area

Sample	Metagabbro			Amphibolite			Metabasalt		
	a	29 (2)	29	29 (1)	30a	30x	117	67	69
SiO_2	48,42	53,05	51,15	47,24	48,81	48,25	47,61	48,34	47,88
TiO_2	1,59	1,87	1,72	1,49	1,43	1,34	1,14	1,2	1,09
Al_2O_3	14,04	14,98	15,35	15,36	14,98	14,82	16,33	17,04	16,87
Fe_2O_3	6,03	2,25	3,05	3,92	4,01	3,88	3,32	3,82	3,61
FeO	6,02	5,42	6	3,74	3,03	3,05	6,57	5,67	6,15
MnO	0,18	0,13	0,18	0,21	0,18	0,21	0,16	0,15	0,13
MgO	7,87	5,9	5,8	11,08	10,59	11,63	9,15	8,27	9,23
CaO	8,06	8,41	9,5	11,46	11,32	10,98	10,08	9,48	9,57
Na_2O	4,33	3,12	2,12	3,04	3,03	3,27	2	2,85	2,53
K_2O	0,79	1,00	0,82	0,55	0,65	0,58	1,03	0,81	0,91
P_2O_5	0,2	0,11	0,12	0,18	0,22	0,34	0,13	0,15	0,16
H_2O^+	1,45	3,24	3,55	1,06	1,1	1,44	1,63	2,02	2,06
H_2O^-	0,46	0,3	0,21	0,65	0,61	0,72	0,52	0,41	0,31
Total	99,44	99,78	99,57	99,98	99,96	100,51	99,95	99,87	99,9
Mg#	56,66	52,12	49,15	74,76	77,75	79,22	58,2	59,32	60,01
Ppm									
Ba	97	108	157	78	68	77	71	64	68
Rb	32	25	23	13	14	15	24	21	19
Sr	343	403	487	127	119	124	151	217	201
Y	33	30	31	35	31	29	18	16	25
Zr	98	92	88	90	77	86	51	47	47
Nb	21	12	13	8	9	9	14	12	13
Th	3	3,1	2,9	2,9	2,7	2,1	3,5	3,4	3,5
Pb	66	66	50	15	9	12	9	-	11
Zn	87	60	71	19	17	20	63	49	57
Cu	51	62	71	44	56	61	46	41	40
Ni	88	189	195	334	311	353	164	151	157
V	234	191	187	30	41	43	205	194	200
Cr	138	236	245	288	301	325	262	247	233
Hf	3,2	2,1	2	2,1	3	2,9	1	1,2	3
Ta	1,5	-	-	2	1,8	-	-	2	-
Co	52	22	44	22	23	31	62	55	49
REE									
La	4,99	6,9	7,2	3,81	3,93	3,78	6,6	8,8	7,5
Ce	9,45	11,5	11	8,36	8,77	9,56	13,9	14,7	13,2
Nd	8,5	8,9	9,2	5,9	5,1	5,33	6,1	5,9	6
Sm	1,68	2,3	2,4	1,4	1,36	1,61	1,7	1,5	1,8
Eu	0,84	0,82	0,79	0,39	0,34	0,33	0,5	0,56	0,57
Gd	2,2	2,4	2	1,6	1,7	1,66	2,1	2,3	1,9
Tb	0,47	0,36	0,35	0,23	0,25	0,24	0,4	0,4	0,4
Dy	2,13	2,41	2,28	1,57	1,85	1,92	1,8	1,82	1,79
Er	2,11	2,1	2,2	1,84	1,81	1,89	2,5	2,9	2,8
Yb	2,01	2,3	2,5	1,4	1,16	1,35	2,4	2,9	2,6
Lu	0,27	0,3	0,4	0,32	0,34	0,33	0,3	0,4	0,3
Ti_{cn}	24,31	28,59	26,29	22,78	21,86	20,49	17,43	18,34	16,66
Anomalies									
Eu/ Eu*	1,33	1,06	1,1	0,80	0,68	0,62	0,81	0,92	0,94
Sr/Sr*	2,65	2,76	3,35	1,25	1,23	1,20	1,14	1,62	1,57
Zr/Zr*	1,89	1,48	1,36	2,29	2,14	2,15	1,16	1,28	1,05
Ti/Ti*	3,83	4,05	4,2	4,91	4,21	4,80	3,06	3,06	3,09

- below detection limit

Table C.3: Major, trace and REE contents in some representative samples of the metasediments exposed in the Um El Tuyor area

Sample	grt-str-bi schist (metapelite)						qz+bi-ms metasiltstones (meta-psammite)				quartzite	
	3t	44	47	5(t)	77	8(t)	4	216	23	rs	21	26
SiO$_2$	51,98	55,16	54,48	54,58	52,2	55,01	55,51	57,01	63,02	64,87	89,27	88,64
TiO$_2$	0,05	0,55	0,57	0,47	0,52	0,26	0,68	0,89	0,71	0,79	0,14	0,19
Al$_2$O$_3$	9,82	8,89	9,47	9,59	10,04	8,01	14,21	16	13,32	14,55	1,97	1,44
Fe$_2$O$_3$	2,08	2,03	1,97	2,31	2,08	2,11	5,54	7,81	4,02	2,11	4,16	4,9
FeO	6,61	4,89	4,98	4,21	6,44	4,68	4,21	2,01	3,03	3,98	0,19	0,54
MnO	0,35	0,25	0,18	0,21	0,44	0,27	0,28	0,12	0,31	0,12	0,01	0,08
MgO	13,62	14,05	14,57	16,21	14,85	15,25	6,82	2,88	4,01	1,68	0,06	0,07
CaO	1,01	0,59	0,64	0,54	1,12	0,6	2,26	3,91	2,49	3,27	0,22	0,29
Na$_2$O	1,21	1,53	1,24	1,74	1,02	2,02	4,42	3,04	4,01	4,04	0,03	0,067
K$_2$O	6,72	8,11	8,08	7,36	6,51	8,01	2,33	2,61	2,39	2,23	0,91	0,93
P$_2$O$_5$	0,1	0,6	0,1	0,04	0,1	0,07	0,05	0,26	0,07	0,16	0,17	0,22
H$_2$O$^+$	3,34	2,32	2,25	2,54	3,61	3,01	2,03	2,29	2,02	1,57	1,74	2,04
H$_2$O$^-$	0,61	0,42	0,43	0,31	0,56	0,52	0,65	0,98	0,41	0,18	0,53	0,64
CO$_2$	1,4	0,21	0,21	0,23	0,44	0,38	0,06	0,22	0,05	0,49	0,23	0,22
Total	99,5	99,6	99,17	100,34	99,93	100,2	99,05	100,03	99,86	100,04	99,63	100,267
Ppm												
Ba	168	75	99				71	88				46
Rb	94	108	112				76	85				19
Sr	56	49	53				63	55				24
Y	25	16	21				10	9				nd
Zr	145	165	115				92	82				102
Nb	18	16	21				3	1				nd
Th	3,6	2,01	1,87				3,7	3,5				1
Pb	61	40	41				12	16				nd
Zn	57	36	45				21	33				13
Cu	38	18	29				9	12				nd
Ni	20	19	24				14	11				nd
V	238	213	252				123	139				2
Cr	266	289	324				175	130				nd
Co	66	48	76				37	16				nd
REE												
La	18,8	16,93	15,7				20,37	22,53				3,6
Ce	36,5	34,6	32,5				33,1	37,32				8,11
Nd	16,11	14,82	15,28				12,21	11,5				2,69
Sm	4,2	3,73	4,1				3,11	2,61				0,55
Eu	0,96	0,83	0,9				0,58	0,61				0,12
Gd	4,7	3,99	3,55				2,83	2,15				0,52
Tb	0,98	0,91	0,85				0,48	0,51				0,09
Er	4,2	3,98	3,73				1,67	1,38				0,42
Yb	3,9	3,26	3,22				1,78	1,61				0,44
Lu	0,71	0,66	0,46				0,28	0,32				0,07
Anomalies												
Eu/ Eu*	0,66	0,66	0,72				0,60	0,79				0,69
Sr/Sr*	0,16	0,15	0,16				0,22	0,18				0,36
Zr/Zr*	1,29	1,62	1,06				1,09	1,09				6,13
La$_N$/Sm$_N$	2,82	2,86	2,41				4,12	5,43				4,12
La$_N$/Yb$_N$	3,26	3,51	3,29				7,73	9,46				5,53

Table C.4: Geochemical data of representative samples of the island arc metavolcanic and metagabbro rocks exposed in the Um El Tuyor area

Major (wt.%) and trace element data of the metavolcanic rocks

Sample	Hb-plag schist 114	14-bas	chlorite schist 18(t)	20	66	metabasalt 69(w)	11(t)
SiO$_2$	58,15	56,69	54,19	53,29	55,08	48,51	50,60
TiO$_2$	0,68	0,76	0,89	0,91	0,85	1,08	1,01
Al$_2$O$_3$	13,03	12,61	16,91	15,41	14,99	17,31	16,92
Fe$_2$O$_3$	3,51	3,69	2,26	2,47	2,13	3,66	4,98
FeO	3,52	2,96	4,03	4,37	4,61	6,04	3,66
MnO	0,12	0,13	0,24	0,23	0,28	0,14	0,19
MgO	9,12	8,90	11,43	12,01	10,64	9,11	8,60
CaO	6,44	7,01	4,99	5,05	4,77	6,99	8,17
Na$_2$O	3,07	3,29	1,33	1,13	1,09	3,02	3,23
K$_2$O	1,16	1,05	0,76	0,69	0,72	1,04	1,11
P$_2$O$_5$	0,15	0,24	0,25	0,20	0,23	0,15	0,11
H$_2$O$^+$	2,01	2,35	3,85	3,69	3,43	2,01	1,65
H$_2$O$^-$	0,25	0,29	0,41	0,43	0,40	0,30	0,43
CO$_2$	0,11	0,09	0,16	0,09	0,1	0,02	0,03
Total	101,32	100,06	101,7	99,97	99,32	99,38	100,69
Ppm							
Ba	417	448	322	304	260	466	405
Rb	22	27	41	41	36	58	46
Sr	333	387	220	226	199	256	300
Y	14	26	30	21	38	16	18
Zr	106	98	100	105	97	149	151
Nb	6	6	4	5	6	13	14
Th	4	4,2	4,1	4	3,6	3,6	3,8
Pb	18	21	30	35	27	34	50
Zn	22	24	42	40	42	61	67
Cu	31	44	19	25	20	38	35
Ni	418	208	29	31	26	151	75
V	201	256	170	154	167	202	206
Cr	561	361	140	121	134	255	234
Hf	-	4	-	4	4	3	5
Ta	2	2	2,1	2	2,5	1	2
Co	16	21	25	30	28	48	50
Li	2	2	3	7	6	6,5	2

REE data (ppm), and some inter-element ratios of the metavolcanic rocks

Sample	hornblende-plagioclase schist 114	14-bas	chlorite schist 18(t)	20	66	metabasalt 69(w)	11(t)
REE							
La	20	21	17,2	16,6	15	13,8	15,9
Ce	45,1	43,8	20,4	28,4	27,7	26,5	28,4
Nd	9,8	10,12	8,6	10,9	11,2	6,3	7,7
Sm	3,2	3,8	3,1	3,2	2,7	2,6	2,2
Eu	1,6	1,5	1,1	1	1,2	1,4	1,2
Gd	2,5	2,5	2,6	3,1	2,9	1,9	2,3
Tb	0,6	0,6	0,52	0,5	0,6	0,54	0,57
Dy							
Er	2,4	2,7	1,8	2,2	2,1	1,7	1,9
Yb	3,1	3,5	2,4	2,8	2,9	1,8	2
Lu	0,4	0,43	0,3	0,4	0,34	0,31	0,3
K$_2$O/Na$_2$O	0,4	0,3	0,6	0,6	0,7	0,3	0,3
K$_2$O/CaO	0,2	0,2	0,2	0,1	0,2	0,1	0,1
Sr/Y	23,8	14,9	7,3	10,8	5,2	16,0	16,7
Zr/Y	7,6	3,8	3,3	5,0	2,6	9,3	8,4
Nb/Y	0,4	0,2	0,1	0,2	0,2	0,8	0,8
Ti/Zr	65,1	79,6	91,0	90,5	91,8	74,5	67,5
Th/Yb	1,3	1,2	1,7	1,4	1,2	2,0	1,9
Eu/ Eu*	1,73	1,49	1,18	0,97	1,31	1,92	1,63
Sr/Sr*	1,10	1,27	1,15	0,89	0,78	1,37	1,41
Zr/Zr*	1,38	1,16	1,42	1,30	1,29	2,69	2,68
[La/Sm]$_N$	3,93	3,48	3,49	3,27	3,50	3,34	4,55
[La/Yb]$_N$	4,36	4,05	4,84	4,01	3,50	5,18	5,37
[Ce/Yb]$_N$	3,77	3,24	2,20	2,63	2,48	3,82	3,68
[Tb/Yb]$_N$	0,83	0,73	0,93	0,76	0,88	1,28	1,22

Major, trace and REE elements in the metagabbro

Sample	100	74	119	73	55'	70	54	111a
SiO$_2$	50,3	52,97	53,67	52,42	52,09	53,08	52,89	53,99
TiO$_2$	0,57	0,77	0,62	0,73	0,77	0,68	0,67	0,71
Al$_2$O$_3$	15,24	16,83	16,57	16,92	16,97	15,06	17,01	16,3
Fe$_2$O$_3$	4,01	0,96	3,86	2,97	4,13	3,01	3,51	4,01
FeO	5,98	6,01	4,91	5,89	4,09	6,68	4,26	4,84
MnO	0,17	0,21	0,08	0,2	0,17	0,17	0,12	0,09
MgO	8,82	8,15	7,31	7,46	7,99	7,52	8,09	7,44
CaO	8,31	7,99	7,66	7,86	8,06	8,21	8,05	8,01
Na$_2$O	4,43	4,13	2,21	3,61	3,23	3,23	3,14	2,67
K$_2$O	0,62	0,74	0,84	0,71	0,77	0,69	0,72	0,71
P$_2$O$_5$	0,21	0,09	0,16	0,11	0,23	0,31	0,18	0,18
H$_2$O$^+$	0,73	0,84	0,96	0,93	1,6	0,85	0,64	0,61
H$_2$O$^-$	0,3	0,32	0,11	0,51	0,51	0,32	0,29	0,14
Total	99,69	100,01	98,96	100,32	100,61	99,81	99,57	99,7
Mg#	0,59	0,57	0,59	0,55	0,65	0,52	0,65	0,60
Ti(cn)	8,83	11,91	9,68	11,29	11,95	10,54	10,38	10,97
Ppm								
Ba	382	303	261	295	277	93	273	269
Rb	17	38	23	20	21	15	20	29
Sr	231	218	224	205	229	211	218	216
Y	14	16	15	19	18	16	19	16
Zr	60	53	75	55	69	65	72	78
Nb	6	5,2	6,5	5,1	6,2	5,7	5,9	5,6
Th	3,7	4	3,4	3,5	3,8	3,7	2,5	4,1
Zn	62	70	53	75	59	83	61	56
Cu	34	42	42	45	61	50	50	49
Ni	80	65	92	67	97	59	104	89
V	124	100	206	193	109	125	114	213
Cr	285	293	370	354	239	289	246	301
Ta	2,4	2,64	3	1,91	2,1	2,6	1,9	-
Co	53	41	31	39	39	46	40	29
REE								
La	5,46	7,16	6,56	7,2	6,09	6,2	6	5,99
Ce	10,73	10,79	11,02	11,23	10,99	10,81	10,12	11,2
Nd	6,03	5,53	5,91	5,61	6,03	5,71	6,01	6,14
Sm	1,73	2,25	1,73	2,03	2,11	1,79	2	2,12
Eu	0,73	0,78	0,68	0,72	0,79	0,72	0,72	0,76
Gd	2,65	2,33	2,33	2,78	2,42	2,63	2,41	2,73
Tb	0,42	0,47	0,43	0,43	0,45	0,42	0,43	0,47
Er	2,13	2	2	2,13	1,98	1,78	1,99	2,38
Yb	1,93	2,09	2,09	2,04	1,66	1,69	1,69	2
Lu	0,36	0,39	0,39	0,31	0,38	0,37	0,36	0,33
Zr/Y	4,29	3,31	5,00	2,89	3,83	4,06	3,79	4,88
Eu/ Eu*	1,04	1,04	1,04	0,93	1,07	1,01	1,00	0,97
(La/Sm)$_N$	1,99	2,00	2,39	2,23	1,82	2,18	1,89	1,78
(La/Yb)$_N$	1,91	2,32	2,12	2,38	2,48	2,48	2,40	2,02
(Gd/Yb)$_N$	1,11	0,90	0,90	1,10	1,18	1,26	1,16	1,11

Table C.5: Geochemical data of some representative samples of the syn-and post orogenic intrusion cropping out in the Um El Tuyor area

	The syn-orogenic granitoids						The post-orogenic granite						The post-orogenic olivine gabbro			
Sample	72	53	83	88	89'	91(1)	116	122	61	62	78	45	Sample 92'	95'	97	99
SiO_2	64,93	62,61	61,75	62,83	63,50	64,02	72,61	72,39	73,95	72,49	74,12	72,23	SiO_2 50,48	50,32	49,41	49,37
TiO_2	0,73	0,93	1,01	1,03	0,99	0,99	0,25	0,19	0,22	0,20	0,23	0,26	TiO_2 0,80	0,77	0,84	0,82
Al_2O_3	16,07	16,86	16,71	16,38	16,09	15,88	13,89	14,15	13,20	13,67	13,55	14,00	Al_2O_3 15,84	14,91	15,79	15,62
Fe_2O_3	2,92	3,14	3,29	3,13	3,12	3,18	1,67	1,60	1,31	1,65	1,02	1,46	Fe_2O_3 3,30	3,29	3,45	3,89
FeO	2,01	2,45	2,35	2,37	2,44	2,33	0,58	0,60	0,68	0,70	0,72	0,84	FeO 6,38	6,47	6,76	6,01
MnO	0,05	0,08	0,09	0,08	0,12	0,09	0,06	0,06	0,04	0,09	0,05	0,06	MnO 0,21	0,22	0,19	0,18
MgO	1,99	2,78	2,85	2,89	2,78	2,88	0,60	0,55	0,63	0,50	0,59	0,72	MgO 8,73	7,98	7,9	8,03
CaO	3,61	3,91	4,07	4,29	3,69	3,74	1,79	1,37	0,83	1,73	0,78	1,75	CaO 9,91	10,34	10,57	11,02
Na_2O	3,66	4,48	3,66	3,79	4,01	3,94	3,56	3,61	3,63	3,94	3,72	3,54	Na_2O 1,49	1,73	1,62	1,59
K_2O	2,55	1,96	1,97	1,64	1,89	2,67	4,62	4,52	4,36	4,71	4,93	3,91	K_2O 0,63	0,68	0,7	0,65
P_2O_5	0,18	0,20	0,21	0,24	0,21	0,18	0,14	0,12	0,11	0,13	0,13	0,14	P_2O_5 0,37	0,38	0,31	0,35
H_2O^+	0,54	0,80	0,51	0,61	0,70	0,85	0,54	0,80	0,51	0,61	0,70	0,85	H_2O^+ 1,47	1,63	1,73	1,56
H_2O^-	0,53	0,50	0,36	0,04	0,27	0,05	0,13	0,12	0,22	0,14	0,17	0,11	H_2O^- 0,39	0,44	0,36	0,43
Total	99,77	100,70	98,83	99,32	99,81	100,80	100,44	100,08	99,59	100,56	100,71	99,87	Total 100	99,16	99,63	99,52
Mg#	0,49	0,52	0,54	0,54	0,52	0,54	0,48	0,45	0,47	0,39	0,43	0,44	Mg# 0,57	0,54	0,53	0,56
Molar Al_2O_3/ $Na_2O + K_2O$	1,83	1,78	2,05	2,04	1,86	1,69	1,28	1,31	1,23	1,18	1,18	1,36				
ASI	1,05	1,02	1,07	1,04	1,05	0,98	0,98	1,06	1,08	0,93	1,05	1,04				
Trace elements (ppm)													ppm			
Ba	374,0	380,0	375,0	377,0	368,0	371,0	291,0	258,0	216,0	202,0	204,0	275,0	Ba 97	118	129	107
Rb	98,0	90,0	87,0	93,0	101,0	98,0	122,0	116,0	190,0	131,0	201,0	196,0	Rb 20	28	23	19
Sr	256,0	245,0	286,0	234,0	244,0	269,0	47,0	44,0	52,0	48,0	53,0	42,0	Sr 593	588	615	618
Li	9,0	15,0	11,0	14,0	15,0	16,0	17,0	23,0	15,0	21,0	56,0	20,0	Y 11	15	13	16
Ta	2,8	2,4	2,0	1,9	2,3	1,8	3.1	3.5	3,0	4,0	3.1	3.1	Zr 63	71	58	69
Nb	14,0	11,0	10,0	10,0	12,0	12,0	42,0	47,0	75,0	57,0	62,0	45,0	Nb 11	13	10	12
Hf	5,0	3,0	6,0	4,0	5,0	5.5	11,0	12,0	13,0	8,7	9,0	12,0	Th 4	3,89	3,5	3,8
Zr	92,0	82,0	105,0	88,0	86,0	98,0	150,0	145,0	214,0	152,0	190,0	161,0	Pb 56	58	61	59
Y	21,0	18,0	17,0	19,0	20,0	22,0	32,0	30,0	32,0	36,0	34,0	29,0	Zn 89	91	93	60
Th	7.5	7.2	7,0	7.9	7,0	8,0	11,0	9.8	12.6	8.9	13.1	7.1	Cu 36	35	34	41
U	2.5	2.1	1.9	3,0	2.2	3,0	5.1	4.5	8.1	3.7	9.2	2.3	Ni 132	149	138	144
Cr	26,0	27,0	21,0	28,0	4,0	28,0	0,0	1,0	0,0	1,0	0,0	0,0	V 147	158	149	163
Ni	13,0	13,0	12,0	14,0	3.5	14,0	1,0	1,0	0,0	1,0	0,0	0,0	Cr 106	115	121	135
Co	11,0	12,0	11,0	11,0	2.5	13,0	0,0	1,0	0,0	1,0	0,0	0,0	Ta 3,07	2,8	2	3
Cu	40,0	19,0	32,0	33,0	18,0	21,0	6,0	9,0	15,0	12,0	13,7	8,0	Co 49	51	37	50
Pb	50,0	55,0	46,0	60,0	56,0	60,0	9,0	12,0	9,0	10,0	20,0	13,0	Li -	3	-	-

Continue

Sample	72	53	83	88	89'	91(1)	116	122	61	62	78	45			92'	95'	97	99
REE																		
La	19,90	19,00	18,80	20,00	19,40	19,70	24,90	29,82	25,92	26,95	27,20	24,10		La	5,56	6	6,4	5,8
Ce	44,50	42,50	42,60	43,90	42,00	44,10	55,80	53,93	54,50	53,80	52,30	47,10		Ce	10,98	11,02	11,1	10,62
Nd	10,30	10,10	9,80	10,98	11,80	11,00	12,90	13,88	12,80	18,90	15,60	11,20		Nd	8,06	7,99	7,5	8,03
Sm	2,60	3,00	2,30	3,01	2,90	3,10	2,70	3,51	2,52	2,86	3,70	3,10		Sm	1,87	2,08	2,03	2,19
Eu	0,50	0,60	0,50	0,60	0,67	0,60	0,55	0,66	0,55	0,70	0,77	0,70		Eu	0,76	0,78	0,81	0,87
Gd	2,40	2,50	2,30	2,60	2,60	2,52	3,87	3,98	3,76	4,70	3,85	3,30		Gd	2,39	2,42	2,28	2,34
Tb	0,50	0,59	0,50	0,56	0,61	0,60	0,65	0,66	0,65	0,76	0,76	0,60		Tb	0,51	0,53	0,49	0,5
Dy	2,55	2,93	2,96	2,70	2,77	2,88	3,21	3,52	3,85	3,87	3,97	2,88						
Er	2,30	2,30	2,20	2,33	2,40	2,47	2,88	3,70	2,88	2,90	2,90	2,40		Er	2,16	2,14	2,08	2,05
Yb	2,10	1,80	1,80	1,87	1,90	2,20	1,98	2,01	2,83	2,82	2,20	2,10		Yb	1,87	1,91	1,8	1,8
Lu	0,40	0,30	0,30	0,29	0,40	0,40	0,55	0,65	0,65	0,76	0,40	0,39		Lu	0,35	0,33	0,31	0,32
Ti/P	4,06	4,65	4,81	4,29	4,71	5,50	1,79	1,58	2,00	1,54	1,00	3,29		Zr/Y	5,73	4,73	4,46	4,31
Sr/Sr*	1,16	1,15	1,36	1,04	1,07	1,19	0,17	0,16	0,19	0,15	0,18	0,18		Zr/Ti	0,008	0,009	0,007	0,008
Rb/Sr	0,38	0,37	0,30	0,40	0,41	0,36	2,60	2,64	3,65	2,73	3,79	2,29		Eu/ Eu*	1,10	1,06	1,15	1,17
Eu/Eu*	0,61	0,67	0,66	0,66	0,75	0,66	0,52	0,54	0,55	0,58	0,62	0,67		Sr/Sr*	4,37	4,34	4,67	4,64
$(La/Yb)_N$	6,40	7,13	7,06	7,23	6,90	6,05	8,50	10,03	6,19	6,46	8,35	7,76		Zr/Zr*	1,19	1,27	1,09	1,20
$(Gd/Yb)_N$	0,93	1,13	1,04	1,13	1,11	0,93	1,58	1,60	1,08	1,35	1,42	1,27		$(La/Sm)_N$	1,87	1,82	1,98	1,67
														$(La/Yb)_N$	2,01	2,12	2,40	2,18
														$(Gd/Yb)_N$	1,04	1,03	1,03	1,05

- below detection limit

Appendix D: Chemistry of the gangue and ore minerals

Chemical analyses of the hydrothermal silicate minerals were carried out using a Jeol JSM-6310 electron microprobe at the Institute of Geology and Mineralogy, Graz University, Austria. The measuring conditions were 15 kV, 30 *n*A, defocused electron beam with a diameter of 5-10 μm.

Table D.1: Microanalyses of carbonate in the quartz-carbonate veins from Um El Tuyor mine

	230_3	230_9	230_1	230_7	230_4	230_5	230_11	230_8	230_10
CaO	26,52	27,08	28,95	25,33	25,45	25,74	27,39	27,14	27,84
MgO	13,39	11,19	11,75	13,46	13,49	14,40	13,45	13,55	13,87
FeO	10,27	9,00	10,14	11,01	9,88	11,38	11,90	10,04	10,56
MnO	0,56	0,39	0,54	0,63	0,60	0,70	0,43	0,42	0,45
Sum	50,73	47,66	93,48	50,43	49,40	52,22	53,16	51,14	52,72
ppm									
Sr	290	488	240	809	919	528	330	477	501
Ba	0	0	8	0	0	0	10	0	0
Formula on basis of total cations =1									
Ca	0,495	0,542	0,540	0,477	0,486	0,466	0,492	0,50	0,50
Mg	0,348	0,311	0,305	0,352	0,358	0,363	0,336	0,35	0,35
Fe	0,149	0,141	0,148	0,162	0,147	0,161	0,167	0,14	0,15
Mn	0,008	0,006	0,008	0,009	0,009	0,010	0,006	0,01	0,01
End members									
$CaCO_3$	49,48	54,18	53,97	47,67	48,58	46,62	49,16	50,12	49,87
$MgCO_3$	34,75	31,15	30,48	35,23	35,81	36,28	33,57	34,80	34,55
$FeCO_3$	14,95	14,06	14,75	16,17	14,71	16,08	16,66	14,47	14,77
$MnCO_3$	0,82	0,61	0,80	0,93	0,90	1,01	0,60	0,61	0,63
Sum	100,00	100,00	100,00	100,00	100,00	100,00	100,00	100,00	99,81
$MgCO_3$	0,00	0,00	0,00	0,00	0,00	0,00	0,00	0,00	0,00
$CaCO_3$	0,00	8,37	7,93	0,00	0,00	0,00	0,00	0,23	0,00
$CaMg(CO_3)_2$	68,46	62,29	60,96	65,79	68,78	65,81	65,46	69,60	69,10
$CaFe(CO_3)_2$	29,90	28,11	29,51	32,35	29,43	32,17	33,33	28,95	29,54
$CaMn(CO_3)_2$	1,64	1,23	1,60	1,86	1,80	2,02	1,21	1,22	1,26
Sum	100,00	100,00	100,00	100,00	100,00	100,00	100,00	100,00	99,89
Fe#	0,301	0,311	0,326	0,315	0,291	0,307	0,332	0,29	0,30
mg#	0,688	0,680	0,662	0,673	0,696	0,680	0,660	0,70	0,69
t	0,505	0,458	0,460	0,523	0,514	0,534	0,508	0,50	0,50
activity	0,430	0,451	0,484	0,459	0,411	0,443	0,496	0,50	0,50
Fe/Mg	0,052	0,044	0,045	0,057	0,053	0,058	0,056	0,42	0,43

Table D.2: Chemistry of the sericite flakes disseminated in the quartz-carbonate veins

	1	2	3	4	5	6	7	8
SiO_2	48,08	46,64	47,03	47,52	47,14	49,01	46,51	48,57
TiO_2	0,05	0,21	0,01	0,17	0,17	0,06	0,12	0,15
Al_2O_3	35,42	35,11	35,90	35,99	36,45	34,67	36,65	35,63
FeO	0,91	0,24	0,60	0,41	0,20	0,23	0,23	0,28
MnO	0,03	0,00	0,00	0,03	0,00	0,03	0,10	0,00
MgO	0,71	3,05	0,60	0,33	0,60	0,67	0,41	0,26
CaO	0,20	0,10	0,14	0,09	0,02	0,08	0,02	0,03
Na_2O	0,90	1,88	1,18	1,50	1,43	1,83	2,99	1,75
K_2O	7,71	6,87	8,10	8,02	8,07	7,43	7,05	8,19
Total	93,35	93,44	92,91	93,41	93,44	93,35	93,43	94,22
T2	7,93	7,93	7,99	7,94	7,93	7,91	7,95	7,87
No Anions	22,00	22,00	22,00	22,00	22,00	22,00	22,00	22,00
Structural formula on basis of 22 oxygens								
Si	6,35	6,15	6,26	6,28	6,23	6,45	6,15	6,36
Ti	0,00	0,02	0,00	0,02	0,02	0,01	0,01	0,01
Al	5,51	5,46	5,63	5,61	5,67	5,38	5,71	5,50
Fe(ii)	0,10	0,03	0,07	0,05	0,02	0,03	0,03	0,03
Mn	0,00	0,00	0,00	0,00	0,00	0,00	0,01	0,00
Mg	0,14	0,60	0,12	0,06	0,12	0,13	0,08	0,05
Ca	0,03	0,01	0,02	0,01	0,00	0,01	0,00	0,00
Na	0,23	0,48	0,31	0,38	0,37	0,47	0,77	0,45
K	1,30	1,16	1,37	1,35	1,36	1,25	1,19	1,37
Cl	0,00	0,00	0,00	0,00	0,00	0,00	0,00	0,00
F	0,00	0,00	0,00	0,00	0,00	0,00	0,00	0,00
Total	13,66	13,91	13,77	13,77	13,78	13,71	13,96	13,78
Fe/(Fe+Mg)	0,42	0,04	0,36	0,42	0,16	0,16	0,24	0,38
XMs	0,85	0,71	0,82	0,78	0,79	0,73	0,61	0,75

Table D.3: Systematic microanalyses across two muscovite flakes in the quartz-carbonate veins

	rim	core	rim	rim	spots every 30 micron							rim
SiO_2	47,84	47,21	46,56	47,07	46,68	46,50	46,60	46,42	47,57	46,44	46,81	47,92
TiO_2	1,57	1,35	0,87	0,88	0,88	0,72	0,73	0,94	0,68	1,28	0,81	0,49
Al_2O_3	32,71	33,36	34,71	34,54	33,09	33,08	33,28	32,99	33,44	32,87	33,22	33,24
FeO	1,49	1,54	1,65	1,79	1,87	1,68	1,74	1,76	1,56	1,71	1,59	1,24
MnO	0,00	0,00	0,03	0,02	0,13	0,00	0,00	0,02	0,04	0,02	0,03	0,00
MgO	2,04	1,70	1,72	2,02	1,60	1,55	1,48	1,64	1,68	1,66	1,60	1,55
CaO	0,01	0,06	0,05	0,04	0,04	0,02	0,07	0,00	0,06	0,06	0,10	0,02
Na_2O	0,32	0,28	0,37	0,33	0,34	0,33	0,28	0,31	0,30	0,36	0,37	0,38
K_2O	8,60	8,78	8,98	8,29	9,32	9,60	9,50	9,49	9,51	9,33	9,46	9,05
Cl	0,00	0,00	0,00	0,00	0,00	0,00	0,00	0,00	0,00	0,00	0,00	0,00
F	0,53	0,52	0,26	0,40	0,36	0,35	0,43	0,33	0,40	0,52	0,39	0,68
TOTAL	94,46	94,16	94,55	94,71	93,65	93,18	93,46	93,25	94,56	93,60	93,74	93,93
O=F,Cl	0,22	0,22	0,11	0,17	0,15	0,15	0,18	0,14	0,17	0,22	0,17	0,29
T2	7,97	8,00	7,97	7,93	8,08	8,12	8,10	8,12	7,99	8,10	8,07	8,02
Formula												
Si	6,34	6,29	6,17	6,21	6,28	6,29	6,28	6,27	6,32	6,26	6,29	6,39
Ti	0,16	0,14	0,09	0,09	0,09	0,07	0,07	0,10	0,07	0,13	0,08	0,05
Al	5,11	5,24	5,42	5,37	5,25	5,27	5,29	5,25	5,24	5,22	5,26	5,23
Fe(ii)	0,16	0,17	0,18	0,20	0,21	0,19	0,20	0,20	0,17	0,19	0,18	0,14
Mn	0,00	0,00	0,00	0,00	0,01	0,00	0,00	0,00	0,00	0,00	0,00	0,00
Mg	0,40	0,34	0,34	0,40	0,32	0,31	0,30	0,33	0,33	0,33	0,32	0,31
Ca	0,00	0,01	0,01	0,00	0,01	0,00	0,01	0,00	0,01	0,01	0,01	0,00
Na	0,08	0,07	0,09	0,08	0,09	0,09	0,07	0,08	0,08	0,09	0,10	0,10
K	1,46	1,49	1,52	1,40	1,60	1,66	1,63	1,63	1,61	1,60	1,62	1,54
Cl	0,00	0,00	0,00	0,00	0,00	0,00	0,00	0,00	0,00	0,00	0,00	0,00
F	0,22	0,22	0,11	0,17	0,15	0,15	0,18	0,14	0,17	0,22	0,17	0,29
TOTAL	13,71	13,74	13,83	13,75	13,85	13,88	13,85	13,87	13,83	13,85	13,86	13,76
Fe/(Fe+Mg)	0,29	0,34	0,35	0,33	0,40	0,38	0,40	0,38	0,34	0,37	0,36	0,31
XMs	0,95	0,95	0,94	0,94	0,95	0,95	0,96	0,95	0,95	0,94	0,94	0,94
K/Mg	3,61	4,42	4,46	3,52	5,00	5,30	5,51	4,94	4,86	4,80	5,05	5,00
K/Na	17,91	20,42	16,15	16,73	18,14	19,32	22,40	20,33	21,13	17,14	16,91	15,63

Table D.4: Electron microprobe data of albite plates in the quartz-carbonate veins

	5	6	7	8	9	10	11	14	15
SiO_2	66,86	67,33	68,39	67,12	68,59	67,78	67,22	66,62	67,37
TiO_2	0,03	0,00	0,04	0,00	0,02	0,00	0,03	0,00	0,00
Al_2O_3	19,36	19,76	19,48	18,84	19,32	19,24	19,65	18,94	19,65
FeO	0,01	0,06	0,11	0,06	0,02	0,00	0,00	0,16	0,04
MnO	0,00	0,08	0,05	0,02	0,02	0,05	0,11	0,00	0,04
MgO	0,00	0,00	0,00	0,00	0,00	0,00	0,00	0,00	0,00
CaO	0,36	0,20	0,46	0,07	0,14	0,58	0,82	0,26	0,06
Na_2O	11,24	11,73	11,82	11,41	11,61	11,49	11,35	11,50	11,68
K_2O	0,07	0,02	0,00	0,06	0,01	0,09	0,00	0,01	0,12
Cl	0,00	0,00	0,00	0,00	0,00	0,00	0,00	0,00	0,00
F	0,15	0,22	0,01	0,19	0,06	0,22	0,21	0,21	0,21
Total	97,43	98,76	99,71	97,12	99,15	98,81	98,74	97,05	98,52
O=F,Cl	0,06	0,09	0,00	0,08	0,03	0,09	0,09	0,09	0,09
T2	2,68	2,65	2,62	2,69	2,63	2,65	2,65	2,70	2,66
No Anions	8,00	8,00	8,00	8,00	8,00	8,00	8,00	8,00	8,00
Formula									
Si	2,98	2,97	2,98	3,00	3,00	2,99	2,97	2,99	2,98
Ti	0,00	0,00	0,00	0,00	0,00	0,00	0,00	0,00	0,00
Al(iv)	1,02	1,03	1,00	0,99	1,00	1,00	1,02	1,00	1,02
Al(vi)	0,00	0,00	0,00	0,00	0,00	0,00	0,00	0,00	0,00
Al	1,02	1,03	1,00	0,99	1,00	1,00	1,02	1,00	1,02
Fe(ii)	0,00	0,00	0,00	0,00	0,00	0,00	0,00	0,01	0,00
Mn	0,00	0,00	0,00	0,00	0,00	0,00	0,00	0,00	0,00
Mg	0,00	0,00	0,00	0,00	0,00	0,00	0,00	0,00	0,00
Ca	0,02	0,01	0,02	0,00	0,01	0,03	0,04	0,01	0,00
Na	0,97	1,00	1,00	0,99	0,99	0,98	0,97	1,00	1,00
K	0,00	0,00	0,00	0,00	0,00	0,01	0,00	0,00	0,01
Cl	0,00	0,00	0,00	0,00	0,00	0,00	0,00	0,00	0,00
F	0,02	0,03	0,00	0,03	0,01	0,03	0,03	0,03	0,03
Total	5,00	5,02	5,01	5,00	4,99	5,01	5,01	5,01	5,01
An	1,73	0,93	2,11	0,34	0,66	2,70	3,84	1,23	0,28
Ab	97,87	98,96	97,89	99,32	99,28	96,80	96,16	98,71	99,08
Or	0,40	0,11	0,00	0,34	0,06	0,50	0,00	0,06	0,64

Table D.5: Trace elements and REE concentrations (ppm) in quartz-carbonate veins of Um El Tuyor gold deposit

Sample	T-230A	T-230B	T-230C	T-230D	T-230E	T-230F	Detection limit
Au	15.48	16.44	12.75	11.93	9.82	14.53	0.002
Ag	3.48	3.63	2.99	2.82	1.84	3.22	0.3
As	3609	7746	4231	3251	4026	3518	0.5
Ba	370	130	334	166	189	298	1
Sr	213	204	218	222	199	246	1
Co	23	44	6	17	3	7	1
Cr	22	<5	19	21	7	11	2
Rb	106	62	99	87	117	111	15
Cs	4	2	4	2	-	5	1
Hf	3	2	3	-	-	3	1
Hg	2	1	-	-	-	-	1
Mo	-	2	-	-	-	-	1
Ni	5	6	5.5	3	4	5.3	1
Sb	-	-	-	-	-	-	0.1
Sc	6.7	3.5	6.3	4.1	3.1	5.9	0.1
Sn	199	138	141	103	127	97	0.01%
Ta	-	0.5	-	-	-	-	0.5
Th	3.3	2	3	2.8	2.5	3.1	0.2
U	-	-	-	-	-	-	0.5
W	-	-	-	-	-	-	1
Zn	54	24	37	35	41	46	1
Pb	18	27	10	9	13	21	3
V	56	28	48	43	32	49	2
Y	-	-	-	4	4	5	1
Cu	13	16	14	12	10	13	1
Mn	345	257	287	208	343	339	1
Bi	-	-	-	-	-	-	2
Cd	0,8	0.5	0.3	-	-	0.5	0.3
Br	0.43	0.39	0.46	0.34	0.45	0.41	0.5
Na	2567	1899	3276	2838	2682	2530	0.01%
K	8753	11598	9090	8011	9796	8634	0.01%
S	6270	4890	6600	7200	7650	6800	0.01%
Fe	26040	34280	30782	22309	22464	23397	0.01%
Mg	5950	6863	4675	5611	5179	5179	0.01%
REEs							
La	12.8	7.6	12.7	12.1	9.3	11.2	0.5
Ce	26	17	25	23	19	21	3
Nd	12	5	9	10	7	11	5
Sm	2.9	1.9	2.8	3.2	2.4	2.7	0.1
Eu	0.9	0.7	0.9	1.2	0.9	0.8	0.2
Tb	0.5	0.51	0.67	<0,5	0.51	0.53	0.5
Yb	0.7	0.5	0.6	0.7	0.5	0.7	0.2
Lu	0.11	0.09	0.1	0.14	0.1	0.11	0.05
Ratios	0.24	0.14	0.21	0.32	0.34	0.29	
Fe/Mg	4.38	4.99	6.58	3.98	4.34	4.52	
K/Na	3.41	6.11	2.78	2.82	3.65	3.41	
Au/Ag	4.45	4.53	4.26	4.23	5.34	4,51	
As/Au	233	471	332	273	410	242	

- below detection limit
Analyses were made by the ACTLABS Group, Canada, using the INAA and ICP-MS techniques (Code 1H).

Table D.6: Mineral chemistry of the laminated quartz veins in the Um El Tuyor mine area

	chlorite,		Muscovite/sericite			
SiO₂	39,09	39,52	48,67	48,19	48,19	49,03
TiO₂	0,24	0,17	0,16	0,29	0,11	0,15
Al₂O₃	34,36	34,20	35,59	36,17	36,97	36,31
FeO	4,67	3,93	0,61	0,48	0,46	0,39
MnO	0,19	0,05	0,05	0,12	0,00	0,13
MgO	7,60	7,82	0,63	0,52	0,57	0,67
CaO	0,05	0,05	0,02	0,09	0,09	0,10
Na₂O	1,92	1,87	1,33	1,76	2,30	1,86
K₂O	0,03	0,16	7,01	6,60	5,63	5,49
Cl	0,00	0,00	0,00	0,00	0,00	0,00
F	0,00	0,00	0,00	0,00	0,00	0,00
TOTAL	87,51	87,14	93,42	93,59	93,69	93,49
O=F,Cl	0,00	0,00	0,00	0,00	0,00	0,00
TOTAL	87,51	87,14	93,42	93,59	93,69	93,49
T2	10,74	10,73	7,88	7,86	7,82	7,81
No Anions	28,00	28,00	22,00	22,00	22,00	22,00
Formula						
Si	6,99	7,06	6,38	6,31	6,27	6,37
Ti	0,03	0,02	0,02	0,03	0,01	0,01
Al^{iv}	1,01	0,94	1,62	1,69	1,73	1,63
Al^{vi}	6,23	6,26	3,88	3,89	3,94	3,93
Al	7,24	7,20	5,50	5,58	5,67	5,56
Fe$^{(ii)}$	0,70	0,59	0,07	0,05	0,05	0,04
Mn	0,03	0,01	0,01	0,01	0,00	0,01
Mg	2,03	2,08	0,12	0,10	0,11	0,13
Ca	0,01	0,01	0,00	0,01	0,01	0,01
Na	0,67	0,65	0,34	0,45	0,58	0,47
K	0,01	0,04	1,17	1,10	0,93	0,91
Cl	0,00	0,00	0,00	0,00	0,00	0,00
F	0,00	0,00	0,00	0,00	0,00	0,00
Total	17,70	17,66	13,61	13,65	13,64	13,52
Fe/(Fe+Mg)	0,26	0,22	0,35	0,34	0,31	0,25
T(°C)	263,78	240,70	<< according to Cathelineau, 1988			

Carbonate (mainly dolomite)

	t16_1_A	t16_1_B	t16_1_C	t16_2_4	t16_2_5	t16_2_6	t16_2_2	t16_2_5	t16_2_7	t16_2_9
MgO	13,44	13,96	15,46	15,02	11,91	13,82	14,98	15,95	15,47	14,78
P₂O₅	0,00	0,00	0,029	0,00	0,00	0,12	0,00	0,00	0,002	0,00
CaO	25,88	25,42	26,61	26,95	26,31	26,03	27,57	26,95	26,57	26,82
TiO₂	0,03	0,01	0,00	0,00	0,07	0,01	0,02	0,02	0,00	0,00
MnO	0,69	0,76	0,65	0,76	0,45	0,45	0,73	0,59	0,53	0,59
FeO	11,96	9,18	7,14	8,00	14,13	9,24	8,39	7,43	7,57	8,93
Ca	0,47	0,48	0,49	0,49	0,48	0,48	0,49	0,48	0,49	0,48
Mg	0,34	0,37	0,40	0,40	0,30	0,35	0,37	0,40	0,39	0,37
Fe	0,17	0,14	0,10	0,11	0,20	0,13	0,12	0,10	0,11	0,13
Mn	0,01	0,01	0,01	0,01	0,01	0,01	0,01	0,01	0,01	0,01
Ti	0,00	0,00	0,00	0,00	0,00	0,00	0,00	0,00	0,00	0,00
CaCO₃	47,40	48,35	49,00	48,61	48,19	48,04	49,45	48,45	48,52	48,43
MgCO₃	34,23	36,94	39,63	39,66	30,34	35,49	37,39	39,90	39,31	37,12
FeCO₃	17,10	13,63	10,26	11,27	20,20	13,31	11,76	10,44	10,80	12,58
MnCO₃	1,02	1,14	0,94	1,09	0,64	0,66	1,04	0,84	0,76	0,85
Sum	99,75	100,06	99,83	100,63	99,38	97,50	99,65	99,64	99,40	98,99
MgCO₃	0,00	0,00	0,00	0,00	0,00	0,00	0,00	0,00	0,00	0,00
CaCO₃	0,00	0,00	0,00	0,00	0,00	0,00	0,00	0,00	0,00	0,00
CaMg(CO₃)₂	65,23	71,35	77,94	76,12	59,24	71,75	74,49	77,92	77,24	73,42
CaFe(CO₃)₂	32,60	26,33	20,18	21,62	39,44	26,91	23,43	20,38	21,23	24,89
CaMn(CO₃)₂	1,95	2,20	1,85	2,10	1,26	1,32	2,08	1,65	1,50	1,68
Sum	99,78	99,88	99,97	99,84	99,94	99,99	100,00	99,94	99,97	99,99
Fe#	0,333	0,270	0,206	0,221	0,400	0,273	0,239	0,207	0,216	0,253
mg#	0,654	0,714	0,780	0,762	0,593	0,718	0,745	0,780	0,773	0,734
T	0,524	0,517	0,508	0,520	0,512	0,495	0,502	0,512	0,509	0,506
Activity	0,474	0,484	0,490	0,486	0,482	0,480	0,495	0,485	0,485	0,484
Fe/Mg	0,500	0,369	0,259	0,284	0,666	0,375	0,315	0,262	0,275	0,339
Fe.Mg	0,059	0,050	0,041	0,045	0,061	0,047	0,044	0,042	0,042	0,047

Activities are calculated assuming ideal activity models (Skippen and Carmichael, 1977)

Ore minerals data

Chemistry of the ore minerals were obtained by a Zeiss 950 DSM electron microprobe at the Institute of General and Applied Geology, Univ. of Munich. The wavelength dispersive technique was employed, with accelerating voltages of 20 kV, and specimen current of 25 nA. A fixed time of 20 second was used and each analysis was based on counts from two or three spots on a single grain.

Table D.7: Electron microprobe data of arsenopyrite belongs to the early sulphide assemblage, disseminated in the quartz-carbonate veins in Um El Tuyor mine

Weight%	core	>>>	rim	core	rim	core	rim	core	rim	core	rim	core	rim	core	rim	core	rim	core	rim	core	rim	core	rim	core	rim
Fe	35,49	35,84	35,33	35,36	34,34	34,65	33,93	34,44	33,69	34,38	34,64	34,09	33,95	34,83	34,47	34,90	34,18	34,62	35,41	35,45	35,43	35,74	34,79	34,72	34,57
S	20,68	20,42	20,03	19,98	19,69	19,87	20,09	20,28	19,57	20,08	19,17	20,18	18,62	21,02	19,64	20,13	20,01	20,57	18,96	20,93	19,93	21,19	19,81	19,70	19,28
As	43,37	43,37	44,54	44,58	46,35	45,17	45,97	45,27	46,42	44,54	46,88	44,71	47,32	44,14	45,28	44,95	46,17	44,81	45,65	43,62	44,54	43,05	45,32	45,52	45,04
Co	0,00	0,00	0,00	0,07	0,00	0,00	0,00	0,00	0,00	0,00	0,00	0,00	0,00	0,00	0,00	0,00	0,00	0,00	0,00	0,00	0,05	0,02	0,07	0,05	0,05
Ni	0,00	0,00	0,00	0,00	0,00	0,00	0,00	0,00	0,00	0,00	0,00	0,00	0,00	0,00	0,00	0,00	0,00	0,00	0,00	0,00	0,04	0,00	0,00	0,00	0,05
Cu	0,00	0,04	0,00	0,00	0,00	0,00	0,00	0,00	0,00	0,00	0,00	0,00	0,00	0,00	0,00	0,00	0,00	0,00	0,00	0,00	0,00	0,00	0,00	0,00	0,00
Zn	0,00	0,07	0,00	0,00	0,00	0,00	0,00	0,00	0,00	0,00	0,00	0,00	0,00	0,00	0,00	0,00	0,00	0,00	0,00	0,00	0,00	0,00	0,00	0,00	0,00
Ag	0,00	0,00	0,00	0,00	0,00	0,00	0,00	0,00	0,00	0,00	0,00	0,00	0,00	0,00	0,00	0,00	0,00	0,00	0,00	0,00	0,00	0,00	0,00	0,00	0,00
Au	0,00	0,00	0,00	0,01	0,02	0,08	0,11	0,03	0,17	0,00	0,14	0,01	0,16	0,01	0,00	0,01	0,23	0,00	0,03	0,00	0,00	0,00	0,07	0,09	0,02
Sum	99,5	99,7	99,9	100,0	100,4	99,8	100,1	100,0	99,8	99,0	100,8	99,0	100,0	100,0	99,4	99,9	100,5	100,0	100,0	100,0	99,9	100,0	100,0	100,1	99,0
Atomic%																									
Fe	34,17	34,55	34,16	34,20	33,28	33,66	32,88	33,27	32,91	33,52	33,64	33,24	33,39	33,38	33,65	33,73	33,04	33,34	34,56	33,95	34,28	34,11	33,75	33,72	33,99
S	34,68	34,28	33,73	33,66	33,24	33,62	33,91	34,13	33,30	34,10	32,42	34,27	31,90	35,08	33,40	33,89	33,69	34,50	32,23	34,90	33,59	35,23	33,48	33,32	33,01
As	31,28	31,29	32,17	32,20	33,47	32,75	33,24	32,66	33,78	32,44	33,86	32,57	34,57	31,67	32,97	32,44	33,29	32,26	33,16	31,29	32,18	30,82	32,80	32,97	33,00
Co	0,00	0,00	0,00	0,02	0,00	0,00	0,00	0,00	0,00	0,00	0,00	0,00	0,00	0,00	0,00	0,00	0,00	0,00	0,00	0,00	0,02	0,01	0,02	0,02	0,02
Ni	0,00	0,00	0,00	0,00	0,00	0,00	0,00	0,00	0,00	0,00	0,00	0,00	0,00	0,00	0,00	0,00	0,00	0,00	0,00	0,00	0,01	0,00	0,00	0,00	0,02
Cu	0,00	0,02	0,00	0,00	0,00	0,00	0,00	0,00	0,00	0,00	0,00	0,00	0,00	0,00	0,00	0,00	0,00	0,00	0,00	0,00	0,00	0,00	0,00	0,00	0,00
Zn	0,00	0,03	0,00	0,00	0,00	0,00	0,00	0,00	0,00	0,00	0,00	0,00	0,00	0,00	0,00	0,00	0,00	0,00	0,00	0,00	0,00	0,00	0,00	0,00	0,00
Ag	0,00	0,00	0,00	0,00	0,00	0,00	0,00	0,00	0,00	0,00	0,00	0,00	0,00	0,00	0,00	0,00	0,00	0,00	0,00	0,00	0,00	0,00	0,00	0,00	0,00
Au	0,00	0,00	0,00	0,01	0,02	0,10	0,13	0,04	0,21	0,00	0,17	0,01	0,19	0,01	0,00	0,01	0,28	0,00	0,04	0,00	0,00	0,00	0,08	0,11	0,02
Sum	100,1	100,1	100,0	100,1	100,0	100,1	100,1	100,1	100,2	100,1	100,1	100,1	100,0	100,1	100,0	100,1	100,3	100,1	99,9	100,1	100,1	100,1	100,1	100,1	100,0
Formula																									
Fe	1,02	1,03	1,02	1,03	1,00	1,01	0,98	1,00	0,99	1,00	1,01	1,00	1,00	1,00	1,01	1,01	0,99	1,00	1,04	1,02	1,03	1,02	1,01	1,01	1,02
S	1,04	1,03	1,01	1,01	1,00	1,01	1,02	1,02	1,00	1,02	0,97	1,03	0,96	1,05	1,00	1,02	1,01	1,03	0,97	1,05	1,01	1,06	1,00	1,00	0,99
As	0,94	0,94	0,96	0,97	1,00	0,98	1,00	0,98	1,01	0,97	1,01	0,98	1,04	0,95	0,99	0,97	1,00	0,97	0,99	0,94	0,96	0,92	0,98	0,99	0,99
Co	0,00	0,00	0,00	0,00	0,00	0,00	0,00	0,00	0,00	0,00	0,00	0,00	0,00	0,00	0,00	0,00	0,00	0,00	0,00	0,00	0,00	0,00	0,00	0,00	0,00
Ni	0,00	0,00	0,00	0,00	0,00	0,00	0,00	0,00	0,00	0,00	0,00	0,00	0,00	0,00	0,00	0,00	0,00	0,00	0,00	0,00	0,00	0,00	0,00	0,00	0,00
Cu	0,00	0,00	0,00	0,00	0,00	0,00	0,00	0,00	0,00	0,00	0,00	0,00	0,00	0,00	0,00	0,00	0,00	0,00	0,00	0,00	0,00	0,00	0,00	0,00	0,00
Zn	0,00	0,00	0,00	0,00	0,00	0,00	0,00	0,00	0,00	0,00	0,00	0,00	0,00	0,00	0,00	0,00	0,00	0,00	0,00	0,00	0,00	0,00	0,00	0,00	0,00
Ag	0,00	0,00	0,00	0,00	0,00	0,00	0,00	0,00	0,00	0,00	0,00	0,00	0,00	0,00	0,00	0,00	0,00	0,00	0,00	0,00	0,00	0,00	0,00	0,00	0,00
Au	0,00	0,00	0,00	0,00	0,00	0,00	0,00	0,00	0,01	0,00	0,01	0,00	0,01	0,00	0,00	0,00	0,01	0,00	0,00	0,00	0,00	0,00	0,00	0,00	0,00
Sum	3,00	3,00	3,00	3,00	3,00	3,00	3,00	3,00	3,00	3,00	3,00	3,00	3,00	3,00	3,00	3,00	3,00	3,00	3,00	3,00	3,00	3,00	3,00	3,00	3,00
As/S	0,90	0,91	0,95	0,96	1,01	0,97	0,98	0,96	1,01	0,95	1,04	0,95	1,08	0,90	0,99	0,96	0,99	0,94	1,03	0,90	0,96	0,87	0,98	0,99	1,00

continue

Weight%	core						rim			core				rim			core		rim				
Fe	35,34	35,51	34,57	35,25	34,60	34,92	34,67	35,31	34,75	34,94	34,68	34,99	34,93	34,68	34,29	34,19	35,47	35,20	34,63	34,40	34,72	34,43	34,32	34,46
S	21,60	21,32	21,42	21,01	21,87	21,86	20,75	19,54	20,15	20,42	20,51	20,51	19,87	19,61	19,74	19,89	20,61	20,71	19,71	20,89	20,16	21,26	20,18	19,35
As	42,15	42,15	44,01	43,74	43,53	43,23	44,57	45,07	45,09	44,55	44,75	44,38	44,89	44,90	45,96	45,91	43,89	44,09	45,65	44,70	45,11	44,31	45,48	45,14
Co	0,01	0,00	0,00	0,00	0,00	0,00	0,00	0,05	0,00	0,07	0,04	0,03	0,00	0,00	0,00	0,00	0,00	0,00	0,00	0,00	0,00	0,00	0,00	0,00
Ni	0,00	0,01	0,00	0,00	0,00	0,00	0,00	0,00	0,00	0,00	0,00	0,09	0,00	0,00	0,00	0,00	0,00	0,00	0,00	0,00	0,00	0,00	0,00	0,00
Cu	0,09	0,02	0,00	0,00	0,00	0,00	0,00	0,00	0,00	0,00	0,00	0,00	0,00	0,00	0,00	0,00	0,00	0,00	0,00	0,00	0,00	0,00	0,00	0,09
Zn	0,00	0,00	0,00	0,00	0,00	0,00	0,00	0,00	0,00	0,00	0,00	0,00	0,00	0,00	0,00	0,00	0,00	0,00	0,00	0,00	0,00	0,00	0,00	0,06
Ag	0,11	0,00	0,00	0,00	0,00	0,00	0,00	0,00	0,00	0,00	0,00	0,00	0,00	0,00	0,00	0,00	0,00	0,00	0,00	0,00	0,00	0,00	0,00	0,01
Au	0,00	0,00	0,00	0,00	0,00	0,00	0,00	0,03	0,09	0,00	0,00	0,00	0,00	0,00	0,02	0,14	0,00	0,00	0,01	0,02	0,03	0,02	0,19	0,15
Sum	99,30	99,01	100,0	100,0	100,0	100,0	99,9	100,0	100,1	99,9	99,9	100,0	99,7	99,2	100,0	100,1	99,9	100,0	100,0	100,0	100,0	100,0	100,2	99,2
Atomic%																								
Fe	33,84	34,11	33,02	33,75	32,90	33,17	33,32	34,30	33,59	33,69	33,42	33,71	33,91	33,90	33,31	33,18	34,07	33,80	33,63	33,04	33,56	32,94	33,20	33,85
S	36,02	35,67	35,62	35,02	36,21	36,17	34,74	33,06	33,92	34,29	34,43	34,41	33,60	33,39	33,40	33,62	34,49	34,63	33,33	34,95	33,94	35,43	34,00	33,05
As	30,34	30,41	31,51	31,37	31,07	30,85	32,05	32,65	32,55	32,11	32,24	31,98	32,53	32,74	33,29	33,22	31,56	31,69	33,05	32,13	32,56	31,77	32,85	33,10
Co	0,00	0,00	0,00	0,00	0,00	0,00	0,00	0,02	0,00	0,02	0,02	0,01	0,00	0,00	0,00	0,00	0,00	0,00	0,00	0,00	0,00	0,00	0,00	0,00
Ni	0,00	0,00	0,00	0,00	0,00	0,00	0,00	0,00	0,00	0,00	0,00	0,03	0,00	0,00	0,00	0,00	0,00	0,00	0,00	0,00	0,00	0,00	0,00	0,00
Cu	0,04	0,01	0,00	0,00	0,00	0,00	0,00	0,00	0,00	0,00	0,00	0,00	0,00	0,00	0,00	0,00	0,00	0,00	0,00	0,00	0,00	0,00	0,00	0,04
Zn	0,00	0,00	0,00	0,00	0,00	0,00	0,00	0,00	0,00	0,00	0,00	0,00	0,00	0,00	0,00	0,00	0,00	0,00	0,00	0,00	0,00	0,00	0,00	0,02
Ag	0,07	0,00	0,00	0,00	0,00	0,00	0,00	0,00	0,00	0,00	0,00	0,00	0,00	0,00	0,00	0,00	0,00	0,00	0,00	0,00	0,00	0,00	0,00	0,01
Au	0,00	0,00	0,00	0,00	0,00	0,00	0,00	0,04	0,11	0,00	0,00	0,00	0,00	0,00	0,03	0,17	0,00	0,00	0,01	0,03	0,04	0,02	0,23	0,18
Sum	100,3	100,2	100,1	100,1	100,2	100,2	100,1	100,0	100,1	100,1	100,1	100,1	100,0	100,0	100,0	100,1	100,1	100,1	100,0	100,1	100,1	100,2	100,3	100,2
Formula																								
Fe	1,01	1,02	0,99	1,01	0,99	0,99	1,00	1,03	1,01	1,01	1,00	1,01	1,02	1,02	1,00	0,99	1,02	1,01	1,01	0,99	1,01	0,99	0,99	1,01
S	1,08	1,07	1,07	1,05	1,08	1,08	1,04	0,99	1,02	1,03	1,03	1,03	1,01	1,00	1,00	1,01	1,03	1,04	1,00	1,05	1,02	1,06	1,02	0,99
As	0,91	0,91	0,94	0,94	0,93	0,92	0,96	0,98	0,97	0,96	0,97	0,96	0,98	0,98	1,00	0,99	0,95	0,95	0,99	0,96	0,98	0,95	0,98	0,99
Co	0,00	0,00	0,00	0,00	0,00	0,00	0,00	0,00	0,00	0,00	0,00	0,00	0,00	0,00	0,00	0,00	0,00	0,00	0,00	0,00	0,00	0,00	0,00	0,00
Ni	0,00	0,00	0,00	0,00	0,00	0,00	0,00	0,00	0,00	0,00	0,00	0,00	0,00	0,00	0,00	0,00	0,00	0,00	0,00	0,00	0,00	0,00	0,00	0,00
Cu	0,00	0,00	0,00	0,00	0,00	0,00	0,00	0,00	0,00	0,00	0,00	0,00	0,00	0,00	0,00	0,00	0,00	0,00	0,00	0,00	0,00	0,00	0,00	0,00
Zn	0,00	0,00	0,00	0,00	0,00	0,00	0,00	0,00	0,00	0,00	0,00	0,00	0,00	0,00	0,00	0,00	0,00	0,00	0,00	0,00	0,00	0,00	0,00	0,00
Ag	0,00	0,00	0,00	0,00	0,00	0,00	0,00	0,00	0,00	0,00	0,00	0,00	0,00	0,00	0,00	0,00	0,00	0,00	0,00	0,00	0,00	0,00	0,00	0,00
Au	0,00	0,00	0,00	0,00	0,00	0,00	0,00	0,00	0,00	0,00	0,00	0,00	0,00	0,00	0,00	0,00	0,00	0,00	0,00	0,00	0,00	0,00	0,01	0,01
Sum	3,00	3,00	3,00	3,00	3,00	3,00	3,00	3,00	3,00	3,00	3,00	3,00	3,00	3,00	3,00	3,00	3,00	3,00	3,00	3,00	3,00	3,00	3,00	3,00
As/S	0,84	0,85	0,88	0,90	0,86	0,85	0,92	0,99	0,96	0,94	0,94	0,93	0,97	0,98	1,00	0,99	0,92	0,91	0,99	0,92	0,96	0,90	0,97	1,00

Table D.8: Electron microprobe data of arsenopyrite belongs to the late sulphide assemblage, disseminated in the quartz-carbonate veins and in the laminated quartz veins in Um El Tuyor mine

Wt%																									
Fe	34,64	34,65	34,78	35,86	35,46	35,07	35,35	34,26	34,64	35,04	35,48	35,69	35,48	35,83	35,46	35,64	35,04	35,62	35,49	34,66	34,33	34,91	35,87	35,59	35,61
S	21,15	21,68	20,63	21,59	22,37	21,72	20,92	21,15	21,46	21,71	21,02	21,07	22,69	21,76	20,87	20,46	20,71	21,01	21,46	23,26	23,06	22,71	21,79	22,12	21,75
As	43,41	42,15	43,63	42,38	42,08	43,21	43,66	43,47	41,89	42,24	43,48	43,21	41,38	42,26	43,48	42,89	43,24	43,27	43,05	41,07	42,36	41,69	41,05	42,19	43,95
Co	0,02	0,00	0,00	0,00	0,00	0,00	0,00	0,00	0,00	0,00	0,00	0,00	0,00	0,00	0,06	0,00	0,00	0,00	0,00	0,00	0,04	0,05	0,05	0,00	0,00
Ni	0,01	0,00	0,00	0,00	0,00	0,00	0,00	0,00	0,00	0,00	0,00	0,00	0,00	0,00	0,11	0,00	0,00	0,00	0,00	0,00	0,00	0,00	0,46	0,00	0,00
Cu	0,00	0,04	0,00	0,00	0,00	0,00	0,00	0,00	0,00	0,00	0,00	0,00	0,00	0,00	0,00	0,00	0,00	0,00	0,00	0,00	0,00	0,00	0,00	0,00	0,00
Zn	0,00	0,06	0,06	0,00	0,00	0,00	0,00	0,00	0,00	0,00	0,00	0,00	0,00	0,00	0,00	0,00	0,00	0,00	0,00	0,00	0,00	0,00	0,00	0,00	0,00
Ag	0,00	0,07	0,17	0,00	0,00	0,00	0,00	0,00	0,00	0,00	0,00	0,00	0,00	0,00	0,00	0,00	0,00	0,00	0,00	0,00	0,00	0,00	0,00	0,00	0,00
Au	0,01	0,01	0,00	0,00	0,00	0,00	0,00	0,00	0,00	0,00	0,00	0,00	0,00	0,00	0,00	0,00	0,00	0,00	0,00	0,00	0,00	0,00	0,00	0,00	0,00
Sum	99,2	98,7	99,3	99,8	99,9	100,0	99,9	98,9	97,9	98,9	99,9	99,9	99,5	99,8	99,9	98,9	98,9	99,9	100,0	99,00	99,79	99,36	99,22	99,90	101,31
Atomic %																									
Fe	33,35	33,35	33,69	34,12	33,49	33,35	33,88	33,09	33,53	33,56	33,94	34,11	33,48	34,03	34,02	34,51	33,90	34,09	33,80	32,72	32,33	33,04	34,33	33,69	33,50
S	35,47	36,35	34,80	35,78	36,80	35,98	34,92	35,58	36,19	36,22	35,03	35,08	37,30	36,00	34,87	34,51	34,90	35,02	35,60	38,24	37,82	37,44	36,32	36,47	35,64
As	31,34	30,50	31,64	30,30	29,93	30,86	31,34	31,48	30,48	30,42	31,18	30,97	29,46	30,17	31,25	31,11	31,34	31,04	30,78	29,29	30,08	29,75	29,58	30,05	31,03
Co	0,01	0,00	0,00	0,00	0,00	0,00	0,00	0,00	0,00	0,00	0,00	0,00	0,00	0,00	0,02	0,00	0,00	0,00	0,00	0,00	0,01	0,02	0,02	0,00	0,00
Ni	0,00	0,00	0,00	0,00	0,00	0,00	0,00	0,00	0,00	0,00	0,00	0,00	0,00	0,00	0,04	0,00	0,00	0,00	0,00	0,00	0,00	0,00	0,17	0,00	0,00
Cu	0,00	0,02	0,00	0,00	0,00	0,00	0,00	0,00	0,00	0,00	0,00	0,00	0,00	0,00	0,00	0,00	0,00	0,00	0,00	0,00	0,00	0,00	0,00	0,00	0,00
Zn	0,00	0,02	0,02	0,00	0,00	0,00	0,00	0,00	0,00	0,00	0,00	0,00	0,00	0,00	0,00	0,00	0,00	0,00	0,00	0,00	0,00	0,00	0,00	0,00	0,00
Ag	0,00	0,05	0,11	0,00	0,00	0,00	0,00	0,00	0,00	0,00	0,00	0,00	0,00	0,00	0,00	0,00	0,00	0,00	0,00	0,00	0,00	0,00	0,00	0,00	0,00
Au	0,01	0,01	0,00	0,00	0,00	0,00	0,00	0,00	0,00	0,00	0,00	0,00	0,00	0,00	0,00	0,00	0,00	0,00	0,00	0,00	0,00	0,00	0,00	0,00	0,00
Sum	100,2	100,3	100,2	100,2	100,2	100,2	100,1	100,1	100,2	100,2	100,1	100,1	100,2	100,2	100,2	100,1	100,1	100,1	100,18	100,25	100,25	100,25	100,41	100,21	100,17
at%As/S	0,88	0,84	0,91	0,85	0,81	0,86	0,90	0,88	0,84	0,84	0,89	0,88	0,79	0,84	0,90	0,90	0,90	0,89	0,86	0,77	0,80	0,79	0,81	0,82	0,87
at% As+S	66,80	66,85	66,44	66,07	66,73	66,83	66,26	67,06	66,67	66,64	66,20	66,04	66,75	66,17	66,12	65,62	66,24	66,06	66,37	67,53	67,90	67,19	65,90	66,52	66,67
Formula																									
Fe	1,00	1,00	1,01	1,02	1,00	1,00	1,01	0,99	1,00	1,00	1,02	1,02	1,00	1,02	1,02	1,03	1,02	1,02	1,01	0,98	0,97	0,99	1,03	1,01	1,00
S	1,06	1,09	1,04	1,07	1,10	1,08	1,05	1,07	1,08	1,08	1,05	1,05	1,12	1,08	1,04	1,03	1,05	1,05	1,07	1,14	1,13	1,12	1,09	1,09	1,07
As	0,94	0,91	0,95	0,91	0,90	0,92	0,94	0,94	0,91	0,91	0,93	0,93	0,88	0,90	0,94	0,93	0,94	0,93	0,92	0,88	0,90	0,89	0,88	0,90	0,93
Co	0,00	0,00	0,00	0,00	0,00	0,00	0,00	0,00	0,00	0,00	0,00	0,00	0,00	0,00	0,00	0,00	0,00	0,00	0,00	0,00	0,00	0,00	0,00	0,00	0,00
Ni	0,00	0,00	0,00	0,00	0,00	0,00	0,00	0,00	0,00	0,00	0,00	0,00	0,00	0,00	0,00	0,00	0,00	0,00	0,00	0,00	0,00	0,00	0,00	0,00	0,00
Cu	0,00	0,00	0,00	0,00	0,00	0,00	0,00	0,00	0,00	0,00	0,00	0,00	0,00	0,00	0,00	0,00	0,00	0,00	0,00	0,00	0,00	0,00	0,00	0,00	0,00
Zn	0,00	0,00	0,00	0,00	0,00	0,00	0,00	0,00	0,00	0,00	0,00	0,00	0,00	0,00	0,00	0,00	0,00	0,00	0,00	0,00	0,00	0,00	0,00	0,00	0,00
Ag	0,00	0,00	0,00	0,00	0,00	0,00	0,00	0,00	0,00	0,00	0,00	0,00	0,00	0,00	0,00	0,00	0,00	0,00	0,00	0,00	0,00	0,00	0,00	0,00	0,00
Au	0,00	0,00	0,00	0,00	0,00	0,00	0,00	0,00	0,00	0,00	0,00	0,00	0,00	0,00	0,00	0,00	0,00	0,00	0,00	0,00	0,00	0,00	0,00	0,00	0,00
Sum	3,00	3,00	3,00	3,00	3,00	3,00	3,00	3,00	3,00	3,00	3,00	3,00	3,00	3,00	3,00	3,00	3,00	3,00	3,00	3,00	3,00	3,00	3,00	3,00	3,00

Table D.9: Electron microprobe data of pyrite (of the early sulphide assemblage) disseminated in the quartz-carbonate veins in Um El Tuyor mine

	pyrite intergrown with arsenopyrite in the quartz-carbonate veins															fine (~20µm) individual pyrite grains disseminated in the quartz-carbonate lode														
Wt%																														
Fe	46,75	46,56	46,63	46,08	45,42	46,26	46,28	46,07	45,36	46,25	46,01	46,49	46,96	46,75	45,59	45,83	45,72	46,20	46,72	46,03	46,25	46,33	45,83	45,72	44,53	45,38	46,86	45,28	44,71	46,56
S	53,24	53,43	52,39	53,23	54,57	52,55	52,58	52,65	52,70	53,10	53,98	53,50	53,03	53,24	54,40	52,78	54,27	53,62	53,27	53,04	52,51	53,04	51,52	53,66	54,87	51,16	52,56	52,03	54,26	53,43
As	0,62	0,68	0,52	0,62	0,28	0,34	0,21	0,22	0,28	0,77	0,27	0,43	0,52	0,62	0,34	0,39	0,21	0,27	0,23	1,57	1,18	1,56	2,27	0,74	0,51	2,35	1,69	1,22	0,94	0,68
Co	0,05	0,07	0,07	0,05	0,03	0,00	0,00	0,00	0,00	0,00	0,08	0,04	0,07	0,05	0,04	0,00	0,08	0,00	0,07	0,05	0,05	0,05	0,03	0,06	0,06	0,03	0,03	0,00	0,08	0,07
Ni	0,00	0,00	0,00	0,00	0,00	0,00	0,00	0,00	0,00	0,00	0,00	0,00	0,00	0,00	0,00	0,00	0,00	0,00	0,00	0,00	0,00	0,02	0,00	0,00	0,00	0,00	0,00	0,00	0,00	0,00
Cu	0,00	0,00	0,00	0,00	0,00	0,06	0,03	0,02	0,02	0,00	0,00	0,00	0,00	0,00	0,00	0,00	0,00	0,00	0,00	0,00	0,00	0,00	0,01	0,00	0,03	0,06	0,00	0,00	0,00	0,00
Zn	0,00	0,00	0,00	0,00	0,00	0,06	0,12	0,20	0,10	0,13	0,00	0,00	0,00	0,00	0,00	0,23	0,00	0,18	0,00	0,01	0,01	0,00	0,04	0,00	0,03	0,06	0,00	0,13	0,00	0,00
Ag	0,00	0,00	0,00	0,00	0,00	0,11	0,00	0,07	0,01	0,00	0,00	0,00	0,00	0,00	0,00	0,17	0,00	0,00	0,00	0,00	0,00	0,00	0,00	0,00	0,03	0,06	0,00	0,00	0,00	0,00
Au	0,02	0,04	0,01	0,02	0,01	0,01	0,00	0,01	0,15	0,09	0,02	0,07	0,09	0,09	0,02	0,00	0,01	0,00	0,00	0,21	0,19	0,23	0,53	0,14	0,09	0,67	0,36	0,42	0,23	0,08
Sum	100,7	100,7	99,6	100,0	100,3	99,4	99,2	99,2	98,6	100,3	100,3	100,5	100,7	100,7	100,4	99,4	100,3	100,3	100,3	100,9	100,2	101,2	100,2	100,3	100,1	99,8	101,5	99,1	100,2	100,8
Atomic %																														
Fe	33,41	33,23	33,72	33,09	32,29	33,51	33,53	33,40	33,02	33,20	32,81	33,21	33,61	33,41	32,42	33,20	32,56	33,05	33,45	32,98	33,37	33,13	33,40	32,72	31,69	33,32	33,56	33,10	31,95	33,23
S	66,26	66,41	66,00	66,58	67,56	66,31	66,35	66,48	66,82	66,39	67,04	66,56	66,11	66,26	67,39	66,59	67,32	66,81	66,43	66,19	66,00	66,05	65,39	66,89	68,02	65,43	65,56	66,24	67,54	66,41
As	0,33	0,36	0,28	0,33	0,15	0,18	0,11	0,12	0,15	0,41	0,14	0,23	0,28	0,33	0,18	0,21	0,11	0,14	0,12	0,82	0,63	0,82	1,20	0,39	0,27	1,25	0,89	0,65	0,50	0,36
Co	0,02	0,03	0,04	0,02	0,02	0,00	0,00	0,00	0,00	0,00	0,04	0,02	0,04	0,02	0,02	0,00	0,04	0,00	0,04	0,02	0,02	0,02	0,01	0,03	0,03	0,02	0,01	0,00	0,04	0,03
Ni	0,00	0,00	0,00	0,00	0,00	0,00	0,00	0,00	0,00	0,00	0,00	0,00	0,00	0,00	0,00	0,00	0,00	0,00	0,00	0,00	0,00	0,00	0,00	0,00	0,00	0,00	0,00	0,00	0,00	0,00
Cu	0,00	0,00	0,00	0,00	0,00	0,03	0,02	0,01	0,01	0,00	0,00	0,00	0,00	0,00	0,00	0,00	0,00	0,00	0,00	0,00	0,00	0,00	0,00	0,00	0,01	0,03	0,00	0,00	0,00	0,00
Zn	0,00	0,00	0,00	0,00	0,00	0,03	0,07	0,11	0,05	0,07	0,00	0,00	0,00	0,00	0,00	0,13	0,00	0,10	0,00	0,01	0,00	0,00	0,02	0,00	0,02	0,03	0,00	0,07	0,00	0,00
Ag	0,00	0,00	0,00	0,00	0,00	0,10	0,00	0,06	0,01	0,00	0,00	0,00	0,00	0,00	0,00	0,15	0,00	0,00	0,00	0,00	0,00	0,00	0,00	0,00	0,03	0,06	0,00	0,00	0,00	0,00
Au	0,02	0,07	0,02	0,04	0,02	0,02	0,00	0,02	0,25	0,15	0,03	0,11	0,15	0,15	0,04	0,00	0,02	0,00	0,00	0,34	0,31	0,38	0,87	0,23	0,15	1,10	0,59	0,69	0,38	0,14
Sum	100,0	100,1	100,0	100,0	100,0	100,1	100,0	100,2	100,3	100,2	100,0	100,1	100,2	100,2	100,1	100,3	100,0	100,1	100,0	100,4	100,3	100,4	100,9	100,2	100,2	101,2	100,6	100,7	100,4	100,2
Co/Ni	50,20	69,28	74,30	50,20	52,65	62,92	-	-	-	-	76,31	40,16	74,30	50,20	40,16	-	76,31	-	73,30	62,76	71,40	64,93	60,39	-	-	-	-	-	79,32	69,28
at%As/S	0,00	0,01	0,00	0,00	0,00	0,00	0,00	0,00	0,00	0,01	0,00	0,00	0,00	0,00	0,00	0,00	0,00	0,00	0,00	0,01	0,01	0,01	0,02	0,01	0,00	0,02	0,01	0,01	0,01	0,01
at% As+S	66,59	66,77	66,28	66,91	67,71	66,49	66,47	66,60	66,98	66,80	67,19	66,79	66,39	66,59	67,57	66,80	67,43	66,95	66,55	67,01	66,62	66,87	66,60	67,28	68,29	66,67	66,44	66,90	68,04	66,77
Formula																														
Fe	1,00	1,00	1,01	0,99	0,97	1,00	1,01	1,00	0,99	0,99	0,98	0,99	1,01	1,00	0,97	0,99	0,98	0,99	1,00	0,99	1,00	0,99	0,99	0,98	0,95	0,99	1,00	0,99	0,95	1,00
S	1,99	1,99	1,98	2,00	2,03	1,99	1,99	1,99	2,00	1,99	2,01	1,99	1,98	1,98	2,02	1,99	2,02	2,00	1,99	1,98	1,97	1,97	1,94	2,00	2,04	1,94	1,95	1,97	2,02	1,99
As	0,01	0,01	0,01	0,01	0,00	0,01	0,00	0,00	0,00	0,01	0,00	0,01	0,01	0,01	0,01	0,01	0,00	0,00	0,00	0,02	0,02	0,02	0,04	0,01	0,01	0,04	0,03	0,02	0,01	0,01
Co	0,00	0,00	0,00	0,00	0,00	0,00	0,00	0,00	0,00	0,00	0,00	0,00	0,00	0,00	0,00	0,00	0,00	0,00	0,00	0,00	0,00	0,00	0,00	0,00	0,00	0,00	0,00	0,00	0,00	0,00
Ni	0,00	0,00	0,00	0,00	0,00	0,00	0,00	0,00	0,00	0,00	0,00	0,00	0,00	0,00	0,00	0,00	0,00	0,00	0,00	0,00	0,00	0,00	0,00	0,00	0,00	0,00	0,00	0,00	0,00	0,00
Cu	0,00	0,00	0,00	0,00	0,00	0,00	0,00	0,00	0,00	0,00	0,00	0,00	0,00	0,00	0,00	0,00	0,00	0,00	0,00	0,00	0,00	0,00	0,00	0,00	0,00	0,00	0,00	0,00	0,00	0,00
Zn	0,00	0,00	0,00	0,00	0,00	0,00	0,00	0,00	0,00	0,00	0,00	0,00	0,00	0,00	0,00	0,00	0,00	0,00	0,00	0,00	0,00	0,00	0,00	0,00	0,00	0,00	0,00	0,00	0,00	0,00
Ag	0,00	0,00	0,00	0,00	0,00	0,00	0,00	0,00	0,00	0,00	0,00	0,00	0,00	0,00	0,00	0,00	0,00	0,00	0,00	0,00	0,00	0,00	0,00	0,00	0,00	0,00	0,00	0,00	0,00	0,00
Au	0,00	0,00	0,00	0,00	0,00	0,00	0,00	0,00	0,01	0,00	0,00	0,00	0,00	0,00	0,00	0,00	0,00	0,00	0,00	0,01	0,01	0,01	0,03	0,01	0,00	0,03	0,02	0,02	0,01	0,00
Sum	3,00	3,00	3,00	3,00	3,00	3,00	3,00	3,00	3,00	3,00	3,00	3,00	3,00	3,00	3,00	3,00	3,00	3,00	3,00	3,00	3,00	3,00	3,00	3,00	3,00	3,00	3,00	3,00	3,00	3,00

Table D.10: Electron microprobe data of pyrite of the late sulphide assemblage in the laminated quartz veins in Um El Tuyor mine

Fe	46,54	47,25	47,57	47,47	47,32	47,63	47,98	47,45	47,65	47,31	46,81	47,28	47,13	47,98	46,67	46,87	47,22	47,44	46,72	47,31
S	52,65	52,07	51,66	51,98	52,17	51,95	51,12	51,74	51,96	52,34	52,86	52,29	52,23	51,53	51,49	51,38	51,33	51,59	52,25	51,62
As	0,52	0,62	0,68	0,49	0,45	0,37	0,82	0,28	0,34	0,27	0,23	0,33	0,57	0,43	1,73	1,63	1,22	0,88	0,97	0,98
Co	0,07	0,07	0,07	0,06	0,05	0,05	0,06	0,04	0,04	0,08	0,07	0,07	0,06	0,04	0,30	0,06	0,23	0,36	0,26	0,07
Ni	0,00	0,00	0,00	0,00	0,00	0,00	0,00	0,00	0,00	0,00	0,00	0,00	0,00	0,00	0,01	0,00	0,01	0,01	0,01	0,00
Cu	0,00	0,00	0,00	0,00	0,00	0,00	0,00	0,00	0,00	0,00	0,00	0,00	0,00	0,00	0,00	0,00	0,00	0,00	0,00	0,00
Zn	0,00	0,00	0,00	0,00	0,00	0,00	0,00	0,00	0,00	0,00	0,00	0,00	0,00	0,00	0,00	0,00	0,00	0,00	0,00	0,00
Ag	0,00	0,00	0,00	0,00	0,00	0,00	0,00	0,00	0,00	0,00	0,00	0,00	0,00	0,00	0,00	0,00	0,00	0,00	0,00	0,00
Au	0,00	0,00	0,00	0,00	0,00	0,00	0,00	0,00	0,00	0,00	0,00	0,00	0,00	0,00	0,00	0,00	0,00	0,00	0,00	0,00
Sum	99,78	100,01	99,98	99,99	99,99	100,00	99,98	99,51	99,99	100,00	99,97	99,97	99,99	99,98	100,19	99,94	100,01	100,27	100,21	99,98
Atomic %																				
Fe	33,57	34,14	34,46	34,31	34,16	34,42	34,86	34,44	34,43	34,12	33,66	34,11	34,02	34,75	33,91	34,07	34,34	34,39	33,75	34,30
As	0,28	0,33	0,36	0,26	0,24	0,20	0,44	0,15	0,18	0,15	0,12	0,18	0,31	0,23	0,92	0,87	0,65	0,47	0,52	0,52
S	66,15	65,53	65,18	65,43	65,60	65,38	64,69	65,41	65,39	65,74	66,21	65,71	65,67	65,01	65,17	65,06	65,01	65,14	65,74	65,18
Co	0,03	0,03	0,03	0,03	0,02	0,02	0,03	0,02	0,02	0,04	0,04	0,03	0,03	0,02	0,15	0,03	0,11	0,18	0,13	0,03
Ni	0,00	0,00	0,00	0,00	0,00	0,00	0,00	0,00	0,00	0,00	0,00	0,00	0,00	0,00	0,00	0,00	0,00	0,00	0,00	0,00
Cu	0,00	0,00	0,00	0,00	0,00	0,00	0,00	0,00	0,00	0,00	0,00	0,00	0,00	0,00	0,00	0,00	0,00	0,00	0,00	0,00
Zn	0,00	0,00	0,00	0,00	0,00	0,00	0,00	0,00	0,00	0,00	0,00	0,00	0,00	0,00	0,00	0,00	0,00	0,00	0,00	0,00
Ag	0,00	0,00	0,00	0,00	0,00	0,00	0,00	0,00	0,00	0,00	0,00	0,00	0,00	0,00	0,00	0,00	0,00	0,00	0,00	0,00
Au	0,00	0,00	0,00	0,00	0,00	0,00	0,00	0,00	0,00	0,00	0,00	0,00	0,00	0,00	0,00	0,00	0,00	0,00	0,00	0,00
Sum	100,04	100,03	100,03	100,03	100,02	100,02	100,03	100,02	100,02	100,04	100,04	100,03	100,03	100,02	100,15	100,03	100,12	100,18	100,13	100,03
Co/Ni	71,29	65,27	69,28	55,22	50,20	47,19	61,25	41,17	40,16	76,31	73,30	68,78	56,23	40,16	49,54	43,79	44,78	52,86	45,01	41,84
Formula																				
Fe	1,01	1,02	1,03	1,03	1,02	1,03	1,05	1,03	1,03	1,02	1,01	1,02	1,02	1,04	1,02	1,02	1,03	1,03	1,01	1,03
S	1,98	1,97	1,95	1,96	1,97	1,96	1,94	1,96	1,96	1,97	1,99	1,97	1,97	1,95	1,95	1,95	1,95	1,95	1,97	1,95
As	0,01	0,01	0,01	0,01	0,01	0,01	0,01	0,00	0,01	0,00	0,00	0,01	0,01	0,01	0,03	0,03	0,02	0,01	0,02	0,02
Co	0,00	0,00	0,00	0,00	0,00	0,00	0,00	0,00	0,00	0,00	0,00	0,00	0,00	0,00	0,00	0,00	0,00	0,01	0,00	0,00
Ni	0,00	0,00	0,00	0,00	0,00	0,00	0,00	0,00	0,00	0,00	0,00	0,00	0,00	0,00	0,00	0,00	0,00	0,00	0,00	0,00
Cu	0,00	0,00	0,00	0,00	0,00	0,00	0,00	0,00	0,00	0,00	0,00	0,00	0,00	0,00	0,00	0,00	0,00	0,00	0,00	0,00
Zn	0,00	0,00	0,00	0,00	0,00	0,00	0,00	0,00	0,00	0,00	0,00	0,00	0,00	0,00	0,00	0,00	0,00	0,00	0,00	0,00
Ag	0,00	0,00	0,00	0,00	0,00	0,00	0,00	0,00	0,00	0,00	0,00	0,00	0,00	0,00	0,00	0,00	0,00	0,00	0,00	0,00
Au	0,00	0,00	0,00	0,00	0,00	0,00	0,00	0,00	0,00	0,00	0,00	0,00	0,00	0,00	0,00	0,00	0,00	0,00	0,00	0,00
Sum	3,00	3,00	3,00	3,00	3,00	3,00	3,00	3,00	3,00	3,00	3,00	3,00	3,00	3,00	3,00	3,00	3,00	3,00	3,00	3,00
at% As+S	66,43	65,86	65,54	65,69	65,84	65,58	65,13	65,56	65,57	65,88	66,34	65,89	65,98	65,24	66,09	65,93	65,66	65,61	66,25	65,70

Table D.11: Electron microprobe data of sphalerite grains and inclusions in the Um El Tuyor gold deposit

	Point no.	sph_9_2	sph_9_4	sph_8_1	sph_2_3	sph_2_7	sph_3_3	sph_8_4	sph_2_5	sph_5_3	sph_5_5	Sph_7_4	sph_8_6	sph_2_8	sph_2_3	sph_2_1	sph_4_6	sph_4_4
		sphalerite inclusions in arsenopyrite in quartz-carbonate lodes								individual sphalerite grains disseminated in the wallrock								
Weight %	Fe	9.41	9.83	10.02	10.77	9.92	9.58	10.26	9.92	12.04	10.13	9.88	10.29	9.84	10.19	9.87	10.03	10.81
	S	32.44	27.46	28.43	28.29	30.01	30.93	30.93	31.74	25.52	32.02	32.79	32.19	32.08	31.76	32.72	31.53	29.40
	As	0.26	0.11	0.26	0.19	0.20	0.27	0.27	0.13	0.51	0.20	0.20	0.188	0.11	0.14	0.16	0.20	0.19
	Co	0.01	0.04	0.01	0.03	0.00	0.03	0.03	0.00	0.04	0.00	0.00	0.00	0.04	0.00	0.00	0.00	0.00
	Cu	0.11	0.00	0.00	0.00	0.00	0.00	0.00	0.00	0.03	0.00	0.00	0.00	0.039	0.00	0.00	0.00	0.00
	Zn	57.33	61.42	61.36	61.09	59.89	59.32	58.72	58.61	62.85	58.22	57.11	58.08	58.65	58.15	58.01	58.01	58.72
	Ag	0.00	0.00	0.00	0.00	0.00	0.00	0.00	0.00	0.00	0.00	0.00	0.00	0.00	0.039	0.04	0.02	0.04
	Au	0.00	0.00	0.00	0.00	0.00	0.00	0.00	0.00	0.00	0.00	0.00	0.00	0.00	0.14	0.19	0.09	0.91
	Sum	99.56	98.86	100.08	100.37	100.02	100.13	100.21	100.40	100.98	100.56	99.98	100.75	100.76	100.42	100.99	99.88	100.08
Atomic %	Fe	0.16	0.18	0.18	0.19	0.17	0.17	0.18	0.17	0.22	0.17	0.17	0.18	0.17	0.18	0.17	0.17	0.19
	S	0.98	0.87	0.88	0.88	0.92	0.94	0.94	0.96	0.80	0.96	0.99	0.97	0.96	0.96	0.98	0.96	0.91
	As	0.00	0.00	0.00	0.00	0.00	0.00	0.00	0.00	0.01	0.00	0.00	0.00	0.00	0.00	0.00	0.00	0.00
	Co	0.00	0.00	0.00	0.00	0.00	0.00	0.00	0.00	0.00	0.00	0.00	0.00	0.00	0.00	0.00	0.00	0.00
	Cu	0.00	0.00	0.00	0.00	0.00	0.00	0.00	0.00	0.00	0.00	0.00	0.00	0.00	0.00	0.00	0.00	0.00
	Zn	0.85	0.95	0.93	0.93	0.90	0.89	0.88	0.87	0.97	0.86	0.84	0.85	0.86	0.86	0.85	0.86	0.89
	Ag	0.00	0.00	0.00	0.00	0.00	0.00	0.00	0.00	0.00	0.00	0.00	0.00	0.00	0.00	0.00	0.00	0.00
	Au	0.00	0.00	0.00	0.00	0.00	0.00	0.00	0.00	0.00	0.00	0.00	0.00	0.00	0.00	0.00	0.00	0.00
	Sum	2.000	2.000	2.000	2.000	2.000	2.000	2.000	2.000	2.000	2.000	2.000	2.000	2.000	2.000	2.00	2.00	2.00
Formula	Fe	8.17	8.92	8.93	9.58	8.74	8.38	8.96	8.60	10.88	8.75	8.52	8.86	8.48	8.83	8.46	8.74	9.60
	S	49.05	43.39	44.15	43.84	46.05	47.11	47.04	47.92	40.18	48.17	49.26	48.29	48.18	47.96	48.87	47.89	45.48
	As	0.17	0.07	0.17	0.13	0.13	0.18	0.18	0.08	0.34	0.13	0.13	0.12	0.07	0.09	0.10	0.13	0.13
	Co	0.01	0.03	0.01	0.03	0.00	0.02	0.02	0.00	0.03	0.00	0.00	0.00	0.03	0.00	0.00	0.00	0.00
	Cu	0.09	0.00	0.00	0.00	0.00	0.00	0.00	0.00	0.02	0.00	0.00	0.00	0.03	0.00	0.00	0.00	0.00
	Zn	42.52	47.59	46.73	46.43	45.08	44.31	43.80	43.40	48.54	42.96	42.09	42.73	43.20	43.07	42.50	43.21	44.55
	Ag	0.00	0.00	0.00	0.00	0.00	0.00	0.00	0.00	0.00	0.00	0.00	0.00	0.00	0.02	0.02	0.01	0.02
	Au	0.00	0.00	0.00	0.00	0.00	0.00	0.00	0.00	0.00	0.00	0.00	0.00	0.00	0.03	0.05	0.02	0.23
	Sum	100.00	100.00	100.00	100.00	100.00	100.00	100.00	100.00	100.00	100.00	100.00	100.00	100.00	100.00	100.00	100.00	100.00
End members	FeS	16.03	15.75	15.99	17.06	16.20	15.84	16.91	16.51	18.19	16.88	16.80	17.14	16.37	16.97	16.55	16.78	17.60
	AsS	0.33	0.13	0.31	0.22	0.24	0.33	0.33	0.16	0.57	0.24	0.25	0.23	0.14	0.17	0.20	0.25	0.23
	CoS	0.02	0.05	0.02	0.05	0.00	0.05	0.05	0.00	0.06	0.00	0.00	0.00	0.06	0.00	0.00	0.00	0.00
	CuS	0.17	0.00	0.00	0.00	0.00	0.00	0.00	0.00	0.04	0.00	0.00	0.00	0.06	0.00	0.00	0.00	0.00
	ZnS	83.45	84.07	83.68	82.67	83.56	83.78	82.71	83.33	81.14	82.88	82.95	82.63	83.37	82.75	83.12	82.91	81.70
	AgS	0.00	0.00	0.00	0.00	0.00	0.00	0.00	0.00	0.00	0.00	0.00	0.00	0.00	0.03	0.03	0.02	0.04
	AuS	0.00	0.00	0.00	0.00	0.00	0.00	0.00	0.00	0.00	0.00	0.00	0.00	0.00	0.07	0.09	0.04	0.42
	Sum	100.00	100.00	100.00	100.00	100.00	100.00	100.00	100.00	100.00	100.00	100.00	100.00	100.00	100.00	100.00	100.00	100.00
	PSph	**3.62**	**3.87**	**3.65**	**2.75**	**3.48**	**3.79**	**2.87**	**3.21**	**1.86**	**2.90**	**2.97**	**2.69**	**3.33**	**2.82**	**3.17**	**2.99**	**2.32**

P_{Sph} =42,3-32,1*(LOG FeS mole%), Scott (1973)

Table D.12: Microanalyses data of pyrrhotite inclusions in arsenopyrite in the quartz-carbonate veins

Fe	59,78	58,51	56,40	58,39	57,87	59,34
S	38,31	38,78	40,42	40,39	40,15	38,02
As	0,81	0,62	2,77	0,11	0,40	2,17
Co	0,07	0,07	0,05	0,03	0,42	0,08
Ni	0,04	0,03	0,02	0,01	0,14	0,03
Sum	99,03	98,03	99,59	98,95	98,98	99,66
Fe	46,99	46,21	43,76	45,31	44,99	46,62
S	52,46	53,35	54,63	54,60	54,37	52,03
As	0,47	0,36	1,60	0,06	0,23	1,27
Co	0,05	0,05	0,02	0,02	0,33	0,06
Ni	0,03	0,02	0,01	0,01	0,08	0,02
Sum	100,00	100,00	100,00	100,00	100,00	100,00
Co/Ni	1,67	2,50	2,00	3,33	4,13	3,00
Fe	0,94	0,92	0,88	0,91	0,90	0,93
S	1,049	1,067	1,093	1,092	1,087	1,041
As	0,01	0,01	0,03	0,00	0,01	0,03
Co	0,00	0,00	0,00	0,00	0,01	0,00
Ni	0,00	0,00	0,00	0,00	0,00	0,00
Sum	2,00	2,00	2,00	2,00	2,00	2,00

Table D.13: Electron microprobe data of chalcopyrite inclusions and individual grains in the Um El Tuyor gold deposit

Fe	30,91	30,81	30,61	30,58	31,97	30,54	30,96	30,63	29,58	29,99	29,94	29,72	30,4	30,4	28,38	28,88	28,58	28,89	28,51	27,71	28,21	30,45	30,32	28,59	31,31	30,4
S	33,96	34,28	34,41	34,67	34	34,67	34,25	34,71	35,25	34,52	35,01	34,21	32,99	33,28	36,52	35,67	36,54	36,71	36,41	35,79	35,74	35,78	35,24	35,51	32,95	33,54
As	0,13	0,1	0,2	0,24	0,43	0,19	0,51	0,25	0,08	0,13	0,21	0,17	0,09	0,24	0,69	0,41	0,69	0,2	0,13	0,17	0,24	0,07	0,17	0,33	0,09	0,12
Co	0,04	0,05	0,05	0,05	0,08	0,06	0,04	0,04	0,04	0,03	0,07	0,05	0	0	0,02	0,06	0,06	0,03	0,06	0,04	0,03	0	0,06	0,06	0	0,07
Cu	35,12	34,91	34,41	34,74	34,03	34,78	34,79	34,67	35,05	35,32	34,8	35,83	35,41	35,49	34,38	34,98	34,11	34,96	34,89	36,29	35,78	33,67	34,17	35,47	35,37	35,83
Sum	100,1	100,1	99,68	100,2	100,5	100,2	100,5	100,3	99,99	99,99	100,0	99,98	99,2	99,46	100	99,99	99,98	100,8	100	100	99,99	99,97	99,96	99,96	99,96	99,99
Fe	25,53	25,39	25,3	25,12	26,31	25,1	25,46	25,15	24,27	24,73	24,6	24,57	25,53	25,39	23,12	23,65	23,28	23,34	23,23	22,69	23,1	24,87	24,87	23,45	26,12	25,23
S	48,86	49,22	49,54	49,61	48,74	49,63	49,06	49,65	50,38	49,58	50,1	49,26	48,27	48,41	51,83	50,88	51,84	51,68	51,67	51,05	50,98	50,91	50,35	50,73	47,89	48,5
As	0,08	0,06	0,12	0,15	0,26	0,12	0,31	0,15	0,05	0,08	0,13	0,1	0,06	0,15	0,42	0,25	0,42	0,12	0,08	0,1	0,14	0,04	0,1	0,2	0,05	0,08
Co	0,03	0,04	0,04	0,04	0,06	0,04	0,03	0,03	0,03	0,02	0,05	0,04	0	0	0,02	0,04	0,05	0,02	0,04	0,03	0,02	0	0,04	0,04	0	0,05
Cu	25,5	25,29	25	25,08	24,62	25,12	25,14	25,02	25,28	25,59	25,13	26,03	26,14	26,05	24,61	25,17	24,42	24,83	24,98	26,12	25,75	24,17	24,63	25,57	25,94	26,14
Sum	100	100	100	100	100	100	100	100	100	100	100	100	100	100	100	100	100	100	100	100	100	100	100	100	100	100
Fe	1,02	1,02	1,01	1	1,05	1	1,02	1,01	0,97	0,99	0,98	0,98	1,02	1,02	0,92	0,95	0,93	0,93	0,93	0,91	0,92	0,99	0,99	0,94	1,04	1,01
S	1,95	1,97	1,98	1,98	1,95	1,99	1,96	1,99	2,02	1,98	2	1,97	1,93	1,94	2,07	2,04	2,07	2,07	2,07	2,04	2,04	2,04	2,01	2,03	1,92	1,94
As	0	0	0	0,01	0,01	0	0,01	0,01	0	0	0,01	0	0	0,01	0,02	0,01	0,02	0	0	0	0,01	0	0	0,01	0	0
Co	0	0	0	0	0	0	0	0	0	0	0	0	0	0	0	0	0	0	0	0	0	0	0	0	0	0
Cu	1,02	1,01	1	1	0,98	1	1,01	1	1,01	1,02	1,01	1,04	1,05	1,04	0,98	1,01	0,98	0,99	1	1,04	1,03	0,97	0,99	1,02	1,04	1,05
Sum	4	4	4	4	4	4	4	4	4	4	4	4	4	4	4	4	4	4	4	4	4	4	4	4	4	4

Table D.14: Electron microprobe data of cobaltite and solid solutions, disseminated in chlorite-sericite rich wallrocks in the Um El Tuyor mine

	Cobaltite (Co, Ni, Fe)AsS						Solid solution/exsolution in the (Fe-Co-Ni-As-S) system				
Wt%											
Co	18,16	18,65	21,41	17,36	21,60	24,58	0,27	0,47	0,18	0,35	0,40
S	19,38	19,84	20,24	20,41	19,81	20,40	23,52	19,49	18,99	19,42	19,77
As	45,43	45,35	44,51	44,60	44,44	44,21	42,23	45,95	45,96	45,64	45,10
Fe	7,47	7,40	6,79	8,14	7,10	5,71	13,22	13,38	13,22	13,17	13,30
Ni	9,12	8,73	7,03	9,46	7,03	4,09	20,72	20,09	21,61	21,37	21,22
Cu	0,00	0,00	0,00	0,00	0,00	0,00	0,03	0,02	0,03	0,03	0,02
Zn	0,00	0,00	0,00	0,00	0,00	0,00	0,00	0,00	0,00	0,00	0,00
Sum	99,56	99,97	99,98	99,97	99,98	98,98	99,99	99,39	99,99	100,00	99,81
Atomic%											
Co	17,04	17,37	19,85	16,06	20,09	22,97	0,24	0,44	0,17	0,33	0,37
As	33,54	33,22	32,46	32,46	32,51	32,50	29,73	33,86	33,82	33,45	32,98
S	33,43	33,96	34,49	34,72	33,86	35,04	38,70	33,56	32,65	33,27	33,78
Fe	7,40	7,27	6,64	7,95	6,97	5,63	12,49	13,23	13,06	12,95	13,05
Ni	8,59	8,16	6,54	8,79	6,56	3,84	18,62	18,90	20,30	19,99	19,81
Cu	0,00	0,00	0,00	0,00	0,00	0,00	0,01	0,01	0,01	0,01	0,01
Zn	0,00	0,00	0,00	0,00	0,00	0,00	0,00	0,00	0,00	0,00	0,00
Sum	100,00	99,99	99,98	99,98	99,99	99,98	99,79	100,00	100,01	100,01	99,99
Formula											
Co	0,51	0,52	0,60	0,48	0,60	0,69	0,01	0,01	0,01	0,01	0,01
S	1,00	1,02	1,03	1,04	1,02	1,05	1,16	1,01	0,98	1,00	1,01
As	1,01	1,00	0,97	0,97	0,98	0,98	0,89	1,02	1,01	1,00	0,99
Fe	0,22	0,22	0,20	0,24	0,21	0,17	0,38	0,40	0,39	0,39	0,39
Ni	0,26	0,24	0,20	0,26	0,20	0,12	0,56	0,57	0,61	0,60	0,59
Cu	0,00	0,00	0,00	0,00	0,00	0,00	0,00	0,00	0,00	0,00	0,00
Zn	0,00	0,00	0,00	0,00	0,00	0,00	0,00	0,00	0,00	0,00	0,00
Sum	3,00	3,00	3,00	3,00	3,00	3,00	3,00	3,00	3,00	3,00	3,00
Estimated Formula	$(Co_{0.48-0.69}, Ni_{0.12-0.26}, Fe_{0.17-0.24}) As_{0.97-1.01} S_{1-1.05}$						$(Co_{0.01}, Ni_{0.56-0.61}, Fe_{0.38-0.40}) As_{0.89-1.02} S_{0.98-1.16}$				

Table D.15: Chemical composition of marcasite grains disseminated in the chlorite-sericite altered wallrocks in the Um El Tuyor mine

Fe	46,89	46,43	46,99	47,42	47,37	46,32	45,39	46,57	47,68	47,64	46,29	46,31	46,79	47,24	46,22	45,57	47,74	47,37	47,37	46,20
S	53,26	52,95	52,87	52,44	52,75	52,66	52,72	51,22	52,35	52,62	53,26	53,55	52,91	52,37	52,70	52,07	52,05	52,22	52,50	52,20
As	0,10	0,09	0,17	0,08	0,09	0,09	0,08	0,12	0,14	0,00	0,10	0,09	0,17	0,08	0,09	0,11	0,14	0,00	0,09	0,08
Co	0,07	0,09	0,05	0,06	0,03	0,15	0,09	0,08	0,07	0,10	0,07	0,07	0,08	0,06	0,21	0,06	0,06	0,07	0,06	0,09
Ni	0,24	0,31	0,23	0,22	0,11	0,66	0,32	0,31	0,31	0,28	0,24	0,21	0,29	0,22	0,66	0,12	0,17	0,28	0,14	0,32
Cu	0,03	0,00	0,04	0,00	0,10	0,00	0,05	0,02	0,05	0,03	0,03	0,00	0,04	0,00	0,00	0,02	0,05	0,03	0,10	0,05
Zn	0,00	0,00	0,03	0,02	0,00	0,00	0,05	0,00	0,00	0,00	0,00	0,00	0,03	0,02	0,00	0,00	0,00	0,00	0,00	0,05
Ag	0,00	0,00	0,00	0,00	0,00	0,00	0,00	0,00	0,00	0,00	0,00	0,00	0,00	0,00	0,00	0,00	0,00	0,00	0,00	0,00
Au	0,00	0,00	0,00	0,00	0,00	0,00	0,00	0,00	0,00	0,00	0,00	0,00	0,00	0,00	0,00	0,00	0,00	0,00	0,00	0,00
Sum	100,59	99,86	100,39	100,25	100,45	99,88	98,70	98,33	100,60	100,67	99,99	100,23	100,31	99,99	99,88	97,96	100,20	99,97	100,25	98,99
Fe	33,56	33,47	33,75	34,16	34,00	33,54	33,07	34,27	34,31	34,20	33,27	33,16	33,64	34,10	33,47	33,42	34,47	34,24	34,11	33,68
As	0,05	0,05	0,09	0,04	0,05	0,05	0,04	0,07	0,07	0,00	0,05	0,05	0,09	0,04	0,05	0,06	0,07	0,00	0,05	0,04
S	66,39	66,48	66,15	65,79	65,95	66,41	66,89	65,66	65,61	65,80	66,68	66,79	66,26	65,85	66,48	66,52	65,46	65,75	65,84	66,28
Co	0,04	0,04	0,03	0,03	0,01	0,08	0,04	0,04	0,03	0,05	0,04	0,03	0,04	0,03	0,10	0,03	0,03	0,03	0,03	0,04
Ni	0,12	0,15	0,11	0,11	0,05	0,32	0,16	0,15	0,15	0,14	0,12	0,10	0,14	0,11	0,32	0,06	0,08	0,14	0,07	0,16
Cu	0,01	0,00	0,02	0,00	0,05	0,00	0,03	0,01	0,03	0,02	0,01	0,00	0,02	0,00	0,00	0,01	0,03	0,02	0,05	0,03
Zn	0,00	0,00	0,01	0,01	0,00	0,00	0,03	0,00	0,00	0,00	0,00	0,00	0,01	0,01	0,00	0,00	0,00	0,00	0,00	0,03
Ag	0,00	0,00	0,00	0,00	0,00	0,00	0,00	0,00	0,00	0,00	0,00	0,00	0,00	0,00	0,00	0,00	0,00	0,00	0,00	0,00
Au	0,00	0,00	0,00	0,00	0,00	0,00	0,00	0,00	0,00	0,00	0,00	0,00	0,00	0,00	0,00	0,00	0,00	0,00	0,00	0,00
Sum	100,17	100,19	100,18	100,15	100,12	100,40	100,25	100,20	100,21	100,20	100,17	100,14	100,22	100,15	100,43	100,10	100,13	100,19	100,15	100,25
Co/Ni	0,30	0,28	0,23	0,29	0,24	0,23	0,28	0,27	0,22	0,35	0,30	0,33	0,28	0,29	0,32	0,53	0,36	0,25	0,42	0,28
Fe	1,01	1,00	1,01	1,02	1,02	1,00	0,99	1,03	1,03	1,02	1,00	0,99	1,01	1,02	1,00	1,00	1,03	1,03	1,02	1,01
S	1,99	1,99	1,98	1,97	1,98	1,98	2,00	1,97	1,96	1,97	2,00	2,00	1,98	1,97	1,99	1,99	1,96	1,97	1,97	1,98
As	0,00	0,00	0,00	0,00	0,00	0,00	0,00	0,00	0,00	0,00	0,00	0,00	0,00	0,00	0,00	0,00	0,00	0,00	0,00	0,00
Co	0,00	0,00	0,00	0,00	0,00	0,00	0,00	0,00	0,00	0,00	0,00	0,00	0,00	0,00	0,00	0,00	0,00	0,00	0,00	0,00
Ni	0,00	0,00	0,00	0,00	0,00	0,01	0,00	0,00	0,00	0,00	0,00	0,00	0,00	0,00	0,01	0,00	0,00	0,00	0,00	0,00
Cu	0,00	0,00	0,00	0,00	0,00	0,00	0,00	0,00	0,00	0,00	0,00	0,00	0,00	0,00	0,00	0,00	0,00	0,00	0,00	0,00
Zn	0,00	0,00	0,00	0,00	0,00	0,00	0,00	0,00	0,00	0,00	0,00	0,00	0,00	0,00	0,00	0,00	0,00	0,00	0,00	0,00
Ag	0,00	0,00	0,00	0,00	0,00	0,00	0,00	0,00	0,00	0,00	0,00	0,00	0,00	0,00	0,00	0,00	0,00	0,00	0,00	0,00
Au	0,00	0,00	0,00	0,00	0,00	0,00	0,00	0,00	0,00	0,00	0,00	0,00	0,00	0,00	0,00	0,00	0,00	0,00	0,00	0,00
Sum	3,00	3,00	3,00	3,00	3,00	3,00	3,00	3,00	3,00	3,00	3,00	3,00	3,00	3,00	3,00	3,00	3,00	3,00	3,00	3,00
at As+S	66,44	66,53	66,25	65,84	66,00	66,46	66,93	65,72	65,68	65,80	66,73	66,84	66,36	65,89	66,53	66,58	65,53	65,75	65,89	66,32

Table D.16: Electron microprobe data of gold grains disseminated in the auriferous quartz veins and dispersed in the wallrocks in the Um El Tuyor mine

Gold inclusions in arsenopyrite and pyrite grains

Wt%																					
Ag	10,68	12,65	12,24	12,51	12,57	11,87	13,08	12,31	12,54	9,51	13,91	13,89	14,04	12,86	12,96	12,03	10,48	9,30	14,32	9,93	10,25
Te	0,00	0,00	0,00	0,00	0,00	0,00	0,00	0,00	0,00	0,00	0,11	0,00	0,00	0,00	0,00	0,04	0,00	0,00	0,00	0,11	0,00
Au	89,31	87,33	87,76	87,49	87,43	88,10	86,92	87,63	87,41	90,39	85,98	86,11	85,87	87,14	87,02	87,93	89,41	90,70	85,68	89,96	89,71
Sb	0,00	0,00	0,00	0,00	0,00	0,00	0,00	0,07	0,04	0,07	0,00	0,00	0,04	0,00	0,00	0,00	0,00	0,00	0,00	0,00	0,04
Total	100,00	99,99	100,00	100,00	100,00	99,97	100,00	100,00	100,00	99,97	100,00	100,00	99,96	100,00	99,98	100,00	99,89	100,00	99,99	100,00	100,00
Atomic%																					
Ag	17,93	20,92	20,29	20,70	20,80	19,74	21,56	20,39	20,75	16,10	22,77	22,75	22,98	21,23	21,38	19,98	17,63	15,77	23,38	16,75	17,25
Te	0,00	0,00	0,00	0,00	0,00	0,00	0,00	0,00	0,00	0,00	0,15	0,00	0,00	0,00	0,00	0,06	0,00	0,00	0,00	0,15	0,00
Au	82,07	79,08	79,71	79,30	79,20	80,26	78,44	79,51	79,19	83,79	77,08	77,25	76,96	78,77	78,62	79,96	82,37	84,23	76,62	83,10	82,69
Sb	0,00	0,00	0,00	0,00	0,00	0,00	0,00	0,10	0,06	0,11	0,00	0,00	0,06	0,00	0,00	0,00	0,00	0,00	0,00	0,00	0,06
Sum	100,00	100,00	100,00	100,00	100,00	100,00	100,00	100,00	100,00	100,00	100,00	100,00	100,00	100,00	100,00	100,00	100,00	100,00	100,00	100,00	100,00
Formula																					
Ag	0,18	0,21	0,20	0,21	0,21	0,20	0,22	0,20	0,21	0,16	0,23	0,23	0,23	0,21	0,21	0,20	0,18	0,16	0,23	0,17	0,17
Te	0,00	0,00	0,00	0,00	0,00	0,00	0,00	0,00	0,00	0,00	0,00	0,00	0,00	0,00	0,00	0,00	0,00	0,00	0,00	0,00	0,00
Au	0,82	0,79	0,80	0,79	0,79	0,80	0,78	0,80	0,79	0,84	0,77	0,77	0,77	0,79	0,79	0,80	0,82	0,84	0,77	0,83	0,83
Sb	0,00	0,00	0,00	0,00	0,00	0,00	0,00	0,00	0,00	0,00	0,00	0,00	0,00	0,00	0,00	0,00	0,00	0,00	0,00	0,00	0,00
Sum	1,00	1,00	1,00	1,00	1,00	1,00	1,00	1,00	1,00	1,00	1,00	1,00	1,00	1,00	1,00	1,00	1,00	1,00	1,00	1,00	1,00
Fineness	893,16	873,45	877,64	874,93	874,29	881,31	869,19	876,85	874,50	904,79	860,75	861,09	859,45	871,41	870,40	879,64	895,07	907,03	861,09	859,45	871,41
Au/Ag	8,36	6,90	7,17	7,00	6,95	7,43	6,64	7,12	6,97	9,50	6,18	6,20	6,11	6,78	6,72	7,31	8,53	9,76	6,20	6,11	6,78

Electrum grains disseminated in the quartz-carbonate veins

Fe	0,662	0,85	0,64	0,49	0,354	0,42
S	0,084	0,06	0,071	0,07	0,068	0,059
As	0,172	0,27	0,204	0,19	0,187	0,209
Zn	1,746	1,18	1,018	0,98	0,987	0,897
Ag	20,32	19,33	19,88	20,12	19,13	19,31
Au	77,20	78,28	78,43	78,30	79,87	79,89
Total	100,18	99,97	100,24	100,15	100,60	100,79
Fe	1,90	2,47	1,87	1,44	1,04	1,23
S	0,42	0,30	0,36	0,36	0,35	0,30
As	0,37	0,59	0,44	0,41	0,41	0,46
Zn	4,28	2,93	2,53	2,44	2,48	2,25
Ag	30,20	29,12	29,99	30,45	29,13	29,32
Au	62,83	64,58	64,80	64,90	66,60	66,44
Sum	100,00	100,00	100,00	100,00	100,00	100,00
Fe	0,02	0,02	0,02	0,01	0,01	0,01
S	0,00	0,00	0,00	0,00	0,00	0,00
As	0,00	0,01	0,00	0,00	0,00	0,00
Zn	0,04	0,03	0,03	0,02	0,02	0,02
Ag	0,30	0,29	0,30	0,30	0,29	0,29
Au	0,63	0,65	0,65	0,65	0,67	0,66
Sum	1,00	1,00	1,00	1,00	1,00	1,00
Fineness	791,64	801,97	797,78	795,58	806,77	805,34
Au/Ag	3,8	4,05	3,94	3,89	4,17	4,13

Dispersed and fracture-filling free gold blebs and wires in the laminated quartz veins

Ag	5.70	5.87	6.84	6.37	6.39	6.70	7.03	7.19	7.31	7.28	7.54	7.18	7.18	6.29	5.60	6.82
Te	0,11	0,00	0,00	0,00	0,00	0,00	0,80	0,00	0,00	0,00	0,00	0,00	0,00	0,00	0,00	0,00
Au	94,19	94,09	93,09	93,60	93,61	93,30	92,89	92,79	92,61	92,65	92,45	92,79	92,81	93,71	94,40	93,18
Sb	0,00	0,00	0,05	0,00	0,00	0,00	0,00	0,00	0,75	0,05	0,00	0,00	0,00	0,00	0,00	0,00
Total	100,0	99,96	99,98	99,97	100,0	100,0	100,7	99,98	100,6	99,98	99,99	99,97	99,99	100,0	100,0	100,0
Ag	0,10	0,10	0,12	0,11	0,11	0,12	0,12	0,12	0,12	0,13	0,13	0,12	0,12	0,11	0,10	0,12
Te	0,00	0,00	0,00	0,00	0,00	0,00	0,01	0,00	0,00	0,00	0,00	0,00	0,00	0,00	0,00	0,00
Au	0,90	0,90	0,88	0,89	0,89	0,88	0,87	0,88	0,86	0,87	0,87	0,88	0,88	0,89	0,90	0,88
Sb	0,00	0,00	0,00	0,00	0,00	0,00	0,00	0,00	0,01	0,00	0,00	0,00	0,00	0,00	0,00	0,00
Sum	1,00	1,00	1,00	1,00	1,00	1,00	1,00	1,00	1,00	1,00	1,00	1,00	1,00	1,00	1,00	1,00
Ag	9,94	10,22	11,81	11,05	11,08	11,60	11,99	12,39	12,45	12,54	12,96	12,39	12,37	10,91	9,78	11,79
Te	0,17	0,00	0,00	0,00	0,00	0,00	0,00	1,15	0,00	0,00	0,00	0,00	0,00	0,00	0,00	0,00
Au	89,90	89,78	88,11	88,95	88,92	88,40	86,85	87,61	86,42	87,38	87,04	87,61	87,63	89,09	90,22	88,21
Sb	0,00	0,00	0,08	0,00	0,00	0,00	0,00	0,00	1,13	0,08	0,00	0,00	0,00	0,00	0,00	0,00
Sum	100,0	100,0	100,0	100,0	100,0	100,0	100,0	100,0	100,0	100,0	100,0	100,0	100,0	100,0	100,0	100,0
Fineness	942,9	941,3	931,6	936,3	936,1	932,9	929,7	928,1	926,8	927,1	924,6	928,1	928,2	937,1	943,9	931,8
Au/Ag	16,52	16,03	13,62	14,71	14,65	13,92	13,22	12,91	12,67	12,73	12,26	12,92	12,93	14,91	16,85	13,67

Appendix E: Mineral chemistry data of the hydrothermal alteration types

Table E.1 Electron microprobe data of some selected metamorphic and hydrothermal biotite flakes in the distal alteration zone in the Um El Tuyor mine area

Sample (points)	Metamorphic biotite							Hydrothermal biotite					
	281(2)	283(3)	241(3)	257(2)	258(2)	280(2)	283(3)	277(2)	275(3)	298(2)	265(3)	250(3)	302(4)
SiO_2	34,83	34,49	35,58	34,58	34,17	35,8	34,24	38,75	38,04	37,98	37,46	37,94	38,18
TiO_2	0,36	0,37	0,46	0,36	0,34	0,56	0,50	0,46	0,53	0,43	0,54	0,46	0,58
Al_2O_3	19,71	20,49	20,21	21,43	21,01	20,91	21,12	14,47	16,68	15,06	15,65	15,84	14,54
FeO	20,37	21,42	21,47	21,25	21,23	21,44	22,36	22,69	22,17	23,12	23,62	23,69	22,98
MnO	0,09	0,10	0,10	0,16	0,10	0,08	0,10	0,10	0,09	0,09	0,13	0,10	0,10
MgO	13,96	13,55	12,81	12,55	13,46	12,93	12,71	11,52	10,96	11,32	10,75	10,29	11,17
CaO	0,03	0,01	0,17	0,13	0,01	0,01	0,05	0,17	0,15	0,14	0,18	0,24	0,18
Na_2O	0,09	0,16	0,12	0,21	0,20	0,17	0,08	0,95	0,87	0,9	0,95	0,95	0,92
K_2O	6,63	6,09	5,66	5,52	5,67	4,84	5,52	7,15	7,16	7,92	7,13	7,14	8,1
F	0,19	0,17	0,26	0,16	0,19	0,00	0,16	0,41	0,34	0,28	0,33	0,32	0,43
Cl	0,00	0,00	0,00	0,00	0,00	0,00	0,00	0,00	0,00	0,00	0,00	0,00	0,00
TOTAL	95,61	96,20	96,19	95,70	95,73	96,09	96,21	96,02	96,34	96,59	96,59	96,32	96,53
O=F,Cl	0,08	0,07	0,11	0,07	0,08	0,00	0,07	0,17	0,14	0,12	0,14	0,13	0,18
T2	8,97	8,93	8,89	8,93	8,95	8,82	8,93	9,07	9,00	9,08	9,07	9,08	9,11
Formula on 22 oxygens (anhydrous basis)													
Si	5,20	5,13	5,27	5,14	5,09	5,25	5,09	5,85	5,70	5,74	5,66	5,74	5,79
Al(iv)	2,80	2,87	2,73	2,86	2,91	2,75	2,91	2,15	2,30	2,26	2,34	2,26	2,21
Al(vi)	0,67	0,72	0,79	0,89	0,78	0,87	0,79	0,43	0,64	0,42	0,44	0,56	0,38
Ti	0,043	0,041	0,05	0,048	0,040	0,06	0,054	0,050	0,062	0,048	0,062	0,053	0,070
Fe^{3+}	1,88	1,80	1,34	1,42	1,69	1,00	1,53	1,79	1,64	2,14	1,85	1,77	1,54
Fe^{2+}	2,54	2,66	2,66	2,64	2,64	2,63	2,78	2,87	2,78	2,92	2,98	2,99	2,96
Mn	0,01	0,01	0,01	0,02	0,01	0,01	0,01	0,01	0,01	0,01	0,02	0,01	0,01
Mg	3,11	3,00	2,83	2,78	2,99	2,83	2,82	2,59	2,45	2,55	2,42	2,32	2,52
Ca	0,00	0,00	0,03	0,02	0,00	0,00	0,01	0,03	0,02	0,02	0,03	0,04	0,03
Na	0,03	0,05	0,03	0,06	0,06	0,05	0,02	0,28	0,25	0,26	0,28	0,28	0,27
K	1,26	1,15	1,07	1,05	1,08	0,91	1,05	1,38	1,37	1,53	1,37	1,38	1,57
TOTAL	15,67	15,64	15,47	15,50	15,60	15,35	15,54	15,64	15,58	15,77	15,66	15,63	15,77
F	0,09	0,08	0,12	0,08	0,09	0,00	0,08	0,20	0,16	0,13	0,16	0,15	0,21
Cl	0,00	0,00	0,00	0,00	0,00	0,00	0,00	0,00	0,00	0,00	0,00	0,00	0,00
X_{Fe}	0,45	0,47	0,48	0,49	0,47	0,48	0,50	0,52	0,53	0,53	0,55	0,56	0,54
X_{Mg}	0,55	0,53	0,52	0,51	0,53	0,52	0,50	0,48	0,47	0,47	0,45	0,44	0,46
Si/Al	1,50	1,43	1,49	1,37	1,38	1,45	1,38	2,27	1,94	2,14	2,03	2,03	2,23
$Fe^{3+}/(Fe^{2+}+Fe^{3+})$	0,43	0,40	0,33	0,35	0,39	0,28	0,35	0,38	0,37	0,42	0,38	0,37	0,34

The number of spot analyses is shown in parentheses after the sample. Fe^{+3} calculated according to Droop (1987).

Table E.2: Representative electron microprobe data of chlorite from the distal alteration zone in the Um El Tuyor mine area

Spot no.	1_1	1_2	3_6	3_7	3_8	6_11	6_13	6_18	6_16	6_9	6_15
SiO_2	30,59	31,28	30,75	29,89	29,49	30,81	29,95	31,41	30,88	29,61	29,82
TiO_2	0,52	0,37	0,48	0,71	0,33	0,39	0,58	0,61	0,54	0,28	0,63
Al_2O_3	19,55	19,67	20,46	20,66	21,59	20,11	21,31	20,33	20,09	21,45	20,83
FeO	20,94	20,17	20,10	21,09	20,80	21,19	20,63	21,05	20,86	21,75	21,68
MnO	0,05	0,05	0,02	0,08	0,00	0,06	0,10	0,00	0,00	0,04	0,10
MgO	14,14	15,08	14,83	13,61	13,36	13,30	13,93	12,53	14,33	13,82	14,99
CaO	0,90	0,88	0,88	0,96	0,68	0,60	0,81	0,80	0,57	0,73	0,44
Na_2O	0,03	0,06	0,13	0,04	0,06	0,21	0,14	0,04	0,19	0,13	0,28
K_2O	0,15	0,12	0,08	0,00	0,07	0,09	0,07	0,07	0,10	0,05	0,11
F	0,14	0,16	0,15	0,09	0,17	0,20	0,08	0,19	0,08	0,10	0,10
Total	86,36	87,19	87,23	86,48	85,90	86,31	86,95	86,38	86,99	87,31	88,33
O=F	0,06	0,07	0,06	0,04	0,07	0,08	0,03	0,08	0,03	0,04	0,04
T2	12,35	12,16	12,15	12,33	12,39	12,35	12,23	12,29	12,21	12,25	12,12
Cations based on 28 oxygens											
Si	6,29	6,33	6,22	6,13	6,08	6,33	6,09	6,42	6,28	6,04	6,02
Al^{IV}	1,71	1,67	1,78	1,87	1,92	1,67	1,91	1,58	1,72	1,96	1,98
Al^{VI}	3,02	3,02	3,10	3,13	3,33	3,20	3,21	3,32	3,09	3,19	2,97
Ti	0,08	0,06	0,07	0,11	0,05	0,06	0,09	0,09	0,08	0,04	0,10
Fe^3	1,99	1,97	1,95	2,06	2,06	2,16	1,97	2,66	2,00	1,75	1,45
Fe^2	3,60	3,41	3,40	3,62	3,59	3,64	3,51	3,60	3,55	3,71	3,66
Mn	0,01	0,01	0,00	0,01	0,00	0,01	0,02	0,00	0,00	0,01	0,02
Mg	4,33	4,55	4,47	4,16	4,11	4,07	4,23	3,82	4,34	4,20	4,51
Ca	0,20	0,19	0,19	0,21	0,15	0,13	0,18	0,18	0,12	0,16	0,10
Na	0,01	0,02	0,05	0,02	0,02	0,08	0,06	0,02	0,07	0,05	0,11
K	0,04	0,03	0,02	0,00	0,02	0,02	0,02	0,02	0,03	0,01	0,03
Cations	19,29	19,29	19,31	19,27	19,27	19,23	19,30	19,05	19,28	19,37	19,48
CF	0,09	0,10	0,10	0,06	0,11	0,13	0,05	0,12	0,05	0,06	0,06
Fe/(Fe+Mg)	0,45	0,43	0,43	0,46	0,47	0,47	0,45	0,49	0,45	0,47	0,45
T(^{o}C)	**233,3**	**226,8**	**238,8**	**250,2**	**255,9**	**229,9**	**253,6**	**221,0**	**234,0**	**260,8**	**261,5**

Fe^{+3} calculated according to Droop (1987). Temperatures (^{o}C) are estimated by using the equation derived by Cathelineau (1988) and the Al^{IV} correction of Kranidiotis & McLean (1987)

Table E.3: Data of the fine hydrothermal biotite flakes from the intermediate alteration zone

SiO_2	35,35	36,04	35,98	35,46	36,94	35,18
TiO_2	0,86	0,63	0,54	0,91	0,67	0,78
Al_2O_3	16,47	17,08	17,06	16,65	16,84	17,13
FeO	24,69	23,17	23,02	23,12	22,69	23,98
MnO	0,10	0,09	0,09	0,13	0,10	0,10
MgO	11,52	11,56	11,32	11,75	11,29	11,17
CaO	0,27	0,25	0,24	0,18	0,24	0,19
Na_2O	0,55	0,47	0,49	0,55	0,69	0,39
K_2O	6,35	6,96	7,02	7,13	6,61	7,03
F	0,41	0,34	0,51	0,38	0,29	0,26
Total	95,92	95,94	95,63	95,61	95,72	95,56
O=F,Cl	0,17	0,14	0,22	0,16	0,12	0,11
T2	9,19	9,11	9,16	9,18	9,07	9,20
Formula on 22 oxygens (anhydrous basis)						
Si	5,41	5,47	5,48	5,42	5,58	5,39
Ti	0,10	0,07	0,06	0,10	0,08	0,09
Al^{iv}	2,59	2,53	2,52	2,58	2,42	2,61
Al^{vi}	0,37	0,52	0,55	0,42	0,57	0,48
Fe	3,16	2,94	2,93	2,95	2,86	3,07
Mn	0,01	0,01	0,01	0,02	0,01	0,01
Mg	2,63	2,61	2,57	2,68	2,54	2,55
Ca	0,04	0,04	0,04	0,03	0,04	0,03
Na	0,16	0,14	0,14	0,16	0,20	0,12
K	1,24	1,35	1,36	1,39	1,27	1,37
Cl	0,00	0,00	0,00	0,00	0,00	0,00
F	0,20	0,16	0,25	0,18	0,14	0,13
Total	15,71	15,68	15,68	15,75	15,58	15,72
Fe/(Fe+Mg)	0,55	0,53	0,53	0,52	0,53	0,55
XMg	0,45	0,47	0,47	0,48	0,47	0,45

Table E.4: Representative electron microprobe data and structural formulae of chlorite from the intermediate alteration zone in the Um El Tuyor mine area

Point no.	t266_1	t266_2	t266_3	t266_5	t266_7	t301_1	t301_9	t301_6	t267_1	t267_4	t267_2	t267_5	t267_7	t269_3	t9_6	t9_c2	t9_c4	t9_chl	t9_10	t9_11	t9_12	t9_2	t9_3	t9_5	T9_7	t9_8
SiO$_2$	27,38	27,62	26,49	28,58	26,31	28,55	25,11	26,11	27,53	28,43	26,56	27,45	27,04	26,23	26,71	27,68	26,44	28,59	28,61	26,12	28,34	27,28	26,72	26,97	26,65	27,12
TiO$_2$	0,36	1,12	0,70	0,46	0,43	0,82	0,80	0,75	0,81	0,87	0,81	0,81	0,16	0,78	0,09	0,01	0,00	0,09	0,07	0,04	0,06	0,00	0,05	0,00	0,74	0,93
Al$_2$O$_3$	21,71	21,53	21,49	21,43	21,12	22,73	22,72	22,38	21,19	20,74	21,45	22,05	22,03	22,16	22,24	22,20	21,79	22,39	22,47	22,29	23,91	22,62	22,37	22,12	21,26	21,33
FeO	23,37	22,61	23,42	23,25	24,13	21,87	23,12	22,79	22,88	24,11	23,75	23,75	24,99	23,49	24,14	22,13	20,20	24,03	21,53	22,55	21,98	21,22	19,95	21,63	24,33	26,08
MnO	0,09	0,12	0,10	0,16	0,11	0,08	0,08	0,06	0,08	0,10	0,04	0,04	0,00	0,00	0,17	0,00	0,13	0,23	0,07	0,13	0,12	0,97	0,02	0,14	0,00	0,10
MgO	14,96	13,70	15,55	13,95	15,63	13,14	15,93	16,48	16,07	13,39	15,80	13,80	14,36	13,84	13,25	15,54	16,44	13,32	14,84	15,00	12,18	13,63	15,94	14,95	13,83	11,70
CaO	0,03	0,02	0,01	0,05	0,03	0,49	0,05	0,03	0,06	0,02	0,73	0,73	0,31	0,48	0,11	0,35	0,07	0,02	0,09	0,06	0,03	0,02	0,05	0,05	0,73	0,44
Na$_2$O	0,00	0,00	0,00	0,00	0,00	0,00	0,00	0,00	0,00	0,01	0,06	0,08	0,02	0,11	0,07	0,08	0,00	0,00	0,09	0,07	0,01	0,09	0,02	0,07	0,11	0,07
K$_2$O	0,05	0,05	0,05	0,06	0,04	0,04	0,05	0,05	0,08	0,03	0,05	0,05	0,05	0,03	0,07	0,00	0,04	0,00	0,00	0,05	0,00	0,09	0,00	0,05	0,05	0,01
F	0,19	0,16	0,17	0,16	0,05	0,25	0,24	0,10	0,16	0,13	0,10	0,10	0,08	0,11	0,10	0,02	0,11	0,19	0,20	0,22	0,00	0,22	0,22	0,05	0,11	0,03
Total	87,95	86,77	87,82	87,94	87,80	87,72	87,86	88,65	88,70	87,70	89,24	88,74	88,95	87,11	86,85	87,98	85,11	88,67	87,76	86,30	86,62	85,91	85,12	85,99	87,69	87,78
O_F	0,08	0,07	0,07	0,07	0,02	0,11	0,10	0,04	0,07	0,05	0,04	0,04	0,03	0,05	0,04	0,01	0,05	0,08	0,08	0,09	0,00	0,09	0,09	0,02	0,05	0,01
T2	12,40	12,51	12,47	12,35	12,53	12,28	12,48	12,31	12,28	12,45	12,32	12,33	12,37	12,58	12,63	12,30	12,65	12,27	12,24	12,63	12,41	12,59	12,59	12,58	12,57	12,63

Cations based on 28 anions (O, F), anhydrous basis

	t266_1	t266_2	t266_3	t266_5	t266_7	t301_1	t301_9	t301_6	t267_1	t267_4	t267_2	t267_5	t267_7	t269_3	t9_6	t9_c2	t9_c4	t9_chl	t9_10	t9_11	t9_12	t9_2	t9_3	t9_5	T9_7	t9_8
Si	5,65	5,75	5,50	5,88	5,49	5,83	5,21	5,35	5,63	5,89	5,45	5,63	5,57	5,49	5,62	5,67	5,57	5,84	5,83	5,49	5,85	5,72	5,60	5,65	5,57	5,70
Al^{IV}	2,35	2,25	2,50	2,13	2,51	2,17	2,79	2,65	2,37	2,11	2,56	2,37	2,43	2,51	2,39	2,33	2,43	2,16	2,17	2,51	2,15	2,28	2,40	2,35	2,43	2,30
Al^{VI}	2,93	3,03	2,75	3,06	2,68	3,30	2,77	2,75	2,73	2,95	2,62	2,96	2,91	2,96	3,12	3,02	2,97	3,23	3,22	3,01	3,66	3,30	3,12	3,10	2,81	2,98
Ti	0,06	0,18	0,11	0,07	0,07	0,13	0,13	0,12	0,13	0,14	0,12	0,13	0,02	0,12	0,01	0,00	0,00	0,01	0,01	0,01	0,01	0,00	0,01	0,00	0,12	0,15
Fe^2	4,03	3,94	4,06	4,00	4,21	3,74	4,02	3,91	3,91	4,18	4,07	4,08	4,30	4,11	4,24	3,79	3,56	4,11	3,67	3,96	3,79	3,72	3,50	3,79	4,26	4,58
Fe^3	0,97	1,59	0,65	1,51	0,43	1,96	0,34	0,47	0,83	1,57	0,42	1,14	0,74	0,92	1,02	0,95	0,69	1,55	1,47	0,68	2,15	1,37	1,04	1,02	0,81	1,34
Mn	0,02	0,02	0,02	0,03	0,02	0,01	0,01	0,01	0,01	0,02	0,01	0,01	0,00	0,00	0,03	0,00	0,02	0,04	0,01	0,02	0,02	0,17	0,00	0,02	0,00	0,02
Mg	4,60	4,25	4,81	4,28	4,86	4,00	4,93	5,03	4,90	4,14	4,83	4,22	4,41	4,32	4,15	4,74	5,16	4,05	4,51	4,70	3,75	4,26	4,98	4,67	4,31	3,67
Ca	0,01	0,00	0,00	0,01	0,01	0,11	0,01	0,01	0,01	0,00	0,16	0,16	0,07	0,11	0,03	0,08	0,02	0,01	0,02	0,01	0,01	0,00	0,01	0,01	0,16	0,10
Na	0,00	0,00	0,00	0,00	0,00	0,00	0,00	0,00	0,00	0,00	0,03	0,03	0,01	0,04	0,03	0,03	0,00	0,00	0,04	0,03	0,00	0,04	0,01	0,03	0,04	0,03
K	0,01	0,01	0,01	0,01	0,01	0,01	0,01	0,01	0,02	0,01	0,01	0,01	0,01	0,01	0,02	0,00	0,01	0,00	0,00	0,01	0,00	0,02	0,00	0,01	0,01	0,00
Cations	19,66	19,43	19,77	19,46	19,85	19,30	19,88	19,83	19,70	19,44	19,85	19,59	19,74	19,67	19,64	19,66	19,75	19,45	19,48	19,76	19,23	19,51	19,63	19,64	19,71	19,52
CF	0,25	0,21	0,22	0,21	0,07	0,32	0,32	0,13	0,21	0,17	0,13	0,13	0,11	0,15	0,13	0,02	0,15	0,25	0,25	0,29	0,00	0,30	0,29	0,06	0,15	0,04
Fe/(Fe+Mg)	0,47	0,48	0,46	0,48	0,46	0,48	0,45	0,44	0,44	0,50	0,46	0,49	0,49	0,49	0,51	0,44	0,41	0,50	0,45	0,46	0,50	0,47	0,41	0,45	0,50	0,56
Si/Al	1,07	1,09	1,05	1,13	1,06	1,07	0,94	0,99	1,10	1,16	1,05	1,06	1,04	1,01	1,02	1,06	1,03	1,08	1,08	1,00	1,01	1,02	1,01	1,04	1,07	1,08
Al^{iv}c	2,678	2,585	2,825	2,461	2,834	2,502	3,101	2,959	2,682	2,458	2,877	2,711	2,773	2,850	2,742	2,640	2,721	2,509	2,486	2,831	2,503	2,612	2,687	2,667	2,776	2,692
T(^{o}C)	302	292	317	279	318	283	347	332	302	279	323	305	312	320	309	298	306	284	282	318	283	295	303	301	312	303

Fe^{+3} calculated according to Droop (1987). Temperature (^{o}C) calculated by using the equation derived by Cathelineau (1988) and the correction proposed by Kranidiotis & McLean (1987), Al^{iv}$_c$ is the corrected Al^{iv}, according to Kranidiotis & McLean (1987).
All formulas are calculated on the basis of 28 negative charges, which corresponds to 10 O^{2-} + 8 OH$^-$.

Table E.5: Composition of carbonate grains and aggregates disseminated in the intermediate alteration zone in the Um El Tuyor mine area

CaO	27,31	27,17	29,11	25,64	24,79	25,49	26,76	26,62	26,54	26,65	27,57
MgO	16,42	17,21	15,49	17,21	16,61	16,06	15,56	15,87	18,29	17,36	14,99
FeO	10,31	11,05	10,90	12,14	11,84	10,92	10,87	11,59	10,58	11,49	8,39
MnO	0,40	0,44	0,73	0,42	0,46	0,42	0,42	0,44	0,42	0,48	0,73
Sum	100,36	103,02	103,14	102,04	98,84	97,39	98,52	100,10	103,37	103,17	95,29
Sr (ppm)	390	170	330	449	400	270	539	509	659	380	330
Ba (ppm)	184	0	0	204	0	0	0	147	0	0	0
Structural formulae on basis of total cations =2.											
Ca	0,467	0,452	0,487	0,432	0,431	0,450	0,468	0,458	0,438	0,443	0,496
Mg	0,390	0,398	0,361	0,403	0,402	0,394	0,378	0,380	0,420	0,401	0,375
Fe	0,138	0,144	0,142	0,160	0,161	0,150	0,148	0,156	0,136	0,149	0,118
Mn	0,005	0,006	0,010	0,006	0,006	0,006	0,006	0,006	0,005	0,006	0,010
$CaCO_3$	46,67	45,22	48,72	43,18	43,11	44,96	46,77	45,84	43,82	44,31	49,64
$MgCO_3$	39,03	39,85	36,07	40,31	40,19	39,41	37,83	38,00	42,00	40,15	37,53
$FeCO_3$	13,75	14,35	14,24	15,95	16,07	15,04	14,82	15,57	13,64	14,91	11,79
$MnCO_3$	0,54	0,58	0,97	0,57	0,63	0,59	0,57	0,59	0,55	0,63	1,04
Sum	100,00	100,00	100,00	100,00	100,00	100,00	100,00	100,00	100,00	100,00	100,00
$MgCO_3$	0,00	0,00	0,00	0,00	0,00	0,00	0,00	0,00	0,00	0,00	0,00
$CaCO_3$	0,00	0,00	0,00	0,00	0,00	0,00	0,00	0,00	0,00	0,00	0,00
$CaMg(CO_3)_2$	71,41	70,14	69,59	66,96	66,60	68,74	69,21	67,67	71,63	68,91	74,33
$CaFe(CO_3)_2$	27,51	28,70	28,47	31,91	32,14	30,08	29,64	31,14	27,27	29,83	23,59
$CaMn(CO_3)_2$	1,08	1,16	1,94	1,13	1,26	1,18	1,15	1,19	1,10	1,26	2,08
Sum	100,00	100,00	100,00	100,00	100,00	100,00	100,00	100,00	100,00	100,00	100,00
Fe#	0,261	0,265	0,283	0,284	0,286	0,276	0,282	0,291	0,245	0,271	0,239
mg#	0,732	0,727	0,703	0,709	0,706	0,716	0,711	0,702	0,748	0,721	0,745
T	0,533	0,548	0,513	0,568	0,569	0,550	0,532	0,542	0,562	0,557	0,504
Activity	0,467	0,452	0,487	0,432	0,431	0,450	0,468	0,458	0,438	0,443	0,496
Fe/Mg	0,352	0,360	0,395	0,396	0,400	0,382	0,392	0,410	0,325	0,371	0,314
Fe.Mg	0,054	0,057	0,051	0,064	0,065	0,059	0,056	0,059	0,057	0,060	0,044

Activities were calculated assuming ideal activity models (Skippen and Carmichael, 1977)

Table E.6: Representative microprobe data of sericite and fluorapatite disseminated in the intermediate alteration zone of Um El Tuyor gold deposit

Sericite data

Sample	1_11	1_12	1_13	1_14	1_15	1_3	1_5	9_22	9_23	9_24	9_25	6_26
SiO_2	48,07	47,83	47,69	47,81	47,49	49,40	47,51	46,08	46,75	47,83	47,09	47,86
TiO_2	1,17	0,69	0,26	0,92	0,71	0,52	0,74	0,87	1,01	0,37	0,60	0,60
Al_2O_3	32,50	32,99	33,62	31,47	34,05	30,87	32,75	33,86	33,42	33,51	33,61	33,20
FeO	1,66	1,46	0,82	2,24	1,36	1,48	1,44	1,68	1,47	1,14	1,50	1,26
MnO	0,00	0,01	0,03	0,05	0,07	0,00	0,01	0,00	0,00	0,00	1,49	0,06
MgO	1,54	1,14	0,75	2,53	0,95	2,32	1,21	2,47	1,42	1,34	1,28	1,03
CaO	0,07	0,04	0,00	0,00	0,00	0,05	0,05	0,01	0,00	0,03	0,05	0,02
Na_2O	0,17	0,24	0,34	0,16	0,22	0,19	0,25	0,45	0,51	0,39	0,52	0,40
K_2O	9,94	10,15	10,99	10,01	10,61	10,23	10,73	9,45	9,88	9,67	9,57	10,09
H_2O(calc)	4,47	4,46	4,37	4,47	4,49	4,47	4,40	4,44	4,41	4,35	4,44	4,38
F	0,10	0,01	0,14	0,00	0,01	0,01	0,01	0,01	0,02	0,08	0,01	0,02
Cl	0,00	0,12	0,17	0,09	0,11	0,16	0,27	0,19	0,24	0,42	0,28	0,41
Total	99,59	99,00	98,87	99,65	99,96	99,54	99,09	99,30	98,87	98,64	100,15	98,90
O_F_Cl	0,04	0,03	0,10	0,02	0,03	0,04	0,07	0,05	0,06	0,13	0,07	0,10

Number of cations on basis of 24 (O, OH, F, Cl)

	1_11	1_12	1_13	1_14	1_15	1_3	1_5	9_22	9_23	9_24	9_25	6_26
Si	6,39	6,39	6,38	6,38	6,30	6,56	6,37	6,15	6,26	6,38	6,26	6,39
Al^{IV}	1,62	1,61	1,62	1,62	1,70	1,44	1,64	1,85	1,74	1,62	1,74	1,61
Al^{VI}	3,47	3,58	3,68	3,33	3,62	3,39	3,53	3,47	3,53	3,64	3,51	3,61
Ti	0,12	0,07	0,03	0,09	0,07	0,05	0,07	0,09	0,10	0,04	0,06	0,06
Fe^{2+}	0,18	0,16	0,09	0,25	0,15	0,16	0,16	0,19	0,17	0,13	0,17	0,14
Mn	0,00	0,00	0,00	0,01	0,01	0,00	0,00	0,00	0,00	0,00	0,17	0,01
Mg	0,31	0,23	0,15	0,50	0,19	0,46	0,24	0,49	0,28	0,27	0,25	0,21
Ca	0,01	0,01	0,00	0,00	0,00	0,01	0,01	0,00	0,00	0,01	0,01	0,00
Na	0,04	0,06	0,09	0,04	0,06	0,05	0,07	0,12	0,13	0,10	0,13	0,10
K	1,68	1,73	1,88	1,70	1,80	1,73	1,84	1,61	1,69	1,65	1,62	1,72
Cations	13,81	13,84	13,92	13,92	13,89	13,86	13,92	13,96	13,90	13,82	13,93	13,85
CF	0,08	0,01	0,12	0,00	0,01	0,01	0,01	0,01	0,02	0,07	0,01	0,01
CCl	0,00	0,05	0,08	0,04	0,05	0,07	0,12	0,08	0,11	0,19	0,13	0,19
OH	3,96	3,97	3,90	3,98	3,97	3,96	3,93	3,95	3,94	3,87	3,93	3,90
Fe/(Fe+Mg)	0,38	0,42	0,38	0,33	0,44	0,26	0,40	0,28	0,37	0,32	0,40	0,41
Mg/(Fe+Mg)	0,62	0,58	0,62	0,67	0,56	0,74	0,60	0,72	0,63	0,68	0,60	0,59
Fe/Mg	0,49	0,39	0,24	0,75	0,34	0,62	0,4	0,68	0,45	0,4	0,42	0,35
Activity	0,84	0,865	0,94	0,85	0,9	0,865	0,92	0,805	0,845	0,825	0,81	0,86

Fluorapatite data

CaO	52,46	53,23	53,1	59,59	54,62	52,59	52,62	51,44
Na_2O	0,04	0,06	0	0	0,04	0	0,04	0,1
FeO	0,18	0,09	0,33	0,46	0,19	0,46	0,19	0,18
MnO	0	0,03	0	0,4	0,3	0,4	0,3	0,04
MgO	0,13	0,09	0,28	0,78	0,07	0,78	0,07	0,57
P_2O_5	45,23	44,54	43,75	46,01	42,12	42,01	43,12	43,31
SiO_2	0,2	0,23	0,37	0,33	0,18	0,33	0,18	0,18
F	3,74	3,67	4,12	0,14	0,23	3,14	3,23	4,21
Total	101,97	101,95	101,96	99,71	99,76	99,71	99,76	100,03
O=F	1,57	1,55	1,74	0,06	0,1	1,32	1,36	1,77
Total	100,4	100,4	100,22	99,65	99,66	98,39	98,4	98,25
Ca	8,86	9,03	9,03	6,61	6	9,22	9,17	8,89
Na	0,01	0,02	0	0	0,01	0	0,01	0,03
Fe	0,02	0,01	0,04	0,06	1,24	0,06	0,03	0,02

Fromula on 25 (O, F)

Mg	0,03	0,02	0,07	2,97	3,15	0,19	0,02	0,14
P	6,04	5,97	5,88	6,07	5,77	5,82	5,94	5,92
Si	0,03	0,04	0,06	0,05	0,03	0,05	0,03	0,03
F	1,86	1,84	2,07	0,07	0,12	1,63	1,66	2,15
OH	-0,86	-0,84	-1,07	0,93	0,88	-0,63	-0,66	-1,15
Total	15,99	16,1	16,08	16,81	17,26	16,4	16,24	16,04
No. Anion /T	9,47	9,51	9,54	9,36	9,73	9,83	9,77	9,7

Average formula $Ca_{4.17} (P_{0.98}O_4)_3F_{0.71}$

Ions and H_2O calculated by MINPET (Geochemical) PROGRAMME.

Table E.7: Electron microprobe data of carbonate in samples collected from the proximal alteration zone and in samples from the mineralized veins of Um El Tuyor deposit

	Disseminated carbonate grains in rock form proximal alteration envleop											Carbonate minerals in the quartz-carbonate veins													calcite coats and traverses former carbonates and fills microfissures (in quartz carbonate veins)					
CaO	27,46	28,95	30,15	27,99	26,30	25,74	27,38	26,35	26,44	26,38	26,46	26,66	24,61	24,62	27,29	27,39	26,96	27,59	27,28	28,27	25,03	27,21	25,29	26,66	49,23	51,18	50,99	51,08	50,12	52,31
MgO	17,34	11,75	14,37	11,87	13,91	14,40	13,75	13,98	14,18	14,25	14,72	13,17	12,36	12,17	15,07	13,45	15,73	16,05	12,51	14,21	11,94	20,29	13,00	13,17	1,090	0,518	0,466	0,156	0,858	0,372
FeO	10,13	10,14	9,98	11,51	10,20	11,38	9,71	10,25	10,30	10,25	10,19	12,94	11,73	11,07	11,00	11,90	10,66	15,70	15,74	12,72	11,27	16,11	14,90	12,94	0,000	0,025	0,020	0,109	0,234	0,024
MnO	0,49	0,54	0,39	0,54	0,58	0,70	0,77	0,64	0,62	0,66	0,57	0,82	0,40	0,37	0,36	0,43	0,49	0,46	0,46	0,59	0,35	0,50	0,49	0,82	0,000	0,021	0,032	0,053	0,030	0,000
CO2cALC	47,00	42,10	45,71	42,32	42,44	43,33	42,93	42,63	42,93	42,95	43,44	43,75	40,24	39,62	44,84	43,73	45,18	49,08	45,00	45,86	39,79	53,69	43,48	43,74	0,002	0,000	0,000	0,009	0,022	0,018
Sum	102,4	93,48	100,6	94,24	93,44	95,56	94,53	93,85	94,46	94,48	95,39	97,34	89,34	87,85	98,56	96,89	99,03	108,9	101,0	101,6	88,37	117,8	97,16	97,34						
Sr (ppm)	330	240	469	398	827	528	370	410	428	511	630	387	539	549	689	799	1198	868	859	318	489	519	819	388						
Ba												0	0	0	0	144	0	200	260	0	0	189	110	100						

Structural formulae basis on cation per 2 oxygens

Ca	0,46	0,540	0,518	0,519	0,486	0,466	0,501	0,485	0,483	0,482	0,478	0,48	0,48	0,49	0,48	0,492	0,47	0,44	0,48	0,48	0,49	0,40	0,457	0,478	0,97	0,99	0,99	0,99	0,97	0,99
Mg	0,40	0,305	0,343	0,306	0,358	0,363	0,350	0,358	0,361	0,362	0,370	0,33	0,34	0,34	0,37	0,336	0,38	0,36	0,30	0,34	0,33	0,41	0,326	0,329	0,03	0,01	0,01	0,00	0,02	0,01
Fe	0,13	0,148	0,134	0,167	0,147	0,161	0,139	0,147	0,147	0,146	0,144	0,18	0,18	0,17	0,15	0,167	0,14	0,20	0,21	0,17	0,17	0,18	0,210	0,181	0,00	0,00	0,00	0,00	0,00	0,00
Mn	0,01	0,008	0,005	0,008	0,009	0,010	0,011	0,009	0,009	0,010	0,008	0,01	0,01	0,01	0,01	0,006	0,01	0,01	0,01	0,01	0,01	0,01	0,007	0,012	0,00	0,00	0,00	0,00	0,00	0,00
C	2,00	2,000	2,000	2,000	2,000	2,000	2,000	2,000	2,000	2,000	2,000	2,00	2,00	2,00	2,00	2,000	2,00	2,00	2,00	2,00	2,00	2,00	2,000	2,000	0,000	0,000	0,000	0,000	0,001	0,000
CaCO$_3$	45,86	53,97	51,78	51,92	48,64	46,62	50,06	48,53	48,34	48,21	47,81	47,83	48,00	48,77	47,78	49,16	46,84	44,12	47,58	48,38	49,37	39,78	45,66	47,83	97,01	98,54	98,66	99,31	97,23	98,94
MgCO$_3$	40,28	30,48	34,32	30,63	35,78	36,28	34,97	35,82	36,06	36,22	37,01	32,88	33,53	33,54	36,70	33,57	38,03	35,70	30,36	33,83	32,75	41,26	32,64	32,88	2,99	1,39	1,25	0,42	2,31	0,98
FeCO$_3$	13,21	14,75	13,37	16,66	14,73	16,08	13,86	14,73	14,70	14,62	14,36	18,12	17,86	17,12	15,02	16,66	14,46	19,60	21,43	16,99	17,34	18,39	21,00	18,12	0,00	0,04	0,03	0,17	0,35	0,03
MnCO$_3$	0,65	0,80	0,53	0,79	0,85	1,01	1,11	0,92	0,90	0,95	0,82	1,17	0,61	0,57	0,50	0,60	0,68	0,58	0,64	0,80	0,54	0,58	0,70	1,17	0,00	0,03	0,05	0,08	0,05	0,00
Sum	100,0	100,0	100,0	100,0	100,0	100,0	100,0	100,0	100,0	100,0	100,0	100,0	100,0	100,0	100,0	100,0	100,0	100,0	100,0	100,0	100,0	100,0	100,0	100,0	99,99	100,00	100,00	99,98	99,94	99,95
MgCO$_3$	0,00	0,00	0,00	0,00	0,00	0,00	0,00	0,00	0,00	0,00	0,00	0,00	0,00	0,00	0,00	0,00	0,00	0,00	0,00	0,00	0,00	0,00	0,00	0,00	0,00	0,00	0,00	0,00	0,00	0,00
CaCO$_3$	0,00	7,93	3,56	3,84	0,00	0,00	0,11	0,00	0,00	0,00	0,00	0,00	0,00	0,00	0,00	0,00	0,00	0,00	0,00	0,00	0,00	0,00	0,00	0,00	94,03	97,12	97,38	98,74	94,51	97,93
CaMg(CO$_3$)$_2$	72,29	60,96	68,65	61,25	68,84	65,81	69,94	68,68	68,80	68,85	69,63	61,42	63,05	64,61	68,95	65,46	69,73	59,64	55,88	64,42	64,24	62,07	56,61	61,42	5,97	2,77	2,51	0,84	4,63	1,96
CaFe(CO$_3$)$_2$	26,42	29,51	26,74	33,32	29,45	32,17	27,71	29,47	29,40	29,24	28,73	36,24	35,72	34,24	30,04	33,33	28,91	39,20	42,85	33,98	34,68	36,77	41,99	36,25	0,00	0,07	0,06	0,33	0,71	0,07
CaMn(CO$_3$)$_2$	1,30	1,60	1,05	1,59	1,70	2,02	2,23	1,85	1,80	1,91	1,64	2,34	1,22	1,14	1,00	1,21	1,36	1,16	1,27	1,61	1,08	1,16	1,39	2,34	0,00	0,07	0,10	0,16	0,09	0,00
Sum	100,0	100,0	100,0	100,0	100,0	100,0	100,0	100,0	100,0	100,0	100,0	100,0	100,0	100,0	100,0	100,0	100,0	100,0	100,0	100,0	100,0	100,0	100,0	100,0	100,0	100,0	100,0	100,1	99,94	99,95
Fe#	0,25	0,326	0,280	0,352	0,292	0,307	0,284	0,291	0,290	0,288	0,280	0,36	0,35	0,34	0,29	0,332	0,28	0,35	0,41	0,33	0,35	0,31	0,391	0,355	0,00	0,03	0,02	0,28	0,13	0,03
mg#	0,74	0,662	0,712	0,637	0,697	0,680	0,700	0,696	0,698	0,699	0,709	0,63	0,64	0,65	0,70	0,660	0,72	0,64	0,58	0,66	0,65	0,69	0,601	0,630	1,00	0,95	0,94	0,63	0,85	0,97
t	0,54	0,460	0,482	0,481	0,514	0,534	0,499	0,515	0,517	0,518	0,522	0,52	0,52	0,51	0,52	0,508	0,53	0,56	0,52	0,52	0,51	0,60	0,543	0,522	0,03	0,01	0,01	0,01	0,03	0,01
activity	0,46	0,540	0,518	0,519	0,486	0,466	0,501	0,485	0,483	0,482	0,478	0,48	0,48	0,49	0,48	0,492	0,47	0,44	0,48	0,48	0,49	0,40	0,457	0,478	0,97	0,99	0,99	0,99	0,97	0,99
Fe/Mg	0,33	0,484	0,39	0,54	0,41	0,44	0,39	0,41	0,41	0,40	0,38	0,55	0,53	0,51	0,41	0,49	0,38	0,55	0,71	0,50	0,53	0,45	0,643	0,551	0,00	0,03	0,02	0,39	0,15	0,04
Fe.Mg	0,05	0,04	0,04	0,05	0,05	0,05	0,04	0,05	0,05	0,05	0,05	0,06	0,06	0,06	0,06	0,05	0,05	0,07	0,07	0,06	0,06	0,08	0,069	0,060	0,00	0,00	0,00	0,00	0,00	0,00

Activities were calculated assuming ideal activity models (Skippen and Carmichael, 1977)

Table E.8: Electron microprobe date of sericite flakes disseminated in the wallrocks adjacent to the laminated quartz veins in the Um El Tuyor mine area

Point no.	1	10	11	12	14	15	16	18	19	2	22	3	4	5	6	7	21
SiO_2	47,69	48,01	47,43	48,57	47,25	47,39	47,35	46,00	48,31	47,60	46,87	48,91	47,92	47,86	46,53	48,49	47,74
TiO_2	0,75	0,20	0,21	0,60	0,17	0,05	0,19	0,16	0,11	0,85	0,19	0,20	0,20	0,41	0,11	0,09	0,37
Al_2O_3	33,67	35,59	35,43	34,58	36,84	36,02	36,38	36,00	34,43	32,88	36,67	34,31	34,32	34,33	36,51	34,36	35,07
FeO	0,76	0,69	0,86	1,41	0,40	0,38	0,29	0,64	0,45	1,23	0,63	0,67	0,91	1,22	0,80	0,88	0,90
MnO	0,01	0,00	0,05	0,00	0,04	0,04	0,00	0,61	0,05	0,09	0,04	0,03	0,09	0,07	0,01	0,00	0,03
MgO	0,92	0,58	0,77	0,93	0,39	0,27	0,24	0,43	0,30	1,34	0,29	0,55	0,83	0,93	0,46	0,65	0,72
CaO	0,31	0,15	0,00	0,01	0,00	0,01	0,61	0,05	0,00	0,02	0,01	0,00	0,11	0,12	0,00	0,02	0,00
Na_2O	1,46	1,74	1,00	1,28	2,00	2,66	2,82	3,08	2,56	1,16	0,99	1,53	1,07	0,73	1,26	1,08	1,56
K_2O	8,97	7,71	8,66	7,78	8,08	7,82	7,08	8,14	7,99	9,10	8,91	8,51	9,01	9,21	8,82	8,76	8,51
H_2O(calc)	4,38	4,50	4,41	4,58	4,51	4,48	4,51	4,44	4,45	4,28	4,48	4,45	4,39	4,45	4,42	4,23	4,45
F	0,26	0,13	0,26	0,00	0,14	0,15	0,13	0,16	0,15	0,42	0,13	0,22	0,25	0,16	0,22	0,64	0,20
Cl	0,04	0,00	0,00	0,00	0,00	0,00	0,01	0,00	0,04	0,03	0,00	0,01	0,04	0,03	0,02	0,00	0,00
Total	98,92	99,17	98,82	99,74	99,68	99,12	99,47	99,55	98,65	98,55	99,08	99,16	98,85	99,33	98,92	98,56	99,35
O_F_Cl	0,12	0,05	0,11	0,00	0,06	0,06	0,06	0,07	0,07	0,18	0,05	0,09	0,11	0,07	0,10	0,27	0,08
Number of cations on basis of 24 (O, OH, F, Cl)																	
Si	6,34	6,31	6,28	6,36	6,19	6,25	6,21	6,10	6,40	6,36	6,19	6,44	6,36	6,34	6,17	6,42	6,30
Al^{IV}	1,66	1,69	1,72	1,64	1,81	1,75	1,79	1,90	1,60	1,64	1,81	1,56	1,64	1,67	1,83	1,58	1,71
Al^{VI}	3,61	3,81	3,80	3,70	3,87	3,84	3,82	3,73	3,77	3,53	3,90	3,76	3,72	3,69	3,87	3,77	3,74
Ti	0,08	0,02	0,02	0,06	0,02	0,01	0,02	0,02	0,01	0,09	0,02	0,02	0,02	0,04	0,01	0,01	0,04
Fe^{2+}	0,08	0,08	0,10	0,15	0,04	0,04	0,03	0,07	0,05	0,14	0,07	0,07	0,10	0,14	0,09	0,10	0,10
Mn	0,00	0,00	0,01	0,00	0,00	0,00	0,00	0,07	0,01	0,01	0,00	0,00	0,01	0,01	0,00	0,00	0,00
Mg	0,18	0,11	0,15	0,18	0,08	0,05	0,05	0,09	0,06	0,27	0,06	0,11	0,16	0,18	0,09	0,13	0,14
Ca	0,04	0,02	0,00	0,00	0,00	0,00	0,09	0,01	0,00	0,00	0,00	0,00	0,02	0,02	0,00	0,00	0,00
Na	0,38	0,44	0,26	0,33	0,51	0,68	0,72	0,79	0,66	0,30	0,25	0,39	0,28	0,19	0,32	0,28	0,40
K	1,52	1,29	1,46	1,30	1,35	1,32	1,18	1,38	1,35	1,55	1,50	1,43	1,53	1,56	1,49	1,48	1,43
Cations	13,89	13,78	13,79	13,72	13,87	13,94	13,91	14,15	13,90	13,89	13,81	13,78	13,83	13,81	13,87	13,77	13,85
CF	0,22	0,11	0,22	0,00	0,12	0,13	0,11	0,13	0,13	0,36	0,11	0,18	0,21	0,13	0,18	0,54	0,17
CCl	0,02	0,00	0,00	0,00	0,00	0,00	0,00	0,00	0,02	0,01	0,00	0,00	0,02	0,01	0,01	0,00	0,00
OH	3,88	3,95	3,89	4,00	3,94	3,94	3,94	3,93	3,93	3,82	3,95	3,91	3,89	3,93	3,90	3,73	3,92
Fe/(Fe+Mg)	0,32	0,40	0,38	0,46	0,37	0,44	0,41	0,46	0,46	0,34	0,55	0,41	0,38	0,42	0,49	0,43	0,41
Mg/(Fe+Mg)	0,68	0,60	0,62	0,54	0,63	0,56	0,59	0,54	0,54	0,66	0,45	0,59	0,62	0,58	0,51	0,57	0,59
Activity	0,76	0,65	0,73	0,65	0,68	0,66	0,59	0,69	0,68	0,78	0,75	0,72	0,77	0,78	0,75	0,74	0,72

Table E.9: Composition of some albite plates disseminated in the quartz-carbonate veins and their alteration envelop in Um El Tuyor mine area

Spot no															Na, K- feldspar solid solution				
position	core	rim	core	rim	core	core	rim	rim	core	core	rim>>>>>	core	<<<<<	rim	??_II_1	??_II_2	??_II_5	??_II_3	??_II_4
SiO$_2$	65,92	66,68	68,57	68,83	67,67	67,20	66,59	65,4	65,11	69,38	67,74	67,87	67,78	67,03	50,30	50,97	50,13	50,65	49,91
Al$_2$O$_3$	18,16	18,17	17,55	17,33	19,50	19,56	20,64	20,52	18,32	17,09	19,38	21,08	21,79	21,26	38,80	38,30	38,62	38,44	39,52
FeO	0,00	0,00	0,00	0,00	0,00	0,00	0,00	0,00	0,00	0,00	0,50	0,28	0,21	0,17	0,33	0,39	0,24	0,08	0,32
CaO	0,52	0,23	0,21	0,48	0,37	0,46	0,62	0,84	0,76	0,37	0,07	0,04	0,14	0,01	0,03	0,11	0,11	0,02	0,00
Na$_2$O	12,24	12,91	12,11	12,33	11,19	12,04	11,90	12,08	13,02	11,74	12,03	9,65	9,39	10,09	7,47	8,36	8,45	8,32	9,00
K$_2$O	1,57	0,74	1,00	0,90	0,66	0,59	0,31	0,49	1,03	1,00	0,04	0,01	0,03	0,04	2,01	1,32	1,59	0,86	0,92
F	0,00	0,00	0,22	0,01	0,19	0,06	0,22	0,21	0,00	0,15	0,12	0,07	0,05	0,06	0,05	0,12	0,18	0,23	0,16
TOTAL	98,41	98,73	99,44	99,88	99,40	99,85	100,06	99,54	98,25	99,58	99,76	98,93	99,33	98,60	98,94	99,45	99,13	98,36	99,68
Formula calculated on basis of 8 oxygens																			
Si	2,97	2,98	3,03	3,04	2,98	2,96	2,93	2,91	2,95	3,06	2,98	2,97	2,95	2,95	2,26	2,29	2,25	2,28	2,23
Al	0,97	0,96	0,92	0,90	1,01	1,02	1,07	1,07	0,98	0,89	1,00	1,09	1,12	1,10	2,06	2,03	2,05	2,04	2,08
Fe(ii)	0,00	0,00	0,00	0,00	0,00	0,00	0,00	0,00	0,00	0,00	0,02	0,01	0,01	0,01	0,01	0,01	0,01	0,00	0,01
Ca	0,02	0,01	0,01	0,02	0,02	0,02	0,03	0,04	0,04	0,02	0,00	0,00	0,01	0,00	0,00	0,01	0,01	0,00	0,00
Na	1,07	1,12	1,04	1,05	0,96	1,03	1,01	1,04	1,14	1,00	1,03	0,82	0,79	0,86	0,65	0,64	0,74	0,73	0,78
K	0,09	0,04	0,06	0,05	0,04	0,03	0,02	0,03	0,06	0,06	0,00	0,00	0,00	0,00	0,12	0,08	0,09	0,05	0,05
Total	5,12	5,12	5,06	5,07	5,01	5,06	5,06	5,09	5,16	5,03	5,03	4,89	4,88	4,93	5,10	5,05	5,14	5,09	5,15
T2	2,71	2,69	2,66	2,65	2,65	2,65	2,64	2,67	2,72	2,65	2,64	2,63	2,62	2,65	2,70	2,70	2,70	2,70	2,68
K/Na	0,084	0,038	0,055	0,048	0,039	0,032	0,017	0,03	0,052	0,056	0,002	0,001	0,002	0,003	0,18	0,13	0,12	0,07	0,06
End members																			
An	2,10	0,95	0,90	2,02	1,75	2,01	2,74	3,61	2,99	1,63	0,32	0,21	0,83	0,05	0,18	0,71	0,61	0,12	0,01
Ab	90,27	95,46	93,97	93,49	94,57	94,93	95,61	93,89	92,20	93,15	99,45	99,73	99,00	99,68	84,78	88,81	88,44	93,53	93,68
Or	7,62	3,58	5,12	4,49	3,68	3,07	1,65	2,51	4,81	5,22	0,23	0,07	0,17	0,27	15,04	10,49	10,95	6,35	6,31

Table E.10: Compositional variations of the least-altered and altered rocks from the different alteration zones of Um El Tuyor gold deposit

Type of alteration	Least-altered host rocks (initial precursor)				propylitized rocks (distal alteration)			sericitized rocks (intermediate alteration)				sericitized-albitized-silicified rocks (proximal alteration)		
Sample	258	291	243	261	293	264	299	252	269	271	265	266	301	9M
SiO_2	53,96	54,02	51,81	52,37	50,51	51,34	51,87	53,93	56,26	55,35	56,44	55,14	57,81	56,12
TiO_2	0,69	0,73	0,57	0,58	0,63	0,77	0,64	0,78	0,64	0,80	0,66	0,49	0,51	0,69
Al_2O_3	9,78	10,13	9,56	9,93	9,14	9,23	8,79	11,62	11,29	12,32	11,14	11,62	11,55	12,00
$Fe_2O_3^*$	8,86	7,87	9,06	10,97	10,05	8,94	9,52	8,28	7,68	8,53	8,66	8,16	9,03	8,18
MnO	0,17	0,21	0,29	0,20	0,36	0,23	0,26	0,31	0,28	0,26	0,30	0,28	0,31	0,24
MgO	13,81	12,37	13,35	11,58	13,44	12,91	13,08	8,94	7,42	7,31	7,32	7,15	6,24	6,42
CaO	2,52	3,23	4,13	3,42	4,82	5,11	5,17	2,98	3,85	3,22	3,95	3,35	2,83	3,71
Na_2O	0,73	0,98	0,93	0,87	0,65	0,94	0,43	0,86	1,23	1,09	1,51	1,97	2,14	1,83
K_2O	4,06	3,99	3,88	3,37	4,47	4,98	4,64	5,95	5,73	5,77	5,43	6,05	5,18	5,06
P_2O_5	0,53	0,39	0,42	0,54	0,38	0,49	0,27	0,17	0,44	0,39	0,42	0,33	0,29	0,38
L.O.I.	4,75	4,33	4,82	4,67	5,03	4,87	5,13	4,98	5,01	4,69	4,20	5,03	4,27	5,02
SO_2	0,05	0,10	0,08	0,07	0,22	0,21	0,35	0,43	0,51	0,49	0,39	0,55	0,47	0,68
Total	99,91	98,35	98,91	98,57	99,70	100,02	100,15	99,21	100,34	100,22	100,42	100,11	100,63	100,34
ppm														
Au	0,03	-	0,02	0,05	0,62	0,65	0,58	1,14	1,33	1,42	1,14	1,72	2,13	1,61
Ag	-	-	-	-	0,21	0,09	0,16	0,21	0,25	0,16	0,09	0,26	0,43	0,28
As	301	296	243	389	557	683	574	1237	1522	1759	1426	2016	2454	2182
Ba	63	60	51	76	196	153	222	219	232	290	271	271,15	199	245
Br	-		-		0,58	0,48	0,59	0,59	0,48	0,36	0,31	0,43	0,5	0,72
Co	19	16	15	16	13	12	13	23	12	17	13	14	8	16
Cr	83	66	67	58	51	68	46	33	49	44	49	48	41	44
Ni	16	15	13	19	15	6	24	37	21	28	21	26	25	42
Rb	36	34	29	41	<15	<15	<15	51	43	56	48	59	64	57
Sb	-	-	-	-	<0,1	<0,1	<0,1	<0,1	<0,1	<0,1	<0,1	<0,1	<0,1	0,2
Sc	0,9	-	0,73	0,66	1,09	0,8	0,41	4,77	7,50	10,9	7,84	11,17	13	8,94
Sn	13	30	11	71	143	165	139	133	109	153	80	126	91	119
Sr	71	73	57	102	365	203	255	237	222	162	118	169	152	196
Th	<0,2	<0,2	<0,2	<0,2	<0,2	<0,2	<0,2	2,34	3,89	7,3	5,13	5,74	3,6	3,93
U	-	-	-	-	<0,5	<0,5	<0,5	<0,5	<0,5	2,26	1,31	1,74	0,8	-
Zn	24	22	19	28	53	77	28	26	31	38	22	30	13	25
Pb	9	8	7	8	8	8	13	0	12	9	11	13	17	10
V	26	32	21	53	44	29	91	123	77	95	74	97	104	108
Y	2	3	2	5	4	1	6	5	6	8	5	7	7	6
Cu	11	10	12	9	6	4	10	0	10	9	11	11	12	8
Mn	413	361	334	393	533	709	293	1237	352	463	405	352	163	234
REEs														
La	23,1	20,7	19,7	22,5	3,06	2,5	18,98	16,81	18,27	27,9	23,70	27,60	26,35	23,55
Ce	48	42	39	46	34	23	42	44	45	55	46	54	50	42
Nd	19	17	15	18	16	14	18	18	16	22	14	21	18	19
Sm	4,6	4,8	5,1	4,7	2,58	1,37	2,89	3,60	4,25	5,3	4,90	5,32	4,8	4,70
Eu	0,9	0,83	0,7	0,8	0,68	0,49	0,74	0,82	0,83	0,9	0,81	0,93	0,9	0,90
Tb	0,6	0,57	0,5	0,6	0,7	0,66	0,61	<0,5	<0,5	<0,5	<0,5	<0,5	<0,5	<0,5
Yb	0,7	0,64	0,6	0,9	<0,1	<0,1	<0,1	2.11	2.01	2,8	1,93	2,78	2,7	2,33
Lu	0,13	0,09	0,11	0,08	0,13	0,15	0,21	0,19	0,15	0,12	0,13	0,15	0,18	0,18
density														
g/cm3	2,713	2,740	2,752	2,813	3,015	2,972	2,967	2,871	2,836	2,894	2,877	2,865	2,886	2,877

The major and trace element analyses have been carried out by using an ICP-MS technique in the Activation Laboratories, ACTLABS Group, Canada (Code 4B)

Table E.11: Mass changes, grams added or removed per 100 gram in the major elements and per 1000 gram in trace elements during hydrothermal alteration in the Um El Tuyor mine area

	least-altered	Distal (propylitized) rocks			% gains and losses				Intermediate (sericitized) rocks				% gains and losses					Inner (sericitized-albitized) rocks			% gains and losses			
	median	293	264	299	293	264	299	av.	252	269	271	265	252	269	271	265	av.	266	301	9M	266	301	9M	av.
g/100g																								
SiO$_2$	53,65	50,51	51,34	51,87	-2,82	-2,72	-2,28	-2,60	53,93	56,26	55,35	56,44	0,88	2,81	2,57	3,85	2,53	56,12	55,14	57,81	4,99	3,97	6,76	5,24
TiO$_2$	0,64	0,63	0,77	0,64	-0,01	0,12	-0,01	0,03	0,78	0,64	0,80	0,66	0,14	0,00	0,17	0,04	0,09	0,69	0,49	0,51	0,08	-0,13	-0,10	-0,05
Al$_2$O$_3$	9,94	9,14	9,23	8,79	-0,74	-0,79	-1,24	-0,92	11,62	11,29	12,32	11,14	1,81	1,39	2,57	1,40	1,79	12,00	11,62	11,55	2,59	2,19	2,12	2,30
Fe$_2$O$_3$*	9,04	10,05	8,94	9,52	1,07	-0,17	0,39	0,43	8,28	7,68	8,53	8,66	-0,67	-1,34	-0,38	-0,22	-0,65	8,18	8,16	9,03	-0,49	-0,51	0,40	-0,20
MnO	0,20	0,36	0,23	0,26	0,16	0,02	0,05	0,08	0,31	0,28	0,26	0,30	0,11	0,08	0,06	0,10	0,09	0,24	0,28	0,31	0,05	0,09	0,12	0,09
MgO	12,98	13,44	12,91	13,08	0,54	-0,17	-0,03	0,11	8,94	7,42	7,31	7,32	-3,94	-5,53	-5,55	-5,52	-5,14	6,42	7,15	6,24	-6,27	-5,51	-6,46	-6,08
CaO	3,36	4,82	5,11	5,17	1,49	1,71	1,77	1,65	2,98	3,85	3,22	3,95	-0,35	0,50	-0,09	0,66	0,18	3,71	3,35	2,83	0,52	0,14	-0,40	0,09
Na$_2$O	0,91	0,65	0,94	0,43	-0,26	0,02	-0,48	-0,24	0,86	1,23	1,09	1,51	-0,04	0,32	0,20	0,63	0,28	1,83	1,97	2,14	1,00	1,14	1,33	1,16
K$_2$O	3,97	4,47	4,98	4,64	0,53	0,97	0,62	0,71	5,95	5,73	5,77	5,43	2,04	1,78	1,89	1,56	1,82	5,06	6,05	5,18	1,32	2,35	1,44	1,70
P$_2$O$_5$	0,48	0,38	0,49	0,27	-0,10	0,01	-0,22	-0,10	0,17	0,44	0,39	0,42	-0,31	-0,04	-0,08	-0,06	-0,12	0,38	0,33	0,29	-0,08	-0,13	-0,17	-0,13
LOI	4,77	5,03	4,87	5,13	0,31	0,08	0,33	0,24	4,98	5,01	4,69	4,20	0,28	0,28	0,01	-0,47	0,02	5,02	5,03	4,27	0,50	0,50	-0,29	0,23
SO$_2$	0,07	0,22	0,21	0,35	0,15	0,14	0,27	0,19	0,43	0,51	0,49	0,39	0,36	0,44	0,43	0,33	0,39	0,68	0,55	0,47	0,64	0,50	0,42	0,52
Total	100,20	99,70	100,02	100,15					99,21	100,34	100,22	100,42						100,34	100,11	100,63				
g/1000 kg																								
S	353	1110	1050	1733	764	688	1363	939	2157	2553	2453	1953	1828	2209	2138	1637	1953	3399	2744	2336	3199	2503	2095	2599
Au	0,03	0,62	0,65	0,58	0,59	0,61	0,54	0,58	1,14	1,33	1,42	1,14	1,13	1,31	1,41	1,13	1,25	2	2	2	2	2	2	2
Ag	0,00	0,21	0,09	0,16	0,21	0,09	0,16	0,15	0,21	0,25	0,16	0,09	0,21	0,25	0,17	0,10	0,18	0	0	0	0	0	0	0
As	298	557	683	574	263	379	270	304	1237	1522	1759	1426	953	1229	1488	1154	1206	2016	2454	2182	1808	2255	1989	2017
Ba	62	196	153	222	135	90	158	128	219	232	290	271	160	171	233	215	195	271	199	245	222	146	195	188
Co	16	13	12	13	-3	-4	-4	-4	23	12	17	13	7	-4	1	-3	0	14	8	16	-2	-8	0	-3
Cr	67	51	68	46	-15	1	-20	-12	33	49	44	49	-33	-17	-22	-16	-22	48	41	44	-17	-24	-21	-20
Ni	16	15	6	24	-1	-9	8	-1	37	21	28	21	22	5	12	6	11	26	25	42	12	10	28	17
Rb	35	<15	<15	<15	-	-	-	-	51	43	56	48	17	8	22	14	15	59	64	57	27	32	25	28
Sn	22	143	165	139	123	142	116	127	133	109	153	80	113	88	134	60	99	126	91	119	110	73	103	96
Sr	72	365	203	255	295	129	180	202	237	222	162	118	167	151	92	49	115	169	152	196	104	86	134	108
Zn	23	53	77	28	30	53	5	29	26	31	38	22	3	8	15	-1	6	30	13	25	8	-10	3	0
Pb	8	8	8	13	0	0	5	1	0	12	9	11	-8	4	1	3	0	13	17	10	6	10	2	6
V	29	44	29	91	16	0	61	26	123	77	95	74	96	48	67	47	65	97	104	108	73	80	84	79
Y	2	4	1	6	2	-1	4	1	5	6	8	5	3	3	5	3	3	7	7	6	5	5	4	5
Cu	11	6	4	10	-5	-6	0	-4	0	10	9	11	-10	-1	-1	0	-3	11	12	8	1	2	-2	0
Mn	377	533	709	293	160	326	-87	133	1237	352	463	405	874	-24	94	36	245	352	163	234	-9	-207	-131	-116
La	21,58	3,06	2,50	18,98	-18,51	-19,11	-2,79	-13,47	16,81	18,27	27,90	23,70	-4,59	-3,26	6,75	2,56	0,37	27,6	26,4	23,6	7,26	5,83	3,11	5,40
Ce	44,13	34,27	23,00	41,69	-9,65	-21,31	-2,84	-11,27	44,39	45,20	55,00	46,12	0,75	1,23	11,73	2,85	4,14	53,6	50,0	41,7	11,85	7,90	-0,41	6,45
Nd	17,52	16,03	14,00	17,83	-1,39	-3,63	0,15	-1,62	18,36	15,94	22,00	13,61	1,05	-1,52	4,83	-3,65	0,17	20,6	18,0	19,2	3,99	1,21	2,66	2,62
Sm	4,73	2,58	1,37	2,89	-2,13	-3,37	-1,86	-2,45	3,60	4,25	5,30	4,90	-1,09	-0,46	0,66	0,27	-0,15	5,3	4,8	4,7	0,84	0,27	0,20	0,44
Eu	0,83	0,68	0,49	0,74	-0,14	-0,34	-0,09	-0,19	0,82	0,83	0,90	0,81	0,00	0,01	0,09	0,00	0,03	0,9	0,9	0,9	0,15	0,11	0,12	0,13
Tb	0,58	0,70	0,66	0,61	-	-	-		<0,5	<0,5	<0,5	<0,5	-	-	-			<0,5	<0,5	<0,5	-	-	-	0,00
Yb	0,67	<0,1	<0,1	<0,1	-	-	-		2,11	2,01	2,80	1,93	1,46	1,35	2,17	1,29	1,57	2,8	2,7	2,3	2,24	2,14	1,77	2,05
Lu	0,10	0,13	0,15	0,21	0,03	0,05	0,11	0,06	0,19	0,15	0,12	0,13	0,09	0,05	0,02	0,03	0,05	0,2	0,2	0,2	0,06	0,09	0,09	0,08

Appendix F: The microthermometric data

Microthermometric measurements of fluid inclusions were determined at the Institute of applied mineralogy and geochemistry, Technical University of Munich. The measurements and the petrographic examination were carried out on seven doubly- polished thick wafers (100-200 μm thick) of samples representing the main auriferous quartz veins in the Um El Tuyor mine area. A Linkam THM 600 heating/freezing stage, provided with a thermal control unit TMS-93 and equipped with a binocular Olympus microscope was employed to obtain the microthermometric data. The stage enables measurements within the range of -196 and 600°C. Freezing and heating runs were, respectively, undertaken using liquid nitrogen and a thermal resistor. Calibration of the stage was carried out by using standard natural and synthetic inclusions. To ensure accurate observation of melting behaviour, heating rates were slow (0.2 to 0.5^{o}C/min), whilst to avoid metastability, freezing rates were very much faster. For all final melting temperatures of CO_2, precision is ±0.1^{o}C. Melting temperature of ice in the aqueous inclusions was relatively difficult to monitor and as such, is less precise.

Data obtained from microthermometry and occasionally volume fraction estimates of the fluid inclusions were evaluated by using several newly designed computer program packages *CLATHRATES* (Bakker 1997) and *FLUIDS* (Bakker 1999) in order to transform melting temperatures, homogenisation temperatures and optical volume fraction estimates into bulk compositions and densities, which are used for isochore calculations. Densities of H_2O and CO_2 are calculated from the equation of state by Saxena and Fei (1987). Equation of state used for isochore calculations are after Bowers & Helgeson (1983) and Bakker (1999).

Table F.1: Microthermometric data of the carbonic inclusions in the quartz-carbonate and laminated quartz veins in the Um El Tuyor mine area

Sample	mode	T_{mCO2}	T_{hCO2}	Hom. mode	dCO2 (g/cm3)	MV	Phom(kbar)
t-230	P	-57.1	20.8	L	0.7656	57.5	0.047
t-230	P	-56.7	20.9	L	0.7645	57.6	0.047
t-230	P	-58.1	10.8	L	0.8559	51.4	0.059
t-230	PS	-58.2	10.9	L	0.8551	51.5	0.058
t-230	PS	-57.9	16.3	L	0.8105	54.3	0.052
t-230	P	-59.3	9.8	L	0.8633	51.0	0.060
t-230	PS	-58.3	11.7	L	0.8490	51.8	0.057
t-230	PS	-57.1	17.4	L	0.8004	55.0	0.051
t-230	PS	-59.3	10.9	L	0.8551	51.5	0.058
t-230	P	-58.6	6.3	L	0.8880	49.6	0.064
t-230	P	-58.5	9.9	L	0.8626	51.0	0.060
t-230	P	-56.9	20.8	L	0.7656	57.5	0.047
t-236	PS	-57.6	13.7	L	0.8330	52.8	0.055
t-236	PS	-56.6	20.5	L	0.7689	57.2	0.047
t-236	PS	-57.1	14.8	L	0.8237	53.4	0.054
t-236	PS	-58.3	12.7	L	0.8411	52.3	0.056
t-236	PS	-57.7	18.6	L	0.7887	55.8	0.049
t-236	PS	-57.1	12.1	L	0.8458	52.0	0.057
t-236	PS	-56.6	26.9	L	0.6794	64.8	0.040
t-236	P	-58.1	8.7	L	0.8713	50.5	0.061
t-236	P	-58.4	6.9	L	0.8839	49.8	0.064
t-236	PS	-57.8	11.3	L	0.8521	51.7	0.058
t-236	PS	-59.2	8.1	L	0.8756	50.3	0.062
t-236	PS	-58.3	11.9	L	0.8474	51.9	0.057
t-236	PS	-58.9	9.1	L	0.8684	50.7	0.061
t-236	PS	-56.8	9.2	L	0.8677	50.7	0.061
t-236	PS	-56.6	26.1	L	0.6939	63.4	0.041
t-230-d	P	-56.8	24.1	L	0.7246	60.7	0.043
t-230-d	P	-56.6	23.2	L	0.7368	59.7	0.044

P: primary, PS: pseudosecondary, S: secondary

continue

Microthermometric data of the carbonic inclusions							
Sample	mode	T_{mCO2}	T_{hCO2}	Hom. mode	dCO2 (g/cm3)	MV	Phom(kbar)
t-236	PS	-58.8	5.8	L	0.8914	49.4	0.065
t-236	PS	-56.6	26.8	L	0.6813	64.6	0.040
t-230-d	P	-58.3	11.4	L	0.8513	51.7	0.058
t-230-d	P	-58.3	19.7	L	0.7775	56.6	0.048
t-230-d	S	-56.7	10.6	L	0.8574	51.3	0.059
t-230-d	S	-56.6	14.8	L	0.8237	53.4	0.054
t-230-d	S	-56.7	26.5	L	0.6868	64.1	0.040
t-16	PS	-56.9	20.3	L	0.7711	57.1	0.047
t-16	PS	-58.9	3.7	L	0.9052	48.6	0.068
t-16	PS	-56.6	25.5	L	0.7038	62.5	0.041
t-16	PS	-56.7	24.7	L	0.7160	61.5	0.042
t-16	PS	-57.2	12.8	L	0.8403	52.4	0.056
t-16	PS	-58.1	14.3	L	0.8280	53.2	0.054
t-16	S	-57.1	19.8	L	0.7764	56.7	0.048
t-218	PS	-56.6	28.8	L	0.6365	69.1	0.039
t-218	PS	-57.1	18.7	L	0.7877	55.9	0.049
t-218	PS	-56.8	20.2	L	0.7722	57.0	0.047
t-218	S	-57.3	4.2	L	0.9019	48.8	0.067
t-218	S	-56.6	13.3	L	0.8362	52.6	0.055
t-218	S	-56.7	5.7	L	0.8921	49.3	0.065
t-218	S	-57.9	10.3	L	0.8596	51.2	0.059
t-218	S	-59.3	4.4	L	0.9006	48.9	0.067
t-218	PS	-57.1	10.6	L	0.8574	51.3	0.059
t-218	PS	-58.5	9.9	L	0.8626	51.0	0.060
t-218	PS	-56.7	24.1	L	0.7246	60.7	0.043
t-17	PS	-57.1	20.4	L	0.1972	223.2	0.052
t-17	PS	-57.2	6.6	L	0.8860	49.7	0.064
t-17	S	-56.8	22.9	L	0.7406	59.4	0.044
t-17	S	-57.1	13.1	L	0.8379	52.5	0.056
t-17	S	-56.7	26.1	L	0.6939	63.4	0.041
t-17	S	-57.8	4.8	L	0.8980	49.0	0.066
t-17	S	-56.7	24.2	L	0.7232	60.9	0.043
t-17	S	-56.9	12.8	L	0.8403	52.4	0.056
t-17	S	-56.7	15.7	L	0.8159	53.9	0.053
t-17	S	-56.6	22.6	L	0.7444	59.1	0.045
t-218	PS	-57.1	14.4	L	0.8274	53.2	0.054
t-218	PS	-56.9	12.6	L	0.8422	52.3	0.056
t-218	PS	-56.9	7.7	L	0.8782	50.1	0.062
t-17	PS	-57.1	9.8	L	0.8636	51.0	0.060
t-16r	PS	-58.0	6.8	L	0.8846	49.7	0.064
t-16r	PS	-58.1	8.4	L	0.8732	50.4	0.062
t-16r	PS	-58.3	8.3	L	0.8742	50.3	0.062
t-16r	PS	-57.4	14.9	L	0.8232	53.5	0.054
t-16r	PS	-57.4	18.1	L	0.7933	55.5	0.050
t-16r	PS	-56.8	17.0	L	0.8038	54.8	0.051
t-16r	PS	-57.0	16.6	L	0.8075	54.5	0.051
t-16r	S	-56.8	14.2	L	0.8288	53.1	0.054
t-16r	S	-56.6	20.7	L	0.7667	57.4	0.047
t-16r	S	-56.7	14.7	L	0.8249	53.4	0.054
t-16r	S	-56.6	18.4	L	0.7910	55.6	0.049
t-16r	S	-56.8	13.9	L	0.8310	53.0	0.055
t-16r	S	-56.6	17.6	L	0.7988	55.1	0.050
t-16r	S	-56.6	17.0	L	0.8038	54.8	0.051

Table F.2: Microthermometric data of the aqueous-carbonic inclusions in the quartz-carbonate veins in the Um El Tuyor mine area

			Microthermometry (°C)				Densities(g/cm3)		Salinity		Bulk composition (mole%)			Total density		
Sample	mode	DF(V_{aq}/V_t)	T_{mCO_2}	T_{mCl}	T_{hCO_2}	T_{htotal}	dCO_2	dH_2O	wt% NaCl equiv.	moles.aq.	XCO_2	XH_2O	XNaCl	d_{total}(g/cm³)	MVtot	Phom(kbar)
t-230	p	0.65	-56.7	6.9	21.6	312.2	0.7565	1.0330	5.9372	1.0801	0.144	0.840	0.016	0.9362	23.95	2.155
t-230	p	0.60	-56.8	5.5	25.1	326.4	0.7100	1.0503	8.2418	1.5370	0.164	0.814	0.023	0.9142	25.35	1.925
t-230	ps	0.75	-57	8.1	20.2	286.4	0.7722	1.0174	3.7742	0.6712	0.096	0.893	0.011	0.9561	21.91	2.234
t-230	ps	0.60	-56.7	7.6	24.6	292.7	0.7175	1.0240	4.6954	0.8430	0.165	0.822	0.013	0.9014	25.30	1.526
t-230	p	0.70	-56.8	7.9	25.1	288.6	0.7100	1.0200	4.1461	0.7402	0.112	0.877	0.012	0.9270	23.07	1.734
t-230	p	0.60	-57.2	5.8	20.5	322.5	0.7689	1.0465	7.7431	1.4362	0.175	0.804	0.021	0.9355	25.01	2.201
t-230-d	p	0.70	-57.2	8.4	11.3	287.3	0.8521	1.0134	3.2074	0.5670	0.131	0.860	0.009	0.9650	22.57	2.522
t-230-d	p	0.80	-56.7	8.8	24.7	243.7	0.7160	1.0080	2.4351	0.4271	0.069	0.924	0.007	0.9496	21.16	1.351
t-230-d	p	0.70	-56.8	7.5	24.9	262.1	0.7131	1.0253	4.8762	0.8772	0.112	0.874	0.014	0.9316	23.06	1.266
t-230-d	p	0.70	-56.7	7.7	24.7	277.4	0.7160	1.0227	4.5134	0.8088	0.113	0.875	0.013	0.9307	23.05	1.558
t-230-d	ps	0.65	-56.6	7.4	25.6	289.1	0.7022	1.0266	5.0558	0.9112	0.135	0.851	0.014	0.9130	24.20	1.519
t-230-d	ps	0.55	-56.7	6.3	24.5	313.2	0.7190	1.0406	6.9586	1.2798	0.196	0.786	0.018	0.8959	26.60	1.689
t-236	ps	0.65	-57.6	7.8	18.9	296.3	0.7857	1.0214	4.3304	0.7745	0.149	0.839	0.012	0.9389	23.81	2.093
t-236	ps	0.60	-56.7	5.8	24.9	309.0	0.7131	1.0468	7.7803	1.4437	0.164	0.815	0.021	0.9133	25.34	1.703
t-236	ps	0.60	-57.9	6.2	13.8	299.7	0.8321	1.0419	7.1250	1.3127	0.187	0.795	0.019	0.9580	24.66	2.244
t-236	ps	0.65	-57.3	6.7	20.2	299.4	0.7722	1.0356	6.2820	1.1470	0.147	0.836	0.017	0.9434	23.88	2.028
t-236	p	0.60	-56.7	6.1	22.6	300.6	0.7444	1.0431	7.2904	1.3456	0.170	0.810	0.020	0.9236	25.15	1.750
t-236	p	0.60	-56.7	8.3	24.6	301.3	0.7175	1.0147	3.3975	0.6018	0.165	0.826	0.009	0.8958	25.30	1.669
t-236	p	0.55	-56.8	7.4	18.4	319.0	0.7907	1.0266	5.0558	0.9112	0.211	0.776	0.013	0.9204	26.09	2.190
t-236	p	0.50	-57	7.1	19.1	321.2	0.7837	1.0305	5.5880	1.0128	0.245	0.742	0.014	0.9071	27.47	2.062
t-230-d	p	0.65	-56.6	6.9	23.0	304.4	0.7394	1.0330	5.9372	1.0801	0.141	0.842	0.016	0.9302	24.03	1.937
t-230-d	p	0.60	-56.7	8.1	21.6	317.5	0.7562	1.0180	3.8676	0.6884	0.172	0.817	0.010	0.9133	25.08	2.116
t-230-d	ps	0.60	-56.8	9.3	20.7	296.1	0.7673	1.0011	1.4423	0.2504	0.174	0.822	0.004	0.9076	25.01	1.891
t-230-d	ps	0.65	-57.1	7.0	19.6	288.3	0.7785	1.0324	5.8503	1.0633	0.148	0.836	0.016	0.9435	23.85	1.888
t-230	ps	0.65	-58.5	7.4	5.2	285.8	0.8955	1.0268	5.0898	0.9177	0.166	0.820	0.014	0.9809	23.33	2.579
t-230	ps	0.70	-57.7	7.9	8.8	267.2	0.8706	1.0203	4.1812	0.7467	0.134	0.855	0.012	0.9754	22.51	2.210
t-230	p	0.60	-57.3	7.5	3.4	278.7	0.9071	1.0251	4.8545	0.8731	0.200	0.788	0.012	0.9779	24.25	2.436
t-230	p	0.70	-59.2	8.5	4.6	259.8	0.8993	1.0119	2.9931	0.5280	0.137	0.855	0.008	0.9781	22.40	2.269
t-230	p	0.75	-57.2	7.7	8.9	277.4	0.8699	1.0226	4.5025	0.8068	0.107	0.880	0.013	0.9844	21.65	2.556
t-230	p	0.70	-58.3	7.9	7.3	262.0	0.8812	1.0195	4.0703	0.7260	0.135	0.854	0.011	0.9780	22.47	2.172
t-230	ps	0.70	-56.7	7.8	23.6	262.2	0.7315	1.0210	4.2881	0.7666	0.115	0.873	0.012	0.9342	23.00	1.363
t-230	ps	0.45	-56.6	6.5	24.7	326.7	0.7160	1.0387	6.7018	1.2292	0.266	0.718	0.016	0.8612	29.68	1.665
t-230	ps	0.7	-56.6	7.7	12.2	286.4	0.8451	1.0226	4.5025	0.8068	0.130	0.857	0.012	0.9693	22.60	2.421
t-230	ps	0.65	-56.6	5.9	18.6	292.7	0.7887	1.0451	7.5512	1.3977	0.149	0.830	0.021	0.9554	23.80	1.987
t-230	p	0.70	-57.6	7.4	22.3	288.6	0.7481	1.0272	5.1345	0.9261	0.117	0.869	0.015	0.9434	22.94	1.903

t-230	ps	0.55	-56.7	7.6	12.3	281.2	0.8443	1.0238	4.6772	0.8396	0.222	0.766	0.012	0.9430	25.72	1.971
t-230	p	0.80	-56.6	8.1	5.9	270.1	0.8911	1.0174	3.7742	0.6712	0.084	0.905	0.011	0.9921	20.81	2.727
t-230	p	0.65	-58.7	8.6	7.0	294.7	0.8832	1.0107	2.8237	0.4972	0.164	0.828	0.007	0.9661	23.38	2.721
t-230	p	0.55	-58.3	9.2	15.7	303.1	0.8162	1.0025	1.6433	0.2859	0.216	0.780	0.004	0.9187	25.90	2.166
t-230	p	0.70	-57.4	8.7	16.7	274.9	0.8072	1.0093	2.6300	0.4622	0.125	0.868	0.007	0.9487	22.72	2.031
t-230	p	0.50	-56.9	5.2	10.6	341.6	0.8570	1.0540	8.7229	1.6353	0.262	0.717	0.021	0.9555	26.86	2.786

Table F.3: Microthermometric data of the aqueous inclusions in the quartz-carbonate veins in the Um El Tuyor mine area

Sample	mode	$T_{m\,ice}$	$T_{h\,total}$	Hom. mode	Salinity (wt% eq. NaCl)	Bulk composition (mole%) XH2O	XNaCl
t-230	PS	-1.1	201.0	L	1.8	0.994	0.006
t-230	PS	-0.8	234.9	L	1.2	0.996	0.004
t-230	PS	-1.8	187.5	L	3.1	0.990	0.010
t-230	PS	-1.8	198.1	L	3.1	0.990	0.010
t-230	S	-1.3	174.3	L	2.1	0.993	0.007
t-230	PS	-2.1	181.6	L	3.6	0.989	0.011
t-230	PS	-1.7	179.6	L	2.9	0.991	0.009
t-230-d	PS	-2.1	187.0	L	3.6	0.989	0.011
t-230-d	PS	-1.5	177.5	L	2.5	0.992	0.008
t-230-d	S	-1.7	167.3	L	2.9	0.991	0.009
t-230-d	PS	-2.9	143.6	L	5.1	0.984	0.016
t-230-d	PS	-2.5	169.2	L	4.4	0.986	0.014
t-230-d	PS	-2.7	158.4	L	4.7	0.985	0.015
t-230-d	PS	-0.8	254.7	L	1.2	0.996	0.004
t-230-d	PS	-2.6	199.2	L	4.5	0.986	0.014
t-230-d	PS	-1.9	183.5	L	3.2	0.990	0.010
t-230-d	S	-2.6	169.7	L	4.5	0.986	0.014
t-230-d	PS	-2.7	154.2	L	4.7	0.985	0.015
t-230-d	PS	-1.1	203.7	L	1.8	0.994	0.006
t-230-d	PS	-1.9	192.2	L	3.2	0.990	0.010
t-230-d	PS	-2.7	168.1	L	4.7	0.985	0.015

Lebenslauf

Persönliche Daten

Name:	Basem Ahmed Zoheir El Safty
Nationalität:	ägyptisch
Geburtsdatum:	02.08.1973
Familienstand:	verheiratet, ein Sohn
E-mail Adresse:	b_elsafty@scientist.com

Schulbildung und Studium:

1979-1985: Elementary School

1985-1988: Preparatory School

1988-1991: Secondary School, Erwerb der allgemeinen Hochschulreife 1990/1991

1991-1995: Studium der Geologie, Universität Benha, mit dem Abschluss Bachelor (Note: Mit Auszeichnung, hons.)

1996/1997: Aufbaustudium (Vorbereitungsphase) im Fachbereich Geologie an der Universität Ain Shams, Ägypten

1997-1999: Studium mit Erlangung des M.Sc. im Fachbereich Geologie, Universität Ain Shams, Ägypten

1999-2002: Wissenschftlicher Assistent im Fachbereich Geologie, Universität Zagazig, Ägypten

2002-2004: Doktorant an der LMU-München (Fachbereich Geologie)

Berufstätigkeit:

1996-1999: Wissenschftlicher Assistent, Fakultät der Wissenschaften, Universität Zagazing, Abteilung Benha.

1999-2001: Teilzeit Mitarbeiter in der Ras Mohamed Nationalpark Verwaltung, Ägypten.

1999 bis heute: Dozent (Assistant Instructor) für Geologie an der Fakultät der Wissenschaften, Abteilung Benha Universität Zagazing.

Sonstige Qualifikationen:

Grade 597 in CB-TOEFL (Computer Based Test of English as Foreign Language)

Goethe Institut Mannheim: Zwei Deutschkurse

Publikationen:

M. Sc. Thesis:

Geology, petrology and mineralogy of copper mineralization in the basement rocks in some occurrences in south Sinai, Egypt (unveröffentlicht).

Wetait, M., Osman, A. Mehanna, A., Zoheir, B. (2000): Contribution to Saint Catherine copper ore genesis: a porphyry model constraints. Delta. Sci. Jr. (2000), 13-32 (veröffentlicht).

Referenzen:

Prof. Dr. Maher A. Takla (Professor für Petrologie, Vorsitzender der Abteilung für Geologie, Fakultät der Wissenschaften), Universität Kairo, Ägypten.

Prof. Dr. Mohamed E. Hilmy (em. Professor für Mineralogie), Universität Ain Shams, Kairo, Ägypten.